Transactions of the ASME® Journal of Engineering for Gas Turbines and Power

Published Quarterly by The American Society of Mechanical Engineers
VOLUME 116 • NUMBER 4 • OCTOBER 1994

Technical Editor,
H. L. JULIEN (1998)
Associate Technical Editors
Advanced Energy Systems
M. J. MORAN (1996)
Fuels and Combustion Technologies
D. W. PACER (1994)
Gas Turbine
C. J. RUSSO (1995)
R. KIELB (1996)
S. SAMUELSEN (1996)
Internal Combustion Engine
W. CHENG (1996)
Nuclear Engineering
H. H. CHUNG (1996)
Power
P. H. GILSON (1996)

BOARD ON COMMUNICATIONS
Chairman and Vice-President
R. D. ROCKE

Members-at-Large
T. BARLOW, N. H. CHAO, A. ERDMAN,
G. JOHNSON, L. KEER, W. MORGAN,
E. M. PATTON, S. PATULSKI, R. E. REDER,
S. ROHDE, R. SHAH, F. WHITE,
J. WHITEHEAD

OFFICERS OF THE ASME
President, **P. J. TORPEY**
Exec. Director
D. L. BELDEN
Treasurer
R. A. BENNETT

PUBLISHING STAFF
Mng. Dir., Publ.
CHARLES W. BEARDSLEY
Managing Editor,
CORNELIA MONAHAN
Sr. Production Editor,
VALERIE WINTERS
Production Assistant,
MARISOL ANDINO

Transactions of the ASME, Journal of Engineering for Gas Turbines and Power (ISSN 0742-4795) is published quarterly (Jan., Apr., July, Oct.) for $150.00 per year by The American Society of Mechanical Engineers, 345 East 47th Street, New York, NY 10017. Second class postage paid at New York, NY and additional mailing offices. POSTMASTER: Send address changes to Transactions of the ASME, Journal of Engineering for Gas Turbines and Power, c/o THE AMERICAN SOCIETY OF MECHANICAL ENGINEERS, 22 Law Drive, Box 2300, Fairfield, NJ 07007-2300.
CHANGES OF ADDRESS must be received at Society headquarters seven weeks before they are to be effective. Please send old label and new address.
PRICES: To members, $40.00, annually: to nonmembers, $150.00.
Add $30.00 for postage to countries outside the United States and Canada.
STATEMENT from By-Laws. The Society shall not be responsible for statements or opinions advanced in papers or . . . printed in its publications (B 7.1, para. 3).
COPYRIGHT © **1994** by The American Society of Mechanical Engineers. Authorization to photocopy material for internal or personal use under circumstances not falling within the fair use provisions of the Copyright Act is granted by ASME to libraries and other users registered with the Copyright Clearance Center (CCC) Transactional Reporting Service provided that the base fee of $3.00 per article is paid directly to CCC, 27 Congress St., Salem, MA 01970. Request for special permission or bulk copying should be addressed to Reprints/Permission Department.
INDEXED by Applied Mechanics Reviews and Engineering Information, Inc.
Canadian Goods & Services Tax Registration #126148048

TECHNICAL PAPERS

ANNOUNCEMENTS

Downloaded 03 Jun 2010 to 171.66.16.159. Redistribution subject to ASME license or copyright; see http://www.asme.org/terms/Terms_Use.cfm

1993 Soichiro Honda Lecture

The Challenges of Change in the Auto Industry: Why Alternative Fuels?

R. J. Nichols
Ford Motor Company,
Dearborn, MI 48124

Development of vehicles to operate on nonpetroleum fuels began in earnest in response to the energy shocks of the 1970s. While petroleum will remain the predominant transportation fuel for a long time, petroleum supplies are finite, so it is not too soon to begin the difficult transition to new sources of energy. In the past decade, composition of the fuel utilized in the internal combustion engine has gained recognition as a major factor in the control of emissions from the tailpipe of the automobile and the rate of formation of ozone in the atmosphere. Improvements in air quality can be realized by using vechicles that operate on natural gas, propane, methanol, ethanol, or electricity, but introduction of these alternative fuel vehicles presents major technical and economic challenges to the auto industry, as well as the entire country, as long as gasoline remains plentiful and inexpensive.

The Rationale for Change

When looking back over the past two decades, it is interesting to note that the answer to the question "Why Alternative Fuels?" has changed considerably, at least for the near term. Development of the technology required to operate transportation vehicles on alternative sources of energy began in direct response to the energy crises of the 1970s, and acknowledgment of the fact that the world has a finite supply of crude oil.

But as gasoline prices fell and the memories of the long refueling lines faded, the work continued because results were emerging from alternative fuel research throughout the world that showed there was the potential for improving air quality by replacing the use of gasoline and diesel fuels with some of these alternatives. It has become widely accepted, as evidenced by the debate associated with the Clean Air Act Amendments in 1990, that almost all of the alternative fuels have the potential to reduce the amount of ozone formed in the atmosphere compared with today's fuels.

Hence, improvement in air quality became the near-term driver for the development of vehicles to use alternative fuels, but long-term the other reason remains, i.e., the need for alternative sources of energy as our reserves of petroleum diminish. Recent events in the Middle East make this need even more compelling. The timing for the long-term need to replace petroleum-based fuels is not clearly defined—it may be 50, or even 100, years from now—but it is a very difficult transition from the old fuel to the new fuel, so it is not too soon to start, providing it can be done in an orderly fashion with justifiable costs and benefits for the consumer.

Table 1 Alternative fuel candidates

- GASEOUS FUELS
  - Methane (natural gas)
  - Propane (LPG)
  - Hydrogen
- LIQUID FUELS
  - Reformulated gasoline and diesel
  - Methanol
  - Ethanol
- ELECTRICITY
  - Battery energy storage
  - (Generated by coal, natural gas, hydro, solar, nuclear, wind, renewables, etc.)

The Alternative Fuel Candidates

The most promising alternative fuel candidates at present are natural gas, propane or LPG (liquefied petroleum gas), methanol and ethanol, and electricity. Future energy needs are not likely to be filled by any one fuel because the alternative fuel of interest varies in different regions of our country, and the world, depending on the availability and economics of the resource in that particular area. The fuels likely to appear in the future are listed in Table 1.

These alternatives fall into three general classes: gaseous and liquid fuels combusted in heat engines on board the vehicle, and electrical energy stored in a battery generated by a variety of energy sources.

There are many fuel properties and combustion characteristics one must consider when designing engines and fuel systems [1]. Many of these inherent properties are quite different

---

Contributed by the Internal Combustion Engine Division and presented at the 15th Annual Fall Technical Conference of the ASME Internal Combustion Engine Division, Morgantown, West Virginia, September 26-29, 1993. Manuscript received by the Internal Combustion Engine Division January 28, 1994. Associate Technical Editor: W. Cheng.

Table 2 Energy densities compared to gasoline

	Mass Ratio	Volume Ratio
Natural Gas		
CNG	0.89	4.8-5.9
LNG	0.89	1.57
Propane (LPG)	0.89	1.29
Hydrogen (LH2)	0.37	3.93
Reformulated Gasoline	1.02	1.01
No. 2 Diesel	1.01	0.88
Methanol		
M100	2.19	2.03
M85	1.87	1.76
Ethanol	1.64	1.53

for the alternative fuels compared to gasoline or diesel fuel, and need to be well understood in order to meet today's stringent emission standards, while maximizing the fuel efficiency and performance.

The energy density of the fuel is the factor that creates the most confusion for the average person when discussing fuel economy or fuel efficiency since miles per gallon (MPG) has been the common basis for so long. As alternative fuels appear in the market, however, it is important to learn to think in terms of miles per energy unit. On this basis, most of the alternatives are more energy efficient than gasoline even though they may require more gallons of fuel to go the same distance down the road. Fuels also should be taxed on an energy basis rather than by the gallon since not every gallon contains the same amount of energy, as shown in Table 2.

Diesel fuel is the only fuel listed in Table 2 that has a volumetric energy density higher than gasoline; i.e., 12 percent of the higher miles per gallon of the diesel-powered vehicle disappears when the fuel efficiency is measured on a miles per energy unit basis. Natural gas and hydrogen can be stored on board the vehicle as a high-pressure gas, or cryogenically stored as a liquid, which reduces the amount of space required for a given amount of energy. Cryogenic storage increases the cost of the fuel and complexity of the system, however.

Gaseous fuels perform quite well in engines, but their physical and chemical characteristics dictate that the engine be dedicated to the use of that fuel in order to achieve performance equivalent to gasoline.

Hydrogen could become an important fuel in the future if definitive evidence of global warming were to emerge (no CO_2 emissions), but for now it remains too expensive for use in the IC engine: about ten times the cost of gasoline per mile. Its best use may be in fuel cell applications where good progress has been made in recent years, but this technology is still very expensive and much research remains to be done.

The liquid fuels are the most compatible with existing distribution systems and engines; i.e., they require the least departure from the technologies in place today for both the vehicles and the refueling infrastructure. The biggest challenge is related to the change in materials required for the fuel system exposure to the alcohols, especially methanol, since they are more corrosive than gasoline.

Reformulated gasoline and reformulated diesel fuel are certainly "fuels of the future" also. They have the advantage of utilization in today's existing vehicle population, whereas the improvements from the other alternative fuels will be much slower because they depend on gradual replacement of the old vehicles with the new ones, or fleet turnover.

A major auto/oil CRC (Coordinating Research Council) program was initiated in the summer of 1989 to determine the possible air quality benefits, and cost of changes in the formulation of gasoline and diesel fuel. In general, reformulated gasoline will have a reduction in aromatic and olefin content, with an increased use of oxygenates such as methyl tertiary butyl ether (MTBE) or ethyl tertiary butyl ether (ETBE) to maintain the octane levels. The primary change in reformulated diesel fuel is a reduction in the sulfur level.

The third category of alternative fuels, electricity, represents the most challenges for the auto industry since the electric vehicle is the biggest departure from the vehicle technology in place today. The ultimate key to its success is development of advanced battery technologies.

Natural Gas. Natural gas is one of the most environmentally benign fuels, with the most potential for ozone reduction. But there is an increase in methane emissions, one of the major constituents of natural gas. Since methane is a greenhouse gas with a rate of warming several times greater than that of CO_2, the increase in methane emissions needs to be well-understood in terms of global warming effects.

Experience has shown there is a 10 to 20 percent power loss associated with the use of gaseous fuels in the IC engine because of the inherent volumetric efficiency loss. In order to achieve performance equal to operation on gasoline, one needs to dedicate the vehicle to the use of natural gas and take advantage of the high octane quality of the methane, the primary constituent of natural gas, which is estimated at 130 RON. This allows engine compression ratios of 13-14:1 depending on the combustion chamber configuration. Other intake system design changes are helpful also [2].

The compressed natural gas (CNG) vehicle has a difficult driving range program, being about one-fourth that of gasoline for a given volume of fuel storage space, even when stored at 3000 psi. It also has a high initial vehicle cost because of the high-pressure tanks, which are inherently expensive. This higher cost can be amortized with the lower cost of the fuel for the high mileage fleet operator. The average private citizen, however, does not drive enough miles per year to amortize the higher initial cost of the vehicle. Also, a fast fill (about 5 minutes) refueling station costs approximately $250,000-300,000, making it unlikely that sufficient infrastructure will appear to justify private consumer ownership. Development of reliable, low-cost home refueling in those areas with natural gas at the place of residence could change this market, however.

Liquefied natural gas (LNG) storage improves the energy density on board, and hence increases the driving range, but there is additional cost associated with liquifaction and cryogenic storage (-258 °F), as well as the need for highly trained personnel for refueling because of the potential for severe human tissue damage if not done properly.

High-pressure storage tanks made of aluminum and wrapped with a high-strength composite such as Kevlar have replaced the heavier steel tanks. Research is in progress using other materials that would allow space-saving noncylindrical shapes to be utilized for the storage of the high-pressure gas. Lower pressure storage using adsorbent materials such as carbon or zeolite has also been studied [3].

As a few natural gas vehicles have begun to operate in the field, the variation in gas composition from region to region has been identified as a problem. Also, lack of temperature compensation on the refueling pumps has resulted in underfill of the fuel tanks and a reduction in an already limited driving range.

Propane (LPG). LPG of the quality for vehicle use (HD-5) is about 95 percent propane. It can be stored as a liquid at nominal pressure (~ 160 psi) making the driving range of the LPG vehicle quite comparable to that of gasoline. It takes 1.3 gallons of propane to equal the energy content of one gallon of gasoline, but the engine can be designed to be more energy efficient so the miles per energy unit is higher. While the octane rating of propane is not as high as methane, it is high enough (~ 112 RON) to permit compression ratios of 10.5-11:1 with engines designed to operate on LPG. Again, the engine should be dedicated to the use of LPG in order to offset the inherent volumetric efficiency loss of gaseous fuel operation. The refueling infrastructure for propane is already quite extensive because of recreational and rural use, with more than 5000 stations across the nation.

Development of liquid fuel injection systems for LPG engines is in progress, which should result in even further gains in performance and efficiency.

LPG comes from several different sources. It is stripped from natural gas because of the disparity in their boiling points (−258 °F for methane compared to −44 °F for propane). If not removed, when the natural gas is pumped through the pipelines with compressors, the propane could liquefy causing problems. Propane is also produced in conjunction with crude-oil wells, and is a byproduct of refinery operations.

Ethanol. Ethanol probably will remain an additive for gasoline in this country unless the economics of its production change radically. There is work in progress at National Renewable Energy Laboratory (NREL) in Golden, Colorado, which shows promise in this area, but the process probably will not be practical until the year 2010 or so.

The production of ethanol vehicles in Brazil has been a technical success. The vehicles have had good reliability, high performance, and high fuel efficiency. The primary problems have been associated with uncertainties in the fuel supply.

The ethanol in Brazil is produced from sugar cane. Every time the price of sugar goes up, it tends to create a fuel shortage because the producers push their production in the direction of sugar instead of fuel. Over 35 percent of the vehicles on the road today in Brazil are ethanol-fueled. Production began in 1979 and by 1987, 99 percent of Ford's passenger car sales in Brazil were ethanol vehicles, but a few years ago there was a severe fuel shortage, and ethanol vehicle sales dropped dramatically. Last year the fuel supply stabilized; in fact, they are supplementing some of the supply with methanol from Chile by selling a 60 percent ethanol, 33 percent methanol, and 7 percent gasoline mix, and sales are moving up again.

Because of these supply and demand problems, the Brazilian government has been interested in the flexible fuel vehicle or FFV (runs on alcohol or gasoline) since it could cope with these swings in the market, but not all of the necessary technology is available in Brazil for FFV production because of their strict local content laws. (This is changing, however.)

Methanol. The alcohols have a difficult cold-start problem because of their low vapor pressure, single boiling point, and high latent heat of vaporization. Ethanol is even more difficult than methanol. In Brazil, a small amount of gasoline is introduced into the intake system ahead of trying to start on the ethanol, but even the lowest ambient temperatures in Brazil (about 14°F) are warm compared to the winter ambients in the United States. One of the major breakthroughs for methanol use came in 1986 when Ford developed a practical cold start system that met our industry standard for cold starts at −20 °F [4].

The need to increase the vapor pressure, combined with the lack of flame visibility of 100 percent methanol (there is only one carbon atom and hence, no soot formation to give the flame color), has led to the common use of M85 or 85 percent methanol and 15 percent gasoline. As shown in Table 2, this also increases the volumetric energy density of a gallon of fuel, which increases the driving range of the vehicle for a given size fuel tank.

There has been a major effort in North America applied to the development of methanol-fueled vehicles since methanol probably is the best candidate for widespread, long-term replacement of petroleum-based fuels, with the gaseous fuel and electric vehicles being more useful in fleets or niche markets. Methanol has a huge potential resource base (it can be made out of any organic material), and it has the engineering and cost advantages of being a liquid fuel in terms of the vehicle and distribution system.

Almost all of today's methanol is made from natural gas, but it can also be made from biomass or municipal waste. Long-term the resource could be coal, which the world has a several hundred year supply, with about 25 percent of it in the U.S.

Development of the methanol vehicle began with engines dedicated to the use of methanol, making it possible to take advantage of its many inherent high quality properties, including octane rating (~110 RON). Compression ratios of 12:1 or higher brought substantial increases in power (~20 percent) and fuel efficiency (~15 percent), while at the same time being able to achieve NO_x emissions levels of 0.4 gm/mi, even with carbureted engines [5].

The major problem associated with the early dedicated methanol vehicles was the fact that a lot of drivers developed a high level of anxiety wondering if they were going to make it to the next methanol refueling station! (There were only eighteen methanol stations in all of California at the time.) Hence the development of the flexible fuel vehicle began. The FFV can operate on methanol or gasoline or any random mixture of the two fuels.

The FFV concept appears to be the only way to get started. Once there are a sufficient number of vehicles in the field to justify the cost of the methanol infrastructure, one can make the transition to the dedicated vehicle. Apparently the federal government adopted this view also, since the development of the FFV led to passage of the "Alternative Motor Fuels Act of 1988." This legislation provides a powerful incentive to the auto industry to begin to produce alternative fuel vehicles, especially those that can operate on either methanol or gasoline, because the legislation recognizes the FFV as a potential nonpetroleum user and gives it favorable treatment in the calculation of the Corporate Average Fuel Economy (CAFE). For example, if one produces a methanol vehicle that gets 15 mpg (or 26.4 miles per energy unit), since only 15 percent of the fuel is petroleum-based (gasoline), for purposes of CAFE it becomes a 100 mpg vehicle. For the FFV, it is the harmonic average of the 100 mpg and whatever the fuel economy is on gasoline (say 26 mpg), which is still a very favorable number! The legislation has similar language for ethanol and natural gas vehicles. One of the nice features of the legislation is that it does not cost the government any money while providing the auto industry with an incentive to produce vehicles that are capable of operating on alternative fuels. There is legislation that provides a similar CAFE benefit for the electric vehicle as well.

The FFV does not require any special action on the part of the driver, other than to buy the fuel of choice. There is only one tank. The key to the flexibility is a fuel sensor which measures the amount of alcohol in the fuel in the tank. The fuel sensor sends a signal to the microprocessor or computer on board, which adjusts the fuel flow and spark timing to the optimum for whatever is in the tank. The oxygen sensor used on today's gasoline vehicles for control of air-fuel ratio does the final trimming so that the engine is always operating as close to stoichiometry as possible, no matter what the fuel. Now that the FFV technology has been developed to production levels, the concept is being expanded to ethanol operation as well.

One of the advantages of operation on methanol is higher performance. Even with the FFV, where the compression ratio must be kept at the lower levels compatible with the use of gasoline, there is a 5 to 7 percent increase in torque when operating on M85 compared to gasoline. This increase in power comes primarily from the inherently higher cylinder pressures produced in the combustion process because of the higher

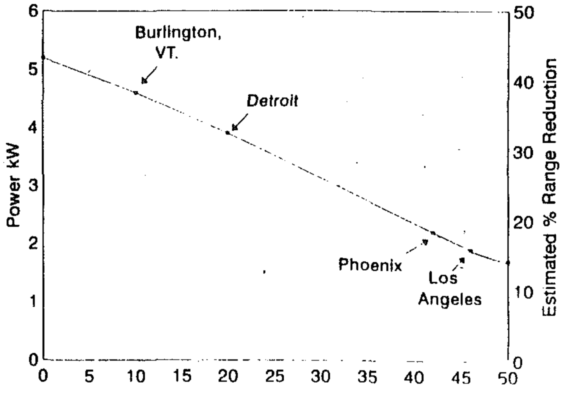

Fig. 1 Heat power requirements

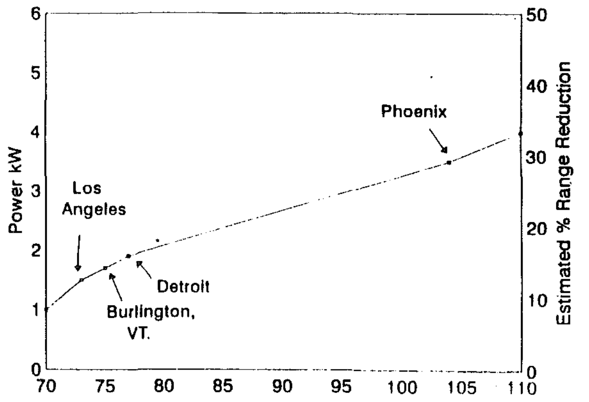

Fig. 2 AC power requirements

molal product to reactant ratio of the alcohols compared to gasoline [1].

The increase in performance, as measured with some of the early demonstration vehicles, showed the reduction in the 0-60 mph acceleration time of the 1.6L FFV Escort to be almost one second less, while the heavier LTD Crown Victoria acceleration time was reduced about half of a second. This kind of performance improvement is enough for the average driver to feel.

One of the open issues for methanol is the future fuel specification, which is expected to evolve with time. As mentioned earlier, M85 is recommended today because of the need to increase the flame visibility. The gasoline addition also raises the vapor pressure to a minimum for starting and good driveability, but it is still lower than a typical gasoline, so M85 has lower evaporative emissons.

Another issue with M100 is the potential for an ignitable vapor above the liquid in the tank at normal ambient temperature. The addition of gasoline makes the vapor too rich to ignite down to much lower temperatures, like those of gasoline. It also makes the fuel smell like gasoline so people will not think it is drinkable, or if they spill it on their hands, they will want to wash them. M100, however, forms virtually no soot, making it attractive as a replacement fuel for the diesel engine, provided the necessary design changes are made to overcome the low cetane number of methanol [6].

Electricity In 1990, California established new emission control requirements for vehicles for the future, including the requirement for introduction of a "Zero Emission Vehicle" (ZEV). By 1998, 2 percent of any large auto manufacturer's sales must be a ZEV, ramping up to 10 percent by 2003. The only vehicle that presently meets this requirement is the electric vehicle (EV), so all of the manufacturers have stepped up their efforts to bring an electric vehicle to market.

Another advantage of the electric vehicle is the flexibility in energy resource that it provides. Since very little electricity is generated by petroleum, the EV energy is primarily derived from a domestic energy resource. Overall there should be a net increase in energy efficiency as well, since the electric motor is a much more energy-efficient device compared to the IC engine.

In order to gain experience with this new technology and an unknown market, Ford plans to put an 82 unit demonstration fleet of EVs in the field later this year. The vehicle, named the ECOSTAR, is based on the European Escort van, with primary use targeted for the intracity environment as a delivery van. The performance targets include a driving range of 100 miles (as measured on the Federal Urban Driving Schedule or FUDS), a 0-50 mph acceleration time of 12 seconds, and a top speed of 75 mph. The vehicle utilizes a 75 HP AC electric motor integrated with a single-speed transaxle [7].

Table 3 Power and energy densities of advanced batteries compared to lead acid

	Power Density (W/kg)	Energy Density (Wh/kg)
Lead-Acid	230	35
Nickel-Cadmium	190	55
Ni-Metal-Hydride*	150	65
Nickel-Iron	115	50
Na-S	120	85
Na-Metal-Chloride	168	130
Li-Iron-Disulfide*	375	165
Zinc-Air	50	130
Lithium-Polymer*	200	160
(Gasoline)		(12200)

*Cells & Modules

With the exception of driving range, the overall performance and feel of the vehicle is quite comparable to the equivalent gasoline vehicle. The vehicle includes climate control, with both a heater and air-conditioning (AC). The driving range is reduced, however, depending on how much the heater and AC are utilized. Figures 1 and 2 show the power requirements for the heater and AC, respectively, as a function of the ambient temperature. The typical power requirement of the vehicle for cruising down the road at 50 mph is about 8 kW. As can be seen, the heater requirement can be as high as 5 kW, so a fuel-fired heater may be more practical for the EV that operates in cold climates. The AC requirement is not quite as severe, with about 3.5 kW maximum required in hot environments.

The energy storage system for the ECOSTAR will be sodium sulfur (NaS) batteries, which have almost four times the energy density of lead acid batteries. The NaS battery technology is not yet commercially available, however, making these early electric vehicles extremely costly to build. In general, development of the electric vehicle is at high risk because of the need for a better battery. At present, the lead acid battery is the only mature, affordable technology, and it has good power density, but its energy density is not good enough except for very small, lightweight vehicles. Table 3 compares the power density and energy density of some of the advanced technology batteries with lead acid, and gasoline. The lithium-based battery technologies hold the most promise long-term, with good power and energy densities, and the potential for low cost and long lifetime.

In order to advance the more promising battery technologies, Ford, GM, and Chrysler formed the U.S. Advanced Battery

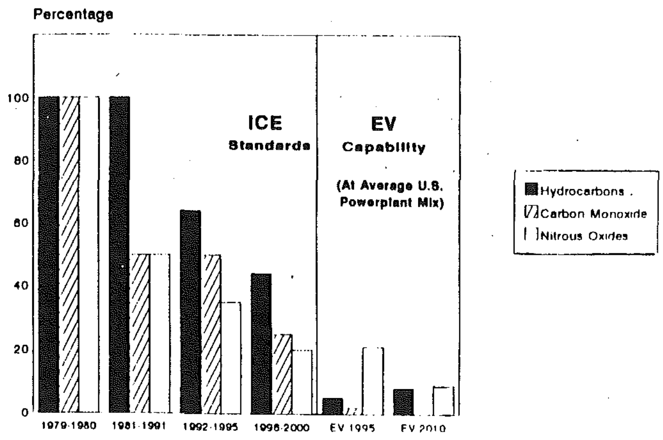

Fig. 3 Federal regulated emission standards

Consortium (USABC) in January of 1991. The prime objectives of both the midterm and long-term goals of the USABC are to reduce the cost and increase the lifetime of the batteries [8].

Impact of Fuels on Air Quality

In order to understand better where the alternative fuel vehicle technologies might be going in the future, it is helpful to review the carmaker's role in air quality compliance. The U.S. Clean Air Act of 1970 included requirements for substantial reductions in automotive emissions. Vehicle manufacturers met this challenge with continued reduction in the main pollutants emitted from motor vehicles. The hydrocarbons (HC) and carbon monoxide (CO) exhaust emission levels have been reduced by 96 percent from precontrol levels, and the oxides of nitrogen (NO_x) are 76 percent lower. In spite of these drastic reductions, a large number of areas of the country are still out of compliance with the air quality standards for ozone and CO. Carbon monoxide concentrations have been declining at the rate of 4 percent per year nationwide for more than a decade, however, so most areas are projected to attain compliance as new vehicles replace old ones.

In 1990, the Clean Air Act was amended to introduce even future reductions in the regulated emissions from vehicles. Figure 3 shows the percent reduction in emissions out to the year 2000, compared to the 1979–1980 levels, as well as the comparable emission levels that could be achieved if the vehicles with IC engines were replaced with electric vehicles. The change in emission levels in the case of the EV, from 1995 to 2010, is due to the expected change in the fuels used to generate the electricity at the powerplant. At present, about 60 percent of the powerplants in the U.S. are coal-fired.

Ozone, or photochemical smog, is formed in the lower atmosphere when sunlight reacts with hydrocarbons and nitrogen oxide, and is generally regarded as the most serious nonattainment problem. The pollution problem in Los Angeles is an order of magnitude worse than any other region of the United States. Los Angeles is the only city in the U.S. out of compliance with the air quality standard for nitrogen oxide.

The U.S. Environmental Protection Agency (EPA) estimates that vehicle emissions make up 44 percent of the total HC emissions inventory, with the balance, 56 percent, coming from stationary source fuel combustion, industrial processes, solid waste disposal, nonvehicle mobile sources, and other miscellaneous sources. The vehicle share of hydrocarbons is divided between exhaust emissions (13 percent) and evaporative emissions (31 percent).

It is important to understand where the opportunities for reduction in ambient HC due to vehicles is likely to be found. Less than 1 percent reduction in hydrocarbon inventory can be realized by lowering the tailpipe levels; i.e., a very small reduction with significant costs.

Vehicle miles traveled (VMT) fell for some period of time after the energy crises of the 1970s, but they are on the rise again, and therefore, the hydrocarbon inventory is expected to increase. Hydrocarbon concentrations will fall, however, with fleet turnover because today's control systems are doing a better job.

One of the opportunities for a substantial reduction in HC inventories is reduction in excess evaporative emissions from the vehicle, including the vapor that is emitted as the vehicle is driving down the road (running loss)—emissions that the auto and oil industries have generally agreed to eliminate. Running losses are caused by an increase in the rate of vapor generation beyond the design control level. Excess evaporative emissions occur when the vehicle is parked for extended periods of time. EPA data indicate that control of these emissions can reduce ambient HC by 25 percent on a warm sunny day.

Part of this reduction has already occurred as a result of the new controls on the maximum summer gasoline volatility put in place by the EPA beginning June of 1989. The remaining evaporative emissions are expected to be handled by further controls on volatility and/or advancements in vehicle technology. Refueling vapors, although the most intensely debated form of evaporative emissions, are only a small part of the problem. They account for only about 1 percent of the ambient HC inventory.

The electric vehicle is aimed at reduction of emissions in the city environment. There will still be a powerplant somewhere generating the electricity required to recharge the batteries of the vehicle. It is easier to control the emissions of one large smokestack, however, than many small "tailpipes." As shown in Fig. 3, the overall air quality benefit will vary depending on the fuel or source of energy used by the powerplant. In France, where 80 percent of the electricity is generated by nuclear power, introduction of the electric vehicle will result in a much bigger air quality benefit compared to those countries where fossil fuel use dominates. Obviously, the air quality benefits also are bigger in those areas that use hydro, wind, or solar energy to generate the electricity.

In the U.S., the overall levels of reactive hydrocarbon and carbon monoxide should decrease, since these emissions are primarily associated with the IC engine-powered automobile, but in some regions there may be an increase in SO_2 and NO_x emissions (and an increase in acid rain), primarily due to the use of coal. On average, there will be only be a small decrease in CO_2 emissions.

Another approach to lowering the motor vehicle contribution to ozone formation is to change the character of the tailpipe emissions. This is the contribution that the alternative fuels can make. It is not the level of the tailpipe emission per se that is lower, it is the character and/or composition of the emission that is different. Hydrocarbon compounds have varying levels of reactivity in the atmosphere, as shown in Table 4. Fuels that produce less reactive exhaust emissions when burned will generate less ozone. It is the way they react in the atmosphere *after* they leave the tailpipe that is important, and this is where the next real opportunity for improvement will be realized. This is also the basis for the improvement in air quality with the use of reformulated gasoline; i.e., the gasoline will be formulated such that some of the exhaust hydrocarbons with high reactivity will be eliminated or reduced. While reformulated gasoline is expected to form less ozone than today's gasolines, the use of the other alternative fuels is expected to result in even further reductions.

Exactly how much reduction in ozone will result is not well quantified at this time, but the California Air Resources Board (CARB) has recognized these reactivity differences by assigning "reactivity factors" to the various alternative fuels. For example, the reactivity factor for methanol is about half that of

Table 4 Photochemical reactivity of organic compounds: rate constants for reaction with hydroxyl (OH) radical

Compound	$K \times 10^{-4}$ (PPM^{-1} MIN^{-1})
Trans-2-Butene	10.5
1,2,4 Trimethyl Benzene	4.9
M-Xylene	3.4
Propionaldehyde	2.2
Acetaldehyde	2.2
Propene	2.1
Formaldehyde	2.1
Ethylene	0.45
N-Butane	0.35
Propane	0.25
Methanol	0.148
Ethane	0.045
Acetylene	0.022
Carbon Monoxide	0.021
Methane	0.0012

gasoline. But the ozone reduction associated with the use of methanol is also dependent on proper control of the formaldehyde emission. Therefore, CARB has adopted a standard for formaldehyde exhaust emissions from methanol vehicles, which began MY 1993, of 15 mg/mi, which is approximately the level of formaldehyde emission of today's gasoline vehicle. Fortunately, the technologies that control hydrocarbons in general are the same kind of controls that control formaldehyde; in both cases, almost all of the emission is produced in the first two minutes of operation after a cold start.

The FFV vehicles now in production are being certified to TLEV (Transition Low Emission Vehicle) emission standards, including the formaldehyde emission standard. Ford production of the FFV Taurus in 1993, however, has been limited to 2800 units in keeping with the need to proceed slowly in order to make sure the technology satisfies the customer and continues to meet environmental standards in use.

Debate continues as to the relative merits of M85 versus M100 (100 percent methanol). The EPA air models show that use of M100 results in more reduction in ozone, but this is based on the assumption that there is "zero" hydrocarbon emission with the use of M100. The amount of formaldehyde emission tends to be proportional to the level of methanol and therefore, M100 results in higher emission levels of formaldehyde than M85, all other factors being equal [9]. Also, the much more difficult cold start could significantly increase emissions due to higher mass emissions at start-up, as well as causing more rapid deterioration of the control system (including engine). All of this needs to be better understood before one can conclude that M100 has a higher air quality benefit than M85.

There is no question that the air quality and energy efficiency benefits of the dedicated methanol vehicle are even better than those of the FFV, but it will take some time before there is sufficient infrastructure in place for the average retail customer to feel comfortable with a dedicated vehicle.

The Challenges of Change

Market research shows that the customer is, in general, wary of change. Gasoline has been doing a good job for the consumer for a hundred years, and it will continue to do so for many years to come. The market also tends to be cost-driven. Compared to the rest of the world, petroleum-based fuels in the United States are a real bargain, which makes it very difficult for some of the alternative fuels to compete with gasoline. In other cases, the vehicle costs are significantly higher. In the case of the EV, both the initial cost and the operating costs are higher when one takes into account the need periodically to replace the battery. There is a growing awareness of environmental concerns on the part of the consumer, however, and at least some of the market has indicated a willingness to pay more (but not very much more) for environmentally friendly products.

How to get started is the most difficult part of change. Traditionally, changes in the automobile and its engine have come about through evolutionary actions. Introduction of alternative fuels may require some revolutionary actions if significant change is to be achieved, but this can create chaos and economic hardships, which will ultimately be counterproductive to attainment of the desirable goals.

When one looks at the history of the automobile in Europe over the past forty years, it is clear that people have a high value for their personal mobility. In the 1950s, very few people owned an automobile, but the European rail and the bus system went everywhere. In spite of the availability of mass transit, however, as people became more affluent, private vehicle purchases began to climb. Today multiple car ownership has become quite common, just as it is in the United States.

It is not likely that the solution to transportation pollution will come about by asking people to give up their automobile. We must continue to make the automobile as clean as possible. The use of alternative fuels could become a major factor in the preservation of our personal mobility for the future, provided their use lives up to the high value that people have come to expect from their automobile.

If the marketplace drives the environmental decisions of the future, then the auto industry will have much to gain by meeting the challenges of change associated with the introduction of alternative fuels.

References

1 Nichols, R. J., "Applications of Alternative Fuels," SAE Paper No. 821573, 1982.

2 Nichols, R. J., "Ford's CNG Vehicle Research," *Proc. 10th Energy Technology Conf.*, Mar. 1, 1983.

3 Golovoy, A., and Nichols, R. J., "Natural-Gas-Powered Vehicles," *Chemtech*, June 1983, pp. 359-363.

4 Nichols, R. J., et al., "Cold Start Studies," *Canadian Flexible Fuel Vehicle Program*, Final Report, Ontario Ministry of Energy, Mar. 31, 1987.

5 Nichols, R. J., et al., "Ford's Development of a Methanol Fueled Escort," *Proc., 5th Internat'l Alcohol Fuel Technology Symp.*, Vol. II, Auckland, Australia, 1982, pp. 109-116.

6 Bennethum, J. E., and Srinivasan, N., "Detroit Diesel Allison's Two Stroke Cycle Compression Ignited Alcohol Engines," *Proc. 6th Internat'l Alcohol Fuel Technology Symp.*, Ottawa, Canada, May 1984, Paper A-7.

7 Sims, R. I., et al., "A Systems Approach to the Development of an Electric Compact Van for Worldwide Commercial Use," *Proc., ISATA Conference*, Florence, Italy, May 21-23, 1991.

8 Nichols, R. J., "The United States Advanced Battery Consortium: Making Longer Life Batteries Affordable," *Proc., The Urban Electric Vehicle Conference*, Stockholm, Sweden, May 25-27, 1992.

9 Nichols, R. J., et al., "A View of Flexible Fuel Vehicle Aldehyde Emissions," SAE Paper No. 881200, 1988.

H.-J. Schiffgens

H. Endres

FEV Motorentechnik GmbH and Co. KG,
Aachen, Federal Republic of Germany

H. Wackertapp

Ruhrgas AG,
Dorsten, Federal Republic of Germany

E. Schrey

FEV Motorentechnik GmbH and Co. KG,
Aachen, Federal Republic of Germany

Concepts for the Adaptation of SI Gas Engines to Changing Methane Number

In a joint project of FEV Motorentechnik and Ruhrgas AG, the design of stoichiometric and lean-burn Otto engines was optimized by selective modifications to the design and operating parameters to accommodate changing methane numbers (LPG addition to CNG). Of particular importance was knock-free engine operation at a low NO_x output to meet the requirements of the German Clean Air Code while concurrently achieving both high efficiencies and mean effective pressures. Based upon the results obtained, concepts for the control of Otto-cycle gas engines to accept changing methane numbers were developed. The newly developed gas engine control device allows these concepts to meet the requirement of the German Clean Air Code with economically viable conditions while preventing engine knock. Furthermore, the test results show that dedicated Otto-cycle gas engines can meet the most stringent emission limits for commercial vehicles while maintaining high efficiencies.

Introduction

During the past few years, the gas engine has seen a renaissance in stationary applications due to its unique characteristics. In 1990, some 2700 stationary gas engines were employed in western Germany with an installed total power generating capacity of some 600 MW.

Against the backdrop of the long-term availability of natural gas and low pollutant and noise emissions, the gas engine is also gaining increasing importance in the transportation sector, especially in the U.S.

The current types of gas engine are listed in Fig. 1. They are either diesel pilot injection gas engines or Otto-cycle engines. For the pilot injection gas engine, combustion is initiated by the high-pressure injection of a small amount of diesel fuel into the cylinder where the fuel auto-ignites. This process is most prevalent in large stationary engines of several MW. Both external and internal mixture preparation with high-pressure gas injection at the end of the compression stroke are used. However, a very significant gas engine concept is the Otto-cycle engine.

There are two types of spark ignited (SI) gas engine currently dominating the market:

1. The stoichiometric engine with a three-way catalytic converter and, optionally, exhaust gas recirculation and turbocharging.
2. The lean-burn engine with an oxidation catalyst.

Characteristics of the stoichiometric engine concept including the three-way catalytic converter are:

- very low emissions over a very narrow range of air/fuel ratios
- relatively low mean effective pressures due to the knock limited charging capability (approximately 8 bar for naturally aspirated (NA) engines; approximately 10 to 11 bar for turbocharged engines with possible exhaust gas recirculation)
- relatively low maximum thermal efficiencies (34 to 36 percent, $CR = 12$ for a methane number of about 80)
- limited fuel gas choice, since fuel gases harmful to the catalysts (e.g., landfill gas) may not be used
- high exhaust gas temperatures
- catalyst and λ (excess air) sensor aging is possible resulting

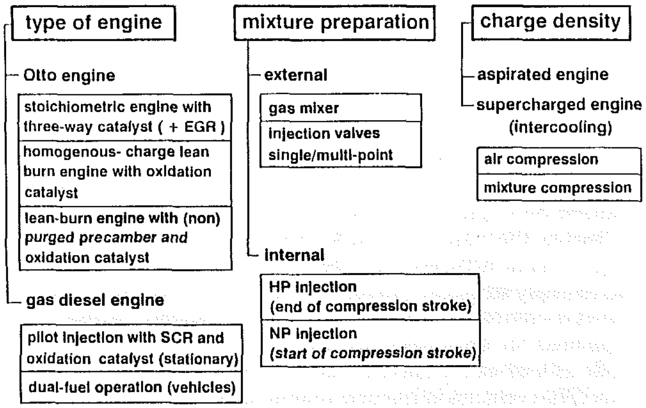

Fig. 1 Current gas engine concepts

Contributed by the Internal Combustion Engine Division and presented at the 15th Annual Fall Technical Conference of the ASME Internal Combustion Engine Division, Morgantown, West Virginia, September 26-29, 1993. Manuscript received by the Internal Combustion Engine Division January 28, 1994. Associate Technical Editor: W. Cheng.

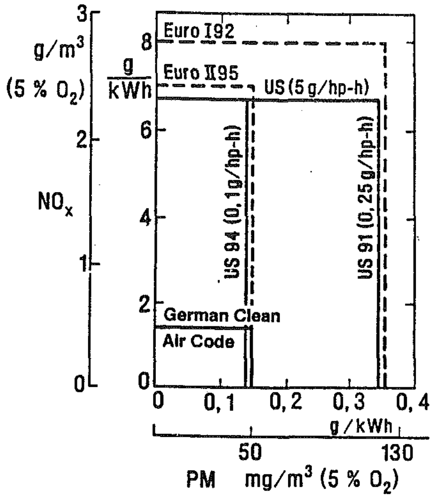

Fig. 2 NO$_x$ and PM emission limits for gas engines in stationary and HD application

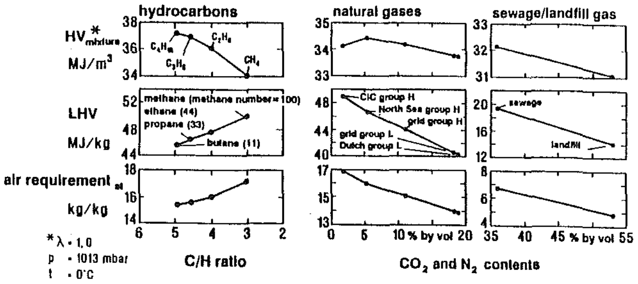

Fig. 3 Gaseous fuel characteristics

in very high pollutant emissions, if exhaust gas treatment fails

Characteristics of the lean-burn engine concept are:

- favorable NO$_x$ output (prior to treatment) over a wider range of air/fuel ratios
- high mean effective pressures due to the high charging capability (12 to 14 bar)
- favorable maximum thermal efficiencies (37 to 41 percent, $CR = 12$ for a methane number of about 80)
- fuel gas choice is not necessarily limited, since various fuels can be used, if no oxidation catalyst is employed
- high demand on combustion stability (smooth operation)
- low conversion rate of methane in the oxidation catalyst
- restriction on cylinder bore diameters, since for diameters of more than 190 mm, split combustion chambers (prechamber, prechamber plug) are required to obtain low NO$_x$ levels

For stationary and heavy-duty vehicle engines, gas mixers are normally used for external mixture preparation together with air or mixture turbochargers. Mixture charging (mixture preparation prior to turbocharger compression) provides a more homogeneous mixture to the engine and thus increases the flexibility of lean-burn operation. Extensive studies have shown that there is little risk of backfiring with this configuration [1]. Natural gas conversion of vehicular engines is typically realized by single or multipoint manifold injection.

During the past few years, development activities of gas engine manufacturers have been substantially influenced by increasingly stringent exhaust emission requirements. Figure 2 shows a comparison of the NO$_x$ and particulate matter limits stipulated for stationary gas engines in the German Clean Air Code as well as the current and future limit values for heavy-duty (HD) vehicles in Europe and the U.S. [2]. The comparison shows that the gas engine, in keeping with German Clean Air Code requirements, offers not only the advantage of using a fuel with long-term availability but is also capable of meeting even the most stringent exhaust emission requirements. Furthermore, natural gas has a very favorable carbon to lower heating value (LHV) ratio reducing carbon dioxide output for natural gas by 30 percent compared with diesel fuel (referred to LHV).

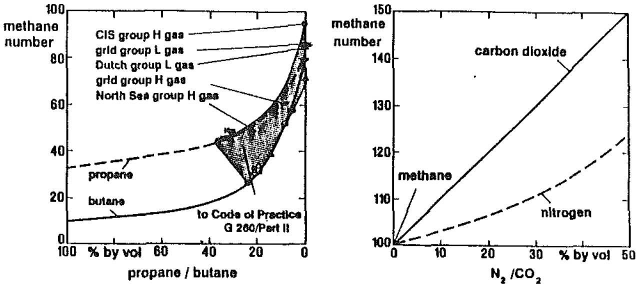

Fig. 4 Methane number as a function of propane/butane concentration in different CNG blends with respect to CO$_2$/N$_2$ concentration in methane

Power, efficiency, and exhaust emission of internal combustion engines are to a considerable extent dependent on the choice and optimization of the engine concept to be used for a specific fuel gas.

Fuel Gas Properties

The most prevalent gaseous fuels for internal combustion engines are natural gases, LPGs, and sewage or landfill gases. Natural gas supplies in Germany come from different sources, consisting mainly of methane (80 to 98 percent by volume), higher hydrocarbons (ethane, propane, butane), carbon dioxide, and nitrogen. Natural gas properties in Germany are subject to regional and seasonal variations [3, 4].

Given the increasing environmental concern, the use of sewage and landfill gases for internal combustion engines is gaining interest. Such gases mainly consist of methane (50 to 60 percent by volume), carbon dioxide (30 to 40 percent by volume) and nitrogen (5 to 10 percent by volume). LPG gases are either propane or butane or propane/butane mixtures, and can be easily stored, since the gas-to-liquid transition at ambient temperature already occurs at relatively low pressures, which represents an advantage over natural gas.

Figure 3 shows important properties of different gaseous fuels (heating value of mixture, lower heating value, and stoichiometric air requirement) as a function of the CO$_2$ and N$_2$ shares and carbon-to-hydrogen (C/H) ratios.

A very important fuel characteristic for homogeneous charge engines is a fuel's knock resistance. For liquid fuels the knock resistance is expressed by the octane number, whereas for fuel gases the knock resistance is characterized by the methane number. The measurement range is defined by methane at the one end of the scale, which has very high knock resistance, and by hydrogen at the other end, which exhibits a very poor ability to resist knock. Pure methane represents a methane number of 100, which corresponds to a research octane number (RON) of about 140, while hydrogen has a methane number of zero [5].

For peak shaving, local utilities in Germany may mix substantial quantities of propane/butane air mixtures to natural gases (DVGW Code of Practice G260). Adding such mixtures may considerably affect important fuel gas properties such as knock resistance and air requirements. Figure 4 shows the methane numbers for propane or butane additions to several base gases and for methane/CO$_2$ and methane/N$_2$ mixtures. Blending natural gas with LPG substantially reduces knock resistance (lower methane number) while the addition of inert gases raises methane numbers to above 100.

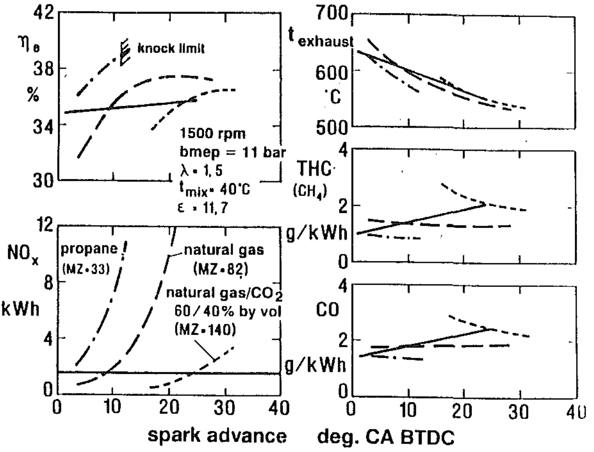

Fig. 5 Impact of ignition timing on engine performance while operating with different gaseous fuels

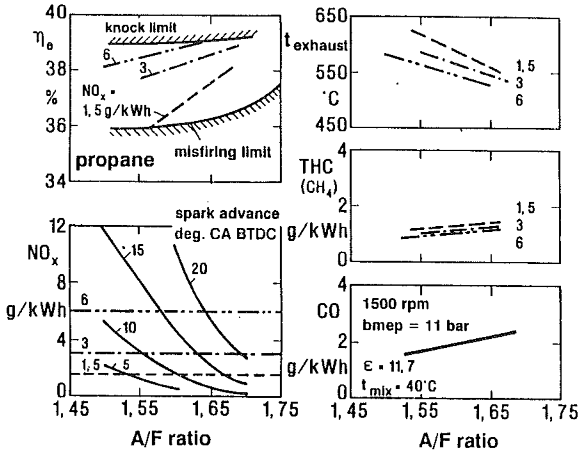

Fig. 7 Impact of ignition timing and air/fuel ratio on gas engine performance using propane

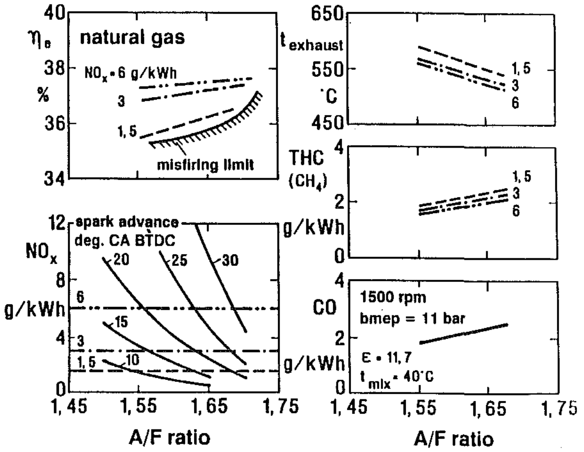

Fig. 6 Impact of ignition timing and air/fuel ratio on gas engine performance using natural gas

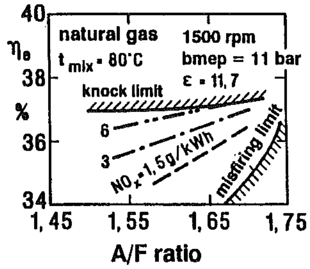

Fig. 8 Impact of increased mixture temperature on efficiency and NO_x emissions

In Germany, optimization measures on Otto-cycle gas engines in stationary applications concentrated on efficiencies and exhaust emissions. It was normal practice to design gas engines to run on the natural gases available on the German market, i.e., with methane numbers ranging from 70 to 90. By adding LPG, methane numbers may fall to 25 and changing gas properties will strongly affect the knocking behavior of the engines, substantially increasing the risk of knock damage.

Optimization of Engine Design for Changing Methane Numbers

In view of the changing methane numbers, the design of stoichiometric and lean-burn engines was optimized during extensive development conducted by FEV Motorentechnik through appropriate modifications to design and operating parameters. Of primary importance were very low exhaust emissions to meet the requirements stipulated in the German Clean Air Code and, at the same time, high efficiencies and mean effective pressures. Tests were conducted on a water-cooled single-cylinder engine boosted by a supercharger (retrofitted standard engine) with a cylinder capacity of about 2 L and a conventional-type transistorized ignition system. The results described below were extrapolated for a standard engine [6]. Emission output is not converted to g/m^3 at 5 percent oxygen to the German Clean Air Code but is shown in terms of g/kWh.

Lean-Burn Engine. An important fact in the design and adjustment of a lean-burn engine is the difficulty to reduce NO_x output, while at the same time increasing efficiency and bmep. Figure 5 shows the effect of ignition timing on efficiency, exhaust emissions, and exhaust gas temperature for propane, natural gas, and natural gas/CO_2 mixture (landfill gas) for an operating point under full-load conditions. With changing gas properties, ignition timing must be adjusted to warrant optimal efficiencies. In contrast to natural gas and natural gas/CO_2 operation, the knock resistance is adversely affected by propane, although a somewhat higher efficiency can be realized at the same compression ratio. At a constant NO_x output (1.5 g/kWh roughly corresponding to the threshold limit value of 500 mg/m^3 stipulated by the German Clean Air Code for stationary engines) virtually equal efficiencies are obtained for all three fuel gases. Total hydrocarbon and CO output is significantly higher for natural gas/CO_2 operation than for propane and natural gas operation.

Figure 6 shows the effect of air/fuel ratio and ignition timing on engine behavior for natural gas. For a clear representation, constant NO_x output (1.5, 3, and 6 g/kWh) levels were assumed. Efficiencies and exhaust emissions clearly develop in opposite directions. For an increasing proportion of air, the operating range is limited by the misfiring limit.

Figure 7 shows engine behavior for propane. Due to the higher burning velocity of propane versus natural gas, higher efficiencies but also higher NO_x output are found for the same engine setting. At a constant NO_x output of 1.5 g/kWh, engine efficiency can be increased by 1.5 percentage points for propane. While for natural gas the knock limit is not reached over the range of air ratios used in this test, propane operation is not only limited by the misfiring limit but also by the knock limit. For propane operation, exhaust gas temperatures and hydrocarbon and CO emissions are lower due to increased flame speeds.

In comparison with Figs. 6 and 7, Fig. 8 shows the effect of increased fuel mixture temperatures (80°C versus 40°C) on efficiencies and NO_x output for natural gas operation under

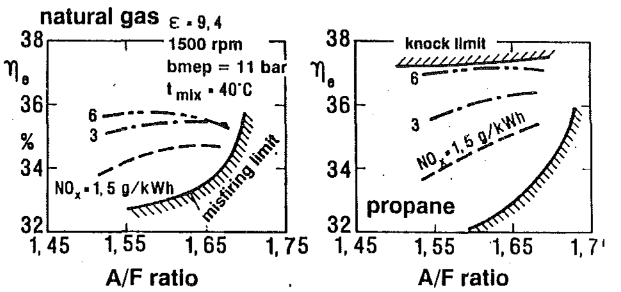

Fig. 9 Correlation between efficiency and NO_x emission with CNG and propane at a low compression ratio

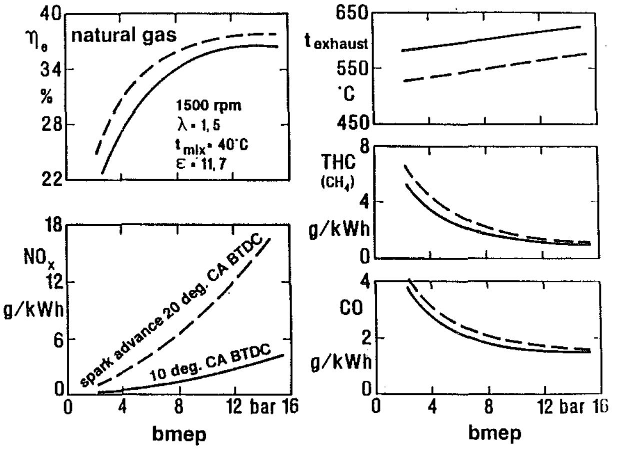

Fig. 10 Impact of engine load on efficiency and emission using CNG

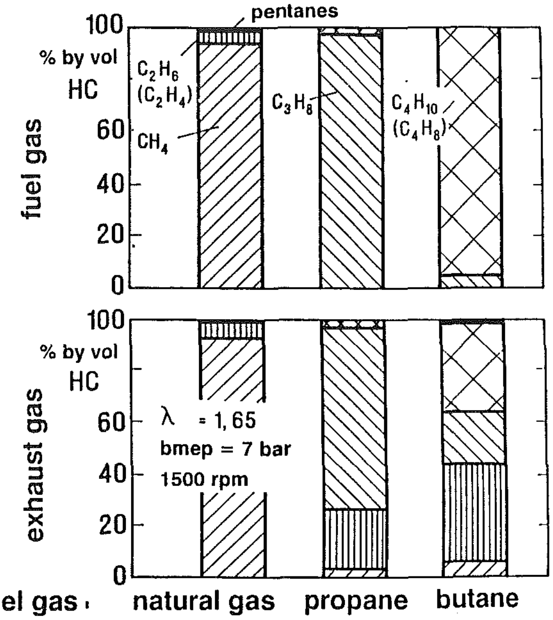

Fig. 11 Composition of hydrocarbons

constant combustion conditions. More favorable ignition conditions at high temperatures offer a clearly improved potential for lean operation. At the same time, however, the operating range is restricted by a more severe tendency toward knocking. At higher NO_x emissions (3 or 6 g/kWh), slight reductions in efficiencies occur when compared with operation at lower mixture temperatures.

Reducing the compression ratio has historically been the preferred method for adjusting engines to lower methane numbers. Figure 9 shows the relationship between efficiency and NO_x output for propane and natural gas operation as compression ratio is reduced from 11.7:1 to 9.4:1. The operating conditions correspond to those in Figs. 6 and 7, allowing a direct comparison of results.

Assuming constant NO_x output, a decrease in the compression ratio by some two units reduces efficiency by approximately two percentage points. At lower compression ratios, engine operation is characterized by a narrower margin for lean operation and a reduced tendency toward knocking. However, the operating range is markedly expanded. The results show that reducing methane number requirements by lowering the compression ratio reduces efficiency to potentially unacceptable levels, if the supply of mixtures with a low methane number is limited to only short time periods (LPG additions).

Figure 10 shows the effect of load on efficiency and emissions for natural gas operation at 1500 rpm, at an air/fuel ratio of 1.5. Ignition timing near MBT, and an ignition delay of 10 deg advance is shown. Most obvious is the clear increase in NO_x output as load increases and the high HC and CO output at low load, which is typical of lean-burn Otto engines. The throttling losses due to metered fuel supply clearly reduce efficiency at partial load operation. For lower NO_x emissions at high mean effective pressures, an even leaner fuel/air mixture may be used. To account for the dynamic operating modes of gas engines in HD vehicles, however, the fuel air mixtures must be selected to be clearly above the lean-burn limit.

Fuel gas properties significantly affect not only engine operating behavior but also levels of unburned hydrocarbon constituents in the exhaust gas (Fig. 11). While exhaust gas composition is very similar to fuel gas composition for natural gas operation, exhaust gas hydrocarbons from propane and butane operation not only consist of the fuel components but also include the short-chain hydrocarbons. For propane operation (C_3H_8), these constituents are ethane (C_2H_6) and methane (CH_4), and for butane operation (C_4H_{10}), propane (C_3H_8), ethane (C_2H_6), and methane (CH_4).

Further development has shown that the following design parameters should be optimized to guarantee safe and efficient engine operation meeting the German Clean Air Code requirements over a wide range of methane numbers (methane numbers of 30 to 90):

- Charge flow—With a suitable adjustment of charge flow, clearly lower HC output can be obtained at a constant NO_x output and constant efficiencies.
- Different cylinder knock limits—Since the cylinder displaying the most unfavorable knocking behavior sets the knock limit for the engine as a whole (if ignition timing is not set individually for each cylinder, which is normal practice for stationary engines) the individual knock limits should not differ too much.
- Oxidation catalyst—A downstream oxidation catalyst should be used to limit CO at low NO_x emissions and limit nonmethane hydrocarbon for LPG admixtures.

The lean-burn engine characteristics in terms of bmep, efficiency, and emissions make it an attractive option for powering commercial vehicles. For a detailed assessment of the engine's potential, a 13-mode test (ECE R49) on a dedicated lean-burn engine was made. The following test data were obtained (no exhaust gas treatment):

• NO_x	= 1.5 g/kWh
• CO	= 3 g/kWh
• THC	= 2.9 g/kWh
• specific fuel consumption	= 260 g/kWh (diesel equivalent)

Full-load operation is characterized as follows:

• bmep (at intermediate speed)	= 15 bar
• specific fuel consumption (bmep, max)	= 235 g/kWh (diesel equivalent)
• bmep (at nominal speed)	= 11 bar

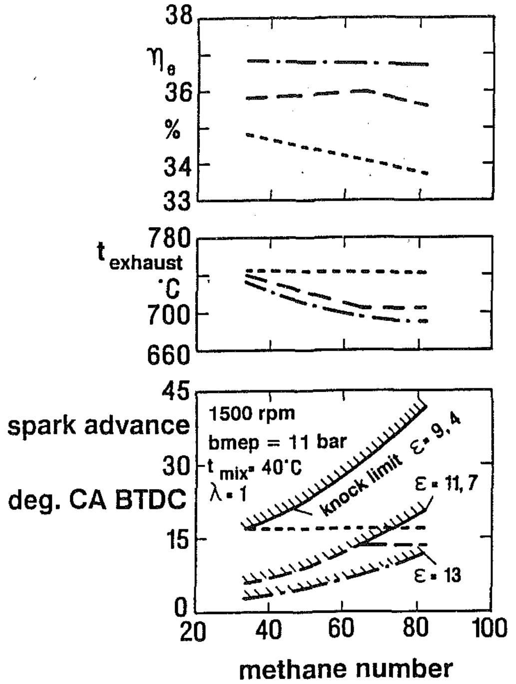

Fig. 12 Impact of compression ratio on efficiency and knocking resistance as a function of methane number

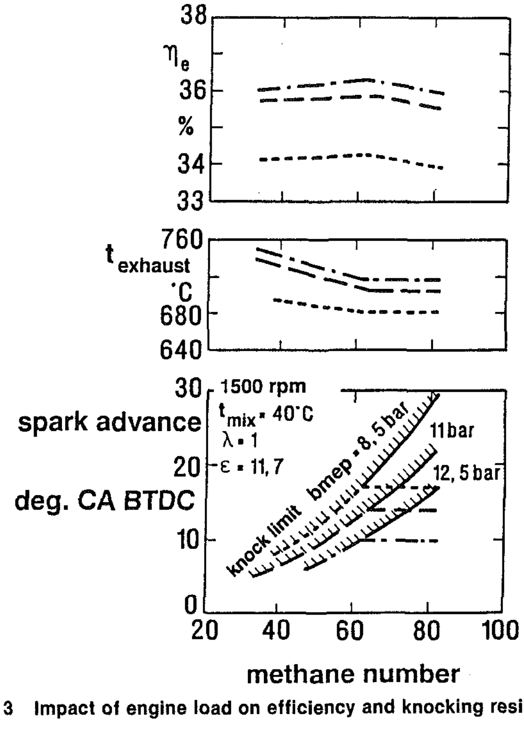

Fig. 13 Impact of engine load on efficiency and knocking resistance

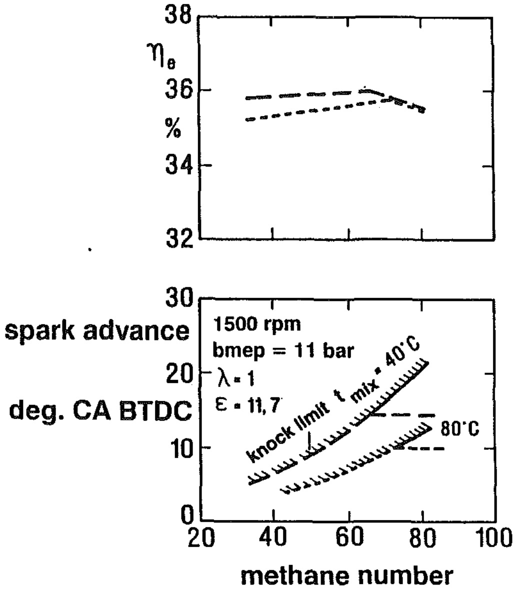

Fig. 14 Impact of increased mixture temperature on efficiency and knock limit

It is obvious that due to the specific properties of natural gas and low emission combustion, Otto-cycle lean-burn gas engines can address the most stringent emission requirements for commercial vehicles at achieving high efficiencies. However, for lower methane numbers, the mean effective pressures identified above cannot be obtained due to limitations from engine knock. Therefore, high methane numbers are required to achieve the mean effective pressures typical of today's diesel engines.

Stoichiometric Engines. In contrast to lean-burn engines, design parameters and operating parameter adjustments have only a minor effect on emissions for stoichiometric engines fitted with a downstream three-way catalyst. Of primary importance for these engines are efficiency, mean effective pressures, knocking behavior, and engine component wear (exhaust gas temperatures, thermal load, valve wear).

Figure 12 shows the effect of three different compression ratios (at reference operating conditions) on efficiency and knock limits as a function of methane numbers. The high compression ratio of 13:1 is subject to a knock limit over the whole range of methane numbers. The 11.7:1 ratio is limited for methane numbers below 70 and the low compression ratio of 9.4:1 for methane numbers below 30. With adjusted ignition timing, efficiencies are practically independent of methane numbers. At low methane numbers, operators cannot benefit from higher efficiencies at high compression ratios due to the extreme retarding of ignition required to avoid unacceptable knocking behavior.

For a change in compression ratios from 11.7:1 to 9.4:1, efficiencies at high methane numbers (natural gases) are reduced by two percentage points. In contrast to lean fuel/air ratios ($NO_x = 1.5$ g/kWh), detrimental effects on efficiency of only about one percentage point occur for stoichiometric conditions (bmep = 11 bar, CR = 11.7:1) at optimized ignition timing.

For stoichiometric engines, CO and NO_x output, which are not shown in the figure, remain virtually unaffected by a change in methane number and/or compression ratios while HC emissions decrease with reduced compression ratios.

In the past, operators usually reduced engine load when knocking combustion occurred to avoid damage to engine parts. Figure 13 shows the effect of load on efficiency and knock limit. By reducing the load, the knock limit may be shifted in the direction of lower methane numbers; at the same time, however, efficiencies markedly decrease.

Figures 12 and 13 show the expected effects of load and compression ratio on exhaust gas temperature. For constant ignition timing, methane numbers do not have any significant effect; however, when the knock limit is reached and ignition must be retarded, exhaust gas temperatures and thus thermal load on engine components increase.

Figure 14 shows the effect of higher mixture temperature on efficiency and knock limit. At a higher mixture temperature of 80°C, a somewhat smaller spark advance is required due to improved combustion conditions; at the same time, how-

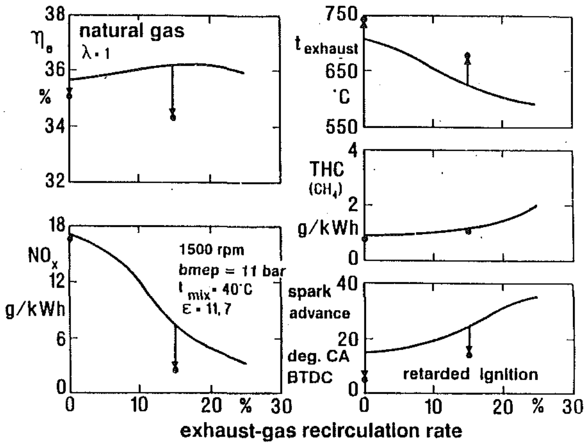

Fig. 15 Variation of exhaust gas recirculation rate with CNG

ever, the knock limit moves considerably toward retarded ignition timing. Thus, the operating range is significantly limited in the case of higher mixture temperatures.

Due to high component wear, stoichiometric engines usually are not boosted. Exhaust gas recirculation improves the operating behavior at richer fuel/air ratios toward lean-burn conditions so that moderate turbocharging, acceptable efficiencies, and low exhaust emissions with downstream three-way catalytic converters can be obtained. Figure 15 shows the effect of exhaust gas recirculation on efficiencies, emission level (before catalyst), and exhaust gas temperatures. The reduction in combustion temperatures due to exhaust gas recirculation clearly reduces NO_x emissions and improves engine knock resistance due to the higher shares of carbon dioxide and nitrogen (Fig. 4).

As with lean-burn engines, an optimized charge flow and a minimum variation in knock limits between the individual cylinders is also recommended for stoichiometric engines.

Engine Operation at Changing Methane Numbers

The test results described above confirm the significant effect methane number has on engine operating behavior. Typically, design engineers are asked to focus on designing the gas engine such that optimized efficiency, power, and emission behavior can be obtained for the base gases. It must further be ensured that even with changing gas properties (LPG additions) the engine operates safely, preventing any damage to engine components due to increased knock, and that acceptable efficiency and power while complying with emission limits are obtained. Therefore, only designing the engine for the lowest possible methane number gas may not be a practical solution.

If LPG is added to the fuel gas of lean-burn engines (reducing the methane number) without changing the other operating parameters (load, air/fuel ratio, ignition timing), NO_x emissions will initially increase so it can normally be expected that the limits stipulated in the German Clean Air Code will be exceeded. As LPG concentration increases, further decreasing methane number, the knock limit will be reached and subsequent adjustment of operating parameters is critical. For stoichiometric operation, LPG additions, except for influencing the composition of unburned hydrocarbons, do not have any significant effect on the engine emission behavior. However, normal engine operation is closer to the knock limit than for lean-burn engines so that the knock limit is reached at relatively high methane numbers.

Engine operation may be adjusted to changing gas properties by:

- ignition timing control/knock control
- load control
- air/fuel ratio control

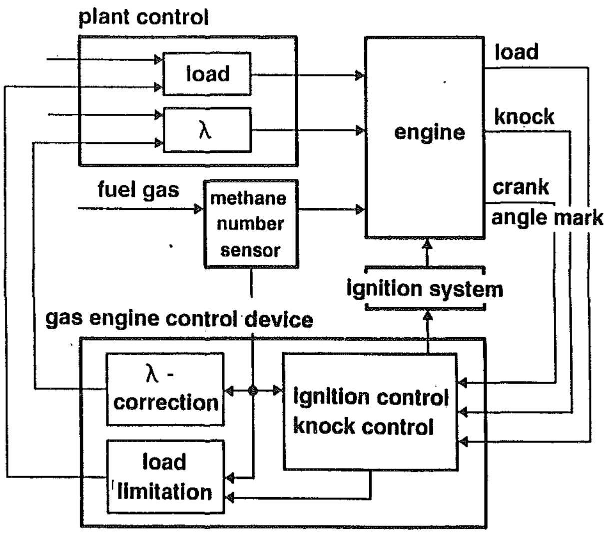

Fig. 16 Structure of a newly developed gas engine control system for SI gas engine adaptation to changing methane numbers because of LPG addition

Figure 16 shows a schematic representation of a new gas engine control device developed on the basis of the above-described research. The data input to the unit are methane number and several engine data such as load, knock sensor signal, and crankshaft angular positions. System output signals control ignition timing, correct air ratio, and limit load.

The engine is precontrolled by a methane number sensor (based on the thermal conductivity of the fuel gas) to maintain acceptable emission levels with fuels of differing methane number ranges before the knock limit is reached. The sensor is screwed into the gas main (3/4 in. thread), where gas enters the sensor by diffusion. Response time on changes in gas composition is a maximum of 1.5 seconds and the output signal ranges from 4 to 20 mA (methane number 30 to 100). Field testing has continued successfully for more than one year and the sensor is expected to be commercially available in the autumn of 1993.

The addition of LPG to CNG decreases methane number and accelerates flame speed. Thus, NO_x increases when air/fuel ratio and ignition timing are held constant. This increase may be compensated to a certain extent by leaning the air/fuel mixture. However, with higher amounts of LPG, the ignition timing has to be adapted.

Figure 17 shows ignition timing adjustment for changing gas properties in a stationary lean-burn standard engine where NO_x and knock limits are taken into account. With decreasing methane numbers, ignition timing is appropriately adjusted based upon input from the fuel sensor. Ignition timing adjustment over this operating range keeps the NO_x output below 500 mg/m^3 (approximately 1.5 g/kWh), while still maintaining sufficient knock margins confirmed by knock monitoring. When the methane number falls below approximately 50, the engine knock limit is reached (intersection of NO_x limit and knock limit lines), i.e., the methane number control is switched to knock control ensuring safe operating and, at the same time, acceptable efficiency without load reduction. Without the knock control feature, load would necessarily be reduced considerably (by approximately 20 percent). Load reduction is only intended when the engine operation cannot be controlled by retarded ignition alone, for example, because of a limited timing range of the ignition system or unacceptably high exhaust gas temperatures.

While engine precontrol is sufficient for lean-burn conditions over a wide range of methane numbers, stoichiometric engines without exhaust gas recirculation require knock-controlled operation for high efficiencies over practically the entire

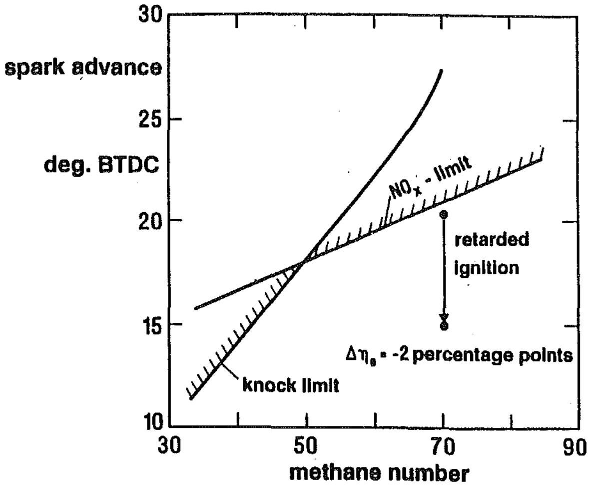

Fig. 17 Ignition timing at NO$_x$ limit and knock limit as a function of gas composition (six-cylinder in-line engine, full load)

action \ effect	stoichiometric			lean		
	tendency to knock	η_e	NO$_x$	tendency to knock	η_e	NO$_x$
retarded ignition	++	--	o	++	-	++
reduced load	+	--	o	+	-	+
leaning of A/F ratio	/	/	/	+	(o)	+
exhaust gas recirculation	++	(o)	+	++	(o)	++
reduced mixture temperature	++	(+)	o	++	(+)	++
reduced cooling water temperature	+	o	o	+	o	(+)
reduced speed	++	+	o	+	+	+
reduced compression ratio	++	--	o	++	-	++

++ very effective/positive
+ effective/positive
o no effect
- negative
– very negative

Fig. 18 Measures to reduce the methane number requirement at full load (cylinder displacement 2 L)

range of relevant methane numbers. Presently, the stoichiometric gas engine control device is being field-tested in cooperation with several engine manufacturers and commercial introduction is planned for the 1993–94 winter season.

Figure 18 lists the most important measures in engine operation and design to reduce methane number requirements and their effects on efficiency and NO$_x$ emissions for lean-burn and stoichiometric operation at full load (cylinder capacity approximately 2 L). Each measure designed to reduce combustion temperatures will produce positive effects on the engine knocking behavior and NO$_x$ emission (feedgas), however, with a detrimental effect on efficiency. The figure clearly shows these conflicting effects. With downstream three-way catalysts for stoichiometric engines, action taken to reduce combustion temperatures has almost no effect on exhaust pipe-out NO$_x$ emission. Also, under comparable operating conditions (load, speed, mixture temperature), it can be concluded that engines operating under stoichiometric conditions are more susceptible to knocking combustion than lean-burn engines.

Conclusions

In the future, Otto-cycle gas engines will have to maintain safe and efficient operation while complying with increasingly stringent emission limits, even for changing methane numbers (LPG addition to CNG). This requirement can only be met if the engine design is optimized and ignition timing, air/fuel ratio, and load can be adjusted properly with a newly developed control device for gas engines.

By optimizing combustion via operating and design parameters such as compression ratio, charge flow, calibration, and exhaust gas recirculation (for stoichiometric engines), high mean effective pressures and efficiencies can be maintained over wide methane number ranges while complying with environmental standards.

When using fuels with associated methane number ranges where the knock limit is not yet reached, a methane number fuel sensor must be used to precontrol lean-burn engines to ensure highest possible efficiency and load while complying with emission regulations. When the knock limit is reached, due to decreasing methane number, engine control is switched to knock control. For stoichiometric engines fitted with three-way catalytic converters, variations in engine design are not primarily necessitated due to exhaust emission behavior. However, to obtain high efficiency and mean effective pressures, knock-controlled operation is necessary over essentially the entire range of methane numbers.

Take advantage of natural gas properties and low-pollutant combustion, lean-burn Otto-cycle gas engines meet even the most stringent environmental requirements, including those for HD vehicles while, at the same time, maintaining high efficiency and mean effective pressures.

Acknowledgments

The authors express their appreciation to H.-J. Schollmeyer of Ruhrgas AG, Dorsten, and P. Hupperich of FEV Motorentechnik, Aachen, for their contributions throughout the various stages of this work.

References

1 Schiffgens, H.-J., "Druck- und Flammenausbreitung in Einiaßsystemen von Gas-Ottomotoren bei Rückzündungen (Thesis on Pressure and Flame Propagation in Inlet Systems of SI Gas Engines in the Case of Backfiring)," Dissertation, RWTH Aachen, 1991.

2 Dietrich, W., "Kriterien zukünftiger Kraftstoffe für stationäre gas- und dieselmotorische Antriebe (New Fuel Characteristics for Stationary Gas and Diesel Engine Drives)," *Motor und Umwelt*, 1991.

3 Wackertapp, H., Schollmeyer, H.-J., and Schiffgens, H.-J., "Konzepte zur Anpassung von Gasmotoren an wechselnde Gasbeschaffenheit (Concepts for Adjusting Gas Engines to Changing Gas Properties)," *VDI-Bericht Blockheizkraftwerke und Wärmepumpen*, 1993.

4 Schollmeyer, H.-J., and Wackertapp, H., "Gasbeschaffenneit und Gasmotoren (Gas Properties and Gas Engines)," *GWF-Gas/Erdgas*, 132, Vol. 2, 1991.

5 Cartellieri, W., and Pfeifer, U., "Erweiterung der Energieerzeugung durch Kraftgase (Energy Generation Using Gas as an Engine Fuel)," *FVV-Bericht*, 120, 1971.

6 Hupperich, P., "Einfluß der Methanzahl auf Auslegung und Betrieb eines *mager laufenden Gas-Ottomotors* (Thesis on the Influence of the Methane Number on the Design and Operation of a Lean-Burn SI Gas Engine)," Dissertation, RWTH Aachen, in preparation.

Coal-Fueled Diesel Development: A Technical Review

T. W. Ryan III
Southwest Research Institute,
San Antonio, TX 78228

The purpose of this paper is to describe and summarize the results of the Coal-Fueled Diesel Engine Development Program, sponsored by the U.S. Department of Energy, Morgantown Energy Technology Center. The results of the program indicate that diesel engines can be designed to operate reliably on coal-water slurries. The engine must be modified to include hard-wear resistant rings and liners. The injection system design must be modified to accommodate the slurry and to incorporate hard materials for wear prevention.

Introduction

The use of coal as a fuel for diesel engines dates back to the early days of the development of the engine. Dr. Diesel envisioned his concept as a multifuel engine, with coal a prime candidate due to the fact that it was Germany's primary domestic energy resource. It is interesting that the focus on coal-burning diesel engines appears to peak about every twenty years as shortages of other energy resources increase the economic attractiveness of using coal.

This cyclic interest in coal started in Germany with the work of Diesel [1] in the time frame 1898–1906. Pawlikowski carried on the work from 1916 to 1928. Two German companies commercialized the technology prior to and during World War II. The next flurry of activity occurred in the United States in the period from 1957–69, with work done at Southwest Research Institute [2], Virginia Polytechnical University [3, 4], and Howard University [5]. This work was summarized very thoroughly by Soehngen [1] and Caton and Rosegay [6]. The current period of activity started in 1978 with work sponsored by the Conservation and Renewable Energy Branch of the U.S. Department of Energy. This work was done at Southwest Research Institute [7–10] and by ThermoElectron and Sultzer Engine Co. in Switzerland [11]. The Fossil Energy Branch of the U.S. Department of Energy, through the Morgantown Energy Technology Center (METC), initiated a concentrated effort to develop coal-burning diesel and gas turbine engines. The diesel engine work in the METC sponsored program was performed at Southwest Research Institute, Bartlesville Energy Technology Center (now NIPER), General Motor Corporation (Electromotive Division), General Electric, Cooper Energy Systems (A.D. Little as the prime contractor), and various universities and other research and development organizations.

The overall scope of the METC Coal Diesel Engine Program is described in the next sections. The following sections describe the technical progress in each of the problem areas, including the fuel system, the combustion system, the fuel, and wear prevention.

Morgantown Energy Technology Center Program

The Morgantown Energy Technology Center (METC) initiated a coal-fueled heat engine program in 1982 involving the use of coal, direct fired in both gas turbine and diesel engine systems. The initial emphasis of the program was on use of coal-water slurries in gas turbine engines, primarily because it was perceived that the continuous combustion systems in these engines would be much easier to adapt to the use of coal than the intermittent combustion in diesel engines. The ultimate successes of the diesel program and the very difficult problems associated with erosion, corrosion, and deposition in the turbine engines focused added interest on the diesels, and the two programs became more competitive in funding levels and in their approach to commercial development.

The gas turbine program has provided significant contributions to the diesel program in the way of fuel developments and emissions control. Efforts will be made to discuss these contributions in the appropriate section of this report. The emphasis of this report is, however, the diesel program. The initial efforts in 1982 and 1983 were devoted to examining the feasibility of the use of CWS and coal powders in diesel engines. The results were promising and a major procurement announcement was released in 1984. Three large feasibility studies were awarded in early 1985 to three major medium-speed engine manufacturers. The goal of the feasibility studies was to identify the technical barriers impeding the development of the engine systems. The focus of the A.D. Little and Cooper project was the development of a stationary cogeneration engine system. General Electric and General Motors were both focused on the development of railroad locomotive systems. All of the studies included economic assessments of utilization of the existing technology in the respective applications. Over the course of the project new technologies were developed and the economic assessments were re-evaluated in terms of the

---

Contributed by the Internal Combustion Engine Division and presented at the Energy-Sources Technology Conference and Exhibition, New Orleans, Louisiana, January 23–27, 1994. Manuscript received by the Internal Combustion Engine Division January 28, 1994. Paper No. 94-ICE-20. Associate Technical Editor: W. Cheng.

new information. The results of the GE and the A.D. Little feasibility studies both indicated that relatively inexpensive coals were feasible. General Motors, on the other hand, concluded that the Electro-Motive engines would require the more expensive ultraclean coals.

A major procurement was issued in 1988 to fund the follow-on work of both the GE and the A.D. Little projects. Work was halted on the General Motors project because of Electro-Motive's insistence on continuing the development efforts using only ultra-clean coals, an approach that the economic studies indicated was not viable.

The A.D. Little/Cooper technology development project was focused on the continued development and demonstration of technologies examined in the feasibility study. The goal was to demonstrate these technologies on a multicylinder engine at the Cooper research facility in Mount Vernon, OH. This goal was achieved in 1993.

The GE Technology Development Project also included continued development of the technologies introduced in the feasibility studies. The goal of this project was to demonstrate these technologies in a multicylinder GE engine operated on the test track at the GE facility in Erie, Pa. This goal was achieved in 1992.

Selection of the medium-speed engines as the focus of the program was based on some modeling work done by Caton and Rosegay [12], which indicated that the maximum engine speed for burn-out of coal particles in the 10 μm size range was 1000 rpm. While these model results were in agreement with modeling work done later [13, 14], some preliminary experiments reported by Kakwani [15] indicated that much higher engine speeds might be possible. These results were verified in a project with Detroit Diesel Corporation and SwRI [16], initiated in 1991, and performed in a 1900 rpm Detroit Diesel 8V-149 engine used in mine haul truck applications.

A project was initiated in 1988 at Caterpillar [17] to examine the use of a novel high-pressure gasifier system in conjunction with a large Caterpillar engine. The scope of the project involved demonstration of operation of the engine on a gas mixture simulating the gasifier output. The project also involved demonstration of the gasifier concept that included the use of preloaded canisters of coal that undergoes gasification at elevated pressure.

As indicated previously, it is felt that the economics will become favorable in the future, as the supplies of other energy resources are depleted. The objective of this paper is to provide a very clear starting point for future work in this area. The following sections contain summaries of the work that was done in this program and specifications of the fuel and engine components.

Fuel System Development

Injection system development has always been the primary obstacle to development of coal-fired diesel engines. While dry powder coal was of primary interest in the early development work, it was not emphasized in the METC Program because of the fuel handling and safety issues associated with the use of these finely divided powders. The emphasis of the METC Program was centered on the development of systems that could handle coal in water slurries with mass loadings of coal on the order of 50 percent. The development of the successful injection systems was actually tied very closely with the development of the fuels. The particle loading, particle size distribution, coal type, and additive package all affected the flow characteristics of the resulting slurry and, in turn, the operation and performance of the injection system. The emphasis of this section is a description of the mechanical components of the successful fuel systems. The resulting mechanical system specification assumes that the fuel will meet the fuel specifications discussed in a later section.

Fuel Storage and Handling. Coal in water slurries will always be unstable systems if the viscosity of the base liquid is kept low, and the particle loading is below the volume-filled condition, a situation where the particle loading is high enough that the entire fluid volume is filled with contacting particles. In other words, if the slurry has the characteristic of a fluid of reasonable viscosity, the density difference between the coal particle and the water will always cause settling.

Coal-fueled systems must therefore incorporate special features in the fuel storage and handling systems that accommodate the separation problem. Piping systems should include smooth internal flow passages, with no rapid volume changes, or changes in flow direction. The goal in the design of the piping system is to eliminate components that allow the formation of recirculation zones and volumes where the flow velocities become very low, and settling can occur. The piping system should also include allowances for flushing of the system with water or other clear fluid prior to shut-down.

Progressive cavity pumps have been used to accomplish recirculation in fuel tanks and for transport of the slurry from the tank to the engine [18–20]. Recent work at SwRI [21] indicates, however, that air-driven intensifier pumps, typically used in high-pressure paint spray systems, can be configured with components designed to handle abrasive materials. A pump in this configuration has operated reliably and at much higher discharge pressures than can be achieved using a progressive cavity pump.

Storage of CWS in tanks presents a problem in that the coal will separate very rapidly if the fuel is not circulated throughout the tank. A system was developed at SwRI that accomplished these goals. The basic concept for the storage tank system is one of removing fuel from the top of the tank and re-introducing it at the bottom through a manifold designed to create two large counterrotating eddies that flow outward along the entire length of the bottom of the tank and down at the center. A floating intake always insured that the pump removed slurry of the lowest concentration at the top of the tank. It was felt that this was important for cyclic operation of the system, and for those situations where the circulation system was shutoff for an extended period of time. In the worst case of total settling the pump takes suction from the water layer on the top of the tank and re-introduces it at the bottom, where its kinetic energy is used to remix the slurry. In nondimensional form, the optimum design condition is one in which $\mathrm{Re} \times H = 5.7$, where the Reynolds number (Re) is based on the tank diameter and the flow velocity at the exit of the manifold, and H is the ratio of the manifold discharge orifice diameter to the tank diameter. A tank system designed to these specifications was used to store a slurry of 51 weight percent coal for a two-year period at SwRI. The system was operated on a 15 minutes on/off cycle over that period.

Injection System Design. Several different slurry injection system designs were evaluated in the various projects of the feasibility study. The work at SwRI included examination of two different pump-line-nozzle systems with increased clearances [22–24], a unit injector with increased clearance [24], a Cummins Pressure-Time system [25], a unit injector equipped with a diaphragm to separate diesel fuel and slurry inside the injector [24], and a pump-line nozzle system equipped with a free piston located between the nozzle and the injection pump, and separating the slurry from diesel fuel that is circulated through the injection pump [21]. The initial efforts at GE [26] also involved the use of a diaphragm system, as well as an accumulator system that used the diaphragm, and later a free piston system as the pressurization system for the accumulator [27]. The basic layout of the GE diaphragm system is shown in Fig. 1. The A.D. Little-Cooper-AMBAC team worked on the development of pump-line-nozzle system that incorporated a free piston (called by AMBAC a shuttle piston) to separate

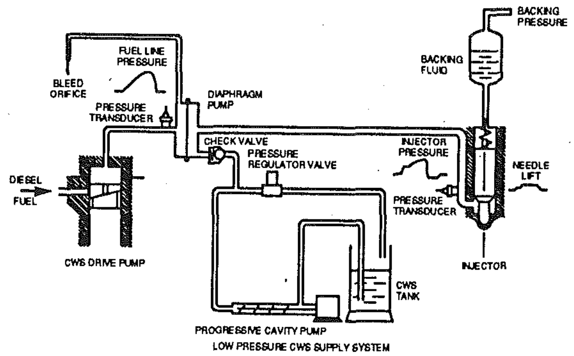

Fig. 1 General Electric fuel system schematic

the two fuels rather that a diagram [28], as well as a common rail system [29] that was not pursued once the shuttle piston system proved reliable. A shuttle piston system was also developed at SwRI for use in the high-speed engine tests on the DDC 8V-149 engine [21].

It was clear from the work at SwRI that it was essential that the slurry be separated physically from the barrel and plunger assemblies of the injection system. The design constraints on the diaphragm systems tested in both assemblies by both GE and SwRI proved to be unacceptable. Fatigue failure was a problem with these systems, almost independent of the material selection, if the diaphragm was made small enough to produce acceptable injection pressure characteristics. Increasing the size of the diaphragm to reduce the magnitude of the deflections resulted in a large increase in the volume of the high-pressure section of the system. The GE Team [30] abandoned the diaphragm approach in favor of the shuttle piston concept.

The shuttle piston approach has evolved as the most reliable CWS injection system concept. Basically, the injection system looks like a conventional pump-line-nozzle system, except that a free piston, or shuttle piston assemble, is installed in the injection line between the pump and the nozzle. The section between the injection pump and the shuttle piston is filled with diesel fuel that acts on one side of the shuttle during the injection event. Motion of the shuttle translates the pressure pulse to the slurry that fills the other side of the system. The pressurized slurry then opens the needle valve in the injection nozzle and slurry is injected into the engine. A drawing showing some detail of the SwRI [16] combined shuttle-piston-nozzle assembly is presented in Fig. 2. Development of this technology and that used in the A.D. Little Project was done with significant guidance from Mr. Jack Kimberley of AMBAC. The designs developed in the other projects share the main features shown in the drawing.

The design details of the shuttle piston assembly are very similar to those use in standard injection system barrel and plunder designs, in terms of the clearances (on the order of 2.5–25 μm clearance on the diameter) and the surface finish. The displacement volume of the shuttle must be approximately 50 percent larger than the fuel delivery required for full load. This excess capacity insures that the shuttle will not bottom and will accommodate those situations where the shuttle does not return completely. Durability of the shuttle piston assembly is greatly improved if the shuttle is coated with titanium nitride and the barrel is made of nitralloy. The GE Team developed a shuttle piston design in which the piston was made from tungsten carbide. Durability of this system was also acceptable [31].

Selection of the shuttle diameter and stroke is governed by the response time required for return of the shuttle and the compressibility of the trapped fuel. The longer the stroke, the longer the return time. The larger the diameter, the larger the trapped volume by the square of the diameter. It appears a good rule of thumb is that the diameter should equal the diameter of plunger in the injection pump, and the length of the stroke should be as close to the diameter as allowed by the 50 percent excess volume requirement.

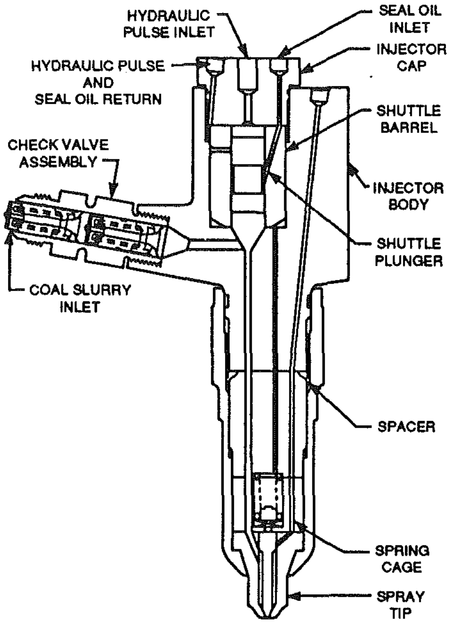

Fig. 2 SwRI combined shuttle-piston-nozzle assembly

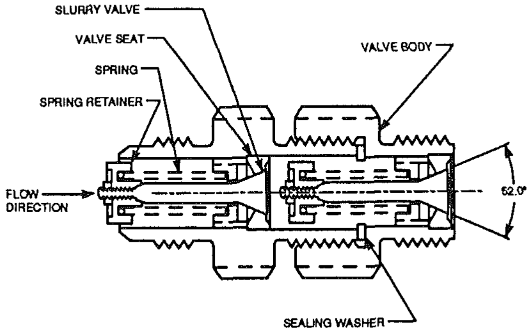

Fig. 3 Slurry fuel supply check valve

Seal oil ports, shown in Fig. 2, supply seal oil to the center of the shuttle piston stroke and to the center of the guide area of the needle valve. The seal oil is usually supplied using intensifier pumps operating with discharge pressures greater than the peak injection pressures. The seal oil acts to lubricate the moving parts and prevent the passage of coal particles into the tight clearances. The experience at SwRI [21] and in the A.D. Little work [32] indicated that the seal oil must be supplied to both locations. Optimum operation of the shuttle piston is accomplished if the piston is undercut in the region where the seal oil is introduced. Experience at SwRI indicated that the method did not work as well if the flow clearance is made in the barrel assembly.

The slurry is supplied through a special double check valve assembly to the shuttle piston. Several iterations of the check valve design were performed as a part of the work on the A.D. Little project and the details are important for reliable operation of the fixture. The configuration of the check valves are as shown in Fig. 3, with spring-loaded poppet valves having very loose fits on the poppet stems and tapered seat faces with an angle of 52 deg. The poppet valve seating face and the valve seats were both made of tungsten carbide to prevent wear.

Injection System Materials. As indicated above, wear prevention in the shuttle piston assembly is greatly improved by the appropriate selection of materials and coatings. Two other significant areas for wear in the injection system are the nozzle holes and the needle valve seat.

Nozzle Holes. Dunlay et al. [33] reported significant nozzle hole wear in the Sultzer engine after a few hours operation on a 34 percent coal in oil slurry. Nydick [34] reported nozzle hole enlargement using sintered tungsten carbide inserts in the same Sultzer engine. Based on results obtained from four different slurries, Nydick concluded that the wear was more dependent on particle size than ash content. Ryan et al. [25] reported a doubling of the nozzle hole diameter after 25 hours operation on a 50 percent CWS during bench tests using a Cummins P-T nozzle made from carbonized steel. Hsu [35] reported 10 percent decreases in the injection pressure after minutes of operation on CWS using conventional carbonized steel injection nozzle tips. Schwalb et al. [21] reported wear rates of from 0.5 to 1.6 percent increase in the nozzle hole flow area per minute of run time, using conventional steel alloys. Rao et al. [28] reported increases in the nozzle hole exit diameter of 50 percent after less than one hour of operation on low ash (less than 1 percent) coal, and substantially more wear with a 3.8 percent ash coal, a conclusion that is in direct conflict with Nydick's [34] conclusion regarding the importance of ash content.

Hard steel alloys, coatings of very hard materials, and monolithic ceramic and hardened materials have been tested in both bench experiments and in actual CWS engine tests. Some caution must be exercised in drawing absolute conclusions from the results of bench experiments. Both the A.D. Little/Cooper [36] and the GE [31] teams reported significant nozzle hole wear in conventional materials during engine tests with CWS. Both teams reported a wear pattern in which the entrance to the hole showed abrasive rounding, the exit showed enlargement that greatly exceeded the entrance enlargement, and wear pattern in the hole with a "trumpeting" appearance.

Efforts to reproduce these wear patterns in bench experiments were unsuccessful at A.D. Little and SwRI [38] and at GE [31]. The bench experiments were all performed using continuous flow through an orifice assembly in which the materials and the configuration of the hole could be easily changed. The two differences between these experiments and the actual engine were continuous versus transient operation, and the temperature. It was concluded that the trumpeted wear was due to cavitation of the CWS, starting at the exit to the nozzle. The boiling point of water is low relative to diesel fuel and the coal particles in the slurry provided high density solids that enhanced the wear during collapse of the cavitation bubbles. Temperatures in the test fixtures were too low to support cavitation. Both the GE and the A.D. Little/Cooper Teams examined several different materials and found some mixed results. It is possible, however, to select some of the more outstanding materials. It is generally agreed that the best material choices are selected formulations of tungsten carbide/cobalt, cubic boron nitride, diamond compact, and sapphire [39, 40].

Needle Valve Seats. Operation of conventional nozzles on CWS results in wear in two areas of the needle valve [36, 39], even with seal oil supplied to the guide section of the needle. The leading edge of the guide section of the valve becomes rounded after approximately 150 hours of operation. The other area of wear is on both elements of the valve seat. The conclusion from both projects is that the seat should be a tungsten carbide insert used in combination with a tungsten carbide plasma-coated needle valve.

Combustion System Development

Some basic combustion considerations are discussed in this section as they relate to operation of CWS in engines. The following sections contain descriptions of the combustion system development work accomplished in the main engine projects.

Combustion of CWS involves several very complex processes that are occurring in the combustion chamber once every engine cycle. The event begins with injection of the non-Newtonian, two-phase fuel at pressures that can exceed 100 MPa, into an environment of high-temperature, high-pressure air and combustion products. The fuel jets, traveling with exit velocities up to 500 m/s, traverse approximate 7.5 to 13 cm, prior to impacting in the combustion chamber, or on the cylinder wall. Conventional wisdom suggests that the jets must entrain and mix with air, and ignite and burn in the half millisecond that is available before they impact on the cold combustion chamber walls. Ignition of CWS is generally thought to involve a two-phase process in which the water evaporates prior to devolatization of the coal and ignition. Conventional theory also suggests that combustion of the volatiles occurs, followed by char combustion via carbon oxidation to CO on the surface and continued oxidation to CO_2 in a region surrounding the char particle.

Estimates of the characteristic time of the overall mechanism of coal combustion in engines suggests that CWS can be used only in very slow-speed engines. The results of both Kakwani et al. [15] and Schwalb et al. [21], however, show that engine speeds up to 1900 rpm can be achieved with acceptable coal combustion efficiencies. The differences between the theoretical and laboratory measured combustion rates and those observed in engines can be attributed to the fact the theory and the laboratory experiments underestimate the importance of the higher turbulence levels that are present in engines.

The fuels are non-Newtonian and can shear thicken during injection, and possibly exhibit poor atomization characteristics. As the apparent viscosity increases, the air entrainment rate can decrease with an accompanying increase in the jet tip velocity, and increasing the probability of jet-wall interactions. Impingement of the unreacted slurry on a solid surface could either enhance the mixing process through secondary atomization off the surfaces, or lead to deposition of the coal on the relatively cold combustion chamber walls. Coal type, source, processing, and particle size distribution all contribute to the rheological properties of the CWS. In addition, these properties control the ignition and combustion characteristics of the CWS both directly, through the volatile content and composition, and indirectly, through the atomization characteristics.

Impingement of CWS on lubricant wetted surfaces in the combustion chamber leads to deposition of the unreacted coal on the surfaces, degraded combustion efficiency, and greatly increased cylinder liner and ring wear. It appears that the CWS can impinge on the piston crown with minimum, or even improved, atomization and ignition characteristics. It is believed, however, that these interactions in the engine designs used in the METC program also resulted in some fuel impingement on the cylinder liner. The engine designs all incorporated very shallow combustion chambers that may have allowed some fuel splash and direct impingement on the liners, depending on the injection timing and the injection rate. In addition, the ash contained in the coal is available in the combustion chamber and can contribute to the ring and liner wear, even if the combustion efficiency is 100 percent.

A great deal of information is available in the literature regarding the basic combustion characteristics of coal and coal water slurries. The conclusions that can be drawn from these basic considerations of coal combustion are that the slurry properties must be tailored to meet the atomization and combustion requirements imposed by the time available and the thermodynamic conditions of the engine environment. The mean particle size of the coal in the slurry should probably be in the range of 10 μm, with a loading on the order of 50 percent by weight. Particles larger than these take too long to burn, and particles much smaller than these are too expensive to produce. The compression temperature must be as high as possible in order to achieve ignition and acceptable combustion rates. In fact, pilot injection of diesel fuel was suggested by the ignition temperature and combustion rate measurements in the basic experiments.

Coal-water slurries in the range of 50 percent by weight coal loading have been successfully tested in eight different engines during the METC Coal Diesel Development Program. Nelson [41] performed experiments in a single-cylinder direct-injection engine equipped with a pilot injection system and a standard diesel fuel pump-line-nozzle system for injection of the CWS. Gurney [42] also performed experiments in a single cylinder research engine. Brehob and Sawyer [43] observed slurry combustion in an optically accessible research engine. Likos and Ryan [23] used both CWS and dry coal powder in a high-swirl, high-temperature prechamber engine, as did Kakwani [44, 45]. The vast majority of the engine experience, however, has been reported by Hsu et al. [35, 46–51] and Rao et al. [28, 52] using two different four-stroke medium-speed engines. Schwalb [21] reported successful operation in a two-stroke high-speed diesel engine operating in compression ignition mode.

Basically, only three different types of engine design were considered in the METC program. The vast majority of the engine development work was done in the four-stroke designs using very open combustion chambers and very low swirl ratios. The General Electric and the A. D. Little/Cooper engine development work were both based on this type of design. The SwRI/General Motors and the SwRI/Detroit Diesel Work were both performed using two-stroke designs that incorporated the use of port scavenging and four exhaust valves. The combustion chamber designs in these two-stroke engines were both very similar to the four-stroke engines, in that they used the open, "Mexican Hat" designs, with very shallow bowls. Some limited work was also done using divided combustion chamber designs at Adiabatics Inc. [15] and at SwRI [22, 40].

As indicated above, the likelihood of fuel impingement on the piston crown was very high in the open chamber designs. The goal of using a divided chamber design was to separate the injection and early combustion from the cold, lubricant wetted walls of the combustion chamber. These designs also offered the opportunity for utilization of thermally insulated surfaces to achieve higher temperatures and correspondingly higher ignition and combustion rates. These designs were not pursued in the latter engine development activities primarily because they represented major changes in the head and piston designs of the category of engines being considered in the METC Program. These design changes would have required significant development work and would have also required very large investments to implement in a commercial engine. In addition, engine experience with CWS in the open chamber designs indicated that the combustion efficiencies were already very high, with ring and liner wear rates that could be controlled by appropriate selection of materials.

The approach that was taken in all projects involved significant injection system development in the beginning, followed by demonstration of operation on CWS in an engine, and then followed by system optimization in either single-cylinder engines, or one cylinder of the actual development engine. The GE Team and the A.D. Little/Cooper Team both achieved several hundred hours of operation on CWS in medium-speed diesel engines. The SwRI/Detroit Diesel Team achieved approximately 100 hours of operation in a high-speed diesel engine. All of this work was performed using basically the same type of CWS fuel, consisting of a coal loading in the range of 50 percent by weight, with appropriate additives for control of sedimentation and viscosity.

The GE Team based their system development on the GE 7FDL, which is a 1050 rpm engine with a bore of 229 mm and a stroke of 267 mm. Full-scale engine development and testing were performed late in the program in a Dash 8 locomotive equipped with a twelve-cylinder CWS engine. A.D. Little/Cooper performed the system development work on a Cooper JS engine, which has a bore of 330 mm, a stroke of 406 mm, and an operating speed of 450 rpm. System demonstration experiments were performed in a six-cylinder LSB engine, which has a bore of 394 mm, a stroke of 559 mm, and a speed of 400 rpm. The high-speed engine work at SwRI was performed in one cylinder of a Detroit Diesel 149 Series engine, which has a bore of 146 mm, a stroke of 146 mm, and a speed of 1900 rpm at rated power. The configurations of the two four-stroke engines were very similar, as can be seen in Fig. 4, where cross-sectional schematics of both engines are compared. The two-stroke, 149 Series engine used in the high-speed work was port scavenged, with four exhaust valves, a central injection nozzle location, and a shallow combustion chamber.

General Electric. The initial engine experiments at GE were performed using a diaphragm separated fuel injection system that produced injection pressures in the range of 40 MPa at full load. Engine optimization included: variation in the intake air temperature from 85 to 100°C; variation of intake pressure in the range from 112 kPa to 329 kPa; and simultaneous variation in the pilot and CWS injection timings. The early results indicated that combustion quality, based on coal burnout, was best at the highest possible intake pressure and temperature. They also found that the engine could be operated in compression ignition mode, but the performance was better if ignition was initiated using a pilot injection of diesel fuel, timed slightly in advance of the CWS injection [46]. Coal burnout was reported to be in the range of 95 percent in these early experiments.

The combustion efficiency was increased to 99 percent and the conclusions regarding the injection timings were later modified after the compression ratio was increased to 13:1 [48], and the CWS injection pressure was increased to 83 MPa [49] using an accumulator injection nozzle, and the number of holes in the injection nozzle tip reduced from ten to eight with the same total flow area [49]. It was concluded that it was best to inject the CWS as early as 35 deg BTDC and to wait as long as possible to inject the pilot (12 deg BTDC) in order to allow time for mixing and evaporation of the water from the slurry. As the load is decreased, however, they found that the trend reversed, and it was better to inject the pilot before the CWS in order to provide sufficient heat for evaporation of the water and ignition of the coal. Hsu [51] verified by in-cylinder, high-speed photography that the high injection pressure resulted in impingement of the CWS on the hot piston crown, leading to improved atomization and more rapid combustion, if the pilot injection was delayed until 15 deg BTDC.

It appeared that pilot quantities equivalent to 5–6 percent of the total energy input at full load are required across the load range in order to achieve stable operation. Optimization of the pilot orientation and configuration resulted in the system shown schematically in Fig. 4(*a*). The pilot nozzle utilized a tip configuration in which the outer two holes had smaller diameter in order to maximize the interaction of the CWS jets with the pilot jets at the lowest possible pilot flow rate.

A.D. Little/Cooper. System optimization in the A.D. Little/Cooper program was performed in a single-cylinder version of the Cooper JS engine. The initial experiments were performed using the shuttle piston injection system designed by AMBAC [52]. Using this system, they were able to achieve injection pressures in excess of 80 MPa, even in the early work.

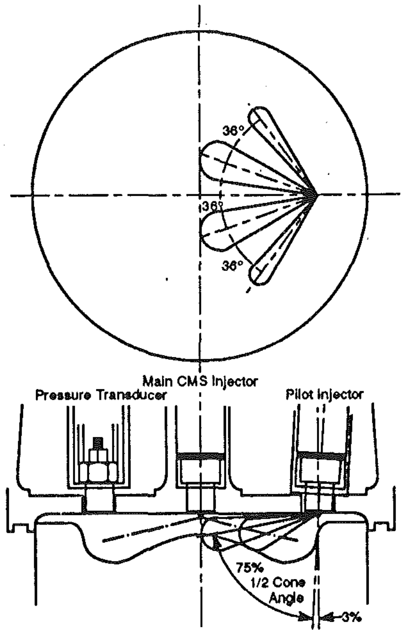

a. General Electric

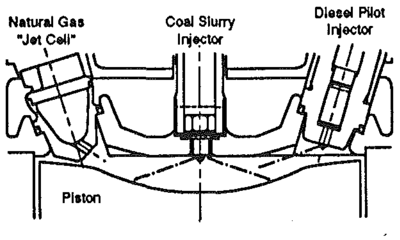

b. A. D. Little / Cooper

Fig. 4 Engine combustion chamber schematics for operation on coal-water slurry

Like the GE engine, the Cooper engines are generally turbocharged and intercooled. The coal engine configuration evolved to a system where the intercooler is bypassed so that the intake air temperature is in the range of 145°C [28]. They found that increasing the intake temperature beyond this level was effective in improving operation in compression ignition mode. They also concluded, however, that pilot injection gave more reliable operation, and that the 145°C intake air temperature was more than adequate when using a pilot to initiate combustion.

The optimum pilot characteristics in the Cooper 400 rpm engine are very similar to the GE engine. It appears that the best pilot quantity is the equivalent of 5–6 percent of the total energy input at full load. In this slower engine, they found that the best pilot timing is to inject at the same time as the CWS, or at 18 deg BTDC.

Injection system optimization work centered on development of reliable components and optimum configurations for combustion. The hole geometry was examined at SwRI [53] in terms of the effects on atomization and mixing. Extensive engine experiments were also performed to determine the optimum configuration for durability of the nozzle and performance of the engine. These experiments included examination of the effects of the hole size, number, and orientation in the nozzle tip.

The Cooper experience in the JS engine was successfully transferred to the larger bore LSB engine, and demonstrated in a six-cylinder configuration. The LSB coal engine was turbocharged with no intercooler so that the intake air temperature was in the range of 135°C, with an injection pressure in the range of 100 MPa, and a CWS timing of 22 deg BTDC. The pilot quantity was in the range of 5 percent of the full power energy input, with a timing adjusted slightly in advance of the CWS injection.

The full-scale LSB demonstration experiments were performed using an extensive exhaust aftertreatment system that included ammonia injection and selective catalytic reduction of NO_x, sodium based sorbent injection and collection for SO_2 control, and the use of a bag house for sorbent recovery and particulate removal.

SwRI/Detroit Diesel. Southwest Research Institute [25] performed CWS experiments early in the METC program in both a 71 Series Detroit Diesel high-speed engine and a General Motors, Electro-Motive Division (EMD) 567 medium-speed engine. The Detroit Diesel engine is geometrically a one-half scale version of the EMD engine. This early work, while limited in duration, pointed out the temperature advantage of using a two-stroke engine for operation on CWS. In addition, Kakwani et al. [15] were the first to point out that high-speed engine can be operated on CWS if the in-cylinder temperatures are sufficiently high at the time of CWS injection. Detroit Diesel also developed technology applicable in these engines to allow for operation in compression ignition mode on methanol. Detroit Diesel and SwRI, therefore, set out in 1990 to demonstrate that high-speed diesel engines could be successfully operated on CWS.

The CWS development experiments were performed using one cylinder of an eight-cylinder engine. The head was modified to accept an in-cylinder pressure transducer, and the piston was changed to increase the compression ratio from the normal 15:1 to 19:1, in order to increase the compression temperature. This change was made based on modeling work [54] that indicated that the higher compression ratio was needed in order to achieve the ignition delays and combustion rates required for operation of the engine at 1900 rpm. A shuttle piston injection system was also developed for operation at these higher speeds. It is important to note the injection system on the 400 rpm Cooper engine operates at 200 injections per minute, the injection system on the 1000 rpm GE engine runs at 500 injections per minute, while the injection system on the 149 engine had to operate at 1900 injections per minute, or almost ten times as fast as the Cooper system, and four times as fast as the GE system.

The results of the experiments indicated that reliable autoignition of the CWS could be achieved at the high load conditions if the intake temperature was made as high as possible. This was accomplished in the experimental engine by closing the blower bypass (route all of the air through the blower) and by stopping the flow of coolant to the intercooler. The problem was one of balancing these conditions across the speed-load range of the engine, when the in-cylinder temperatures tend to decrease as the load decreases. Injection timing was found to be critical for operation in compression ignition mode, where the peak cylinder pressure was excessive if the injection timing was advanced too far, and misfire occurred due to progressively lowering temperature as the injection timing was either retarded or advanced too far in the cycle. These results are demonstrated in Figs. 5 and 6, where the cylinder pressure and heat release rate data are presented for different injection timing settings. The best combustion results were obtained with an injection timing of 20 deg BTDC and the highest achievable air box pressure and temperature, or 192 kPa and 125°C, respectively.

Coal-Water Slurry Properties

Coal-water slurries (CWS) are two-phase mixtures that generally exhibit complex flow and combustion characteristics. Important characteristics of these slurries include flow at no,

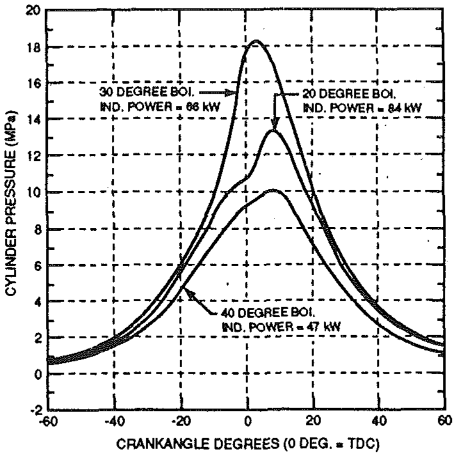

Fig. 5 Combustion pressure traces for 149 engine operation on coal-water slurry

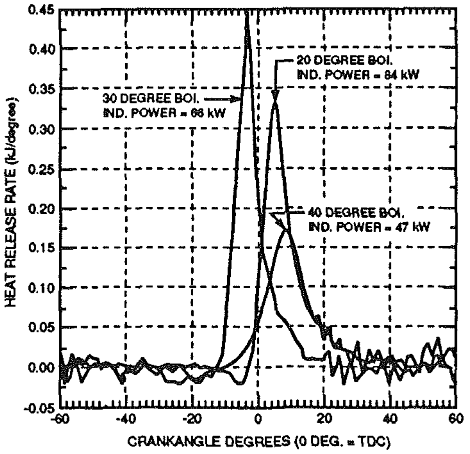

Fig. 6 Heat release rated computed from the pressure data

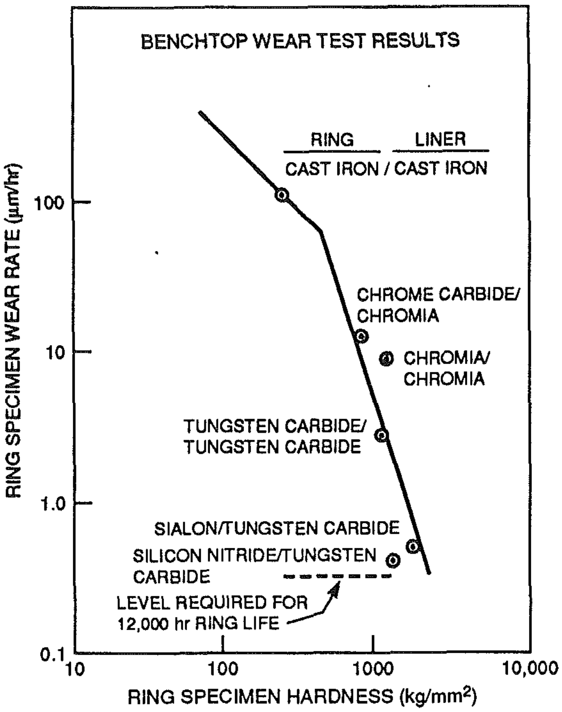

Fig. 7 A.D. Little ring and liner wear data [37]

or low, shear for settling properties of the solids, flow at high shears normally encountered in diesel injection systems, atomization and evaporation properties of slurry sprays, and ignition and combustion properties at conditions normally achievable in engines. These properties of the slurry are dependent on the coal rank and source, the particle size distribution of the solids in the slurry, the mass loading of the coal, and the types and concentrations of additives that are used to improve stability, compatibility, and flow at high shear rate. This section is not meant to be an all inclusive review of slurry technology, but rather a brief summary of the findings of the METC Program related to the more important interactions of the slurry properties and performance in the engine hardware.

There were at least eleven suppliers of CWS in 1985. Otisca Industries, AMAX, and United Coal were the main sources for the CWS used in the early METC sponsored projects. Many of the companies were not in business by 1988, and Energy International, University of North Dakota Energy & Environmental Research Center, CQ Inc., and Otisca supplied most of the slurry for the work completed late in the program.

CWS property effects were examined as a part of the engine development activities at GE, A.D. Little/Cooper, SwRI/Detroit Diesel, and Adiabatics Inc. The initial goals were generally to improve the handling and combustion characteristics as a part of the engine optimization. The results of the GE studies indicated that while smaller coal particles produced faster burn rates, selection of the appropriate additive can be used to increase the burn rate of larger particles, at least for the Otisca cleaned coal. The results of the A.D. Little/Cooper [55] fuel evaluations indicated that the lower speed Cooper engine was not very sensitive to the CWS properties, as long as the slurry did not exhibit flow problems that prevented operation in the engine.

The slurries generally exhibited shear thinning in the range from 1 to 30 s^{-1}, and relatively constant viscosity in the range from 30 to 1000 s^{-1}. The low shear rheology is advantageous for storage (high viscosity at no shear) and transport through piping system (shear thinning at low shear rate). The CWS with the larger particles exhibited shear thickening tendencies beyond 1000 s^{-1}, but the CWS with the smaller particles had nearly constant viscosity beyond 10,000 s^{-1}.

Engine Wear

The other major wear problems in CWS engines occur in the ring and liner areas. Work in reciprocating wear fixtures indicates the ring and liner wear is a combination of soft abrasive wear, due to the presence of coal in the wear couple, and three-body wear associated with the ash particles that enter the wear region. The three-body wear associated with the presence of the ash particles is a much more significant contributor to the wear rate than the soft abrasive wear, but it should be noted that ring and liner wear would still be a problem if unburned coal enters the wear couple, even if the ash were totally removed from the coal. Increased surface roughness was found to increase the thickness of the hydrodynamic oil film and detergent additives were found to minimize the abrasive wear, suggesting that surface finish and lubricant formulation could be tailored to minimize wear rates [56].

The magnitude of the ring and liner wear problem is demonstrated in Fig. 7 from Mayville et al. [37], where the ring wear rates on CWS are compared to that required to achieve diesel fuel durability. Also shown on the figure are the wear rates for other material combinations, indicating that the wear rates are greatly reduced through the use of hard coatings.

The hard coatings were examined in some detail by both the A.D. Little/Cooper Team and the GE Team. The A.D. Little/Cooper work, performed by Mayville et al. [57], indicated that tungsten carbide coated ring and liners exhibited acceptable wear characteristics during operation on CWS. Similar data

Table 1 CWS Specification

Coal	Bituminous
Mean coal size	5 μm
Top particle size	15 μm
Ash content	1 percent by mass
Sulfur	1 percent by mass
Viscosity	>300 centipoise @ 1000 s^{-1}
Additive	Dispersant

from the GE Team were reported by Flynn et al. [31]. The GE Team also concluded that the tungsten carbide coatings provided acceptable wear characteristics.

Summary—CWS Engine Status (1993)

The use of coal-water slurry has been demonstrated to be technically feasible. This conclusion is based upon the use of well-formulated slurries (CWS) in the range of 45-50 weight percent coal loading, using bituminous coals ground to 5-12 μm mean size particles, with a top size limit of 30 μm, and sulfur and ash contents in the range of 1 percent each by mass. Higher ash contents may be usable in the engines, but the technology for coal cleaning has advanced to the point where 1 percent ash is reasonable. Several hundred hours of engine operation have been achieved in the GE and the A.D. Little/Cooper programs.

It appears that the economic factors are currently favorable for use of CWS in terms of the system, fuel, and operating costs, if the environmental impact is neglected. It appears that the level of exhaust aftertreatment required to meet current and future standards may be such that the first costs and the operating costs are too large to be offset by the lower fuel cost.

The current state of the technology is such that the engine designs can be very well defined for engines that operate in the speed range below 1000 rpm. The design details for higher speed engines are not as well defined because the operating experience in these engines is less extensive. The purpose of this section is to outline the details of the current understanding of CWS engines, and by doing so, clearly define the starting point when either the economics become more favorable, or the environmental issues can be handled.

Fuel Specification. The fuel specification is somewhat dependent on the engine speed, in that the operating experience indicates that the slower 400 rpm engines are much less sensitive to fuel factors than the 1000 rpm engine. Table 1 therefore represents an attempt to satisfy the requirements of the 1000 rpm engines, realizing that the fuel will be marginally better than required for operation of the slower engines.

Fuel System Specification. Details of the fuel system design can be obtained above, or from the cited references. The following are the salient points that are common to all designs and should be considered as the starting point for future work in this area.

Piping: Smooth pipe, no dead volumes, no rapid changes in flow area.

Tank: Continuously recirculating, horizontal-cylindrical tank equipped with a floating suction, and discharge through a manifold with exit holes designed to produce flow with $\mathrm{Re} \times H = 5.7$.

Injection Pump: Conventional diesel injection pump sized to inject the required amount of slurry to achieve full load and coupled to the engine, supplying diesel fuel pressure pulses to a shuttle piston assembly.

Shuttle Piston Assembly: Conventional injection pump barrel and plunger assembly design parameters of surface finish and clearances, titanium nitride coated, sized to displace 150 percent of the required full load slurry flow, and with an L/D of approximately 1.

Nozzle Holes: Sapphire or diamond compact inserts.

Needle Valve Seat: Tungsten carbide seat insert.

Needle Valve: Tungsten carbide plasma-coated steel.

Engine Design. The results of the METC program indicate that conventional open chamber, direct injection, low-swirl combustion chambers are acceptable for operation on CWS. Combustion efficiencies of 99 percent were routinely demonstrated in these designs if the intake air temperature and pressure are made as high as practical for the mechanical limitations of the engine components. The bowl shape can be either a shallow "Mexican Hat" design, as used in the GE and SwRI/Detroit Diesel projects, or a shallow bowl as used in the Cooper engine.

It is clear that turbocharging is required to achieve acceptable breathing characteristics, especially with the higher intake air temperatures required for operation on CWS. The intake air temperature should be at least 135°C and the pressure should be in the range of 300 kPa. While auto-ignition was demonstrated in the GE, the Cooper, and the Detroit Diesel engines, positive ignition timing control is essential for reliable and efficient operation of these CWS engines. Pilot injection of small quantities of diesel fuel appears to be the best method of ignition control. It offers the opportunity for cold starting and operation at part-load conditions, especially idle, where the demonstrated experience on CWS indicates that the engine temperatures drop below the levels required for reliable operation on CWS.

The rings and liner should be tungsten carbide coated and the lubricant should contain high concentrations of dispersant additive to prevent excessive wear of these components. It appears that filtration of the lube oil using the best available filter technology (pleated paper filter with 5 μm pore size) is sufficient to control wear rates in the rest of the engine.

Acknowledgments

The author acknowledges the financial and technical support provided by the U.S. Department of Energy, Morgantown Energy Technology Center. The author would also like to thank the Project Team at A.D. Little/Cooper for their efforts in making it possible to complete this paper.

References

1 Soehngen, E. E., "Development of Coal-Burning Diesel Engines in Germany," Final Report prepared for the Energy Research and Development Administration/Offic of Fossil Energy, Report No. FE/WAPO/3387-1, Aug., 1976.

2 Tracy, E. W., Jr., "Feasibility Study of the Use of Powdered Coal as a Fuel for Diesel Engines," SwRI Report No. 8-681-1, Southwest Research Institute, 1957.

3 Marshall, H. P., and Shelton, C., "The Coal Burning Piston Engine," *Bulletin of the Virginia Polychemical Institute*, Engineering Experimental Station, No. 135, Vol. 53, 1959.

4 Marshall, H. P., and Walters, D. C., Jr., "An Experimental Investigation of a Coal-Slurry Fueled Diesel Engine," SAE Technical Paper No. 770795, 1977.

5 Rich, L. L., and Waker, M. L., "Pulverized Coal Burning Diesel Engine," Howard University, Office of the Coal Research, R&D Report No. 46, USGPO, Washington, DC, 1969.

6 Caton, J. A., and Rosegay, K. H., "A Review and Comparison of Reciprocating Engine Operation Using Solid Fuels," SAE Technical Paper No. 831362, *SAE Transactions*, Vol. 92, 1984, pp. 1108-1124.

7 Ryan, T. W., III, Likos, W. E., and Moses, C. A., "The Use of Hybrid Fuels in a Single-Cylinder Diesel Engine," SAE Technical Paper No. 801380, 1980.

8 Ryan, T. W., III, Callahan, T. J., Dodge, L. G., and Moses, C. A., "Injection, Atomization, and Combustion of Carbon Slurry Fuels," SAE Technical Paper No. 821199, 1983.

9 Ryan, T. W., III, and Dodge, L. G., "Diesel Engine Injection and Combustion of Slurries of Coal, Charcoal, and Coke in Diesel Fuel," SAE Technical Paper No. 840119, 1984.

10 Ryan, T. W., III, and Dodge, L. G., "Development of Carbon Slurry Fuels for Transportation (Hybrid Fuels—Phase II)," prepared for National Aeronautics and Space Administration, Lewis Research Center under Contract No. DEN3-263 for U.S. Department of Energy Report No. DOE/NASA/0263-1, 1984.

11 Nyrick, S. E., Porchet, F., and Steiger, H. A., "Continued Development of a Coal/Water Slurry-Fired Slow-Speed Diesel Engine: A Review of Recent Test Results," ASME Paper No. 87-ICE-10; ASME Journal of Engineering for Gas Turbines and Power, Vol. 109, 1987, pp. 465–476.

12 Caton, J. A., and Rosegay, K. H., "Cycle Simulation of Coal Particle Fueled Reciprocating Internal Combustion Engines," presented at the SAE International Off-Highway Meeting, 1983.

13 Wahiduzzaman, S., Blumberg, P. N., Keribar, R., and Rackmil, C. I., "A Comprehensive Model for Pilot-Ignited Coal/Water Mixture Combustion in a Direct-Injection Diesel Engine," ASME ICE-Vol. 12; also ASME Journal of Engineering for Gas Turbines and Power, Vol. 112, 1990, pp. 384–390.

14 Wahiduzzaman, S., Blumberg, P. N., and Hsu, B. D., "Simulation of Significant Design and Operating Characteristics of a Coal Fueled Locomotive Diesel Engine," *Coal-Fueled Diesel Engines*, ASME ICE-Vol. 14, 1991.

15 Kakwani, R., and Kamo, R., "Extending and Enhancing the Scientific Base for Advanced Coal-Fueled Power Systems Utilizing Heat Engines," Contract No. DE-AC21-86MC23258, *Proceedings of the Annual Coal Fuel Heat Engines and Gas Stream Cleanup Systems Contractors Review Meeting*, DOE/METC-88/6094 (DE88001088), 1988, pp. 396–408.

16 Schwalb, J. A., Ryan, T. W., III, Kakwani, R. M., and Winsor, R. E., "Study of Coal-Water-Slurry Fuel Combustion in a High-Speed Diesel Engine: Part 2, Bench Test Results," presented at the ASME Energy-Sources Technology Conference and Exhibition, Houston, TX, 1993.

17 Greenhalgh, M. L., "High-Pressure Coal Fuel Processor/Engine Development," *Coal-Fueled Diesel Engines*, ASME ICE-Vol. 14, 1991, pp. 49–55.

18 Urban, C. M., Mecredy, H. E., Ryan, T. W., III, Ingalls, M. N., and Jett, B. T., "Coal-Water Slurry Operation in an EMD Diesel Engine," ASME Paper No. 88-ICE-28; also ASME Journal of Engineering for Gas Turbines and Power, Vol. 110, 1988, pp. 437–443.

19 Hsu, B. D., and Confer, G. L., "Progress on the Investigation of Coal-Water-Slurry Fuel Combustion in a Medium Speed Diesel Engine: Part 4—Fuels Effect," *Coal-Fueled Diesel Engines*, ASME ICE-Vol. 14, 1991, pp. 1–8.

20 Wilson, R. P., personal communication with T. W. Ryan III, 1989.

21 Schwalb, J. A., Ryan, T. W., III, Kakwani, R. M., and Winsor, R. E., "Coal-Water-Slurry Autoignition in a High-Speed Diesel Engine," SAE Paper No. 941907, 1994.

22 Likos, W. E., and Ryan, T. W., III, "Combustion Characteristics of Coal Fuels in a High Temperature Diesel Engine," ASME Paper No. 87-ICE-56, 1987.

23 Likos, W. E., and Ryan, T. W., III, "Experiments With Coal Fuels in a High Temperature Diesel Engine," ASME Paper No. 88-ICE-29; also ASME Journal of Engineering for Gas Turbines and Power, Vol. 112, 1990, pp. 376–383.

24 Ryan, T. W., III, Callahan, T. J., Mecredy, H. E., Baker, Q. A., and Jett, B. T., "Coal Slurry Combustion—Bomb and Small Engine Test Results," ASME Paper No. 87-ICE-31, 1987.

25 Ryan, T. W., III, Callahan, T. J., Schwalb, J. A., Mecredy, H. E., Urban, C. M., Baker, Q. A., Ingalls, M., and Fanick, E. R., "Coal Fueled System Research," Final Report, Subcontract to Allison, P.O. No. H524201, U.S. DOE Contract DE-AC21-85MC22123, 1989.

26 Leonard, G. L., and Fiske, G. H., "A Comparison of a Positive Displacement Fuel Injection System With an Accumulator-Based System for Coal-Fueled Diesel Engine Applications," ASME Paper No. 87-ICE-32, 1987.

27 Flynn, P. L., Hsu, B. D., and Leonard, G. L., "Coal Fueled Diesel Engine Progress at GE Transportation Systems," ASME ICE-Vol. 12; also ASME Journal of Engineering for Gas Turbines and Power, Vol. 112, 1990, pp. 369–375.

28 Rao, A. K., Wilson, R. P., Balles, E. N., Mayville, R. A., McMilliam, M. H., and Kimberley, J. A., "Cooper-Bessemer Coal-Fueled Engine System—Progress Report," *Coal-Fueled Diesel Engines*, ASME ICE-Vol. 7, pp. 9–17; also ASME Journal of Engineering for Gas Turbines and Power, Vol. 111, 1989, pp. 498–506.

29 Wilson, R. P., Balles, E., Benedek, K., Mayville, R., Rao, K., and Kimberely, J., "Coal Fueled Diesel Systems Research Coal Fueled Diesel Combustion: Cooper-Bessemer Test Results," Contract No. DE-AC21-85MC22182, *Proceedings of the Annual Coal Fuel Heat Engines and Gas Stream Cleanup Systems Contractors Review Meeting*, DOE/METC-88/6094 (DE88001088), 1988, pp. 371–382.

30 Hsu, B. D., Leonard, G. L., and Johnson, R. N., "Progress on the Investigation of Coal Water Slurry Fuel Combustion in a Medium-Speed Diesel Engine, Part 3—Accumulator Injector Performance," *Coal-Fueled Diesel Engines*, ASME ICE-Vol. 7, pp. 19–25; also ASME Journal of Engineering for Gas Turbines and Power, Vol. 111, pp. 516–520.

31 Flynn, P. L., Leonard, G. L., and Mehan, R. L., "Component Wear in Coal-Fueled Diesel Engine," ASME Paper No. 89-ICE-15; also ASME Journal of Engineering for Gas Turbines and Power, Vol. 111, 1989, pp. 521–529.

32 Kimberley, J. A., personal communication with T. W. Ryan III, 1992.

33 Dunlay, J. B., et al., "Slow Speed Two Stroke Diesel Engine Tests Using Coal Based Fuels," ASME Paper No. 81-DGP-12, 1981.

34 Nydick, S. E., "Development of a Coal/Water-Slurry-Fueled Diesel Engine for Industrial Cogeneration," Final and Summary Report Under Contract No. AC02-82CE40539, U.S. DOE/Argonne, IL., Thermo Electron Corp. (Waltham, MA), 1987.

35 Hsu, B. D., "Progress on the Investigation of Coal Water Slurry Fuel Combustion in a Medium-Speed Diesel Engine, Part 2. Preliminary Full Load Test," ASME Paper No. 88-ICE-5; also ASME Journal of Engineering for Gas Turbines and Power, Vol. 110, 1988, pp. 423–430.

36 Mayville, R. A., Rao, A. K., and Wilson, R. P., "Durable Component Development Progress for the Cooper-Bessemer Coal-Fueled Diesel Engine," ASME Paper No. ICE-Vol. 14, *Coal-Fueled Diesel Engines*, 1989, pp. 23–27.

37 Mayville, R. A., Rao, A. K., and Wilson, R. P., "Cooper-Bessemer Coal-Fueled Engine System: Recent Developments in Durable Components," *Coal-Fueled Diesel Engines*; ICE-Vol. 12, 1990, pp. 17–22.

38 Schwalb, J. A., Dodge, L. G., Ryan, T. W., III, Callahan, T. J., and Mannheimer, R. J., "Coal-Water Slurry Fueled Diesel Engine—Injector Atomization and Wear Tests," Final Report for DOE/METC Contract DE-AC2188MC25124, A.D. Little Subcontract 61366, SwRI Project 03-2976, 1991.

39 Flynn, P. L., Mehan, R. L., Leonard, G. L., and Johnson, R. N., "Hardened Materials in Coal-Fueled Diesels," Contract No. DE-AC21-88MC23174, *Proceedings of the Annual Coal Fuel Heat Engines and Gas Stream Cleanup Systems Contractors Review Meeting*, DOE/METC-88/6094(DE88001088), 1988, pp. 211–225.

40 Wilson, R. P., et al., "Stationary Coal-Fueled Diesel System," Contract No. DE-AC21-88MC25124, *Proceedings of the Seventh Annual Coal-Fueled Heat Engines and Gas Stream Cleanup Systems Contractors Review Meeting*, DOE/METC-90/6110 (DE90000480), 1990, pp. 3–10.

41 Nelson, L. P., Seker, W. R., and Sampson, P. W., "The Combustion Characteristics of Slurried Fuels in Diesel Engines: Detailed Measurements in Analysis," *Proceedings of the First Annual Heat Engines Contractors Meeting*, DOE/METC/84-31 (DE85001953), METC, 1984, pp. 225–234.

42 Gurney, M. D., "Investigation of Diesel Fuel Injection Equipment Response to Coal Slurry Fuels," *Proceedings of the First Annual Heat Engines Contractors Meeting*, DOE/METC/84-31 (DE85001953), METC, 1984, pp. 221–224.

43 Brehob, D. D., and Sawyer, R. F., "Compression Ignition of Coal Slurry Fuels," ASME Paper No. 87-ICE-11, 1987.

44 Kakwani, R. M., Kamo, R., Cutlip, R. G., and Smith, W. C., "Combustion Characteristics of Dry-Coal-Powder-Fueled Adiabatic Diesel Engine," *Coal-Fueled Diesel Engines*, ASME ICE-Vol. 7, 1989, pp. 27–34.

45 Kakwani, R. M., Badgley, P. R., and Smith, W. C., "Development of Fuel Injection and Combustion Systems for Coal-Water-Slurry Fueled Diesel Engines," *Coal-Fueled Diesel Engines*, ASME ICE-Vol. 12, 1990, pp. 41–50.

46 Hsu, B. D., and Flynn, P. L., "Coal Fueled Diesel Engine Technology Development: GE Single-Cylinder Engine Results," DOE/METC Contractor Review Meeting, Paper No. 3.1, 1989.

47 Hsu, B. D., Leonard, G. L., and Johnson, R. N., "Progress on the Investigation of Coal-Water-Slurry Fuel Combustion in a Medium-Speed Diesel Engine: Part 3—Accumulator Injector Performance," ASME ICE-Vol. 7, pp. 52–57; ASME Journal of Engineering for Gas Turbines and Power, Vol. 111, 1989, pp. 516–520.

48 Hsu, B. D., Confer, G. L., and Shen, Z. J., "Progress on the Investigation of Coal Water Slurry Fuel Combustion in a Medium Speed Diesel Engine: Part 5—Combustion Studies," ASME ICE-Vol. 16; also ASME Journal of Engineering for Gas Turbines and Power, Vol. 114, 1992, pp. 515–521.

49 Hsu, B. D., and Branyon, D. P., "Progress on the Investigation of Coal Water Slurry Fuel Combustion in a Medium Speed Diesel Engine, Part 6—In-Cylinder Combustion Photography Studies," *Coal Fueled Diesel Engines—1993*, ASME ICE-Vol. 19, pp. 1993, pp. 15–23.

50 Hsu, B. D., "Coal-Fueled Diesel Engine Development Update at GE Transportation Systems," ASME ICE-Vol. 16, pp. 1–10; also ASME Journal of Engineering for Gas Turbines and Power, Vol. 114, 1992, pp. 502–508.

51 Hsu, B. D., "Progress on the Investigation of Coal Water Slurry Fuel Combustion in a Medium-Speed Diesel Engine: Part 1. Ignition Studies," ASME Paper No. 88-ICE-4; also ASME Journal of Engineering for Gas Turbines and Power, Vol. 110, 1988, pp. 415–422.

52 Rao, A. K., Melcher, C. H., Wilson, R. P., Balles, E. M., Schaub, F. S., Kimberley, J. A., "Operating Results of the Cooper-Bessemer JS-1 Engine on Coal-Water Slurry," ASME Paper No. 88-ICE-12; ASME Journal of Engineering for Gas Turbines and Power, Vol. 110, 1988, pp. 431–436.

53 Dodge, L. G., Callahan, T. J., Ryan, T. W., III, Schwalb, J. A., Benson, C. E., and Wilson, R. P., "Injection Characteristics of Coal-Water Slurries in Medium-Speed Diesel Equipment," ASME ICE-Vol. 16, also ASME Journal of Engineering for Gas Turbines and Power, Vol. 114, 1992, pp. 522–527.

54 Kakwani, R. M., Winsor, R. E., Ryan, T. W., III, Wahiduzzaman, S., and Wilson, R. P., Jr., "Study for Coal-Water-Slurry Fuel Combustion in a High-Speed Diesel Engine," *Coal-Fueled Diesel Engines*, ASME ICE-Vol. 16, 1992, pp. 25–32.

55 Wilson, R. P., Benson, C. E., Ryan, T. W., III, Schwalb, J. A., Dodge, L. G., and Callahan, T. J., "Coal-Water Slurry Spray Characterization," Contact No. DE-AC21-88MC2124, *Proceedings of the Eighth Annual Coal-Fueled Heat Engines and Gas Stream Cleanup Systems Contractors Review Meeting*, DOE/METC-90/6110 (DE90000480), 1991, pp. 263–272.

56 Schwalb, J. A., and Ryan, T. W., III, "Surface Finish and Particle Size Effects on Wear in Coal-Fueled Diesel Engines," *Coal-Fueled Diesel Engines*, ASME ICE-Vol. 14, 1991, pp. 29–37.

57 Mayville, R. A., Rao, A. K., and Wilson, R. P., "Cooper-Bessemer Coal-Fueled Engine System: Recent Developments in Durable Components," *Coal-Fueled Diesel Engines—1990*, ASME ICE-Vol. 14, 1991, pp. 23–27.

The General Electric Coal-Fueled Diesel Engine Program (1982-1993): A Technical Review

J. A. Caton
Department of Mechanical Engineering,
Texas A&M University,
College Station, TX 77843

B. D. Hsu
General Electric—Transportation Systems,
Erie, PA 16531

In the early 1980s, General Electric—Transportation Systems (GE-TS), a manufacturer of locomotive diesel engines, announced plans to develop a coal-fueled locomotive due to the availability and low cost of coal. In 1985 and 1988, the General Electric Company (GE) was awarded major contracts from the Department of Energy, Morgantown Energy Technology Center, to continue the research and development of a coal-fueled diesel engine. This paper is a review of the technical accomplishments and discoveries of the GE coal-fueled diesel engine research and development program during the years 1982–1993. The results of an economic assessment completed by GE-TS indicated the merits for the development of a coal-fueled diesel engine for locomotive applications and therefore, GE-TS embarked on an ambitious program to develop and commercialize a coal-fueled diesel engine. Among the major accomplishments of this program were the development of specialized fuel injection equipment for coal-water slurries, diamond compact inserts for the nozzle tips for wear resistance, and an integrated emissions control system. Over 500 hours of engine operation was accumulated using coal fuel during the duration of this program. A major milestone was attained when, during November and December 1991, a coal-fueled diesel engine powered a locomotive on the General Electric test track.

Introduction

General Electric-Transportation Systems (GE-TS), located in Erie, PA, is one of two U.S. manufacturers of locomotive diesel engines. General Electric has a long history of being active in coal technology from the early coal-fired steam engines to more recent developments involving coal gasification, and coal-fueled gas turbines and diesel engines. Although the coal-fired steam engine was displaced by the diesel engine to power locomotives, the recent price and availability of coal fuels relative to petroleum fuels has motivated an examination of a new, modern coal-fueled locomotive. The prime mover for such a locomotive could be a steam engine, gas turbine, or diesel engine. After a detailed comparison, the diesel engine was deemed to be one of the most attractive options.

Development of a coal-fueled diesel engine has been attempted on and off for about 100 years (Soehngen, 1976; Caton and Rosegay, 1984). The motivations for these past developments have been largely economic and strategic. Economic motivations are due to the low cost of coal relative to petroleum fuels. The strategic motivations are due to the domestic source of coal as opposed to imported fuels. Secondary motivations, which have led to these past developments, have included potential fire and explosion reductions and the potential for emergency fuels in times of oil shortages. Past development activities have included the design, construction, and testing of laboratory and full-scale engines to operate on a variety of coal fuels (Soehngen, 1976; Caton and Rosegay, 1984).

In the early 1980s, General Electric announced plans to develop a coal-fueled locomotive. These plans were at least partially motivated by Burlington Northern (BNR) and Norfolk Southern Railroads (NSR). Burlington Northern Railroad was interested in a coal-fueled engine since they own large amounts of coal reserves near their railroads. At about this time, the Department of Energy initiated major programs to promote the development of coal fueled heat engines. Programs for developing both coal-fueled diesel engines (Dunlay et al., 1980; Carpenter and Crouse, 1985) and gas turbines (Crouse et al., 1984) were initiated in the late 1970s. Beginning in 1984, the U.S. Department of Energy, Office of Fossil Energy, Morgantown Energy Technology Center, initiated significant programs to stimulate the development of coal-fueled diesel engines (Carpenter and Crouse, 1985, 1986). The more recent of these programs were directed at U.S. manufactured, heavy-duty diesel engines. The diesel engine manufacturers that participated included General Electric—Transportation Systems, Cooper-Bessemer, General Motors—Electromotive Division, Caterpillar, Inc., and Detroit Diesel Corporation. In 1985 and 1988, the General Electric Company (GE) was awarded major contracts from the Department of Energy,

---

Contributed by the Internal Combustion Engine Division and presented at the Energy-Sources Technology Conference and Exhibition, New Orleans, Louisiana, January 23–27, 1994. Manuscript received by the Internal Combustion Engine Division January 28, 1994. Paper No. 94-ICE-8. Associate Technical Editor: W. Cheng.

Morgantown Energy Technology Center, to continue the research and development of a coal-fueled diesel engine.

Since most of the following work involves one of the General Electric diesel engines, a brief description of this engine is provided next. The diesel engine used on most of their locomotives is a four-stroke cycle engine with twelve or sixteen cylinders, each with a bore of 229 mm and a stroke of 267 mm. Each cylinder of these engines produces about 190 kW of power (at full load), and operates between 450 and 1050 rpm. These engines typically have a compression ratio of 12 and, at full load, operate with an equivalence ratio of about 0.5. These full-load conditions result in a need to inject, atomize, ignite, and combust the coal-water slurry within about 10 ms.

This paper is a review of the technical accomplishments and discoveries of the GE-TS coal-fueled diesel engine research and development program during the years 1982–1993. As mentioned above, other groups were conducting similar research during this period. In the following review, therefore, descriptions of accomplishments by GE-TS are not meant to preclude similar accomplishments by others. For the most part, these past activities are reviewed in chronological order. For convenience, these activities are discussed in three major sections: (1) economic and technical assessments, (2) single-cylinder engine and laboratory research, and (3) multiple-cylinder engine developments.

Economic and Technical Assessments

Hapeman and Savkar (1986) reported on the initial economic and technical assessments completed by GE-TS. This original work was cofunded largely by Burlington Northern and Norfolk Southern Railroads. They indicated that due to escalation of diesel fuel prices in the early 1980s and the relatively inexpensive and plentiful coal resources in the USA, the development of a coal-fueled locomotive should be explored. The three criteria they listed for the success of a coal-fueled locomotive were: (1) technical feasibility, (2) financial feasibility, and (3) economic attractiveness to the railroads.

The technical feasibility was examined by reviewing the literature, and by conducting laboratory experiments (Hapeman and Savkar, 1986). These activities are reviewed in more detail below, but a brief overview is presented here to substantiate the technical feasibility of coal-fueled diesel engines. As mentioned above, the literature indicates that past development activities have included the design, construction, and testing of laboratory and full-scale engines to operate on a variety of coal fuels (Soehngen, 1976; Caton and Rosegay, 1984). Although not conclusive, this literature was encouraging. GE-TS then conducted their own experiments both in test rigs and in single-cylinder test engines.

The major technical issues were recognized to be: (1) formulation of acceptable engine-grade coal fuels, (2) successful injection of a coal fuel, (3) successful ignition and combustion of the fuel, (4) minimization of engine wear, and (5) minimization of engine emissions. As described below, the major accomplishments of these early technical feasibility studies were the development of initial fuel injection equipment for coal fuels, quantification of the ignition and combustion processes of the coal fuels for engine conditions, and successful operation of a single-cylinder test engine using a coal-water slurry. Although engine wear was not addressed at this time, some innovative solutions were being considered. At the end of these early studies, Hapeman and Savkar (1986) and Savkar (1987) concluded that a coal-fueled, medium-speed diesel engine would be feasible. They recognized the higher initial capital costs, higher maintenance costs, and impacts on the railraod industry. These costs and impacts were considered in the economic studies described next.

Further economic assessment included the impact of coal-fueled locomotives on six aspects of the railroad industry: (1) railroad infrastructure, (2) maintenance costs, (3) environmental considerations, (4) capital costs, (5) training and crew costs, and (6) coal fuel costs (Flynn et al., 1989a, b). A concept locomotive was selected for purposes of the economic assessment. Figure 1 is a schematic of this concept locomotive. As shown, the primary modifications to a conventional six-axle locomotive were the engine, fuel tank, and emissions control system. Additional equipment was specified to store, pump, and inject the coal–water slurry, was needed to resist wear, and was required to control emissions. They estimated that this equipment would cost an additional $280,000 (1989 dollars) relative to a similar oil-fueled engine (Flynn et al., 1990a, b).

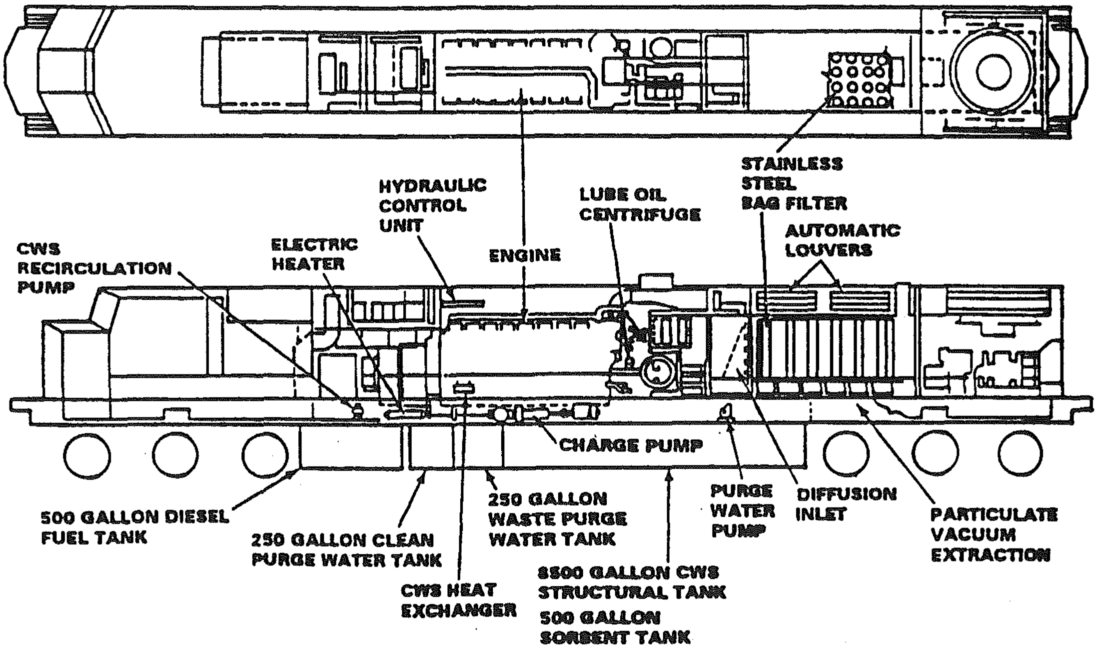

Fig. 1 Schematic of the concept coal-fueled diesel engine locomotive

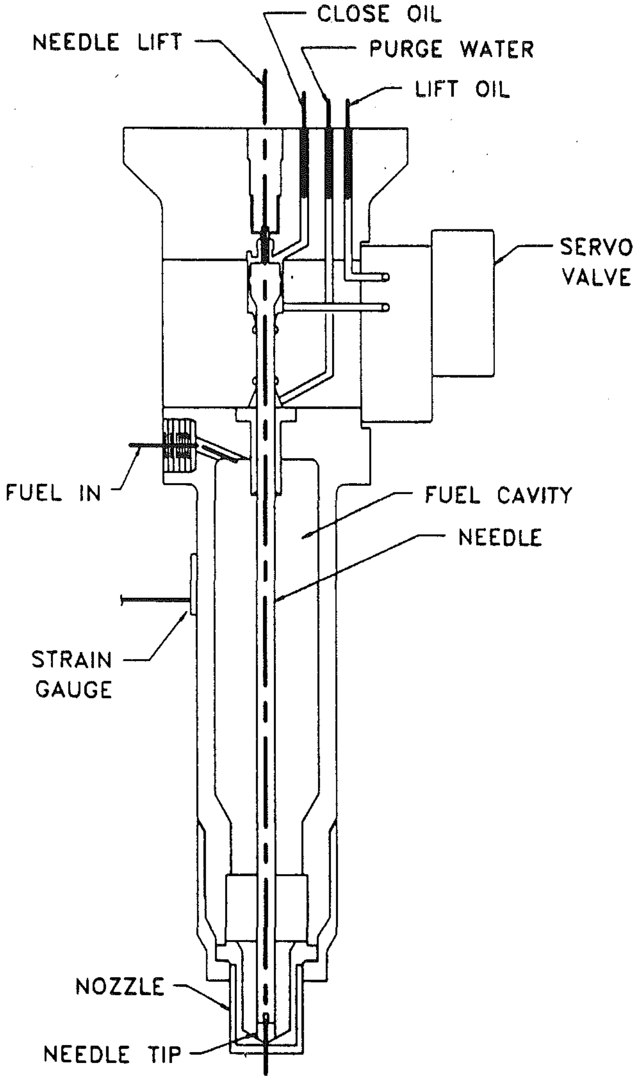

Fig. 2 A schematic of the accumulator injector

Since no commercial, engine-grade coal fuel was available, this study considered that the railroads would build, own, and operate the fuel plants. They estimated that the coal-water slurry would be about half the cost of diesel fuel on an energy basis. They estimated the additional maintenance costs to be about $22,000 (1989 dollars) per engine. Including the costs of capital for new locomotive fleets and coal fuel plants, the economic analysis indicated a simple payback of about 10 years. In addition, the study described the railroad industry and engine manufacturer's expectations with respect to risk and financial reward (Hapeman and Savkar, 1987). In summary, the results of the economic assessments indicated the merits for the development of a coal-fueled diesel engine for locomotive applications.

Single-Cylinder Engine and Laboratory Research: 1985–1988

In 1985, General Electric was awarded an initial contract from the U.S. Department of Energy, Office of Fossil Energy, Morgantown Energy Technology Center, to pursue the development of a coal-fueled diesel engine for a locomotive application (Savkar, 1985, 1986). Initial research for this program was conducted at General Electric's Corporate Research and Development Center. This work included the development of fuel injection equipment, studies of the ignition and combustion of coal-water slurries for engine conditions, and investigations of wear. Leonard and Fiske (1986) reported on the combustion characteristics of coal-water slurries using a modified, conventional jerk-pump, positive displacement fuel injection system. For this and subsequent tests, the coal-water slurry was typically about 48 percent coal by mass, 2 percent additives, and balance water. The average coal particle diameter was about 3 μm, and the coal was cleaned to less than 1.0 percent ash. They injected the coal-water slurry into a closed vessel, which utilized a preburn of hydrogen to provide the temperatures and pressures representative of a medium-speed diesel engine at the time of fuel injection. For the engine described above, the full-load conditions result in a gas temperature of about 900 K and a gas density of 25 kg/m^3 at the time of injection.

Leonard and Fiske (1986) found that the coal-water slurry ignited and burned for conditions simulating full-load engine operation, but did not auto-ignite as consistently for conditions simulating part-load conditions. They attributed the reduced performance to poorer atomization due to the reduced gas density at part-load conditions. At full-load conditions, the ignition delay was about five times longer than for diesel fuel. Although the coal-water slurry fuel would auto-ignite for appropriate conditions, the authors recommended a small amount of diesel fuel be used as a pilot to insure consistent ignition and to shorten the ignition delay.

Leonard and Fiske (1987) continued their investigation on the combustion characteristics of coal-water slurries. In this work, they compared a new, electronically controlled accumulator fuel injection system with the original, positive-displacement injection system. Figure 2 is a schematic of the accumulator fuel injector. The higher initial injection pressures (up to 80 MPa) obtainable with the accumulator injector led to a significant improvement in the coal-water slurry ignition process (Leonard, 1987). The accumulator injector was also capable of delivering fuel to the diesel engine over a wide range of engine operating conditions. The authors stated that these features should help to improve the part-load engine operation when using coal fuels.

Hsu (1987, 1988a, b) reported on the first successful GE-TS engine tests using a coal-water slurry fuel similar to the above studies. For these studies, a two-cylinder version of the GE locomotive engine was used with one cylinder firing diesel fuel and the other cylinder firing the coal-water slurry. In the first study (Hsu, 1987, 1988a), three ignition methods were investigated: (1) compression ignition, (2) separate pilot of diesel fuel, and (3) diesel pilot through main injector. Only about one-third of the full fuel energy was supplied due to fuel injection limitations. Ignition was achieved with all three types of ignition techniques. In all successful tests, the average cylinder gas temperature needed to be above 890 K (Hsu and Flynn, 1989).

In the second study (Hsu, 1988b), full-load operation (186 kW/cylinder) was achieved using coal-water slurry. For the standard inlet temperature (358 K), 3-5 percent pilot diesel fuel was needed to insure consistent ignition and combustion. For the conditions examined, the maximum heat release for the coal-water slurry was higher than for diesel fuel. The coal burn-out was estimated at about 95 percent. The nitric oxide and carbon monoxide emissions were about one-half of the levels obtained with diesel fuel. The combustion characteristics were examined as a function of inlet air temperature and pressure, amount of pilot fuel, and injection pressure.

Flynn and Hsu (1988) summarized the program's past accomplishments, as well as presenting new results on the issue of wear. Wear in a coal-fueled diesel engine is a result of the initial coal particles and the ash (mineral) content in the final combustion products. The coal particles are less important with respect to wear as the coal burn-out approaches 100 percent. The remaining ash particles are known to fuse into spheres

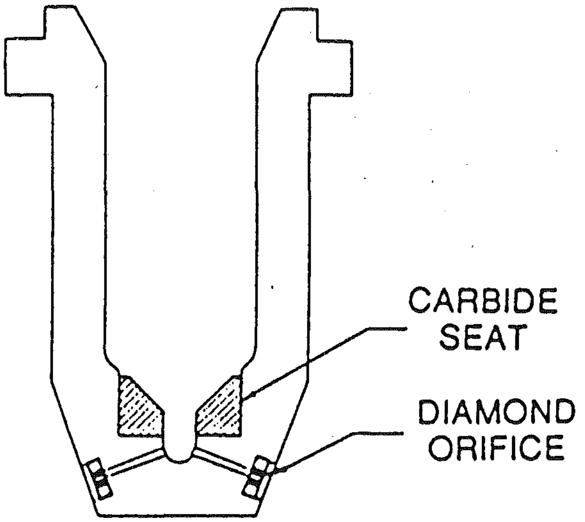

Fig. 3 A schematic of the prototype fuel injection nozzle with a carbide seat and diamond inserts

due to the high combustion temperatures with about the same size distribution as the original coal fuel. Most of the ash spheres are swept out with the exhaust gases, but some are trapped in the lubricating oil. This latter ash acts as an abrasive material and causes additional wear between the piston rings and cylinder liner. Original estimates of the wear rates for the cylinder liner were about six times higher for operation on coal-water slurry fuel as compared to diesel fuel. For standard materials, the ring wear rate as determined by measuring the end gap were between two and twenty times (depending on the ring location). Solutions proposed for these wear problems included the use of hardened materials and special coatings. For example, the authors suggested exploring the use of high-density, low metal content, tungsten carbide, plasma coatings for the cylinder liner. Chrome carbide coated piston rings also were proposed. Other new developments included the description of a proposed injector nozzle tip with compact sintered diamond orifice inserts. Figure 3 is a schematic of the proposed nozzle tip design to accommodate the diamond orifice inserts (Flynn and Hsu, 1988; Hsu and Flynn, 1989).

The most significant concern with respect to wear was the nozzle tip orifices. The high-velocity slurry through the small orifices caused erosion. With standard materials, original nozzles only had a useful life of about five hours. The use of superhard materials for the nozzle orifices also meant a need for a new design of the nozzle tips that could accommodate these materials. A prototype nozzle, designed to contain a tungsten carbide insert in a metal housing was proposed for future testing (Flynn and Hsu, 1988).

Hsu et al. (1989) reported on the continued testing of the single-cylinder locomotive engine using coal-water slurry fuel. In this phase of the experiments, the accumulator injector (originally described by Leonard and Fiske, 1987) was used. They reported improved engine performance and higher coal burn-out levels especially at part load. These improvements were attributed to the higher initial fuel injection pressures possible with the accumulator injector relative to the more conventional positive displacement injector. In addition, they examined the effects of injector flow area, hole shape, hole length-to-diameter ratio, and engine operating conditions on engine performance and coal burn-out (Leonard and Hsu, 1988).

Flynn et al. (1989a) discussed the progress obtained in the durability development of the coal-fueled engine. The major components of concern were the cylinder liner, piston rings, and nozzle tip. Other concerns such as ash deposition and erosion in the combustion chamber, bearing wear, and valve seat and stem wear were monitored, but no significant problems were noted. Candidate wear-resistant materials for the cylinder liner, piston rings and nozzle tip were sorted by bench-scale tests. The best material combinations then were tested on a small-scale engine using contaminated diesel fuel to simulate operation on coal fuels. Final material combinations were tested on the full-scale locomotive engine. Results at this stage of the program indicated practical solutions for the wear problems and positive initial progress in establishing the material requirements for a coal-fueled engine.

Flynn (1989) and Hapeman (1990) summarized the status of the General Electric coal-fueled diesel engine program at the end of the 1980s. These reports discussed the various issues and the progress obtained with respect to fuels, emissions, combustion, durability, and economics. The plans for continued development of the coal-fueled diesel engine, discussed in the following section, were described.

Multiple-Cylinder Engine Research: 1988–1993

In 1988, General Electric was awarded a five-year "proof-of-concept" contract to develop a full-sized, multiple-cylinder coal-fueled diesel engine. This program included the use of an eight-cylinder engine for durability testing and the development of a twelve-cylinder engine for a locomotive track test. Results and the corresponding publications resulting from this contract began to appear in about 1990. Although single-cylinder engine and other research was reported in this period, this section is titled "multiple-cylinder engine research," to reflect the increased emphasis during this time period on full-scale engine developments.

Flynn et al. (1988) outlined the GE-TS coal-fueled engine development plan. They reviewed past accomplishments of the original DOE contract (from 1985) and described the goals and objectives of the new DOE contract (1988). The program objective of this new contract was to develop the technology necessary for the future commercialization of a coal-fueled diesel locomotive. Specific objectives included defining the fuel specifications, developing emissions technology, demonstrating the operation of a full-size engine, demonstrating component life of more than 1000 hours, and demonstrating a coal-fueled locomotive in freight hauling service.

Flynn et al. (1989b) described the program's status as of this date. This paper included a design of the overall prototype coal-fueled test locomotive, a detail design of the production version of the accumulator fuel injection system, and a preliminary design for the emission control systems. Hsu (1989) continued the detail discussion of the program's status by describing the progress in the design of the fuel injection system and overall engine performance with particular emphasis on the part-load operation. Mehan et al. (1989) discussed the status of the durability portion of the program. Details of the problems, solutions and test results were provided (Rairden et al., 1990; Mehan et al., 1991). For example, the injector nozzle tip with compact sintered diamond orifice inserts were evaluated. The compact diamond inserts had 0.4 mm (0.016 in.) diameter orifices. Ten holes were staggered around the nozzle tip end to increase the amount of metal between each insert. After about forty hours of engine operation no measurable wear was noted (Mehan et al., 1989).

Flynn et al. (1990a, b) summarized the overall progress of the program and provided a project description. This discussion included comments on the various technical areas of the project including combustion, fuel injection, durability, and emissions. They stated that good progress was obtained in all areas, promising solutions were available for the wear and emissions problems, and the economics still looked favorable. The biggest challenge to the development of a coal-fueled diesel engine that they anticipated was the integration of all the systems into a commercial product. They outlined plans for the construction of a twelve-cylinder coal-fueled diesel engine. The first phase of this development will be based on the positive-displacement fuel injection system. Later phases were to incorporate the accumulator fuel injection system technology (McDowell et al., 1990). Figure 4 is a schematic cross section of one of the cylinders of the twelve-cylinder engine equipped with the mechanical, positive-displacement fuel injection systems. Two cylinders of an eight-cylinder engine were converted to coal-water slurry to provide a test bed for durability tests. This engine was to be operated for 1000 hours to obtain long-term component wear data (Mehan et al., 1990).

The experimental program aimed at reducing the emissions of the coal-fueled locomotive engine was described (Slaughter et al., 1990; Gal et al., 1990). A number of options for reducing sulfur oxides and particulates from a coal-fueled diesel engine were examined. Calcium and copper oxide sorbents were tested for the reduction of sulfur dioxide, and cyclones, metal fabric filters, and granular beds were tested for particulate removal. Forty percent of the sulfur dioxide was removed by injecting calcium sorbent (either wet or dry) into the exhaust manifold, while the use of copper oxide resulted in up to 80 percent removal of the sulfur dioxide. The cyclone was effective in removing particulates larger than abut 5 μm. The authors suggested that a granular bed of copper oxide followed by a high-efficiency cyclone would be a viable system.

Hsu and Confer (1990, 1991), using one cylinder of the two-cylinder test engine, evaluated the effects of nine different coal-water slurry fuels on the combustion and overall engine performance. The nine fuels possessed different mean particle sizes, additive packages, coal sources, and coal cleaning processes. Even without engine optimization for the various fuels, almost in all cases close to 99 percent coal burn-out was achieved. The authors concluded that the coal-fueled engine was tolerant to fuel properties; however, for optimum performance the engine design parameters should be adjusted for the individual fuels.

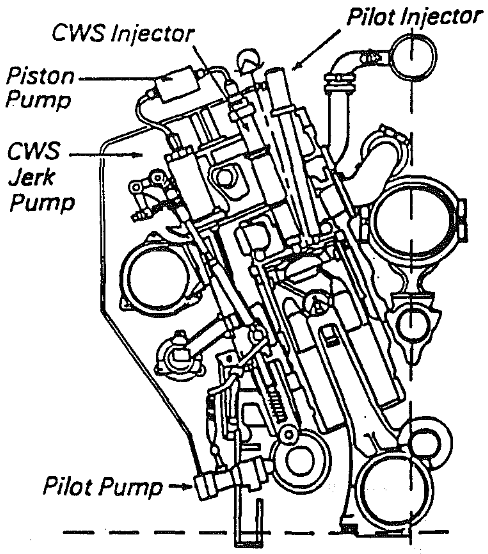

Fig. 4 A schematic of the coal-fueled engine with the mechanical fuel injection system

Hsu et al. (1991) provided an overview of the status of the GE-TS coal-fueled diesel engine powered locomotive program. An electronic start/pilot injector was developed for the single-cylinder test engine. This system was to be used for 12-cylinder engine. A cycle simulation of the coal-water fueled diesel engine was developed, validated, and used in the combustion optimization process (Wahiduzzaman et al., 1990, 1991). Eight different compact diamond injector nozzle tip designs were tested on the single-cylinder engine. The proof-of-concept, 12-cylinder coal-fueled engine was equipped with dual positive-displacement fuel injection systems (McDowell et al., 1991, 1992a). One is the main system for the coal-water slurry and the other is for the pilot diesel fuel. Controls were designed and installed to provide for the regulation of the two fuels as a function of notch settings and operation requirements during start-up and shut-down. Although full power operation of all cylinders was not possible, the engine completed over ten hours of operation at up to 1860 kW. The emissions control technology development was discussed by Gal et al. (1991). They reported that a total emission control system for sulfur dioxide, particulates, and nitric oxide to fit on board a modified GE locomotive was designed. Bench scale and single cylinder tests verified much of the design.

Hapeman (1992) reviewed the development activities of the coal-fueled locomotive. This paper stated that the coal-fired diesel engine concept was finally a reality. The fact that a 12-cylinder, medium-speed locomotive size engine was operated at power levels comparable to an oil-fueled engine was noted. The paper concluded by stating that at some point in the future when either price or availability of petroleum products again becomes an issue, the coal-fueled diesel will become a commercial product.

Hsu (1992) provided an update on the coal-fueled diesel engine development program at GE-TS. He described the successful testing of a complete coal-fueled diesel engine powered locomotive system on a test track for about ten hours in November and December 1991. This engine used the earlier modified positive displacement fuel injection system. The twelve-cylinder engine developed 1864 kW (2500 hp) in the engine laboratory. Figure 5 is a schematic of this test locomotive and shows the separate fuel tender car coupled to the locomotive, which facilitated this initial test. In addition, highlights of the component development announced in this report included the successful testing of over ten diamond insert injector nozzles. Over 500 hours of engine equivalent testing was completed using laboratory equipment with no significant wear. The eco-

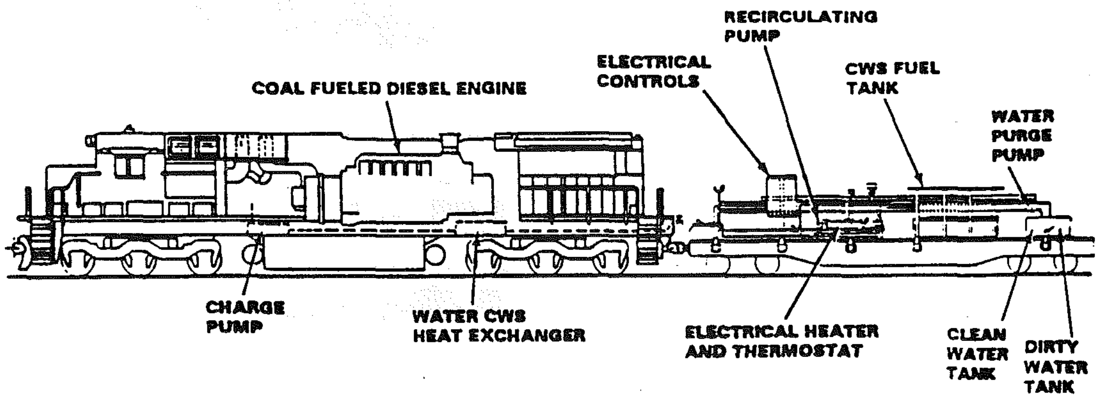

Fig. 5 Schematic of the stage I coal-fueled diesel engine locomotive test configuration

nomic analysis was updated to include the current concept design of a coal-fueled diesel engine powered locomotive.

Hsu et al. (1992a, b) completed a detailed investigation on the combustion characteristics for the single-cylinder engine equipped with electronically controlled accumulator fuel injection systems for both the coal-water slurry and the diesel pilot fuel. Peak firing pressure, combustion efficiency (coal burn-out), and specific fuel consumption were evaluated as a function of slurry and pilot injection timings, nozzle tip orifice size, shape and number, spray angle, and injection pressures. Heat release rates and gaseous and particulate exhaust concentrations were obtained and analyzed for each case.

They (Hsu et al., 1992a, b) found that utilizing the maximum amount of residence time for the slurry to allow water vaporization followed by later pilot injection resulted in the best results. Since the residence time of the slurry was long and the slurry spray traveled fast, impingement of the slurry on the piston crown seemed to be unavoidable. For high piston crown temperatures, such as at full load, this impingement appeared to be favorable or, at least, not unfavorable. Under low-load conditions, the temperatures were too low for sufficient water vaporization without early pilot fuel combustion. This resulted in retarded slurry timing relative to the full load conditions.

In addition, Hsu et al. (1992a, b) stated that the effect of injector hole number or shape had little effect on the combustion characteristics for the conditions examined. They speculated that this may be a result of the dependence on secondary atomization due to the impingement. They also found that higher injection pressures (up to the maximum tested of 85 MPa) resulted in better engine combustion results. Finally, they reported that for the best set of parameters for the full-load case the combustion efficiency was 99.5 percent and the engine cycle efficiency was comparable to operation with diesel fuel.

Seshadri et al. (1992) reported on coal-water slurry spray characteristics for intermittent diesel engine injections using a modified, positive-displacement fuel injection system consisting of General Electric fuel injection system components. Since the combustion process is a strong function of the fuel spray, full characterization of the spray is a necessity for successful engine design and for modeling the combustion processes. A constant volume vessel equipped with optical-quality windows was used to provide the same gas density as in the engine at the time of injection (Caton et al., 1991, 1992; Caton and Kihm, 1991).

This investigation included high-speed movies and direct photography of the coal-water slurry sprays. Spray growth, tip penetration, and cone angles were obtained as a function of operating conditions and nozzle design. Instrumentation included instantaneous fuel pressure and needle lift. For the conditions studied, the spray tip penetration was similar for coal-water slurry, diesel fuel, and water. The time-averaged cone angles for the coal-water slurry were between 11 and 16 deg and for the diesel fuel was 16.3 deg.

McDowell et al. (1992b) described the GE-TS coal-fueled 12-cylinder diesel engine test results from early 1991. They reported that the engine developed up to 1860 kW at 1050 rpm in the laboratory. This engine was subsequently installed onto a locomotive for track testing. McDowell et al. (1992a) later reviewed the successes of the first-stage locomotive including the stationary locomotive testing in July 1991 and the test track testing in November 1991. They stated that the biggest challenges to the development of a commercially acceptable coal-fueled diesel-electric locomotive are integrating all systems into a working unit that can be operated in railroad service. In addition to the engine, major system development was reported for the locomotive, the engine controls, and the fuel supply systems.

Future work that eventually would be needed for commercialization of the coal-fueled diesel engine was also described. This future work included the development of a second, more advanced engine and locomotive. This engine would have dual electronic accumulator fuel injection systems. This future work was originally part of the overall contract, but due to reductions in government funding and the predictions for continued low petroleum prices, this aspect of the program was eliminated.

Gal et al. (1992) and Cook et al. (1993) described the final selection of the emissions control technology for the coal-fueled engine. A system composed of a barrier filter with sorbent and ammonia injection upstream was selected for controlling particulates, sulfur dioxide, and nitric oxide emissions. Removal efficiencies greater than 90 percent for sulfur dioxide and 85 percent for nitric oxide were achieved during bench scale and slip-stream experiments. Particulate emissions were maintained below the new source performance standards (NSPS) limits. A full-scale system to treat the total engine exhaust flow was designed for the twelve-cylinder engine.

Hsu and Branyon (1993) reported on detailed in-cylinder photography results for coal-water slurry engine operation. Instantaneous cylinder pressures were obtained simultaneously. Distinct flames of the coal and the diesel pilot were noted. The coal appeared to burn after impingement and secondary atomization on the piston crown. Agglomerated coal particles were noted when the combustion process was non-optimal. These findings confirmed earlier speculations on the ignition and combustion processes of coal-water slurry fuels.

Caton et al. (1993a) described the second part of the spray atomization study reported above by Seshadri et al. (1992). In this part of the study, the coal-water slurry spray characteristics were determined for the accumulator fuel injection system. The other experimental facilities were identical to those reported by Seshadri et al. (1992). In addition to high-speed movies and direct photography, this investigation included detailed determinations of the droplet sizes using a laser diffraction particle analyzing instrument and employing a unique synchronization technique (Kihm and Caton, 1992).

Spray growth, tip penetration, mean droplet sizes, and cone angles were obtained as a function of operating conditions and nozzle design. Figure 6 shows eight frames from a high-speed movie of one injection of coal-water slurry at 70 MPa. Based on movies such as these, correlations were developed for spray tip penetration and spray tip droplet sizes as a function of operating and design parameters. For the conditions of these studies, the initial jet velocity was 15 percent greater for the coal-water slurry than for diesel fuel (Caton et al., 1993b). In addition, a major conclusion of these studies was that the

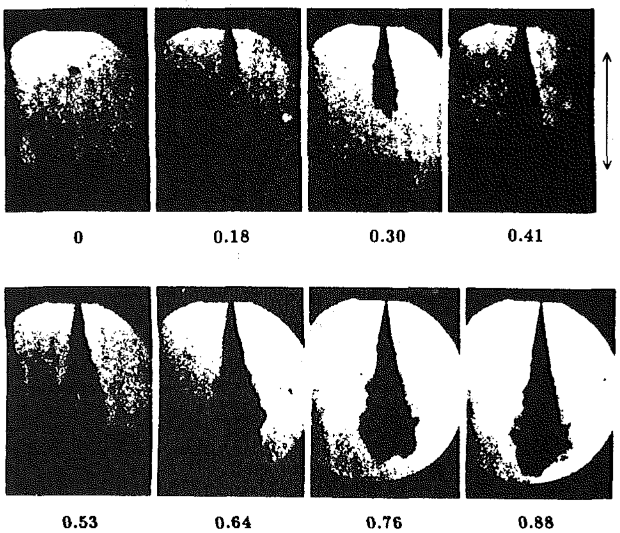

Fig. 6 Eight sequential frames (0.116 ms apart) from a movie of one injection of coal-water slurry at 70 MPa (10,200 psi). The numbers below the frames denote the time in milliseconds from the start of injection.

ability to generate well-atomized sprays was a strong function of the coal-water formulation. Of two nearly identical coal-water slurries, only one was injected consistently while the other was never injected successfully. Kihm et al. (1993a, b) reported the detail results of the droplet sizing experiments. Depending on the operating conditions, the Sauter mean diameter of droplets in the coal-water slurry spray tip ranged between 18 and 92 μm. To a limited degree, these spray atomization results were modeled (Prithiviraj and Andrews, 1993).

Hsu et al. (1993) provided an update and summary of the overall program as the program entered the last months of its duration. They summarized past accomplishments of the program in the four major activities: (1) conceptual locomotive design and economic analysis, (2) technology research and development, (3) engine component development, and (4) locomotive system test. The development of a concept locomotive design and the associated economics was the initial work. The technology research and development activities included completing bench scale and single cylinder engine tests to develop fuel injection equipment, to understand the ignition and combustion processes, to define the fuels, to develop durable components, and to develop successful emission control technology.

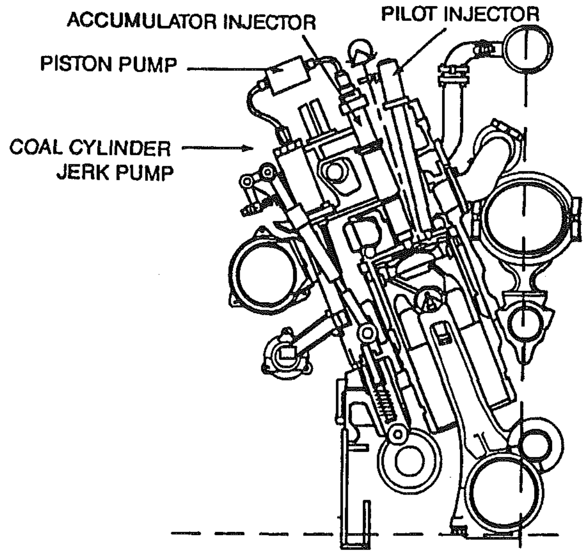

Fig. 7 A schematic of the coal-fueled engine with the electronic fuel injection system

The engine component development activities focused on the design, construction and operation of two twelve-cylinder engines to confirm the component designs in an integrated test. This group of activities also included the development and use of an eight-cylinder engine of which two cylinders were used to conduct long-term durability tests (McDowell et al., 1994). The final group of activities was the locomotive system tests. As mentioned above, the purposes of the locomotive tests were to verify that the various engine support and control systems functioned as required, to gain operational experience, and to identify problems. A 12-cylinder engine was equipped with diamond insert injector nozzles, tungsten carbide coated piston rings and liners, and electronically controlled fuel injection systems. Figure 7 is a schematic cross section of one of the cylinders of the 12-cylinder engine equipped with the electronically controlled fuel injection systems. Figure 8 is a schematic of the complete emissions clean-up system designed and constructed for installation on board a locomotive. Performance tests indicated that the system could remove over 90 percent of the sulfur dioxide and 99 percent of the particulates Hsu et al. (1994).

Summary and Conclusions

Due to the availability and low cost of coal, General Electric Transportation Systems (GE-TS) announced plans to develop a coal-fueled locomotive in the early 1980s. With co-support from the Department of Energy, the Energy Development Authorities of the States of New York and Pennsylvania, and the railroad industry (BNR and NSR), GE-TS embarked on an ambitious program to develop and commercialize a coal-fueled diesel engine. Among the major accomplishments of this pro-

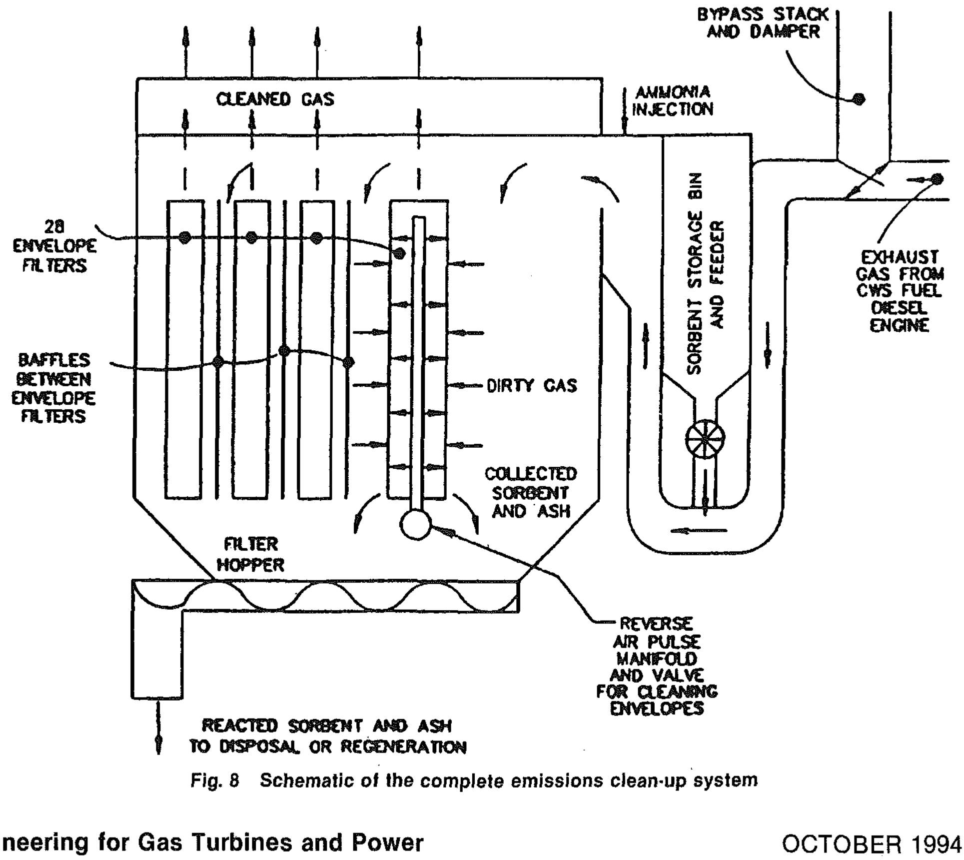

Fig. 8 Schematic of the complete emissions clean-up system

Table 1 Highlights of the GE-TS coal-fueled diesel engine program

EVENT	FIRST COMPLETED	FIRST REPORTED
Successful Coal-Water Slurry Injection	1985	1985
Successful Coal-Water Slurry Autoignition	1985	1985
Accumulator Fuel Injection System	1986	1987
Diamond Compact Nozzle Tip Inserts	1987	1988
Electronic Engine Control System	1988	1989
Tungsten Carbide Coated Rings and Liners	1989	1989
Comprehensive Cycle Simulation	1989	1990
Importance of Coal Fuels Formulations	1990	1990
First Twelve-Cylinder Engine Operation	1990	1991
Engine Combustion Optimization	1991	1991
Detailed Atomization Results	1991	1992
First Coal-Fueled Diesel Locomotive Test	1991	1992
Complete Emission Clean-Up System	1992	1992

gram were the development of specialized fuel injection equipment for coal-water slurries, diamond compact inserts for the nozzle tips, and an integrated emissions control system. Over 500 hours of engine operation was accumulated using coal fuel during the duration of this program. A major milestone was attained when, during November and December 1991, a coal-fueled diesel engine powered a locomotive on the General Electric test track. Table 1 is a list of the major accomplishments of the GE-TS coal-fueled diesel engine research and development program.

At the time of this writing (1993), commercial interest in coal-fueled engines is waning because of the current low oil prices. Also, in view of the federal deficit, General Electric was asked to wind down the development program in an orderly fashion. GE has developed the critical technologies in the completion of the second phase, electronically controlled fuel-injection engine with all durable parts and a complete emissions clean-up system. When the market environment again becomes favorable in the future, the technologies can be further improved and packaged into a commercial system very quickly.

Acknowledgments

This work was supported by a contract with the U.S. Department of Energy, Morgantown Energy Technology Center for BDH and by a sub-contract from General Electric—Transportation Systems as part of the contract with the U.S. Department of Energy, Morgantown Energy Technology Center for JAC. The contents of this paper, however, do not necessarily reflect the views of General Electric or the Department of Energy.

References

Carpenter, L. K., and Crouse, F. W., Jr., 1985, "Coal-Fueled Diesels Fossil Energy Activities," ASME Paper No. 85-DGP-18.

Carpenter, L. K., and Crouse, F. W., Jr., 1986, "Coal-Fueled Diesels: Progress and Challenges," ASME Paper No. 86-ICE-6.

Caton, J. A., and Rosegay, K. H., 1984, "A Review and Comparison of Reciprocating Engine Operation Using Solid Fuels," *Transactions of the Society of Automotive Engineers*, Paper No. 831362, Vol. 92, pp. 1108–1124.

Caton, J. A., Kihm, K. D., Seshadri, A. K., and Zicterman, G., 1991, "Micronized-Coal-Water Slurry Sprays From a Diesel Engine Positive Displacement Fuel Injection System," *Proceedings of the Central States Section/Combustion Institute Spring Technical Meeting*, Apr., Paper No. 58, pp. 361-366.

Caton, J. A., and Kihm, K. D., 1991, "Coal-Water Slurry Atomization Characteristics," *Proceedings of the Eighth Annual Coal-Fueled Heat Engines and Gas Stream Cleanup Systems Contractors Review Meeting*, H. A. Webb, R. C. Bedick, D. W. Geiling, and D. C. Cicero, eds., U.S. Department of Energy, Morgantown Energy Technology Center, Report No. DOE-METC-91-6122, pp. 273-282.

Caton, J. A., Seshadri, A. K., and Kihm, K. D., 1992, "Spray Tip Penetration and Cone Angles for Coal-Water Slurry Using a Modified Medium-Speed Diesel Engine Injection System," *Proceedings of the Central States Section/Combustion Institute Spring Technical Meeting*, Apr., pp. 234-239.

Caton, J. A., Payne, S. E., Terracina, D. P., and Kihm, K. D., 1993a, "Coal-Water Slurry Spray Characteristics of an Electronically-Controlled Accumulator Fuel Injection System," *Coal-Fueled Diesel Engines 1993*, J. A. Caton and H. A. Webb, eds., ASME ICE-Vol. 19, pp. 25-32.

Caton, J. A., Payne, S. E., Terracina, D. P., and Kihm, K. D., 1993b, "Coal-Water Slurry Sprays From an Electronically Controlled Accumulator Fuel Injection System: Break-up Distances and Times," *Proceedings of the 1993 Joint Central and Eastern States Section/Combustion Institute Spring Technical Meeting*, Mar., Paper No. 76, pp. 405-409.

Cook, C., Gal, E., Mengel, M., and Van Kleunen, W., 1993, "Coal-Fueled Diesel Emissions Control Technology Development," *Coal-Fueled Diesel Engines 1993*, J. A. Caton; ed., ASME ICE-Vol. 19, pp. 9-14.

Crouse, F. W., Jr., Halow, J. S., and Wilson, J. S., 1984, "Coal-Fueled Gas Turbine Program," ASME Paper No. 84-GT-296.

Dunlay, J. B., Davis, J. P., Steiger, H. A., and Eberle, M. K., 1980, "Performance Tests of a Slow Speed Two-Stroke Diesel Engine Using Coal Based Fuels," Thermo Electron Corporation, Report No. TE 7905-267-80.

Flynn, P. L., and Hsu, B. D., 1988, "Coal Fueled Diesel Developments," SAE Paper No. 881159.

Flynn, P. L., Hsu, B. D., Leonard, G. L., and Cook, C. S., 1988, "Coal-Fueled Diesel Technology Development," *Proceedings of the Annual Coal-Fueled Heat Engines and Gas Stream Cleanup Systems Contractors Review Meeting*, R. J. Dellefield and H. A. Webb, eds., U. S. Department of Energy, Morgantown Energy Technology Center, Report No. DOE-METC-88-6094, pp. 11-19.

Flynn, P. L., 1989, "Coal Fueled Locomotives: Energy Independence and Economic Sense," Landmarc, National Coal Association Publication.

Flynn, P. L., Leonard, G. L., and Mehan, R. L., 1989a, "Component Wear in Coal Fueled Diesel Engines," ASME Paper No. 89-ICE-15.

Flynn, P. L., Hsu, B. D., Leonard, G. L., and Cook, C. S., 1989b, "Coal-Fueled Diesel Technology Development," *Proceedings of the Sixth Annual Coal-Fueled Heat Engines and Gas Stream Cleanup Systems Contractors Review Meeting*, R. C. Bedick, T. P. Dorchak, N. F. Rekos, and H. A. Webb, eds., U. S. Department of Energy, Morgantown Energy Technology Center, Report No. DOE-METC-89-6101, pp. 79-90.

Flynn, P. L., Hsu, B. D., and Leonard, G. L., 1990a, "Coal Fueled Diesel Engine Progress at GE Transportation Systems," in: *Coal-Fueled Diesel Engines 1990*, J. A. Caton, ed., ASME ICE-Vol. 12, pp. 1-9; also ASME JOURNAL OF ENGINEERING FOR GAS TURBINES AND POWER, Vol. 112, pp. 384-390.

Flynn, P. L., Hsu, B. D., Leonard, G. L., and Cook, C. S., 1990b, "Coal-Fueled Diesel Locomotives Overview," *Proceedings of the Seventh Annual Coal-Fueled Heat Engines and Gas Stream Cleanup Systems Contractors Review Meeting*, H. A. Webb, N. F. Rekos, V. P. Kothari, and R. C. Bedick, eds., U.S. Department of Energy, Morgantown Energy Technology Center, Report No. DOE-METC-90-6110, pp. 11-22.

Gal, E., Samuel, E. A., and Cohen, M., 1990, "Coal-Fueled Diesel Technology Development Emissions: A Status Report," *Proceedings of the Seventh Annual Coal-Fueled Heat Engines and Gas Stream Cleanup Systems Contractors Review Meeting*, H. A. Webb, N. F. Rekos, V. P. Kothari, and R. C. Bedick, eds., U.S. Department of Energy, Morgantown Energy Technology Center, Report No. DOE-METC-90-6110, pp. 206-215.

Gal, E., Van Keunen, W., Hamilton, R. W., and Cohen, M., 1991, "Coal-Fueled Diesel Emissions Control Technology Development: A Status Report," *Proceedings of the Eighth Annual Coal-Fueled Heat Engines and Gas Stream Cleanup Systems Contractors Review Meeting*, H. A. Webb, R. C. Bedick, D. W. Gelling, and D. C. Cicero, eds., U.S. Department of Energy, Morgantown Energy Technology Center, Report No. DOE-METC-91-6122, pp. 459-466.

Gal, E., Mengel, M., and Van Kleunen, W., 1992, "Coal-Fueled Diesel Emissions Control Technology Development: A Status Report," *Proceedings of the Ninth Annual Coal-Fueled Heat Engines and Gas Stream Cleanup Systems Contractors Review Meeting*, D. W. Geiling, ed., U.S. Department of Energy, Morgantown Energy Technology Center, Report No. DOE-METC-93-6129, pp. 190-197.

Hapeman, M. J., and Savkar, S. D., 1986, "Economic Assessment of Coal-Burning Diesel Locomotives," ASME Paper No. 86-ICE-14.

Hapeman, M. J., and Savkar, S. D., 1987, "Economic Assessment of Coal-Burning Locomotives," presented at ASME/IEEE Joint Railroad Conference, Toronto, Canada, Apr. 22-23.

Hapeman, M. J., 1990, "Review and Update of the Coal Fired Diesel Engine," *Proceedings of Opportunities in the Synfuels Industry*, University of North Dakota Energy and Environmental Research Center, Aug.

Hapeman, M. J., 1992, "The Coal Fired Locomotive Development," *Proceedings of the Fifteenth Annual Seminar on Transportation Policies and Coal Distribution*, Jan. 29-31.

Hsu, B. D., 1987, "Ignition Study of Coal Water Slurry Fuel in GE-7FDL Engine," *Proceedings of the Annual Heat Engines and Gas Stream Cleanup Systems Contractors Review Meeting*, J. W. Byam, Jr., and K. E. Markel, Jr., eds., U.S. Department of Energy, Morgantown Energy Technology Center, Report No. DOE-METC-87-6077, pp. 450-464.

Hsu, B. D., 1988a, "Progress on the Investigation of Coal-Water Slurry Fuel Combustion in a Medium Speed Diesel Engine: Part 1. Ignition Studies," ASME Paper No. 88-ICE-4; also ASME JOURNAL OF ENGINEERING FOR GAS TURBINES AND POWER, Vol. 110, pp. 415-422.

Hsu, B. D., 1988b, "Progress on the Investigation of Coal-Water Slurry Fuel Combustion in a Medium-Speed Diesel Engine: Part 2. Preliminary Full Load Test," ASME Paper No. 88-ICE-5; also, ASME JOURNAL OF ENGINEERING FOR GAS TURBINES AND POWER, Vol. 110, pp. 423-430.

Hsu, B. D., Leonard, G. L., and Johnson, R. N., 1989, "Progress on the Investigation of Coal-Water-Slurry Fuel Combustion in a Diesel Engine: Part 3, Accumulator," in: *Coal-Fueled Diesel Engines*, M. H. McMillian and H. A. Webb, eds., Vol. 7, pp. 19-25.

Hsu, B. D., 1989, "Coal-Fueled Diesel Technology Development GE Single Cylinder Diesel Engine Results," *Proceedings of the Sixth Annual Coal-Fueled Heat Engines and Gas Stream Cleanup Systems Contractors Review Meeting*, R. C. Bedick, N. F. Dorchak, N. F. Rekos, and H. A. Webb, eds., U.S. Department of Energy, Morgantown Energy Technology Center, Report No. DOE-METC-89-6101, pp. 169-175.

Hsu, B. D., and Flynn, P. L., 1989, "Preliminary Study of Using Coal-Water Slurry Fuel in GE-7FDL Medium Speed Diesel Engine," *Proceedings, 18th International Congress on Combustion Engines*, Tianjin, China, June.

Hsu, B. D., and Confer, G. L., 1990, "Coal-Fueled Diesel Engine Performance—Fuels Effect," *Proceedings of the Seventh Annual Coal-Fueled Heat Engines and Gas Stream Cleanup Systems Contractors Review Meeting*, H. A. Webb, N. F. Rekos, V. P. Kothari, and R. C. Bedick, eds., U.S. Department of Energy, Morgantown Energy Technology Center, Report No. DOE-METC-90-6110, pp. 262-271.

Hsu, B. D., and Confer, G. L., 1991, "Progress on the Investigation of Coal-Water-Slurry Fuel Combustion in a Medium Speed Diesel Engine: Part 4—Fuels Effect," in: *Coal-Fueled Diesel Engines 1991*, J. A. Caton and H. A. Webb, eds., ASME ICE-Vol. 14, pp. 1-8.

Hsu, B. D., Kalafala, A. K., and Cook, C. S., 1991a, "Coal-Fueled Diesel Locomotives Overview," *Proceedings of the Eighth Annual Coal-Fueled Heat Engines and Gas Stream Cleanup Systems Contractors Review Meeting*, H. A. Webb, R. C. Bedick, D. W. Gelling, and D. C. Cicero, eds., U.S. Department of Energy, Morgantown Energy Technology Center, Report No. DOE-METC-91-6122, pp. 72-80.

Hsu, B. D., Johnson, R. N., and Jones, A. G., 1991, "Fuel Injection Equipment for a Coal-Water Slurry Fuelled Medium Speed Diesel Engine," *Diesel Fuel Injection Systems*.

Hsu, B. D., 1992, "Coal Fueled Diesel Engine Development Update at GE Transportation Systems," in: *Coal-Fueled Diesel Engines 1992*, J. A. Caton and H. A. Webb, eds., ASME ICE-Vol. 16, pp. 1-11.

Hsu, B. D., Confer, G. L., and Shen, G. J., 1992a, "Progress on the Investigation of Coal Water Slurry Fuel Combustion in a Medium Speed Diesel Engine: Part 5—Combustion Studies," in: *Coal-Fueled Diesel Engines 1992*, J. A. Caton and H. A. Webb, eds., ASME ICE-Vol. 16, pp. 39-46.

Hsu, B. D., Shen, Z., and Caton, J. A., 1992b, "Combustion Characteristics of Coal-Water Slurry Fuel in a Medium Speed Diesel Engine," *Proceedings of the Ninth Annual International Pittsburgh Coal Conference*, "Coal—Energy and the Environment," Pittsburgh, PA, Oct. 12-16, PA, pp. 335-340.

Hsu, B. D., and Branyon, D. P., 1993, "Progress on the Investigation of Coal-Water Slurry Fuel Combustion in a Medium Speed Diesel Engine: Part 6—In-Cylinder High Speed Photography Studies," *Coal-Fueled Diesel Engines 1993*, J. A. Caton, ed., ASME ICE-Vol. 19, pp. 15-24.

Hsu, B. D., Najewicz, D. J., and Cook, C. S., 1993, "Coal-Fueled Diesel Engines for Locomotive Applications," to be published in the *Proceedings of the Joint Contractors Meeting* (FE/EE Advanced Turbine Systems Conference/FE Fuel Cells and Coal-Fired Heat Engines Conference), U.S. Department of Energy, Morgantown Energy Technology Center, Morgantown, WV, Aug. 3-5.

Hsu, B. D., Confer, G. L., McDowell, R. E., Gal, E., Van Kleunen, M., and Mengle, M., 1994, "Design and Operation of a Medium Speed 12-Cylinder Coal-Fueled Diesel Engine," presented at the ASME Energy-Sources and Technology Conference and Exhibition, New Orleans, LA, Jan. 23-27.

Kihm, K. D., and Caton, J. A., 1992, "Synchronization of a Laser Fraunhofer Diffraction Sizing Technique With Intermittent Spray Systems," *Journal of Applied Optics*, Vol. 31, No. 23, pp. 1914-1916.

Kihm, K. D., Terrracina, D. P., Payne, S. E., and Caton, J. A., 1993a, "Synchronized Droplet Size Measurements for Coal-Water Slurry (CWS) Diesel Sprays of an Electronically-Controlled Fuel Injection System," *Coal-Fueled Diesel Engines 1993*, J. A. Caton and H. A. Webb, eds., ASME ICE-Vol. 19, pp. 33-42.

Kihm, K. D., Terracina, D. P., Payne, S. E., and Caton, J. A., 1993b, "Properly Synchronized Measurements of Droplet Sizes for High-Pressure Intermittent Coal-Water Slurry Fuel Sprays," *Proceedings of the 1993 Joint Central and Eastern States Section/Combustion Institute Spring Technical Meeting*, Mar., Paper No. 50, pp. 271-275.

Leonard, G. L., and Fiske, G. H., 1986, "Combustion Characteristics of a Coal/Water Mixture in a Simulated Medium Speed Diesel Engine Environment," ASME Paper No. 86-ICE-15.

Leonard, G. L., and Fiske, G. H., 1987, "A Comparison of a Positive Displacement Fuel Injection System With an Accumulator-Based System for Coal-Fueled Diesel Engine Applications," ASME Paper No. 87-ICE-32.

Leonard, G. L., 1987, "Combustion Bomb Studies—A Comparison of an Accumulator-Based Injection System With a Positive Displacement-Based Systems for Coal-Fueled Diesel Engine Applications," *Proceedings of the Annual Heat Engines and Gas Stream Cleanup Systems Contractors Review Meeting*, J. W. Byam, Jr., and K. E. Markel, Jr., eds., U.S. Department of Energy, Morgantown Energy Technology Center, Report No. DOE-METC-87-6077, pp. 398-403.

Leonard, G. L., and Hsu, B. D., 1988, "Coal-Fuel Diesel Combustion: General Electric Test Results," *Proceedings of the Annual Coal-Fueled Heat Engines and Gas Stream Cleanup Systems Contractors Review Meeting*, R. J. Dellefield and H. A. Webb, eds., U.S. Department of Energy, Morgantown Energy Technology Center, Report No. DOE-METC-88-6094, pp. 361-370.

McDowell, R. E., Confer, G. L., and Basic, S. L., 1990, "12-Cylinder Coal-Fired Engine Design," *Proceedings of the Seventh Annual Coal-Fueled Heat Engines and Gas Stream Cleanup Systems Contractors Review Meeting*, H. A. Webb, N. F. Rekos, V. P. Kothari, and R. C. Bedick, eds., U.S. Department of Energy, Morgantown Energy Technology Center, Report No. DOE-METC-90-6110, p. 440.

McDowell, R. E., Confer, G. L., and Basic, S. L., 1991, "Design and Operation of a Coal-Fueled 12 Cylinder Medium Speed Diesel Engine," *Proceedings of the Eighth Annual Coal-Fueled Heat Engines and Gas Stream Cleanup Systems Contractors Review Meeting*, H. A. Webb, R. C. Bedick, D. W. Gelling, and D. C. Cicero, eds., U.S. Department of Energy, Morgantown Energy Technology Center, Report No. DOE-METC-91-6122, pp. 283-292.

McDowell, R. E., Confer, G. L., and Basic, S. L., 1992a, "Coal Fueled Diesel Locomotive Test," *Proceedings of the Ninth Annual Coal-Fueled Heat Engines and Gas Stream Cleanup Systems Contractors Review Meeting*, D. W. Geling, ed., U.S. Department of Energy, Morgantown Energy Technology Center, Report No. DOE-METC-93-6129, pp. 39-50.

McDowell, R. E., Basic, S. L., and Confer, G. L. 1992b, "Design and Operation of a Medium Sized 12-Cylinder Coal-Fueled Diesel Engine," in: *Coal-Fueled Diesel Engines 1992*, J. A. Caton and H. A. Webb, eds., ASME ICE-Vol. 16, pp. 33-38.

McDowell, R. E., Giammarise, A. W., and Branyon, D. P., 1994, "Durability Testing of Medium Speed Diesel Engine Components Designed for Operating on Coal-Water Slurry Fuel," presented at the ASME Energy-Sources and Technology Conference and Exhibition, New Orleans, LA, Jan. 23-27.

Mehan, R. L., Leonard, G. L., and Johnson, R. N., 1989, "Hardened Materials in Coal-Fueled Diesels," *Proceedings of the Sixth Annual Coal-Fueled Heat Engines and Gas Stream Cleanup Systems Contractors Review Meeting*, R. C. Bedick, N. F. Dorchak, N. F. Rekos, and H. A. Webb, eds., U.S. Department of Energy, Morgantown Energy Technology Center, Report No. DOE-METC-89-6101, pp. 211-225.

Mehan, R. L., Rairden, J. R., and Giammarise, A. W., 1990, "Wear Resistant Materials and Processes for the 7FDL Diesel Engine," *Proceedings of the Seventh Annual Coal-Fueled Heat Engines and Gas Stream Cleanup Systems Contractors Review Meeting*, H. A. Webb, N. F. Rekos, V. P. Kothari, and R. C. Bedick, eds., U.S. Department of Energy, Morgantown Energy Technology Center, Report No. DOE-METC-90-6110, pp. 328.

Mehan, R. L., Flynn, P. L., and Giammarise, A. W., 1991, "Evaluation of Piston Ring Materials in Oil Containing Abrasive Using a Ring-on-Block Test Machine," *Wear*, No. 147, pp. 41-57.

Prithiviraj, M., and Andrews, M. J., 1993, "Simulation of Coal-Water Slurry Sprays," *Coal-Fueled Diesel Engines 1993*, J. A. Caton, ed., ASME ICE-Vol. 19, pp. 43-52.

Rairden, J. R., Mehan, R. L., and Giammarise, A. W., 1990, "The Effects of Processing Conditions on the Wear Resistance of Plasma Sprayed WC-Co Coatings," *Proceedings of the DOE Conference on Coatings for Heat Engines*, Castine, ME, Aug.

Savkar, S. D., 1985, "Coal-Fueled Diesel Systems Research," *Proceedings of the Second Annual Coal-Fueled Heat Engines Contractors Meeting*, F. W. Crouse, ed., U.S. Department of Energy, Morgantown Energy Technology Center, Report No. DOE-METC-85-6023, pp. 292-296.

Savkar, S. D., 1986, "Coal-Fueled Diesel Systems Research," *Proceedings of the Third Annual Coal-Fueled Heat Engines Contractors Meeting*, F. W. Crouse, ed., U.S. Department of Energy, Morgantown Energy Technology Center, Report No. DOE-METC-86-6041, pp. 21-30.

Savkar, S. D., 1987, "Coal-Fueled Diesel Systems Research," *Proceedings of the Annual Heat Engines and Gas Stream Cleanup Systems Contractors Review Meeting*, J. W. Byam, Jr., and K. E. Markel, Jr., eds., U.S. Department of Energy, Morgantown Energy Technology Center, Report No. DOE-METC-87-6077, pp. 67-80.

Seshadri, A. K., Caton, J. A., and Kihm, K. D., 1992, "Coal-Water Slurry Spray Characteristics of a Positive Displacement Fuel Injection System," *Coal-Fueled Diesel Engines 1992*, J. A. Caton and H. A. Webb, eds., ASME ICE-Vol. 16, pp. 55-62; also, ASME JOURNAL OF ENGINEERING FOR GAS TURBINES AND POWER, Vol. 114, No. 3, pp. 528-533.

Slaughter, D., Cohen, M., Samuel, E., Mengel, M., and Gal, E., 1990, "Control of Emissions in the Coal Fueled Diesel Locomotive," in: *Coal-Fueled Diesel Engines 1990*, J. A. Caton, ed., ASME ICE-Vol. 12, pp. 11-16.

Soehngen, E. E., 1975, "The Development of the Coal Burning Diesel in Germany," U.S. ERDA Report No. WA76-3387.

Wahiduzzaman, S., Blumberg, P. N., Keribar, R., and Rackmil, C. I., 1990, "A Comprehensive Model for Pilot-Ignited, Coal/Water Mixture Combustion in a Direct Injection Diesel Engine," *Coal-Fueled Diesel Engines 1990*, J. A. Caton, ed., ASME ICE-Vol. 12, pp. 59-68.

Wahiduzzaman, S., Blumberg, P. N., and Hsu, B. D., 1991, 'Simulation of Significant Design and Operating Characteristics of a Coal Fueled Locomotive Diesel Engine," in: *Coal-Fueled Diesel Engines 1991*, J. A. Caton and H. A. Webb, eds., ASME ICE-Vol. 14, pp. 39-48.

X. Sun[1]

W. G. Wang

R. M. Bata

West Virginia University,
Morgantown, WV 26506

X. Gao

Wuhan University of Transportation,
Wuhan, People's Republic of China

Performance Evaluation of Low Heat Rejection Engines

Improving the performance of the Chinese B135 six-cylinder direct injection turbocharged and turbocompounded Low Heat Rejection Engine (LHRE) was based on experimental and analytical studies. The studies were primarily applied on a B1135 single-cylinder LHR engine and a conventional water-cooled B1135 single-cylinder engine. Performance of the B1135 LHRE was worse than that of the conventional B1135 due to a deterioration in the combustion process of the B1135 LHRE. The combustion process was improved and the fuel injection system was redesigned and applied to the B135 six-cylinder LHRE. The new design improved the performance of the LHRE and better fuel economy was realized by the thermal energy recovered from the exhaust gases by the turbocompounding system.

Introduction

Reducing the heat transfer through the walls of the internal combustion engine was the main focus of the adiabatic engines, LHRE. This heat, which amounts to approximately 25 percent of the heat released by the fuel, decreases the overall thermal efficiency, and requires a cooling system with a driving pump and internal walls to bear the thermal load. Since the 1970s, substantial interest has been focused on the development of the LHRE and the use of ceramic materials to isolate the metals of the combustion chamber [1-10]. Controversial conclusions were published about the LHRE since then. The potential benefits claimed were [5]: (1) reduced fuel consumption and heat rejection, (2) increased capability to burn a wide range of fuels, (3) reduced cooling system volume, (4) increased reliability and durability with reduced service and maintenance, (5) reduced emissions, and (6) increased system power density. However, increased fuel consumption of ceramic insulated engines was reported [11-14].

Woschni [11] and some other researchers [19-21] studied the heat transfer between the gases in the cylinder and the cylinder wall. They pointed out that taking insulation measures could not reduce the heat transfer from the gases in the cylinder wall. They also pointed out that taking insulation measures could not reduce the heat transfer, thus resulting in an increase of fuel consumption. This point of view, in fact, denied the advantages of LHREs. Nevertheless, many other experiments and almost all computer simulations revealed that LHREs did reduce in-cylinder heat transfer and fuel consumption [3, 4, 6-10]. So, to some extent, LHREs seem to be perplexing.

Since 1985, development of LHREs has been undertaken at Wuhan University of Transportation. This research was a part of a large research project sponsored by the National Scientific Committee of China. At first, experimental and analytical investigations were focused on the development of the B1135 single-cylinder, direct-injection LHREs. Then multicylinder LHREs were developed based on the study of single-cylinder LHREs. This strategy was due to theoretical and economic considerations. In 1989, the study of ceramic components of the B135 series LHREs was completed and many good ceramic components were produced. In 1990 a B6135 turbocompounded LHRE (six-cylinder, direct-injection) was developed. In the mean time, two successful tests were conducted by other researchers [4], which included a 400-h-endurance test of a model 6105 LHRE and a 10,000-km-road test with the 6105 LHRE in a bus. All these suggested that great success had been achieved. However, it was found that many of the LHREs did not show the expected high thermal efficiency. The fuel consumption rate of some LHREs even increased, especially when they were operated under high loads. For instance, the fuel consumption rate of the B1135 LHRE increased by 8.9 percent at 90 percent load. Did it mean that the LHRE was not practical? Definitely not! The authors believe that it was the poor fuel combustion that subsequently weakened the advantage of these LHREs in reducing fuel consumption. If the characteristics of the fuel combustion of these LHREs can be understood, effective measures can be taken to improve it. Therefore a great part of the research was converted to the performance optimization of LHREs. Since that time, some progress has been made.

To evaluate the performance of the B135 series LHREs, comparison experiments between the B1135 LHRE and the baseline conventional water-cooled engine were conducted. The objective of these experiments was to explore the cause of poor performance and then take measures to improve it. If success was met, the procedures of performance improvement would be applied to the B6135 LHRE.

---

[1] Graduate student, presently with Michigan State University.

Contributed by the Internal Combustion Engine Division and presented at the 15th Annual Fall Technical Conference of the ASME Internal Combustion Engine Division, Morgantown, West Virginia, September 26-29, 1993. Manuscript received by the Internal Combustion Engine Division January 28, 1994. Associate Technical Editor: W. Cheng.

Table 1 Engine specifications

	B1135	B6135
Bore (mm)	135	135
Stroke (mm)	150	150
Compression Ratio	16.5	16.5
Number of Cylinders	1	6
Rated Engine Speed (rpm)	1500	1500
Rated Engine Power	26.47	176.47
Method of Turbocharging	External Compressor	Exhaust Turbine
Valve Timing (same)		
Intake Valves	open at 11 CA BTDC close at 37 CA ABDC	
Exhaust Valves	open at 51 CA BBDC close at 13 CA ATDC	

The B135 Series Engine

The B135 series diesel engines are manufactured by the Shanghai Diesel Engine Factory, and are used throughout China. Listed in Table 1 are the basic specifications of the B1135 and B6135 conventional diesel engines. The B1135 LHRE and the B6135 LHRE were designed and constructed based on their conventional baseline engine. The cast iron piston was replaced by a piston with a HPSN (Heat-Pressed Silicon Nitride) piston cap 96 mm in diameter. The cast iron head was covered by a 7-mm-thick PSZ (Partially Stabilized Zirconia) plate. The cast liner was replaced by a PSZ ring of 25 mm in height and 2.5 mm in thickness. The steel valve was coated with a 2-mm-thick PSZ layer using a plasma spraying technique. The cooling system was eliminated. A specially designed synthetic oil was used for lubrication.

The ceramic-to-metal attachment joint was one of the most difficult designs encountered. During the previous long-term research of the ceramic-insulated components for the B135 series LHREs, a total of 60 pistons, heads, and liners were tested. It was found that PSZ worked well on heads, liners, and valves, but it could not bear the high thermal shock when it was made as a cap for a piston. HSPN, however, provided better thermal shock resistance for pistons than PSZ. Therefore, HSPN was selected as the ceramic material for the piston, while PSZ was still used for other components.

Experimental

The important part of the evaluation was the comparison experiment between the B1135 LHRE and a similar B1135 conventional water-cooled engine. Both engines were four stroke, single cylinder, direct injection, and turbocharged. They had identical fuel systems, injection timing, and valve timings. They were also operated under identical conditions. It was noted that the volumetric efficiency of the LHRE would decrease because of low heat rejection of the cylinder chamber wall. This was offset by increasing the inlet pressure until the desired quantity of air, which was equal to that of the conventional metal engine, was attained. The engines were run at a steady state of each specific operating condition for approximately fifteen minutes before taking the initial testing data. The engine to be tested was installed on a test stand and connected to an eddy-current dynamometer. The turbocharged operation was simulated by supplying regulated high-pressure air from an external compressor. Exhaust back pressure was controlled by a valve in the exhaust pipe. A set of thermocouples was used to record the temperatures of the cylinder wall, the inlet air, and the exhaust gases. Inlet air flow was recorded by a flowmeter. Engine speed and fuel consumption rate were indicated by a digital speed-fuel flow indicator. An AVL quartz pressure transducer, an AVL inductance type needle lift sensor, and a pressure sensor were used to record the cylinder pressure, the needle lift, and the fuel line pressure, respectively. These electric signals, along with other electric signals such as the TDC signals, were logged by an AVL-657 high-speed, multichannel data acquisition system. During the experiments, a Nicolet digital oscillograph was used to monitor the cylinder pressure, which was useful for selecting and appropriating time to record data. All data was recorded over a large number of cycles and then averaged. A specific computer program was developed to process the data.

Basic Equations

From the in-cylinder pressure data, heat release rate was calculated by the following formulas [1]:

$$\frac{dm_f}{d\theta}=\frac{\dfrac{\left(k\bullet p\,\dfrac{dv}{d\theta}+v\,\dfrac{dp}{d\theta}\right)}{(k-1)}+\sum\dfrac{dQ_i}{d\theta}}{H_{VL}+C_vT-U_s-m\,\dfrac{L_0}{m_a}\bullet\left(\dfrac{\partial U_s}{\partial F}+\dfrac{C_vT}{W}\bullet\dfrac{dW}{dF}\right)} \tag{1}$$

where C_v = specific heat of working gases at constant volume
F = fuel–air ratio
H_{VL} = lower heating value of fuel
k = specific heat ratio
L_0 = theoretical mass of air required for burning 1 kg fuel
m = mass of working gases
m_a = mass of air
m_f = mass of fuel burned
p = in-cylinder pressure
Q_i = quantity of heat transfer of the ith region on the cylinder wall
T = in-cylinder temperature
U_s = internal energy of the working gases
v = volume of the cylinder
W = equivalent molecular weight of the working gases
θ = crank angle

$$\frac{dQ_{\text{com}}}{d\theta}=H_{VL}\bullet\frac{dm_f}{d\theta} \tag{2}$$

where Q_{com} = quantity of heat release of fuel.

The convective heat transfer coefficient between the working gases and the cylinder wall was calculated by Woschni's formula [11, 20]

$$\alpha=130D^{-0.2}T^{-0.53}P^{0.8}\left[C_1C_m+C_2\frac{V_HT_1}{p_1V_1}(P-P_0)\right]^{0.8} \tag{3}$$

The radiant heat transfer flux between the working gases and the cylinder was calculated by Annand's formula [15]:

$$Q_x=\Sigma 1.5\sigma(T^4-T_{wi}^4)S_i \tag{4}$$

Performance Evaluation

The B135 series LHREs were based on a B1135 single-cylinder, so performance evaluation was focused on this type of LHRE. Comparison experiments between the B1135 LHRE and a similar B1135 conventional water-cooled diesel engine were conducted. During the experiments, efforts were made to maintain the two engines on a comparable level. The processed results of the experiments are displayed in Figs. 1–5. The main data are listed in Table 2.

It should be pointed out that the B1135 LHRE had successfully passed the 100-hour-endurance test before the comparison experiments were undertaken. During the experiments, no fatigue failures of insulated components were observed. It was noted that there were great differences in the combustion process between the two engines. A heat release rate analysis

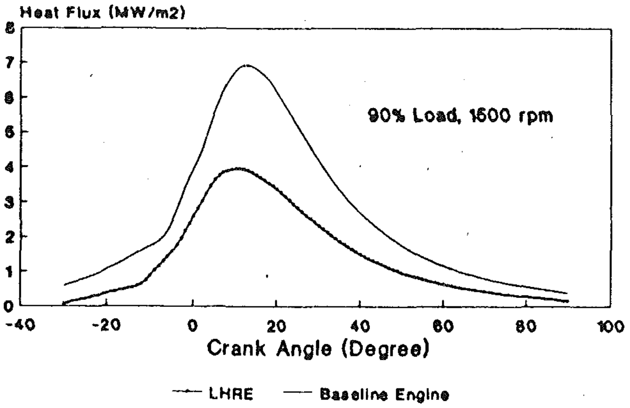

Fig. 1 Comparison of heat flux to cylinder wall

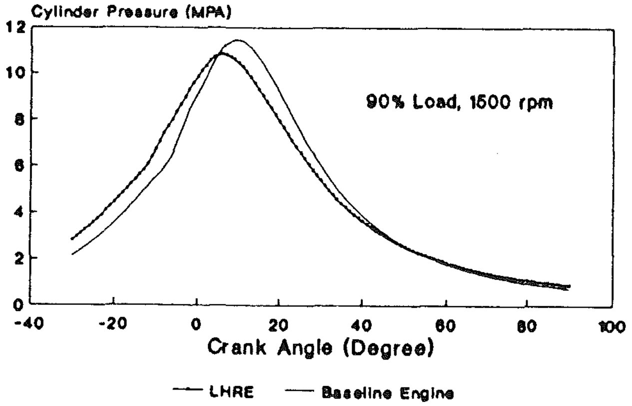

Fig. 2 Comparison of cylinder pressure

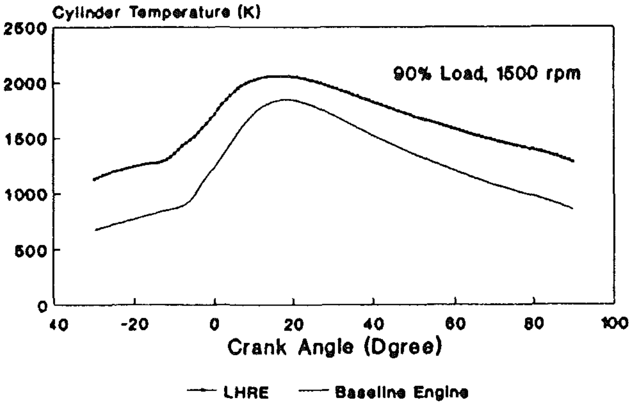

Fig. 3 Comparison of gas temperature

method was employed to study the differences. Compared with that of the B1135 conventional water-cooled diesel engine, the combustion process and heat transfer of the B1135 LHRE are characterized accordingly:

1 The convective heat transfer to combustion chamber wall is decreased;
2 The ignition delay is shortened;
3 The proportion of premixed combustion is decreased while the proportion of late stage combustion is increased;
4 The whole combustion duration is extended;
5 The heat release rate during the main stage of combustion is decreased;
6 The fuel consumption rate is increased;
7 The volumetric efficiency is decreased;

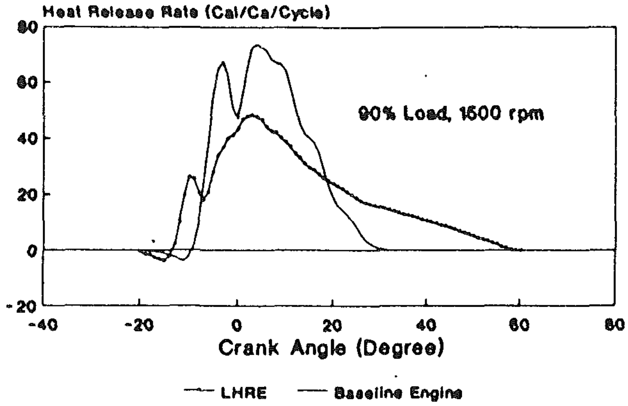

Fig. 4 Comparison of heat release rate

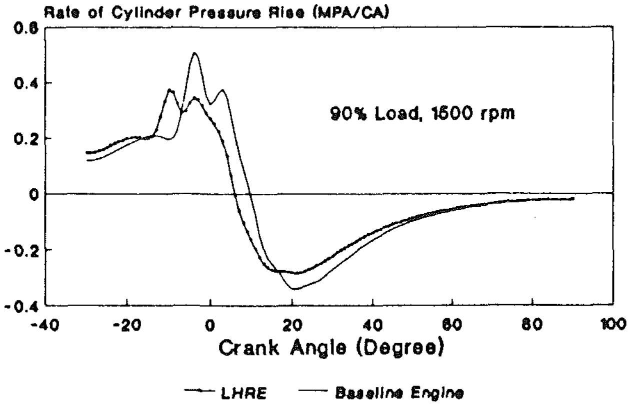

Fig. 5 Comparison of rate of cylinder pressure rise

Table 2 Performance comparison between the B1135 LHRE and the conventional engine

	Conventional	LHRE
Fuel Type	Diesel #0	Diesel #0
Start of Injection (CA)	-20	-20
Engine Speed (RPM)	1500	1500
Inlet Pressure (MPA)	0.163	0.183
Inlet Temperature (K)	318	318
Volumetric Efficiency	0.91	0.85
Start of Ignition (CA)	-8	-12
Ignition Delay (MS)	1.33	0.89
End of Combustion (CA)	32	58
Proportion of Premixed Combustion	27.4%	6.67%
Duration of Combustion (CA)	40	70
Mean Head Temperature (K)	533	1191
Mean Piston Temperature (K)	498	1230
Mean Liner Temperature (K)	419	858
Peak Heat Release Rate (Cal/CA/Cycl)	73.86	48.24
Peak Cylinder Temperature (K)	1847	2055
Peak Cylinder Pressure (MPA)	11.46	10.84
Peak Rate of Pressure Rise (MPA/CA)	0.453	0.356
Peak Heat Flux to wall (MW/M^2)	6.936	3.956
Exhaust Gases Temperature (K)	490	624
Fuel Consumption Rate (G/KW · H)	245	266.7
Engine Power (KW)	23.5	23.5

8 The rate of cylinder pressure rise is decreased;
9 The temperatures of working gases and exhaust gases are elevated;
10 The mean wall temperatures of the combustion chamber are elevated.

Figure 1 shows that the in-cylinder convective heat transfer of the B1135 LHRE did decrease as a result of the insulation

Table 3 Mixture fuels experiment of the B1135 LHRE

Fuel Type	Di.0#	75%Di.#0 +25%Gas.	50%Di.#0 +50%Gas.
Start of Injection (CA)	-20	-20	-20
Engine Speed (RPM)	1500	1500	1500
Inlet Pressure (MPA)	0.183	0.183	0.183
Inlet Temperature (K)	318	318	318
Start of Ignition (CA)	-12	-9	N/A
Ignition Delay. (MS)	0.89	1.22	N/A
End of Combustion (CA)	58	42	N/A
Duration of Combustion (CA)	70	51	N/A
Prop. of Premixed Combus.	6.67%	23.6%	N/A
Fuel Cons. Rate (G/KW · H)	266.7	253.1	269.4
Engine Power (KW)	23.5	23.5	23.5

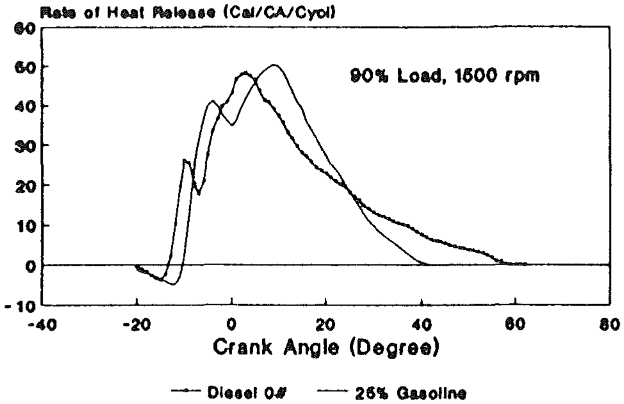

Fig. 6 Change in heat release rate when the B1135 LHRE uses mixture fuels

of the combustion chamber wall. This, as expected by many researchers, should have resulted in an improved thermal efficiency. However, the fuel consumption rate of the B1135 LHRE rose (about 8.86 percent at 90 percent load). Why? The results of the experiments suggested that the problem was the deteriorated fuel combustion.

It is evident that the deterioration of fuel combustion of B1135 LHRE is mainly caused by the shortened ignition delay. Table 2 shows that at 90 percent load, the ignition delay of the B1135 LHRE was shortened by 33.1 percent. After insulation measures are taken in the LHRE, the heat transfer between the working gases and the cylinder wall decrease. Therefore, the in-cylinder temperature and the combustion side surface temperature increase greatly (Table 2), which makes the "pumping heat" effect more serious. After being inhaled into the cylinder of the LHRE, the fresh air gets more heat than it does in conventional diesel engines, so its pressure and temperature are much higher at the end of compression (Figs. 2 and 3). Consequently, the fuels injected into the cylinder can finish the physical and chemical preparation stage more quickly, prior to ignition. It follows that the ignition delay is shorter and that, with a given injection rate, the quantity of fuel injected during the ignition delay is much smaller. The proportion of premixed combustion is decreased (from 27.4 to 6.67 percent), while the proportion of diffusion combustion and late-stage combustion are increased. These factors result in a reduced heat release rate during the main stage of combustion (Fig. 4), lowered rate of cylinder pressure rise (Fig. 5), and incomplete fuel combustion.

To improve the performance of LHREs, a new combustion process that suits the characteristics of LHREs should be organized. It is certain that the working gases in the cylinder of internal combustion engines have the full potentiality to do work near the TDC. So, the crux of the matter is to increase the proportion of premixed combustion and decrease the proportion of late stage combustion. Then the heat release rate during the main stage of combustion will be increased and the combustion process will be improved.

Prolonging Ignition Delay

The quantity and quality of premixed combustion in an internal combustion engine are dependent on the quantity of fuel injected during ignition delay and the quality of the fuel evaporated and distributed, fuel air ratio, and the fuel injection rate. So, to increase the proportion of premixed combustion of LHREs, two methods may be used. One is to prolong the ignition delay. The other is to increase the fuel injection rate, which will be discussed in the next section. Studying combustion theory, prolonging of the injection delay is inversely temperature dependent, which means the higher the temperature, the shorter the ignition delay. Unfortunately, very high in-cylinder temperatures are a characteristic of LHREs. So the method that prolongs ignition delay of LHREs by reducing the in-cylinder temperature cannot be used. The other option was to explore the ignition quality of fuels, which is related to their composition and chemical structure. Fuel consumption, mainly of straight-chain paraffinic compounds, naphthenes, and aromatics, was studied. The greater the percentage of paraffin, the shorter the ignition delay is. Increasing the ring chain molecules, naphthenes, and aromatic compounds prolongs the ignition delay. Considering diesel fuels, cetane number is used to rate the ignition quality. But the higher the cetane number, the shorter the ignition delay. Gasoline, which is usually blended with benzol and some aromatics, has a lower cetane number. Its ignition delay under high temperature and pressure is relatively longer, while its volatility is better, compared with those of diesel. Therefore, if diesel is blended with gasoline at an appropriate rate, a kind of mixture fuel will be obtained. Using this mixture fuel in LHREs will result in an increased quantity of well-evaporated and distributed fuels, and in turn, will substantially raise the proportion and heat release rate of premixed combustion.

Some experiments were done to verify the effectiveness of this method. Table 3 shows that by blending diesel 0# with 25 percent gasoline, the ignition delay of the B1135 LHRE at 90 percent load is increased by 37.1 percent. The proportion of premixed combustion is increased from 6.67 to 23.6 percent. The fuel consumption rate is reduced by 5.1 percent. This proves that using appropriate mixture fuel that has a low cetane number and good volatility can improve the thermal efficiency of LHRE's. Figure 6 also shows the improvement of the combustion process of the B1135 LHRE. However, using mixture fuel that has 50 percent gasoline did not improve the thermal efficiency of the LHRE. On the contrary, the detonation was aggravated and the fuel consumption rate was increased by 1.01 percent. This is because the configuration of diesel LHRE is not suitable for gasoline dominant mixture fuel.

Adjustment of Fuel System

With a given ignition delay and a given injection quantity per cycle, and by increasing the fuel injection rate, the quantity of fuels injected into the cylinder before the moment of ignition will be increased. This will increase the proportion and the heat release rate of premixed combustion. The proportion of late-stage combustion will be decreased; thus the combustion process of LHREs will be improved and the fuel consumption rate reduced. Several methods are investigated to increase fuel injection rate. All of these methods require that the fuel system be adjusted.

1 Raising the Opening Pressure of the Needle Valve. Pressure difference across the injector's nozzle is determined by the cylinder pressure at injection and the fuel injection pressure. Increasing the fuel injection pressure can result in

Table 4 Experiment of the B1135 LHRE with different opening pressure of the needle valve

Opening Pressure (MPA)	14.71	19.61	24.03
Fuel Type	Di.0#	Di.0#	Di.0#
Start of Injection (CA)	-20	-20	-20
Engine Speed (RPM)	1500	1500	1500
Inlet Pressure (MPA)	0.183	0.183	0.183
Inlet Temperature (K)	318	318	318
Start of Ignition (CA)	-11.5	-12	-12
Ignition Delay (MS)	0.94	0.89	0.83
End of Combustion (CA)	65	58	51
Duration of Combus. (CA)	76.5	70	63.5
Prop. of Premixed Combus.	3.52	6.67	17.9
Fuel Cons. Rate (G/KW · H)	272.1	266.7	259.9
Engine Power (KW)	23.5	23.5	23.5

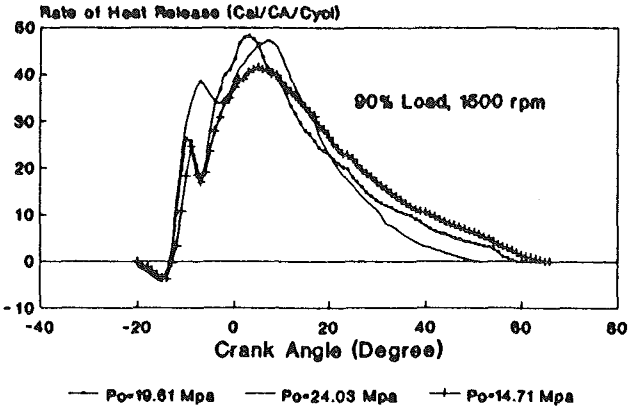

Fig. 7 Change in heat release rate when the B1135 LHRE uses different opening pressures of the needle valve

Table 5 Experiment of the B1135 LHRE with different types of nozzles

Nozzle Type	4×0.35×150°	6×0.32×152°	9×0.26×152°
Number of orifices	4	6	9
Orifices Diameter (MM)	0.35	0.32	0.26
Injection Angle (Degree)	150°	152°	152°
Cross Sectional Area (MM^2)	0.3847	0.4823	0.4776
Fuel Type	Di.0#	Di.0#	Di.0#
Start of Injection (CA)	-20	-20	-20
Engine Speed (RPM)	1500	1500	1500
Inlet Pressure (MPA)	0.183	0.183	0.183
Inlet Temperature (K)	318	318	318
Start of Ignition (CA)	-12	-12.5	N/A
Ignition Delay (MS)	0.89	0.83	N/A
End of Combustion (CA)	58	57	N/A
Duration of Combus.(CA)	70	59.5	N/A
Prop. of Premixed Combus.	6.67%	21.7%	N/A
Fuel Cons. Rate (G/KW · H)	266.7	255.6	N/A
Engine Power (KW)	23.5	23.5	N/A

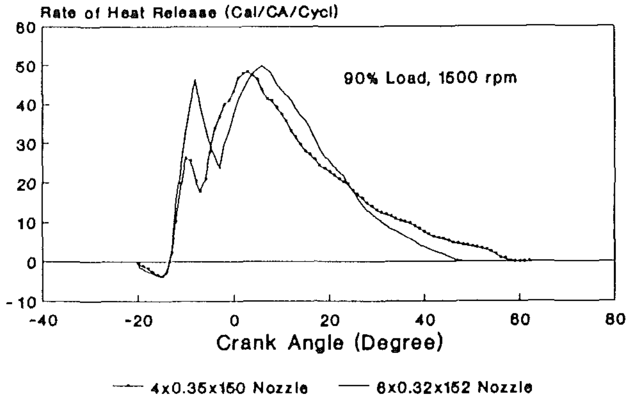

Fig. 8 Change in heat rate release when the B1135 LHRe uses different nozzles

an increase of the pressure difference and, in turn, increase the fuel injection rate. This can be obtained by raising the opening pressure of the needle valve. Then, the outlet velocity and outlet pressure of the fuel flow, and the length of visible spray will also increase. Since the air resistance to the spray will increase relatively, the cone angle and the turbulence of the spray will increase. All these factors mean that an increased quantity of well-mixed combustible gases will be present before ignition. Related experiments done on the B1135 LHRE confirmed the effectiveness of this method. In the experiment, only the opening pressure of the needle valve of the B1135 LHRE was adjusted. Listed in Table 4 are the results of the experiment. Shown in Figure 7 is the improvement of heat release rate.

When the opening pressure of the needle valve was adjusted from 19.61 MPA to 23.5 MPA, the proportion of premixed combustion increased from 6.67 to 17.3 percent, and the fuel consumption rate decreased by 2.55 percent. On the contrary, when the opening pressure of the needle valve was adjusted from 19.61 MPA to 14.71 MPA, the proportion of premixed combustion decreased from 6.67 to 3.52 percent, and the fuel consumption rate increased by 2.03 percent.

2 Increasing the Nozzle Cross-Sectional Area. With a given injection quantity per cycle, the injection rate will increase when the nozzle cross-sectional area is increased. If appropriately selected, the increase of the cross-sectional area can be attained by increasing the number of orifices and slightly decreasing the diameter of the orifices. The objective of this selection is to improve the quality of fuel distribution and fuel vaporization. Before the performance evaluation was conducted, the B1135 LHRE used a type of nozzle that was claimed to be most suitable for the 135 series conventional water-cooled engines. However, it was proved that this type of nozzle was no longer suitable for the B1135 LHRE. It was therefore replaced by a nozzle that had a larger cross-sectional area. The results of the experiment are shown in Table 5 and Fig. 8.

The experiment revealed that when the 6 × 0.32 × 152 deg nozzle was used, the proportion of premixed combustion increased from 6.67 to 21.7 percent, and the fuel consumption rate decreased by 4.16 percent. However, with approximately the same cross-sectional area as that of the 6 × 0.32 × 152 deg nozzle, the 9 × 0.26 × 152 deg nozzle was not suitable for the B1135 LHRE. During the experiment, some orifices of this nozzle were blocked and burned because with a given cross-sectional area, selecting too many orifices will result in a great decrease of the orifice diameter. Since the in-cylinder temperature of the LHRE is very high, orifices that have too small a diameter will likely be blocked or burned. Even if the nozzle can work, the spray penetration and the injection rate will decrease. Therefore, this type of nozzle is not recommended for the B1135 LHRE.

3 Increasing the Diameter of the Fuel Pump Plunger. Increasing the diameter of the fuel pump plunger will also increase fuel injection rate. A related experiment was done on the B1135 LHRE. Table 6 lists the results of the experiment. When the plunger diameter was increased from 11 mm to 12 mm, the proportion of premixed combustion increased from 6.67 to 19.5 percent, and the fuel consumption rate decreased by 3.26 percent. The change in heat release rate is shown in Fig. 9.

In addition to the three methods mentioned above, other methods, such as increasing the effective plunger stroke, raising the speed of the cam axle, etc., can also increase the fuel injection rate. However, improving the performance of LHREs is complex because many factors are involved which vary from one engine to another. The methods introduced here are the initial steps toward further research.

After applying the methods (not including the method of using mixture fuel) discussed above comprehensively on the B1135 LHRE, its fuel consumption rate at 90 percent load was 242.2 g/kW•h, which indicated a 1.14 percent reduction of fuel consumption rate over that of the B1135 conventional engine. This reduction is, to some extent, less than expected. The main cause is that the increased thermal energy in the exhaust was not used by the B1135 LHRE. For a typical turbocharged LHRE, about 41 percent of the energy is converted into output mechanical power; about 15 percent is rejected to the cooling and lubricating fluids, with the remaining 44 percent in the exhaust [5].

The B6135 Turbocompounded LHRE

The B6135 (six-cylinder) turbocharged and turbocompounded LHRE was based on the conventional B6135 turbocharged diesel engine (Table 1). Adjustment of the fuel system was first made according to the performance optimization of the B1135 LHRE. Then the conventional water cooling system was eliminated. Insulation measures were the same as that of the B1135 LHRE, which has been described above. Located downstream of the turbocharger turbine, a second turbine was used in the exhaust system to recover the energy in the exhaust. It was connected to the crankshaft through a gearbox. Charge cooling with an intercooler after compression was used to increase the air density further. The distribution of power between the reciprocating engine and the turbines was adjusted by changing the equivalent cross-sectional area of the nozzles. Listed below are the basic data of the turbocharger and the turbines:

Compressor speed: 70000 rpm
Compressor efficiency: 0.73
First turbine efficiency: 0.75
Second turbine speed: 35000 rpm
Second turbine efficiency: 0.78

It was found that the maximum benefit of turbocompounding over the B6135 LHRE occurred at full load (Table 7). Compared with that of the conventional water-cooled B6135 turbocharged engine, its fuel consumption rate was decreased by 4.05 percent. The output of the power turbine was 11.6 kW, which was about 6.49 percent of the total engine power produced. This indicates that the high pressure and temperature exhaust of LHREs do have great potential to do useful work. At 75 percent load, the fuel consumption rate of the B6135 turbocompounded LHRE was decreased by 2.73 percent compared with that of the conventional water-cooled B6135 turbocharged engine. The output of the power turbine was 5.32 kW, which was about 4.00 percent of the total engine power produced. At 50 percent load, its fuel consumption rate was only decreased by 1.25 percent and the output of the power turbine is fairly low. The reason is that at part-load, the pressure and temperature of the exhaust are lower than those at full load, or in other words, the thermal energy of exhaust is lower at part-load. Therefore, the turbocompounding technique is most suitable to those LHREs that are in most cases operated at high load (more than 75 percent load). In China, the B6135 diesel engines are widely used in water transportation (as the main engine of some inland waterway ships, as power station engines of large ocean ships, etc.), agriculture, and mini-power-plants. In these cases, the engines are often operated at full load. So, the B6135 turbocompounded LHREs have great potential for commercial use. Those engines that

Table 6 Experiment of the LHRE with different plungers

Plunger Diameter (MM)	10	12
Fuel Type	Diesel 0#	Diesel 0#
Start of injection (CA)	-20	-20
Engine Speed (RPM)	1500	1500
Inlet Pressure (MPA)	0.183	0.183
Inlet Temperature(K)	318	318
Start of Ignition (CA)	-12	-12
Ignition Delay (MS)	0.89	0.89
End of Combustion (CA)	58	50
Duration of Combustion (CA)	70	62
Prop. of Premixed Combustion	6.67%	19.5%
Fuel Consumption (G/KW · H)	266.7	258
Engine Power (KW)	23.5	23.5

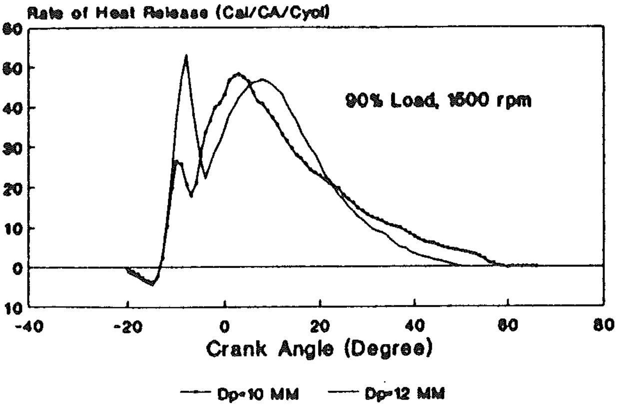

Fig. 9 Change in heat release rate when the B1135 LHRE uses different plungers of the fuel pump

Table 7 Experimental data of the B6135 turbocompounded LHRE

Determination	Convent.	LHRE	Convent.	LHRE	Convent.	LHRE
Engine Load Rate	50%	50%	75%	75%	100%	100%
Fuel Type	Diesel #0	Diesel #0	Diesel #0	Diesel #0	Diesel #0	Diesel #0
Inlet Pressure (MPa)	0.1400	0.1466	0.1703	0.1784	0.207	0.2186
Inlet Temperature (K)	311	311	334	336	356	363
Air Fuel Rate (Kg/S)	0.226	0.226	0.266	0.266	0.301	0.300
1st Turbine Inlet Pressure (MPa)	0.157	0.1780	0.180	0.2024	0.2089	0.2297
1st Turbine Inlet Temperature (K)	686	771	743	878	836	1028
2nd Turbine Inlet pressure (MPa)	N/A	0.1283	N/A	0.1307	N/A	0.1360
2nd Turbine Inlet Temperature (K)	N/A	705	N/A	796	N/A	895
Engine Speed (RPM)	1500	1500	1500	1500	1500	1500
Engine Power (KW)	88.24	89.56	132.06	132.89	176.47	178.82
2nd Turbine Power (KW)	N/A	1.89	N/A	5.32	N/A	11.6
Fuel Consumption (G/KW · H)	168.3	166.2	161.2	156.8	157.9	151.5

are often used in light load or often required to change working conditions, such as city buses, passenger cars, or light-duty trucks, are not suitable for turbocompounding.

Summary and Conclusions

The performance of the Chinese B135 series LHREs was studied to investigate its potential in fuel economy and commercial use. It was found that the performance of the B1135 LHRE was very poor compared with that of a similar B1135 conventional water-cooled engine. The poor performance was caused by a deteriorated fuel combustion, which was characterized by a shortened ignition delay, a decreased proportion of premixed combustion, an increased proportion of late-stage combustion, and a reduced heat release rate during the main stage of combustion. To improve the combustion process, two effective methods were studied. One method was using fuels that had a low cetane number. Findings indicated that by blending diesel with 25 percent gasoline, the fuel consumption rate of the B1135 LHRE could be decreased. The other method was increasing fuel injection rate. It was found that by raising the opening pressure of the needle valve, appropriately increasing the cross-sectional area of the multi-orifice nozzle, and increasing the diameter of the fuel pump plunger, the fuel consumption of the B1135 LHRE could be decreased. However, after the adjustment of the fuel system was made, the fuel consumption rate of the B1135 LHRE was only slightly lower than that of the conventional water-cooled engine.

For the B6135 six-cylinder turbocharged LHRE, the fuel system was adjusted based on the performance optimization of the B1135 LHRE. Then the turbocompounding technique was applied. It was noted that at full load its fuel consumption rate was reduced greatly. At part-load, this benefit was modest. Since B6135 engines are widely used in China and often operated at full load, the B6135 turbocompounded LHRE has great potential for commercial use.

Some general conclusions regarding LHREs can be drawn from this study:

1 The combustion process of a LHRE will be enhanced with an optimized fuel system.
2 Turbocharging plus turbocompounding is an effective method to recover the thermal energy in the exhaust of multicylinder LHREs and improves the overall thermal efficiency, especially at full load.

Acknowledgments

The authors wish to thank the Laboratory of Internal Combustion Engines at Wuhan University of Transportation. In particular, they wish to thank Professor R. S. Luo and Professor J. X. Wu for their research advice. Thanks are also due to J. W. Gui and X. M. Luo for their experimental support.

References

1 Sun, Xiaobo, "Measurement of Cylinder Pressure and Calculation of Heat Release Rate of Turbocharged Low Heat Rejection Engines," MS Thesis, WUWTE, 1991.

2 Sun, Xiaobo, Wang, W. G., Donald, W. L., and Gao, Xiaohong, "Experimental Analysis and Performance Improvement of Single Cylinder Direct Injection Turbocharged Low Heat Rejection Engines," SAE Paper No. 930989, 1993.

3 Zhang, N. L., Zhong, S. Y., Feng, J. T., Cai, J. W., Pu, Q. N., and Fan, Y., "Development of Model 6105 Adiabatic Engine," SAE Paper No. 930984, 1993.

4 Kamo, R., and Bryzir, W., "Performance Assessment of U.S. Army Truck With an Adiabatic Diesel Engine," SAE Paper No. 890142, 1989.

5 "A Review of the State of the Art and Projected Technology of Low Heat Rejection Engines," A report prepared by the Committee on Adiabatic Diesel Technology, Energy Engineering Committee, and Commission on Engineering and Technical Systems, National Research Council, National Academy Press, Washington, DC, 1987.

6 Hoag, K. L., Brando, M. C., and Bryzik, W., "Cummins/TACOM Adiabatic Engine Program," SAE Paper No. 850356, 1985.

7 Morel, T., Wahiduzzaman, S., and Fort, E. F., "LHR Engine Design Analysis Methodology—Heat Transfer Measurements in an Insulated Diesel," SAE Paper No. 880186, 1988.

8 Havstard, P. H., Gervin, I. J., and Wade, W. R., "A Ceramic Insert Uncooled Diesel Engine," SAE Paper No. 860447, 1986.

9 Moore, C., and Hoehne, J., "Combustion Chamber Insulation Effect on the Performance of a Low Heat Rejection Commins V-903 Engine," SAE Paper No. 860313, 1986.

10 Assanis, D., and Heywood, J., "Development and Use of a Computer Simulation of the Turbocompounded Diesel System for Engine Performance and Component Heat Transfer Studies," SAE Paper No. 860329, 1986.

11 Woschni, G., Spindler, W., and Kolesa, K., "Heat Insulation of Combustion Chamber Walls—A Measure to Decrease the Fuel Consumption of I.C. Engine?" SAE Paper No. 870339, 1987.

12 Cheng, W. K., Wong, V. W., and Gao, F., "Heat Transfer Measurement Comparison in Insulated and Noninsulated Diesel Engines," SAE Paper No. 890570, 1989.

13 Dickey, D. W., "The Effect of Insulated Combustion Chamber Surface on Direct-Injection Diesel Engine Performance, Emissions and Combustion," SAE Paper No. 890292, 1989.

14 Alkidas, A. C., "Experiments With an Uncooled Single-Cylinder Open-Chamber Diesel," SAE Paper No. 870020, 1987.

15 Annand, W. D., "Heat Transfer in the Cylinder of Reciprocating Internal Combustion Engines," *Proc. IMechE*, Vol. 177, No. 36, 1963.

16 Miyairi, Y., Matsuhisa, T., Ozawa, T., Oikawa, H., and Nakashima, N., "Selective Heat Insulation of Combustion Chamber Wall, for a DI Diesel Engine With Monolithic Ceramics," SAE Paper No. 890141, 1989.

17 Morel, T., Fort, E. F., and Blumberg, P. N., "Effect of Insulation Strategy and Design Parameters on Diesel Engine Heat Rejection and Performance," SAE Paper No. 850506, 1985.

18 Miyairi, Y., "Computer Simulation of an LHR DI Diesel Engine," SAE Paper No. 880187, 1988.

19 Reday, C. S., Domingo, N., and Graves, R. L., "Low Heat Rejection Engine Research Status: Where Do We Go From Here?" SAE Paper No. 900620, 1990.

20 Woschni, G., and Anisitis, F., "Experimental Investigation and Mathematical Presentation of Rate of Heat Release in Diesel Engines, Dependent Upon Engine Operating Condition," SAE Paper No. 740086, 1974.

21 Taylor, F. C., *The Internal-Combustion Engine in Theory and Practice*, Vol. 2, Halliday Lithograph Corp., 1968.

Development and Test of a Fractional Sampling System for Diesel Engine Particulate Measurement

R. R. Graze, Jr.
Technical Center,
Measurement Systems
Development Division,
Caterpillar, Inc.,
Dunlap, IL 61525

Diesel engine particulate certification, heretofore limited to on-highway truck engines, will be expanded in scope beginning in 1996. "Mini-dilution" tunnels have been the European and Japanese systems of choice for dilute particulate emissions certification for non-U.S. truck diesel engines. However, repeatability, steady-state test correlation versus full dilution systems, portability, sampling time, size, and system cost have precluded universal industry and regulatory acceptance of existing "mini-system" designs. To address corporate particulate measurement needs, the author developed a device known internally as the "Micro-Dilution Particulate Measurement System," which meets the following objectives: (1) correlation with full dilution systems within ISO 8178 equivalency standards, (2) short sampling time, (3) reduced setup effort, and (4) excellent portability. Since the system is a true fractional sampler, it is insensitive to engine size, requiring only a simple stack probe change to provide accurate, representative steady-state diesel stack sampling on any size diesel engine.

Introduction

Measurement of diesel engine particulate mass effluent has typically been limited to on-highway truck engines in the U.S., Europe, and Japan. In some areas, state and local air boards require at-site certification of stationary diesel engines. On-highway engine certification requires either transient cycle evaluation with a full dilution system (USEPA) or modal-based, steady-state testing with either full or mini-dilution systems (EEC and Japan). Due to revisions in the Clean Air Act and pending international regulations, engines powering off-highway vehicles (agriculture, mining, construction), ships and recreational vessels, and lawn care and utility powerplants will eventually require particulate testing for certification. To provide uniform test protocol and measurement system recommendations for the vast power range (1–50,000 hp) to be regulated in the future, ISO has in the last three years convened a technical subcommittee, which is developing the 8178 [1] series of test procedure documents. The ISO document permits testing with several particulate sampling system configurations, including both partial-flow and full-flow systems, and suggests criteria for equivalency testing against the full dilution standard. "Particulate" in the ISO 8178 document is defined in similar terms to those found in the U.S. CFR for on-highway truck engines, i.e., exhaust effluent trapped on a filter paper after dilution to a filter temperature of no greater than 52°C. During development of the ISO document, it became apparent that several of the particulate sampling configurations proposed therein may lack flexibility to achieve suitable accuracy and repeatability values over the array of engine sizes, power ranges, and configurations (single cylinder included) to be tested. While partial-flow systems that operate acceptably have been developed for particulate sampling, they are at times limited in flexibility to specific, narrow engine output ranges unless substantially modified. The use of full dilution is in general practice limited to engines below about 400 kW due to facility size constraints. Therefore, for particulate sampling over a wide range of engine output power values, and ISO-defined "total sampling system," which extracts an extremely small fraction of engine exhaust, and then dilutes and filters this fraction, represents a suitable approach.

Participation by the author on the ISO subcommittee developing the 8178 document yielded insight to the needs of non-truck engine manufacturers worldwide. Use of the USEPA Method 5 nondilute particulate sampling technique, along with its international derivatives, continues to be an issue where "at site" data is required. Although the majority of engine manufacturers worldwide favor elimination of Method 5 in favor of an ISO 8178-based dilution technique, certain regulatory agencies have indicated that until a commercial portable dilution-based sampler is available worldwide, ISO 8178-2 [2] will not be adopted. Also, adoption of the 8178-1 [3] laboratory test procedure for worldwide off-highway engine certification is of great importance to engine manufacturers.

Design Objectives

Initially, this system was intended for use only within an

Contributed by the International Combustion Engine Division and presented at the Energy-Sources Technology Conference and Exhibition, New Orleans, Louisiana, January 23–27, 1994. Manuscript received by the Internal Combustion Engine Division January 28, 1994. Paper No. 94-ICE-19. Associate Technical Editor: W. Cheng.

engine development lab on engines that range from 60–5600 kW. Many of these engines will be regulated for the first time for particulate emissions output within the next several years, requiring substantial engine development and certification effort for off-highway engine manufacturers. The power range of engines to be tested, along with facility test cell space constraints, demanded a small, portable system, which could be used on any engine in the test lab. The system's ease of use was crucial due to the fact that the test units would not have dedicated operators, but instead be run by engine test personnel. It was assumed that since air and fuel flow measurement capabilities are already in place, no provisions for stack gas flow measurement would be added to the particulate sampling device.

Of primary concern when initially assessing existing fractional sampling systems was the transfer tube, which transports hot, undiluted exhaust from the engine stack to the dilution tunnel. In-house testing revealed significant particulate deposition (up to 30 percent measured particulate mass reduction) in a long (8 m) line, heated to ISO 8178-1 [3] requirements. While ISO limits the length of heated line to five meters, it was observed by the author that the presence of virtually any transfer tube can yield a biased measured particulate value. These in-house findings agreed with the results of a joint Coordinating Research Council Smoke and Particulate Panel/ Engine Manufacturer's Association Calibration Task Force study performed by Professors David Kittelson and John Johnson [4] as well as work performed by AVL [5], which highlight the effects of thermophoresis, outgassing, and re-entrainment within exhaust transfer tubes, exhaust stacks, and dilution tunnels as significant contributors to particulate measurement variability. It should also be realized that the additional challenge of sampling particulate from large engines with high exhaust sampling locations is frequently met with elongated transfer tubes, exacerbating their deleterious effects. While appropriate dilution system conditioning between operating points may alleviate this problem somewhat, increases in test times and costs result.

Development of an in-house particulate sampling system was therefore initiated and directed toward addressing the following objectives:

1 Reduced deposition/re-entrainment.
2 Correlation versus full dilution (steady-state) acceptable per ISO.
3 Brief sampling times, preferably below five minutes per mode.
4 Portable, modest setup effort.
5 Usable by broad spectrum of personnel.
6 High repeatability (eight-mode weighted average C.O.V. ≤ ±3 percent.

In addition to the aforementioned general design requirements, system accuracy (i.e., correlation with full dilution systems operated in steady-state modes) and repeatability goals were quite aggressive. A specific repeatability criteria is difficult to derive, specifically due to the number of interacting engine operating characteristics which determine particulate output. Given constant CO and engine soluble organic fraction (SOF) output, a goal of ±3 percent C.O.V. (s/x) for day-to-day cycle-weighted particulate values was established for the system as compared to ±5 percent as observed in transient particulate testing. With respect to correlation, ISO 8178 [3] provides criteria for testing of non-full dilution systems against full dilution during operation in a series of steady-state modes defined in ISO 8178-4 [6] as the "C1" (commonly known as the California eight-mode) cycle. Per ISO, the average of seven eight-mode cycle-weighted results are recommended to agree within ±5 percent of the full dilution eight-mode average results to be considered "equivalent."

Prototype Design

Due to the wide range of engine sizes to be tested, the "total sampling system" was the configuration of choice. It was decided to eliminate the transfer tube by performing all dilution and filtering functions at the exhaust stack. To accomplish this, a dilution assembly was made by constructing a small outer shell pressure vessel around a sintered, stainless steel tube with a nominal 2 μm pore size mounted concentrically within the vessel. End sections were fabricated and welded in place, yielding a leak-free annulus between the dilution air chamber and the porous stainless steel tube (Fig. 1). The dilution air enters the chamber at the axial center of the chamber. This critical component will be discussed in detail later in the paper; see Appendix A for tunnel hardware dimensions.

Dilution air was provided via pressurized shop air source, and was filtered, hydrocarbon scrubbed, and dried prior to introduction to the dilution assembly. Sample vacuum was provided via diaphragm pump; flow apportionment was handled via critical flow orifices in the individual dilution air and sample sides of the system. Dry gas meters were used to measure dilution air and total dilute sample flows and, therefore, to infer actual extracted stack sample volume. This approach represented a considerable deviation from the "tracer" system, which employs CO_2 or NO_x measurements in the raw and dilute exhaust to ascertain dilution ratio (DR) as per the following formula:

$$DR = \frac{CO_2\,(\text{wet, raw}) - CO_2\,(\text{background})}{CO_2\,(\text{wet, dil}) - CO_2\,(\text{background})}$$

CO_2 concentration in the dilute exhaust is measured via NDIR analyzer; raw CO_2 concentration can either be measured in a

Nomenclature

A = wall area
ASME = American Society of Mechanical Engineers
BSFC = brake specific fuel consumption
C1 = ISO 8178-4 off-highway vehicle test cycle
CO = carbon monoxide
C.O.V. = coefficient of variation
CO_2 = carbon dioxide
CVS = constant volume sampler
DR = dilution ratio
EEC = European Economic Community
ISO = International Standards Organization
NDIR = non-dispersive infrared
P = precision
P_T = particulate
NO_x = oxides of nitrogen
R^2 = coefficient of determination
SLM = standard liters per minute
SOF = soluble organic fraction
U = uncertainty
V_o = boundary layer injector velocity
V_T = thermophoretic deposition velocity
V = velocity
ρ = density
Pr = Prandtl number
η = dynamic viscosity
k = thermal conductivity
d = dilution chamber inside diameter
Re = Reynolds number
Nu = Nusselt number
ν = kinematic viscosity
T = temperature
a = thermal accommodation coefficient

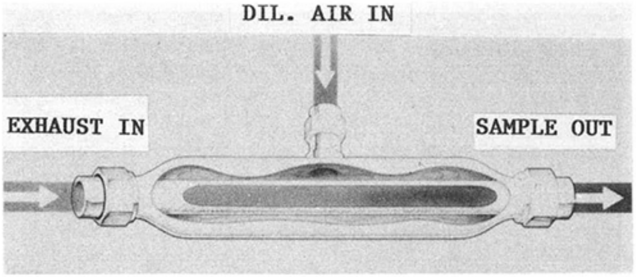

Fig. 1 Dilution assembly cutaway drawing

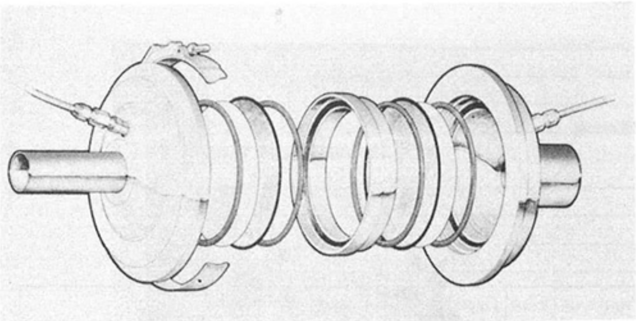

Fig. 2 Filter holder-exploded view

similar manner or be calculated from fuel consumption. While fuel combustion and raw CO_2 concentration can typically be determined to within ±2 percent in the lab, dilute CO_2 concentration measurement is more difficult at higher dilution ratios, as background CO_2 measurement errors are also an issue. In order to guarantee conformance reasonably to ISO 8178 accuracy requirements for determination of the exhaust mass extracted from the stack, an NDIR with multiple ranges, each with full calibration and linearizing characterization, is necessary. This approach was discarded as it was believed that the problems of inferring a small sample flow from large dilution air and dilute sample valves could be addressed by developing a calibration loop that provided a series flow scheme for the gas meters. A typical operating flow rate was passed through the meters in series during calibration using three-way ball valves. This proved successful as a means of eliminating the effects of flowmeter relative calibration accuracies on inferred sample flow values, which must be defined to within ±4 percent of direct measurement values per ISO 8178-1 [3]. While the accuracy of the gas flow meters is specified to be ±1 percent of reading, in the case of 10:1 dilution ratio, a worst case error in the inferred value for the mass extracted from the stack of around 20 percent is possible. Since the repeatability for the gas meters was around 0.15 percent, the maximum inferred value error, now in the form of data scatter, was now 2–3 percent. Also, since the "master" meter is the standard, there is reduced reliance on frequent calibration to lab standard devices (yearly calibrations to lab standard units is required).

System Modifications

The original system remained in operation for approximately five months. During this time various refinements were made, and by late 1991 the Caterpillar technical facility had requested procurement of three redesigned dilution systems. The modified design incorporated two digital mass flow controllers with microprocessor function replacing the conventional gas meters. These devices provided improvements over prior art in both calibration and flow accuracy. Utilizing a 386 PC, the mass flow controllers were verified for flow value agreement through a calibration loop (developed on the prototype), and recalibrated if a calibration shift occurred. Initial flow controller calibration to a transfer standard within ±0.25 percent was now achievable. Individual mass flow controller repeatability values of ±0.05–0.08 percent were consistently observed over the period of a week or more at Caterpillar. The flow controllers also incorporated an autobalance feature to reduce the effects of zero shift. The response time (1 s) of the flow controllers has also allowed the elimination of the conventional bypass filter configuration typically used with fractional sampling systems. In-house data indicate, that sample flow is within ±5 percent of setpoint values within less than 3 seconds after sampling initiation.

The original system filter scheme, consisting of a single, 142-mm-dia filter membrane, was inadequate per ISO and EPA, which require using a pair of filter membranes in line, located a maximum of 100 mm apart. Fractional samplers are normally equipped with two single-element filter housings, connected serially by an abbreviated length of tubing. Since stack mounting of the dilution assembly with minimal cantilevered mass was a desired feature, the filter holder was redesigned, which provided unified encapsulation of two 90 mm diameter filter membranes in a leak-free, easily accessed housing having minimal mass (Fig. 2). The filter holder is mounted immediately after the air-activated dilution chamber ball valve and can be removed for test filter media replacement via full-flow, quick-disconnect fittings. The stainless steel outer shells are internally streamlined to minimize inertial impaction. Reassembly after changing filters is simplified by the use of two pins, which locate the two filter shell halves and provide a positive stop so the bottom half does not have to be held during filter changing. The assembly consists of a filter screen spacer (provides 12.7 mm spacing between the filter elements), Teflon-coated filter support screens, high-quality over-center clamp and Teflon coated "O"-rings for leakage integrity. The support screens and spacers are nested within the housing to reduce filter holder mass. Pressure differential and filter gas stream temperature taps are provided.

An additional benefit from the filter redesign was that filter net weight errors resulting from rough handling, droppage, and filter media transfer to sealing surfaces, which contribute directly to particulate measurement inconsistencies, were significantly reduced.

The air-activated ball valve is employed between the filter holder and the dilution chamber to eliminate stack pressure fluctuations at the filter element, both before and after sampling. This feature was added shortly after initial testing began, as either particulate-laden filters would rupture after testing due to stack vacuum, or hot gases would escape through the probe during filter changing when testing a pressurized stack. While inclusion of any valve or flow restriction upstream of the filter represents a design compromise regarding particle deposition/re-entrainment, the relatively unencumbered flow path through the full-port ball valve compares favorably with respect to deposition/re-entrainment potential against other valve styles. The broad usage of the system guaranteed testing on stacks with both positive and negative pressure characteristics, precluding exclusion of the dilution chamber valve for all practical purposes.

Redesign of the system was extended to exhaust stack probe that supports the dilution chamber (Fig. 3). This component experiences significant levels of loading, especially during periods of stack vibration. To minimize spurious results from breakage and to reduce particle deposition, the probe was welded into a 90 deg stainless steel compression fitting, which was subsequently affixed to a stainless steel pipe extension and coupling. The probe fit concentrically inside the coupling and exterior and protruded into the stack, across approximately 90 percent of the stack diameter (Fig. 4). The secondary benefit to this design is that the threaded extension provides a dead air insulating buffer, reducing thermal gradient and deposition across the length of the probe.

Random observations of high particulate values when ini-

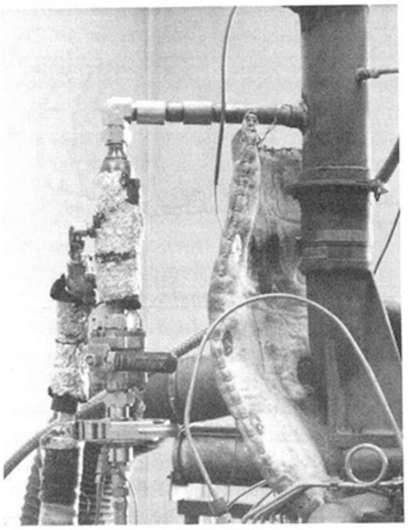

Fig. 3 Dilution chamber mounted on stack

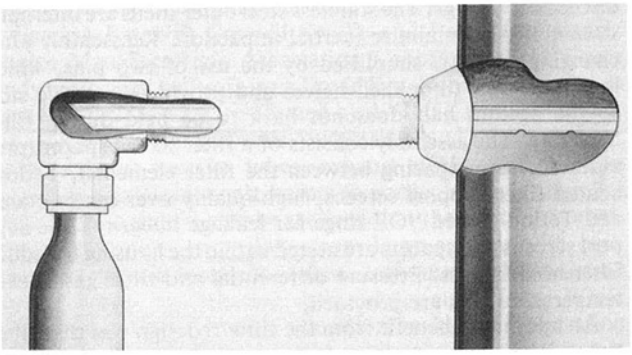

Fig. 4 Stack probe cutaway drawing

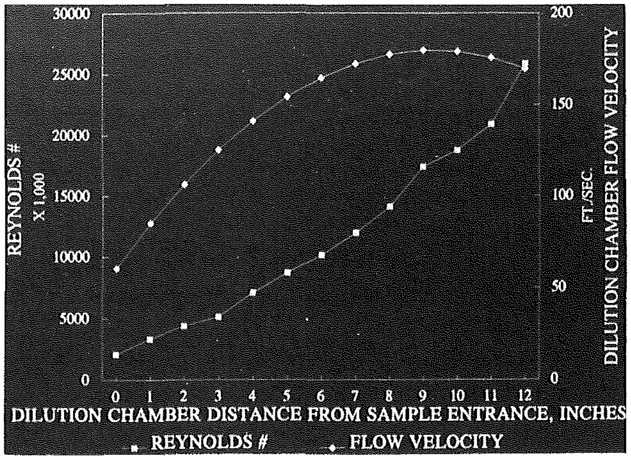

Fig. 5 Reynolds number, gas velocity versus axial position in dilution chamber

Table 1

	Precision	Bias
	Airflow = ±0.5 percent	±2.0 percent
*	Fuel flow = ±0.5 percent/25	±1.0 percent/25
**	Microbalance = ±1.0	±2.0 percent
***	Sample flow = ±1.59 percent	±0.25 percent
****	Sample flow = ±.51 percent	$B = \pm 0.25$ percent
$P =$	1.85 if dilution ratio = 10:1,	$U = \pm 4.70$ percent
$P =$	1.22 if dilution ratio = 6.0:1,	$U = \pm 4.07$ percent
*	Reflects air/fuel ratio of 25:1	
**	Based on 3.0 mg sample net weight	
***	Based on 10:1 dilution ratio	
****	Based on 6:1 dilution ratio	

tiating sampling after a period of time during which the engine has operated while the probe was in the stack prompted development of a purge cycle. During purge, a high volume of dilution air (4–6× normal sampling flow, which is approximately 90 percent of the dilution-side mass flow controller flow capacity) would be directed to the dilution probe, through the tunnel pores, and through the sample ports in the stack probe. The stack probe is cross-drilled at its far end to minimize stagnation and subsequent re-entrainment of loosened particulate. Introduction of this feature has eliminated occurrences of statistically significant (> 10 percent) first sample errors in stacks where probes have been installed during extended engine operation without sampling.

Dilution Chamber Analysis

A significant deviation in the micro-dilution system from prior art is the residence time of particulate in the dilution chamber. Figure 5 shows Reynolds number and velocity values versus axial location in the dilution chamber for a 500°C inlet exhaust condition with 20°C dilution air and assumed constant heat transfer properties. The average free-stream velocity in the dilution tunnel is 48.2 m/s (157 ft/s) at a 200 SLM flow rate, yielding a total residence time from start of dilution to trapping on the filter of 0.0382 seconds. In-house testing on full dilution facilities indicates no difference in particulate composition when residence time is reduced by a factor of 14. Research by Schindler [7] concluded that the residence time scale for particulate formation is likely below 0.1 second. The high degree of correlation between the in-house micro-dilution system and full dilution facilities with longer residence times indicates that the residence time scale is either below 0.0382 seconds or dependent on alternate parameters [8].

Refinement of the dilution system to achieve operating objectives, such as reduced sampling time, provided a suitable juncture for analysis of the dilution process. Beyond initial modifications to increase dilution air chamber volume, the dilution chamber itself received very little modification as it has achieved the objective of reducing deposition on the tunnel walls. Calculations based on the updated system flow rates (200 SLM nominal sampling rate) yield insight into the in situ characteristics of the dilution process and aid in explaining the minimal deposition of particulates observed on the micro-dilution chamber wall. If the boundary layer injection velocity created by the dilution air permeating the porous dilution tunnel wall is greater than the thermophoretic deposition velocity, then theoretically no thermophoretic deposition will occur. Appendix A presents a sample calculation [8], which describes the thermophoresis conditions at a specific point in the tunnel. Briefly, it was determined that the velocity of the air emanating from the porous tube is approximately ten times higher than the calculated thermophoretic deposition velocity at a dilution ratio of 12:1. In addition, when considering the effect of transpiration cooling, the bulk average injection parameter was calculated to be significantly above the value where the boundary layer is separated from the porous wall. In theory, therefore, the boundary layer is separated from the walls, further precluding particulate deposition.

Error Analysis

Development of an error analysis is difficult, since the potential precision error contribution from the mass flow controllers changes with the dilution ratio. Table 1 is an example of two cases, one with a dilution ratio of 6:1 and the others with 10:1 (typical values range from 4:1 to 15:1). The precision and bias errors due to fuel flow metering are based on an

****

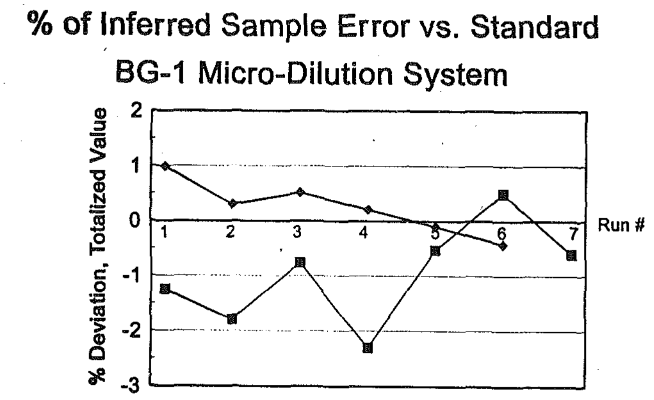

11:1 DR ■	(1.25)	(1.80)	(0.76)	(2.30)	(0.53)	0.50	(0.60)
6:1 DR ◆	0.99	0.30	0.52	0.21	(0.10)	(0.43)	

Fig. 6 Percent of inferred value versus standard meter, BG-1 commercial micro-dilution system

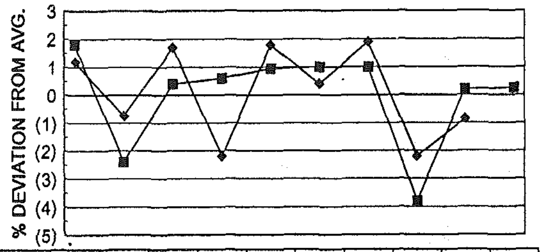

	Run 1	Run 2	Run 3	Run 4	Run 5	Run 6	Run 7	Run 8	Run 9	Run 10
On-Highway Engine ■	1.80	(2.40)	0.40	0.60	0.95	1.00	1.00	(3.80)	0.20	0.25
Off-Highway Engine ◆	1.20	(0.75)	1.70	(2.20)	1.80	0.40	1.90	(2.20)	(0.85)	

Fig. 7 Run-to-run (within-day) variability, rated speed and load, stationary and on-highway truck engines

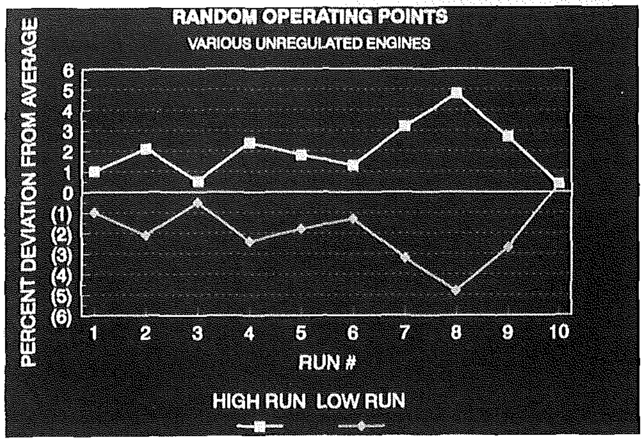

Fig. 8 Run-to-run (within-day) variability, random operating points on unregulated engines; each point run twice

average 25:1 air/fuel combustion mixture. This analysis does not consider the effects from processes such as particle deposition and re-entrainment from tunnel walls, adsorption and condensation of volatile materials, engine test setup, and physiochemical effects of varying dilution ratios and filter temperature on particulate composition.

The inferred sample flow precision uncertainty values for a 6:1 and 11:1 dilution ratio have been verified using a third flow meter (both dry gas meter and thermal flowmeter) in the sample inlet line and comparing flow meter totalized values as shown in Fig. 6. The air and fuel flow precision and bias values are as demonstrated in-house, and are offered as an example of typical lab capability.

Engine Data Variability

Both day-to-day and run-to-run repeatability characteristics are critical to the users of emissions equipment. Emissions, in conjunction with BSFC, noise, durability, and cost, determine the acceptability of a given component or system in an engine. In many cases the measured emissions output is the predominant criterion for deciding if a component will receive further scrutiny. Literally all combustion-related systems and parameters are evaluated for their emissions performance. For this reason, the observed level of variability of any emission measurement system is critical. In many noncertification instances, low test system variability, as opposed to correlation with full dilution, is preferable, especially when attempting to evaluate various engine hardware configurations.

Measured particulate output emissions variability is typically higher than that of NO_x. Stein et al. [9] evaluated various labs equipped with transient CVS capabilities and found significantly higher within-lab and among-lab standard deviation and reproducibility values for both CO and particulates than for NO_x. This is due to the complexity of the measurement and the characteristics of formation of the particulate in the combustion chamber and in the stack prior to the point of sampling [10]. Therefore, system variability must be based on results obtained on engines of various sizes, combustion control strategies and brake-specific particulate output. A breakdown of these general criteria aided in developing a dilution system test matrix, which addressed the following issues:

- Eight-mode composite, day-to-day variability
- Run-to-run variability, rated speed, and load
- Run-to-run variability, rated speed, low load

The types of engines to be tested were:

- USEPA on-highway truck (regulated)
- Large off-highway mine vehicle or stationary engine (heretofore unregulated)

Figure 7 shows typical within-day run-to-run variability levels observed on an on-highway truck and a large stationary engine run at the Caterpillar Tech Center. Both series of tests were run at the engine's rated power conditions. The "0" point indicates the average g/kW-h value (x) of the observed data; the individual points are denoted at their respective percentage deviation from the group average. Figure 8 shows typical within-day run-to-run variability on various operating points on unregulated engines at which each point was repeated only once (hence the "high" and "low" point nomenclature). Again, the "0" point is the average brake-specific particulate value for the given engine power output point (idle, intermediate, and rated speeds are all randomly included but not denoted as such). Figure 9 shows within-day run-to-run variability on an extremely low emitting (<0.10 g/BkW-h) off-highway engine at rated conditions. This is shown as an example of system measurement variability on a very high percent SOF-emitting unit (90+percent in all cases). The significance of this is that SOF is very difficult to measure repeatably when using gravimetric techniques.

Table 2 shows results of tests conducted over a one week time frame on an off-highway mining truck. All eleven modes of ISO 8178-4 [11] were run on this engine; the complete data set can be found in Appendix B. Due to the observed correlation between CO and particulate in earlier studies [9], gaseous emissions information was also taken to aid in determining the course of data variability. As can be seen, both brake-specific particulate and brake-specific CO deviated between the three runs, specifically between the first and second runs

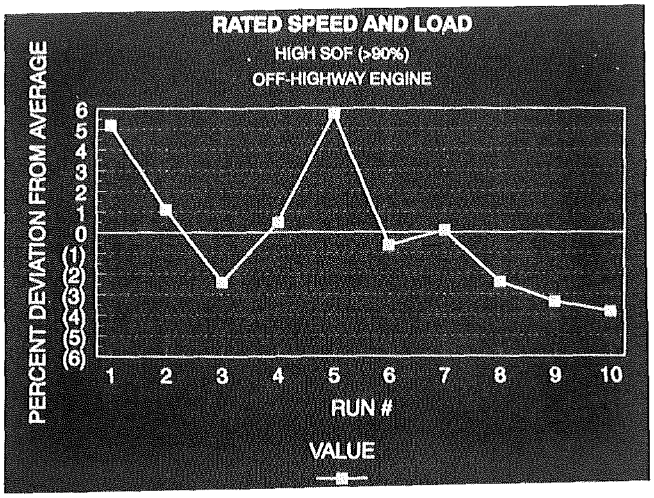

Fig. 9 Run-to-run (within-day) variability on a low emitting engine with high (90+ percent SOF, rated speed and load

Table 2 Weighted results from three eight-mode emissions tests on an off-highway mining truck engine

Run No.	CO	P_T
One	1.0220	1.0420
Two	0.9940	0.9840
Three	0.9820	0.9720

(an engine electronic control fault may have prompted this change). Regardless, the C.O.V. for the eight-mode cycle weighted results of the three tests was ±3.93 percent for particulate and ±2.17 percent for CO. In all three runs, average SOF values for the eight-mode weighted composite ranged from 52–56 percent. In Table 2, the average of the three eight-mode results is expressed as 1.00; results from each of the individual eight-mode runs are expressed in their relationship to unity (i.e., the average is expressed as 1.00; if an eight-mode composite result was 2 percent higher than average, it would be expressed as 1.02). Upon detailed data inspection, the carbon monoxide-particulates relationship holds fairly well in modes 1 through 7, where SOF values are typically 50 percent or less. It is concluded that in this case the modest deviation between expected (<3 percent) and actual (3.93 percent) COV in this series of tests is caused by actual engine operating condition changes, as characterized by measured CO output, instead of inherent particulate measurement system variability. This illustration is used here because it represents the reality of testing on heretofore unregulated engines. Observed cycle particulate variability was not appreciably different from that observed day-to-day within-lab on engines in USEPA transient test cells.

Correlation With Full Dilution

The ISO 8178 [3] correlation study was performed with two "micro-dilution" units against two full dilution tunnels on two unique engine bore size families (242 and 343 kW). Figure 10 denotes individual test point correlation; Figs. 11 and 12 show soluble organic fraction (SOF) and weighted eight-mode ISO cycle C1 correlation, respectively. The coefficient of determination value (R^2) for Fig. 10 is 0.986 and includes testing at modes having engine particulate output values of 0.7 to over 40 g/h. The ratio of micro-dilution system composite C1 test cycle results to those of the full dilution system run simultaneously on the same test cycle is 1.01, well within the ISO equivalency criteria of 0.95–1.05, per the data shown in Fig. 12.

The filter temperature between the two systems was held to within ±3°C, including at low idle. Dilution ratios varied significantly between the two systems at low idle (85°C exhaust

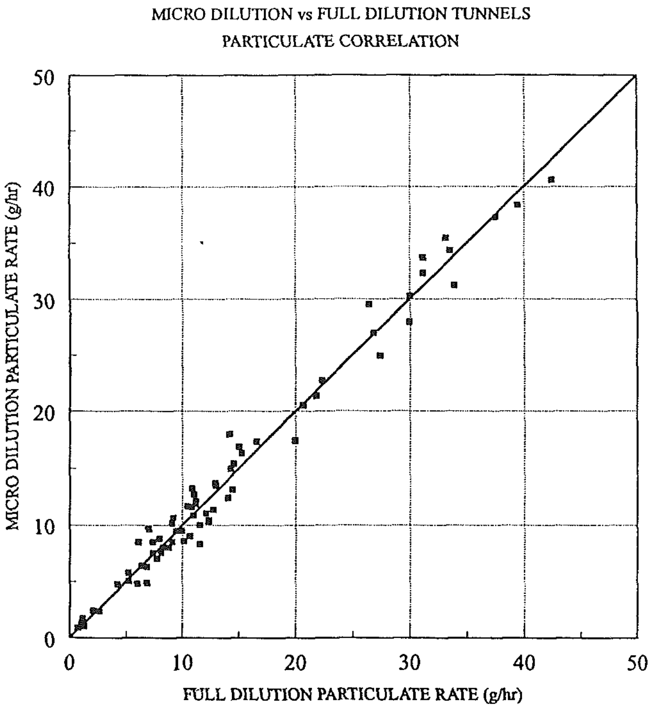

Fig. 10 Micro versus full dilution individual test point correlation

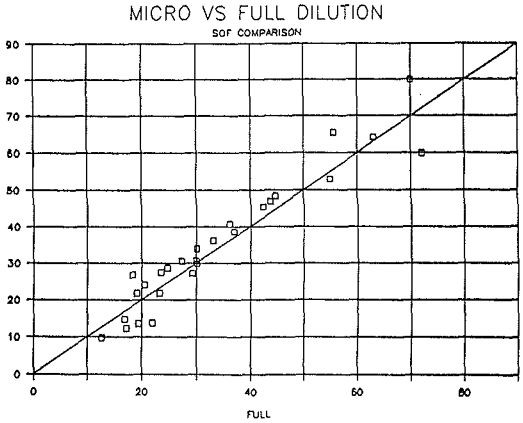

Fig. 11 Micro versus full dilution soluble organic fraction correlation

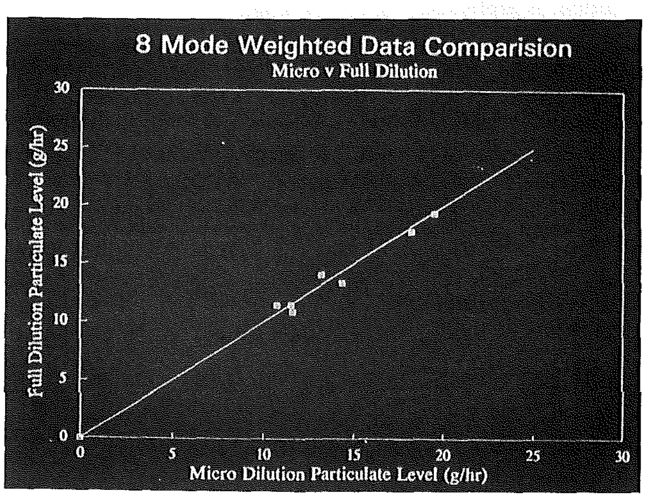

Fig. 12 Micro versus full dilution weighted eight-mode cycle correlation

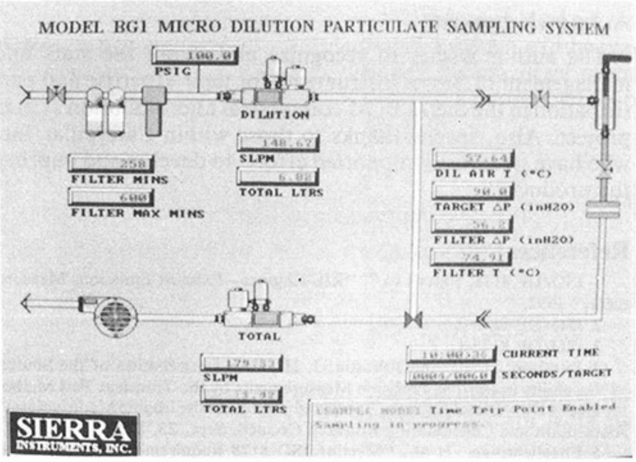

MODEL BG1 MICRO DILUTION PARTICULATE SAMPLING SYSTEM

100.0 PSIG

DILUTION

148.67 SLPM

6.88 TOTAL LTRS

258 FILTER MINS

600 FILTER MAX MINS

57.64 DIL AIR T (°C)

90.0 TARGET ΔP (inH2O)

56.2 FILTER ΔP (inH2O)

74.91 FILTER T (°C)

TOTAL

179.33 SLPM

13.92 TOTAL LTRS

10:00:36 CURRENT TIME

0004/0060 SECONDS/TARGET

[SAMPLE MODE] Time Trip Point Enabled

Sampling in progress

Fig. 13 BG-1 commercial system setup screen capture example

temperature), with the micro-dilution unit operating at a 4:1 dilution ratio and the full dilution unit operating approximately 27:1. This high dilution ratio value reflects the operational characteristics of the CVS full dilution tunnel, as opposed to representing the dilution requirement of the sample being taken. The lower dilution air temperature to the probe of the micro-dilution system explains the parity in filter temperature versus the differences in dilution ratio. The sampling location for the micro-dilution unit ranged from 2.5 to 4.0 meters from the turbocharger outlet, well past areas of the high oxidation rate characteristics, which are encountered immediately upon turbocharger exhaust exit [10]. The full dilution tunnel was fully conditioned prior to testing (the conditioning time was not factored into the total test time); the modes were performed in order as per 8178-4 [11]. The engine was allowed to stabilize exhaust, oil, and jacket water temperature values, then spend an additional five minutes at each point prior to initiation of sampling. Engine air and fuel flow values were measured using ASME nozzles and turbine flowmeters, respectively. Full dilution system sampling durations ranged from 10–20 minutes versus 2–5 minutes for the micro-dilution unit. A minimum of 2.0 mg of particulate mass was typically obtained for each sample. The micro-dilution system pressure differential increase across the filter was limited via sampling time to minimize previously observed vacuum volatilization at the high system flow rates.

Coefficient of variation (COV, repeatability) values for the partial-flow system range from ±10 percent or less at low idle to less than ±3 percent at rated power, run-to-run, depending on engine configuration and operating stability (see also Appendix B). Rated power COV values in full dilution test cells on truck engines are typically around ±1–3 percent, due to their upgraded load control systems and reduced engine brake specific oil consumption. These partial-flow system results are consistent with estimates made in the uncertainty analysis discussed earlier.

Production Intent Redesign

In-house satisfaction with the micro-dilution system, in concert with a perceived paucity of suitable commercial devices, prompted licensing of the system patent to an outside organization for redesign, commercial sales, and support. Considerable improvements were made in the areas of ease of use, robustness of construction, and flow controller flow verification. The lab-developed unit required considerable operator interaction, whereas the commercial device employs a PC for all functions. Considerable software development effort resulted in a graphics package that enhances the system ease of use (Figs. 13 and 14). Finally, the system was significantly repackaged into a more modern enclosure, which was more

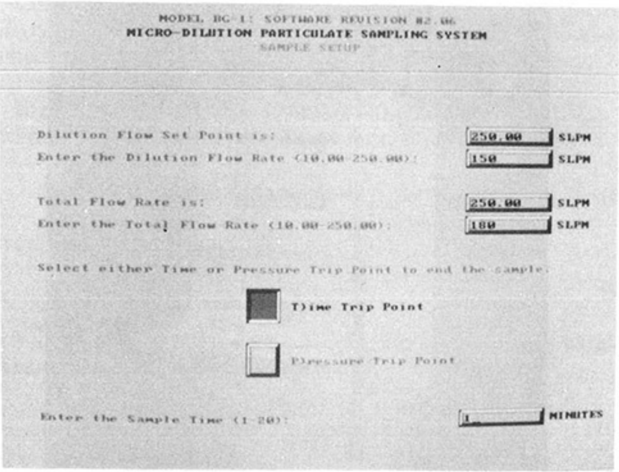

MODEL BG-1: SOFTWARE REVISION #2.06
MICRO-DILUTION PARTICULATE SAMPLING SYSTEM
SAMPLE SETUP

Dilution Flow Set Point is: 250.00 SLPM
Enter the Dilution Flow Rate (10.00-250.00): 150 SLPM

Total Flow Rate is: 250.00 SLPM
Enter the Total Flow Rate (10.00-250.00): 180 SLPM

Select either Time or Pressure Trip Point to end the sample.

■ T)ime Trip Point

☐ P)ressure Trip Point

Enter the Sample Time (1-20): 1 MINUTES

Fig. 14 BG-1 commercial system operating screen capture example

Fig. 15 Micro-dilution prototype lab version

appropriate for a PC-controlled device (see photo of old unit, Fig. 15, and redesigned commercial offering, Fig. 16). Production of the commercial offering began in early July 1993.

Conclusions

Based on the experimental results obtained from operating a porous-tube dilution chamber mounted directly to the exhaust stack via modified sampling probe hardware, the author has developed a miniaturized commercially viable sampling system for particulate emissions. An earlier version of the commercial system has been correlated against full dilution systems operated in a steady-state manner and exhibits reasonable correlation over a wide range (0–343 kW) of engine speed, power, and particulate output. The repeatability of the measurement system is also within acceptable boundaries and similar in value to the USEPA full dilution system. The system is not limited to engine or exhaust stack size and requires only compressed shop air and electrical power to operate. The primary results obtained through development of this system are as follows:

1 The dilution air and total sample flow apportionment and measurement processes are highly critical for accurate

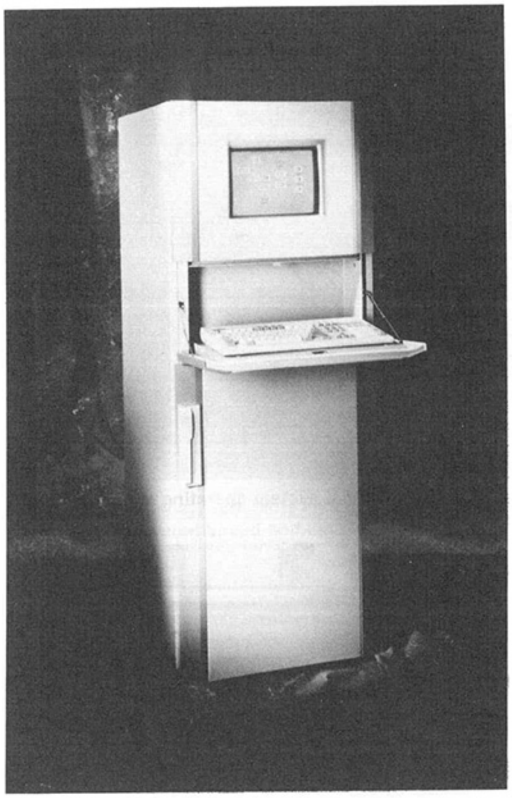

Fig. 16 BG-1 commercial system

determination of the inferred sample flow value. To accomplish this, a daily calibration check of the two flow controllers in a serially connected configuration is required and has been developed for the micro-dilution system.

2 To provide uniform, non-preferential flow through the porous dilution tube for sample dilution, the volume and configuration of the dilution air chamber are critical.

3 An erroneously high measured value for particulate observed when the stack probe has been installed for extended periods with the engine running was corrected by adding a "purge" mode to the software. This diverts a high mass flow of air through the dilution chamber pores and the sample ingress ports in the stack probe, just prior to sampling. This has eliminated spurious results caused by accumulated particulate in the probe.

4 The observed repeatability of the system on a run-to-run basis meets the ±3 percent C.O.V. goal and is typically below ±2 percent at points other than low idle. Day-to-day repeatability is also below the ±3 percent C.O.V. goal if independent emissions parameters such as CO and SOF do not vary.

5 The combination of transpiration cooling along with the comparatively high velocity of air emanating from the dilution chamber pores causes a substantial reduction in particle deposition on the tunnel walls. Based on the equivalency criteria set forth in ISO 8178-1, the ratio of the composite ISO 8178-4 C1 test cycle results of the micro-dilution system to those of the full dilution systems in-house is 1.01, based on test data taken to date. This is well within the ISO 8178-1 acceptability criteria of 0.95–1.05.

7 The system probe design minimizes spurious test results caused by probe breakage, stress, and vibration by suspending the mass of the dilution chamber from a stainless steel pipe coupling and threaded extension as opposed to through the inner probe tube that protrudes into the stack. A secondary benefit of the threaded extension is that it provides an insulating buffer to the probe.

Acknowledgments

The author wishes to recognize and thank the staff and management of Sierra Instruments for their expertise and participation in the Sierra BG-1 commercial micro-dilution system project. Also, special thanks to those within Caterpillar Inc. who have steadfastly supported efforts to develop and improve the product.

References

1 ISO/DP 8178, Parts 1 to 7, "RIC Engines—Exhaust Emissions Measurement," 1992.
2 ISO/DP 8178-2.
3 ISO/DP 8178-1.
4 Kittelson, D. B., and Johnson, J. H., "An Examination of the Sources of Variability in Particle Emission Measurements by the Transient Test Method for Heavy Duty Diesel Engines," prepared jointly for the Engine Manufacturer's Association and Coordinating Research Council, Sept. 25, 1990.
5 Engeljehringer, et al., "Meeting ISO 8178 Requirements for the Measurement of Diesel Particulates With Partial Flow Dilution Systems," SAE Paper No. 932466, 1993.
6 ISO/DP 8178-4.
7 Schindler, W., "Gravimetric Measurements of Diesel Particulates With Partial Flow Dilution Systems," IMechE Seminar on Stationary Combustion Engines and Environmental Protection Act, London, Dec. 16, 1992.
8 Graze, R. R., "Development of a Miniaturized, Dilution-Based Diesel Engine Particulate Sampling System for Gravimetric Measurement of Particulates," SAE Paper No. 931190, 1993.
9 Stein, H. J., et al., "Emissions Correlation of Heavy-Duty Transient Test Facilities," SAE Paper No. 892492, 1989.
10 Abbas, M. K., et al., "Diesel Particulate Composition Changes Along an Air Cooled Exhaust Pipe and Dilution Tunnel," SAE Paper No. 890789, 1989.
11 ISO/DP 8178-4.
12 Holman, J. P., *Heat Transfer*, 5th ed., McGraw-Hill, New York, 1981.
13 Friedlander, S. K., *Smoke, Dust, and Haze: Fundamentals of Aerosol Behavior*, Wiley, New York, 1977.
14 Kays, W. M., *Convective Heat and Mass Transfer*, McGraw-Hill, New York, 1966.

APPENDIX A

The following from Graze [8] describes the deposition scenario in the dilution tunnel at 50.8 mm past the point of sample entrance into the tunnel.

V_o = boundary layer injection velocity
V_T = thermophoretic deposition velocity
Total sample flow = 200 SLM
Dilution air flow = 185 SLM
V sample = 3.43 m/s
Stack temperature = 500°C
Diluted sample temperature = 425°C
$\rho = 0.501$ kg/m^3 (density)
Pr = 0.684 (Prandtl number)
$\eta = 3.33 \times 10^5$ kg/m s (dynamic viscosity)
$k = 0.05230$ W/m°C (thermal conductivity)
$d = 0.009525$ m (porous tube dilution tunnel ID)

$$\mathrm{Re} = \text{Reynolds number} = \frac{\rho V d}{\eta} = 4690 \tag{1}$$

(from Holman [12]).

The heat transfer coefficient for fully developed, well-mixed turbulent flow with uniform concentration and temperature in the turbulent core in a tube with cooling is:

$$\mathrm{Nu}_d = \frac{hd}{k} = 0.023\ \mathrm{Re}^{0.8}\,\mathrm{Pr}^{0.4} = 17.07 \tag{2}$$

where Nu_d = Nusselt number:

$$h = \frac{k}{d}\,\mathrm{Nu}_d = 93.72\ \mathrm{W/m^2\,°C} \tag{3}$$

This describes the heat transfer coefficient of the dilute sample after traveling 50.8 mm into the dilution tunnel. The hot gas in the dilution chamber creates a temperature gradient at the wall, forcing particles toward the relatively cold wall, i.e., thermophoresis. The heat transfer coefficient is used to estimate the temperature gradient at the wall, which will be used to calculate the thermophoretic velocity V_T for diesel particulate of 0.15 μm diameter and below with Knudsen values of between about 1 and 8, estimated by [13]:

$$V_T = -\frac{3\nu\Delta T}{4(1+\pi a/8)T} \tag{4}$$

when ν = kinematic viscosity = 66.25×10^{-6} m^2/s

T = temperature

a = thermal accommodation coefficient $\cong 1.0$

The mass fraction of particles in the mixture is assumed to be independent of radial position within the turbulent core in this case, with thermophoresis transporting the aerosol from the mixed core to the walls. Therefore,

$$\nabla T = \frac{dt}{dr}\ (\mathrm{W}) \tag{5}$$

Conservation of energy requires [14]:

$$hA(T-T_W) = -kA\frac{dt}{dr}\ (\mathrm{W}) \tag{6}$$

which yields

$$\frac{dt}{dr}\ (\mathrm{W}) = -\frac{h}{k}(T-T_W) \tag{7}$$

assuming a 425°C dilute mixture temperature (approaches "worst case" conditions), 60°C porous tube wall temperature, and a value h of 93.72 W/m^2 °C,

$$\frac{dt}{dr}\ (\mathrm{W}) = 6.54\times10^5\ \mathrm{K/m}$$

and

$$V_T = 0.0334\ \mathrm{m/s} = 0.1097\ \mathrm{ft/s}$$

This value of V_T compares with an average dilution air ingress velocity over the total area of the porous dilution section of 0.256–0.307 m/s (0.84–1.1 ft/s) at a typical range of dilution ratio values, well above the theoretical thermophoretic deposition velocity of 0.0334 m/s (0.11 ft/s). Therefore, it is believed that thermophoretic losses in the dilution chamber are negligible, when the value of V_T is superimposed against the ingress air flow velocity.

While the preceding analysis yields overall positive theoretical results regarding deposition reduction potential, a more appropriate approximation may be made when the secondary effects of transpiration cooling are considered. In transpiration cooling, the process of air or fluid permeation of a porous plate or tube carries additional energy (heat) away from the surface of the plate or tube, beyond that typically conducted into the boundary layer to the wall. In this case, the cooling medium (air) is being injected into the free stream, rather than being drawn in by suction. Injection results in a reduction of heat transfer from the free stream, whereas suction causes an increase [12].

Considering the previous scenario where the characteristics of the sample at 50.8 mm into the dilution process are evaluated, the following estimates can be made:

From Holman [12], and the previous scenario,
Injection velocity, $V_o = 1.99$ ft/s = 0.606 m/s
Free-stream velocity, $V = 32.43$ m/s.

$$\text{Injection parameter} = \frac{V_o}{V}\,\mathrm{Re} = 1.23 \tag{8}$$

From tables [12],

$$\frac{\mathrm{Nu}}{\mathrm{Re}} = 0.10 \tag{9}$$

For a "snapshot" of a zero air injection situation, we would have, from Eq. (2) $\mathrm{Nu}_d = \mathrm{Nu} = 17.07$

$$\frac{\mathrm{Nu}}{\mathrm{Re}} = \frac{17.07}{66.37} = 0.257 \tag{10}$$

The percentage reduction in heat transfer is provided by:

$$\frac{0.257-0.10}{0.257}\times100 = 61.1\ \text{percent} \tag{11}$$

At the bulk average conditions of the dilution system, the injection parameter value obtained from Eq. (8) is 1.41; the boundary layer is believed to be blown away from the plate at injection parameters of 0.619 or higher. The effects of transpiration cooling are therefore believed to reduce thermophoretic deposition further via reduced heat transfer to the walls potential while providing necessary dilution air for free-stream cooling.

APPENDIX B

	Run 1		Run 2		Run 3	
*Mode #	PT	CO	PT	CO	PT	CO
(Rated S & L) 1	1.0610	1.0440	0.9690	0.9360	0.9720	1.0200
2	1.0390	1.0290	0.9810	0.9630	0.9820	1.0070
3	1.0250	1.0400	1.0420	0.9790	0.9830	0.9790
4	0.9920	0.9700	1.0020	1.0390	1.0060	0.9910
5	1.0260	0.9920	1.0180	1.0700	0.9570	0.9450
(Peak Torque) 6	1.0750	1.0790	0.9640	0.9790	0.9640	0.9840
7	1.0200	1.0050	0.9760	0.9910	1.0040	1.0050
8	1.1020	1.0100	0.9660	1.0250	0.9370	0.9380
9**	1.0810	0.9620	0.9920	1.0210	0.9300	1.0210
10**	1.1640	0.9650	0.9840	0.9640	0.9000	1.0730
(Idle) 11**	1.1960	1.0490	0.9620	0.9660	0.8520	1.0300
*** Cycle	1.0420	1.0220	0.9840	0.9940	0.9720	0.9820

* As defined in ISO 8178-4,
** Points 9, 10, and 11 exceeded 90% SOF
*** 8-mode cycle weighted results

Exhaust Emissions From Two Intercity Passenger Locomotives

S. G. Fritz
Department of Emissions Research,
Southwest Research Institute,
San Antonio, TX 78228

To enhance the effectiveness of intercity passenger rail service in mitigating exhaust emissions in California, the California Department to Transportation (Caltrans) included limits on exhaust emissions in its intercity locomotive procurement specifications. Because there were no available exhaust emission test data on which emission reduction goals could be based, Caltrans funded a test program to acquire gaseous and particulate exhaust emissions data, along with smoke opacity data, from two state-of-the-art intercity passenger locomotives. The two passenger locomotives (an EMD F59PH and a GE DASH8-32BWH) were tested at the Association of American Railroads Chicago Technical Center. The EMD locomotive was eqiupped with a separate Detroit Diesel Corporation (DDC) 8V-149 diesel engine used to provide 480 V AC power for the trailing passenger cars. This DDC engine was also emission tested. These data were used to quantify baseline exhaust emission levels as a challenge to locomotive manufacturers to offer new locomotives with reduced emissions. Data from the two locomotive engines were recorded at standard fuel injection timing and with the fuel injection timing retarded 4 deg in an effort to reduce NO_x emissions. Results of this emissions testing were incorporated into the Caltrans locomotive procurement process by including emission performance requirements in the Caltrans intercity passenger locomotive specification, and therefore in the procurement decision. This paper contains steady-state exhaust emission test results for hydrocarbons (HC), carbon monoxide (CO), oxides of nitrogen (NO_x), and particulate matter (PM) from the two locomotives. Computed sulfur dixoide (SO_2) emissions are also given, and are based on diesel fuel consumption and sulfur content. Exhaust smoke opacity is also reported.

Introduction

The Department of Emissions Research at Southwest Research Institute (SwRI), under contract with California Department of Transportation (Caltrans)—Division of Rail, measured selected exhaust emissions from two passenger locomotives at the Association of American Railroads (AAR) Chicago Technical Center. The two locomotives, a model F59PH manufactured by the Electro Motive Division of General Motors Corporation, and a model DASH8-32BWH manufactured by the Transportation Systems Division of the General Electric Company, represent today's state-of-the-art offering in diesel-electric intercity passenger locomotives in North America.

The purpose of this work was independently to characterize the exhaust emissions from locomotives of the type most likely to be considered for purchase by the Caltrans-Division of Rail. During these tests, fuel efficiency and exhaust smoke opacity were also quantified. This information should assist Caltrans in assessing the ambient air environmental impact of its locomotive operations, and to base its locomotive procurement decisions, in part, on the exhaust emissions performance of the candidate locomotives.

Technical Approach

Test Locomotives. Two types of locomotive were tested in this program. Figure 1 shows the GO Transit-owned EMD F59PH locomotive, Unit No. 560, manufactured in Sept. 1990. Figure 2 shows the Amtrak Unit No. 514 GE DASH8-32BWH locomotive manufactured in Dec. 1991. Table 1 gives identification details on both locomotives. Both locomotives were inspected and adjusted to the manufacturer specifications by builder representatives prior to emissions testing.

These two test locomotives were configured very differently with regard to providing 480-V, 60-Hz head-end power (HEP) for trailing passenger cars. The GE locomotive provided HEP using the 12-cylinder 7FDL12J8 main engine operating at a synchronous speed of 900 rpm. With this configuration, the engine provided the required HEP load, with the remaining power available for propulsion of the locomotive. The GE locomotive produced 2770 hp (flywheel-corrected hp) at 900 rpm. It could also operate in a non-HEP mode, in which the engine speed could change, as required, with throttle notch position, as is the case with freight variants of GE and EMD

Contributed by the Internal Combustion Engine Division and presented at the 15th Annual Fall Technical Conference of the ASME Internal Combustion Engine Division, Morgantown, West Virginia, September 26-29, 1993. Manuscript received by the Internal Combustion Engine Division January 28, 1994. Associate Technical Editor: W. Cheng.

Fig. 1 EMD F59PH locomotive used for emission testing

Table 1 Test locomotive information

Manufacturer	EMD	GE
Locomotive Model	F59PH	DASH8-32BWH
Locomotive Serial Number	A4926	46850
Date of Manufacture	9-90	12-91
Owner	GO Transit	Amtrak
Unit Number	560	514

Fig. 2 GE DASH8-32BWH locomotive used for emission testing

locomotives. When operating in the non-HEP mode, the GE engine operated at 1050 rpm at throttle Notch 8 and produced 3275 hp (flywheel corrected).

The EMD F59PH locomotive had a separate generator set located in the rear of the locomotive to supply HEP needs. With this arrangement, the main EMD 12-710G3A engine operated at selected engine speeds in each throttle notch position, with all the engine power (less normal accessories) available for propulsion. At Notch 8, the EMD engine produced 3190 hp (flywheel corrected) at 904 rpm. The HEP engine, a DDC 8V-149, operated at a synchronous speed of 1800 rpm and provided up to 500 kW of HEP, as required.

Engine Power Measurement. All engine power measurements were performed by the locomotive manufacturer representatives, and the results were provided to SwRI for computing brake specific emissions. A calibrated shunt supplied by GE was used for testing both locomotives. Each locomotive used its self-load feature (used for train braking) for engine power absorption. The self-load capability on the EMD locomotive was engine power absorption. The self-load capability on the EMD locomotive was unable to absorb full rated power, so an auxiliary load bank was added for testing. Main alternator voltage and current were recorded at each test point, along with various test parameters. Main engine and accessory power, used in computing brake specific emission results, was corrected to AAR standard conditions of 60°F and 28.86 in. Hg, and was further corrected to a fuel higher heating value of 19,500 Btu/lb.

EMD locomotive test procedures were utilized for computing EMD locomotive performance data. Auxiliary generator output was assumed to be constant at all notches. The traction motor blower, cooling fans, and inertial blower power requirements were derated with the cube of the ratio of engine speed and the Notch 8 (rated) engine speed (900 rpm). Because actual power consumption of these components also is dependent on ambient air density, the power consumption of these components also is dependent on ambient air density, the power consumption was corrected to AAR standard conditions. The locomotive air compressor was always considered to be unloaded, and was directly measured, and an EMD alternator efficiency factor was applied to voltage and current measurements to compute flywheel horsepower.

The EMD locomotive was equipped with an auxiliary engine to provide HEP, which is typically 480-V AC, 60-Hz power for passenger cars. The HEP engine on the EMD locomotive was a DDC 8V-149 engine packaged with a Stamford alternator having a rated output of 500 kW. For emission testing of the HEP engine, a separate load bank was used. The load bank had the capability to load the HEP engine in 50-kW increments. Midwest Power, which worked with EMD in packaging the DDC HEP unit into the GO Transit locomotive, supplied SwRI with alternator efficiencies used to compute flywheel horsepower. The HEP engine water cooling system was independent of the main engine cooling system, and had its own electric cooling fan. This fan was fixed in the "on" position for all

Nomenclature

AAR = Association of American Railroads
ASTM = American Society for Testing and Materials
Caltrans = California Department of Transportation
CO = carbon monoxide
CO_2 = carbon dioxide
EMD = Electro-Motive Division of General Motors Corp.
EPA = Environmental Protection Agency
°F = degrees Fahrenheit
g = gram
GE = GE Transportation Systems Division
HC = hydrocarbons
HEP = head-end power
HFID = heated flame ionization detector
hp = horsepower
hr = hour
lb = pound
LHV = lower heating value
NDIR = nondispersive infraread
NO_x = oxides of nitrogen
PHS = Public Health Service
PM = particulate matter
scfm = standard cubic feet per minute
SCAQMD = South Coast Air Quality Management District
SO_2 = sulfur dioxide
SwRI = Southwest Research Institute

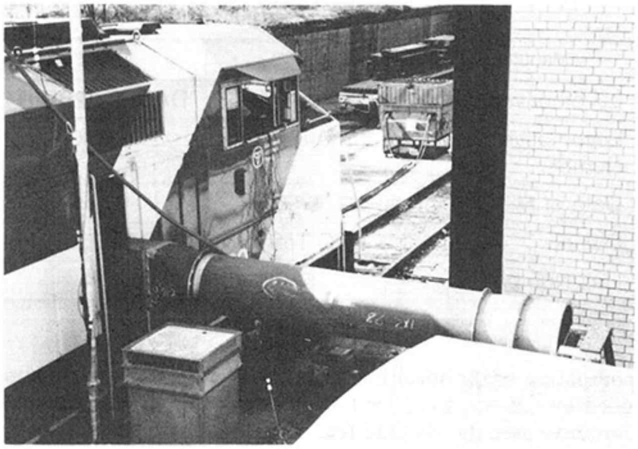

Fig. 3 Airflow meter mounted outside EMD locomotive car body

HEP engine testing to avoid erratic power measurements, which would have occurred had the fan been allowed to cycle normally.

GE locomotive test procedures were utilized for computing GE locomotive performance data. Like the EMD locomotive, auxiliary generator output was assumed to be constant at all notches. Power was corrected to AAR standard conditions. The locomotive air compressor was considered to be always unloaded. Main alternator output was directly measured, and a GE alternator efficiency factor was applied to voltage and current measurements.

Diesel Fuel Consumption Measurement. Diesel fuel consumption rates were measured on a mass basis using equipment supplied by EMD. This system was used for testing both locomotives as well as the HEP engine on the EMD locomotive. The fuel measurement system was equipped with a heat exchanger to control fuel temperature to 90 ± 10°F. The EMD main engine and the HEP DDC 8V-149 engine had a significant amount of hot return fuel to cool before returning to the fuel measurement "day" tank. This cooling assured consistent fuel supply temperatures for the engine fuel injection equipment. The engine brake specific fuel consumption given was corrected for barometric pressure, air temperature, fuel temperature, fuel specific gravity, and fuel heating value. Accessory horsepower was corrected for engine speed and ambient air density, as applicable.

Engine Airflow Measurement. Locomotive and HEP engine airflows were measured as part of the emission testing. Although engine airflow is not always necessary for computing mass emission rates of pollutants, it was used as a data integrity check by comparing measured fuel/air ratio to that computed using measured exhaust emissions data.

Locomotive engine airflow was measured using a pitot tube type airflow sensor, which had a maximum airflow measurement capacity of 12,000 scfm (at 68°F and 29.92 in. Hg). This sensor was installed on the EMD locomotive as shown in Fig. 3. The airflow meter was mounted to an air duct system, which was fabricated on site. This duct was mounted to the face of the locomotive bag-type engine intake air filter housing. This configuration allowed the engine intake air filter system to remain intact during emissions testing. The ducting entered each of the locomotive car bodies through an access door to the air filter compartment. With these doors open, the locomotive inertial air filters were not functional. The airflow meter pressure differential, along with ambient air temperature, barometric pressure, and humidity, were recorded and used to compute the engine intake air volumetric and mass flow rates.

The airflow measurement ductwork on the EMD locomotive presented a challenge in that the F59PH locomotive was equipped with a bag-type air filter housing located in a second compartment within the external car body. This design necessitated several bends in the ductwork, which resulted in additional intake air restriction inside the filter housing. Typing filter restriction at Notch 8 on the EMD locomotive is approximately 3 to 4 in. H_2O. With the airflow meter and the necessary ductwork installed, the intake air restriction measured at the air filter housing was 11 in. H_2O. This level of intake restriction was below the level at which the locomotive control system derates the engine (14 in. H_2O), but was higher than expected. The same ductwork was used for testing the GE locomotive, and the intake air restriction was also observed to be 11 in. H_2O during Notch 8 operation.

For testing the HPE engine on the EMD locomotive, a separate, smaller airflow meter was used. After the engine air flowed through the airflow meter, the air was split into two ducts, each feeding one of the two turbochargers on the DDC 8V-149 engine. Note that the intake air restriction measured at the two turbocharger inlets of the HEP engine was 6 in. H_2O at rated power.

Test Fuel. Tests on both locomotives were performed using an ASTM 2-D "Chevron Special Diesel" fuel supplied by Chevron in California. This fuel was of the type expected to be used for planned intercity service by Caltrans. A sample of the diesel fuel was analyzed by SwRI, with the results given in Table 2. The test fuel was shipped to the AAR Chicago Technical Center and stored on-site. One batch of test fuel was used for all locomotive and HEP engine testing.

Exhaust Emissions Test Procedure. No "standard" emission measurement procedures exist in the U.S. for testing locomotive engines. However, commonly accepted emission measurement practices and procedures are currently being proposed by the AAR [1]. These proposed test procedures have been developed using proven Environmental Protection Agency (EPA) procedures as a basis for steady-state measurements of gaseous [2] and particulate exhaust emissions. In addition, procedures very similar to those being developed by the International Standards Organization [3], which include procedures and weighting factors for locomotive engines, are also incorporated in the proposed AAR test procedure. For this work, the measurement procedures used conform to those under development for the AAR.

Analytical Procedures. To facilitate exhaust gas sampling while minimizing modifications to the locomotive exhaust system, a locomotive stack extension containing probes for both gaseous and particulate sampling systems was fabricated at SwRI. Figure 4 shows the particulate probe located across the stack extension. Figure 5 shows the stack extension as placed on the roof of the GE locomotive during emission testing. Note the connections for the gaseous and particulate sample lines. A separate stack extension was fabricated for testing the HEP engine on the EMD locomotive.

Gaseous emissions were sampled directly from the exhaust stack extension on the roof of the locomotive. A heated sample line was used to transfer the raw exhaust sample to the emissions instruments for analyses. Measured gaseous emissions included total hydrocarbons (THC), carbon monoxide (CO), carbon dioxide (CO_2), oxygen (O_2), and oxides of nitrogen (NO_x).

Hydrocarbon concentrations in the raw exhaust were sampled using a Beckman 402 heated flame ionization detector (HFID), calibrated on propane. Following diesel emission measurement protocols, steady-state NO_x concentration in the raw exhaust was measured using a chemiluminescence instrument with continuous sampling techniques. NO_x correction factors for engine intake air temperature, humidity, and fuel/

Table 2 Caltrans locomotive test fuel analysis

Determinations[a]	ASTM Test Method	Test Fuel Result	ASTM 2-D Spec.	EPA Type 2-D Fuel Spec.[b]
API Gravity @ 60°F	D4052	34.0		32 - 37
Viscosity @ 40°C (cSt)	D445	3.5	1.9 - 4.1	2.0 - 3.2
Sulfur (Wt%)	D2622	0.023	0.5% max.	0.08 - 0.12
Cetane Index	D976	48.8	40 min.	
Cetane Index	D4737	49.2		
Cetane Number	D613	50.4		40-48
Heat of Combustion	D240			
Gross BTU/lb BTU/gal		19,500 139,000		
Net BTU/lb BTU/gal		18,300 131,000		
Carbon-Hydrogen Ratio	D3178	1.78		
% Carbon		87.0		
% Hydrogen		13.0		
Hydrocarbon Type	D1319			
Aromatics (%)		32.1		27 (min)
Olefins (%)		4.0		
Saturates (%)		63.9		
Specific Gravity		0.855		
Distillation, Temp. in °F @ 90 recovered	D86			
	% Recovered	Temp. °F		
	IBP	329		*340 - 400*
	5	400		
	10	459		400 - 460
	20	493		
	30	509		
	40	527		
	50	542		470 - 540
	60	559		
	70	575		
	80	596		
	90	626	540 - 640	560 - 630
	95	651		
	EP	663		610 - 690

Note: *a - Locomotive diesel fuel sample taken during emission testing and analyzed at SwRI.*
b - 40 CFR §86.1313-91(b)(2) Type 2-D Diesel Fuel Specification.

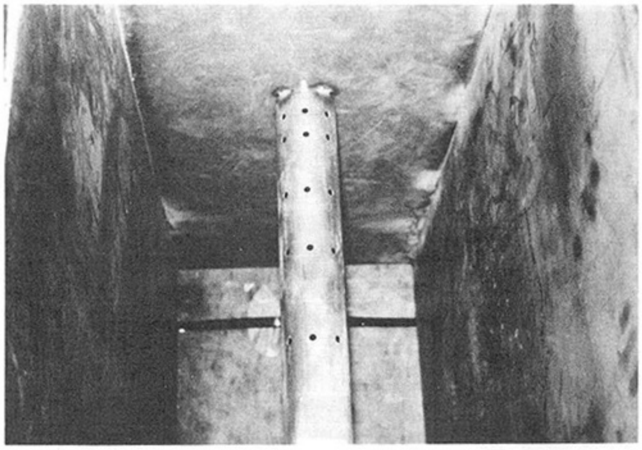

Fig. 4 Particulate sample probe located within stack extension

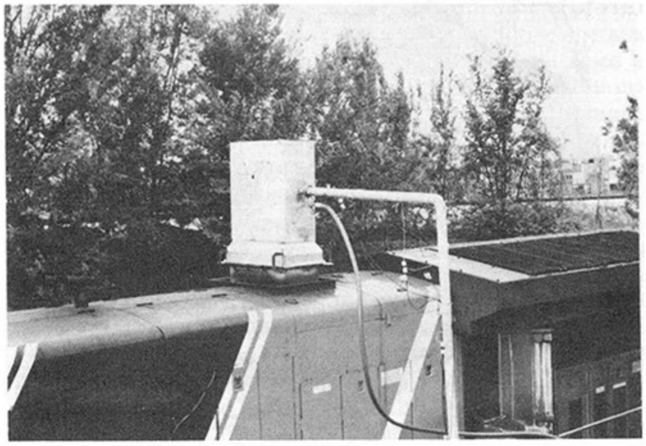

Fig. 5 Exhaust stack extension on GE locomotive

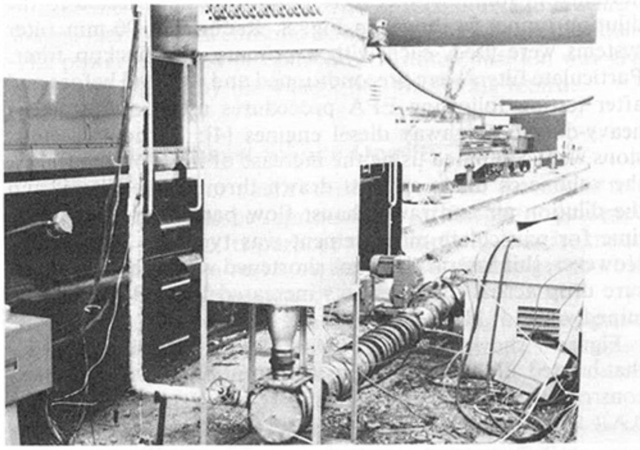

Fig. 6 Dilution tunnel located next to EMD locomotive

air ratio were applied as specified by EPA for steady-state testing of diesel-fueled engines [2]. Concentrations of CO and CO_2 in the raw exhaust were determined by nondispersive infrared (NDIR) instruments [2]. Gaseous and particulate mass emission rates were computed using the measured fuel consumption rate and performing a carbon balance on the carbon-containing constituents in the exhaust (CO_2, CO, and HC).

Particulate emissions were measured using a "split then dilute," technique, in which a portion of the raw locomotive exhaust was mixed with dilution air. For this work, an 8-in.-dia dilution tunnel was used for mixing dilution air with a portion of the raw exhaust. A portion of raw exhaust was sampled or split from the total exhaust at the stack extension and transferred through a 2-in.-stainless steel tube to the dilution tunnel located next to the locomotive, as shown in Fig. 6. The particulate transfer tube was insulated and electrically heated to 375°F. The dilute exhaust stream was sampled using probes shown in Fig. 7. Particulate was accumulated on 90-mm fluorocarbon-coated glass fiber filters. The filters were

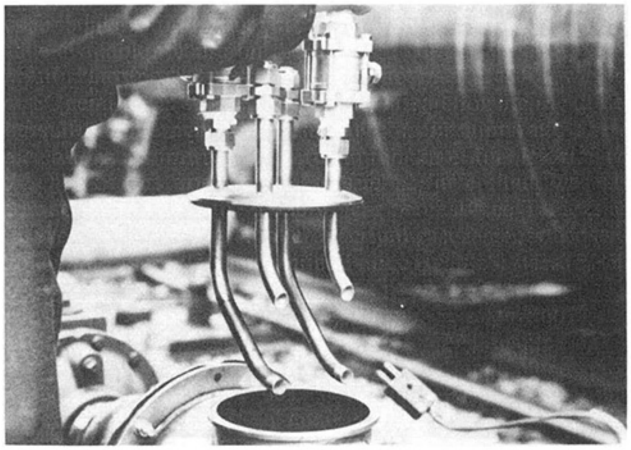
Fig. 7 Dilution tunnel particulate sample probes

Fig. 9 AAR-SwRI mobile emissions test facility

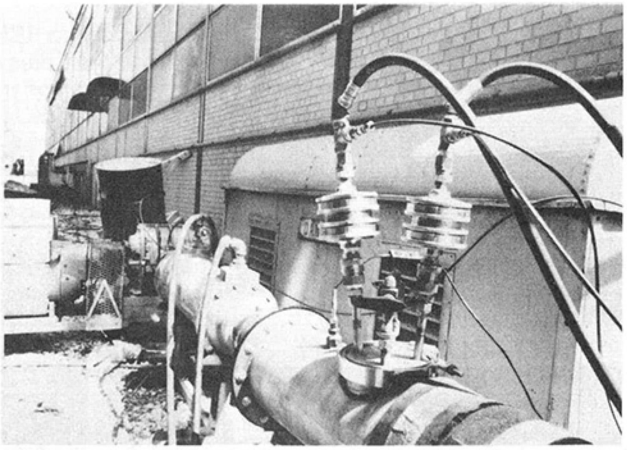
Fig. 8 90-mm particulate filter holders

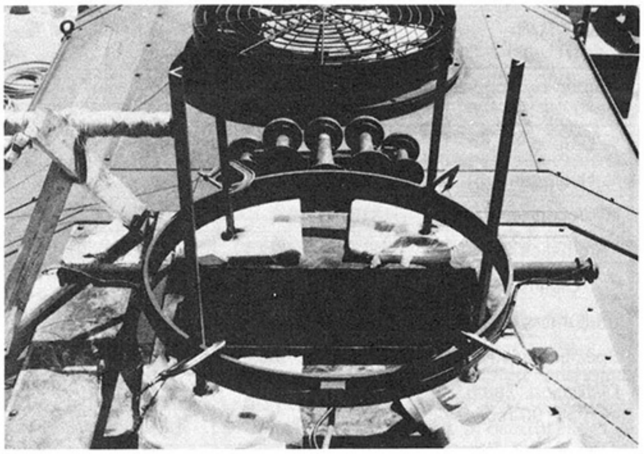
Fig. 10 SwRI smokemeter installed on the EMD locomotive

mounted in stainless steel filter holders and connected to the dilution tunnel as shown in Fig. 8. Redundant 90-mm filter systems were used, each with a primary and backup filter. Particulate filters were preconditioned and weighed before and after testing following EPA procedures used for testing of heavy-duty on-highway diesel engines [4]: Particulate emissions were computed using the increase of mass on the filters, the volume of dilute exhaust drawn through the filters, and the dilution air and raw exhaust flow parameters. Sampling time for particulate measurement was typically 30 minutes. However, this sample time was shortened when observed pressure drop across the filter sets increased beyond a predetermined value of 20 in. H_2O.

Figure 9 shows the SwRI-AAR Mobile Emissions Facility that housed all the sampling instrumentation. This facility was constructed in 1989 in a joint effort between SwRI and the AAR [5]. The facility houses the gaseous emissions measurement instrumentation, calibration gases, and the particulate dilution tunnel sample pumps and control system. This equipment is normally in use on-site at the SwRI locomotive engine research laboratories, but with approval from the AAR, it was made available for use on the project.

Sulfur dioxide (SO_2) emissions were not measured. However, the SO_2 emissions can be readily calculated knowing the diesel fuel sulfur content and the diesel fuel consumption rate. These calculations assume all the sulfur in the diesel fuel is oxidized to SO_2. For this work, the diesel fuel sulfur content was determined by SwRI to be 0.023 weight percent (see Table 2).

Locomotive exhaust smoke opacity measurements for this project were made with a modified Public Health Service (PHS) full-flow opacity meter. It used standard optics and electronics, and was modified for large plume diameters. The modification enlarged the size of the ring used to hold the light source and the detector tubes to a 40-in. diameter. Figure 10 shows the smokemeter assembly installed on the EMD locomotive. The smokemeter control unit was located in the AAR mobile trailer. Output signals were recorded on a stripchart readout. The smokemeter was aligned with the long axis of the rectangular exhaust stack for each locomotive. Through-exhaust path length for each locomotive was approximately 36 in.

Exhaust smoke opacity was recorded over the 317-second throttle notch cycle given in Table 3. The same smoke test throttle notch schedule was used for testing both locomotives. This throttle notch cycle was based on a schedule provided by EMD, but was modified to increase the time allowed between some notch changes. This modification was deemed necessary during practice smoke tests on the EMD locomotive when it became apparent that the locomotive load control system had not allowed the locomotive to reach the engine speed or power at the specified notch before the next throttle notch change was due. For preconditioning, the test engine was fully warmed at Notch 8, then the engine was stopped to calibrate the smokemeter. This procedure involved setting the zero output signal, checking the opacity at three known levels using calibrated lenses, and checking the 100-percent opacity level. The engine was restarted, and at least two consecutive smoke test sequences were performed. Smoke opacity levels were recorded during these tests using a stripchart recorder. No smoke measurements were taken on the DDC 149 HEP engine on the EMD locomotive.

Table 3 Throttle notch schedule for SwRI locomotive smoke test used for testing the EMD and GE locomotives

Throttle Notch	Elapsed Time (sec)
Idle	0
Idle → 1	12
1 → 2	24
2 → 3	36
3 → 4	48
4 → 5	60
5 → 6	72
6 → 7	84
7 → 8	96
8 → Idle	118
Idle → 4	143 -- a
4 → 8	168 -- b
8 → 6	213
6 → 8	225 -- c
8 → Idle	250
Idle → 8	262 -- d
8 → Idle	307
Idle → End of Test	317

Note: The smoke test throttle notch schedule provided by EMS was modified as shown below to allow the engine to reach the notch setting.

a–increased EMD smoke test by 15 seconds
b–increased EMD smoke test by 20 seconds
c–increased EMD smoke test by 10 seconds
d–increased EMD smoke test by 20 seconds

Test Results

Presented below is a summary of the engine performance, fuel consumption, exhaust emissions, and smoke opacity tests performed on the two locomotives. These tests were performed at both standard timing and with the fuel injection timing retarded 4 deg. Additional details are available in the final report prepared by SwRI for Caltrans [6].

EMD 12-710G3A Engine Test Results. At the conclusion of field testing, raw and dilute emissions measurement data, diesel fuel consumption rates, along with engine and alternator load parameters, were used to compute exhaust emissions. Results of emission tests are presented in Table 4 on a mass emission rate basis (g/hr) for each point. All power levels were corrected to AAR standard conditions of 60°F and 28.86 in. Hg.

The data in Table 4 have been separated into three groups. The first group gives results from tests performed with the fuel injection timing retarded 4 deg. Tests were performed at each of the eight throttle notch positions, plus high and low idle, and a dynamic brake (Notch 4) simulation, for a total of 11 test points. These same 11 test points were repeated after the fuel injection timing was returned to standard OEM settings. Finally, an AAR 3 × 3 test matrix (Notches 8, 5, and low idle repeated three times) was performed at standard timing to establish data repeatability.

The EMD locomotive load control system maintains a constant power level at each throttle notch; as a result, the power observed at each throttle notch position was generally unaffected by the 4-deg injection timing retard.

DDC 8V-149 HEP Engine Test Results. A summary of HEP electrical power output, engine flywheel brake horsepower, fuel consumption, and exhaust emissions is given in Table 5. All tests were performed at the HEP synchronous engine speed of 1800 rpm. Eight test points ranged from 0-kW output (no load) to maximum HEP output of 500 kW. Flywheel power was computed using measured alternator power output, plus 20 hp for the HEP radiator cooling fan that was operated continuously, and with alternator efficiencies provided to SwRI from Midwest Power. Note that all test data were recorded with the DDC engine fuel injection timing retarded 2 deg, the DDC-recommended configuration for NO_x reduction.

GE 7FDL12J8 Engine Test Results. A summary of GE locomotive test results is given in Table 6. Note that the test point labeled "8F" represents Notch 8 operation in the non-HEP mode (i.e., Notch 8 speed was 1050 rpm instead of HEP Notch 8 speed of 900 rpm.) When the GE locomotive operated in the HEP mode, maximum tractive power was attained at Notch 7; moving the throttle to Notch 8 provided no additional tractive power. Therefore, when operating in the HEP mode, the data for Notch 8 were equal to that for Notch 7. The "stand-by" mode was run at 720 rpm, and HEP was provided from the auxiliary alternator.

The data in Table 6 are separated into three groups. The first group gives results from tests performed with the fuel injection timing retarded 4 deg. For the GE locomotive, tests were performed at Notch 8 in the non-HEP mode (i.e., 1050 rpm), at each of the eight throttle notch positions during HEP operation (900 rpm), in the "stand-by" mode (720 rpm), plus high and low idle, for a total of 12 test points. These 12 test points were repeated after the fuel injection timing was returned to standard original equipment manufacturer timing. One AAR 3 × 3 test matrix (Notches 8, 5, and low idle, repeated three times) was performed at standard timing during HEP mode operation to establish data repeatability.

Like the EMD locomotive, the GE locomotive load control system maintained a constant power level at each throttle notch. The power observed at each throttle notch position was generally unaffected by the 4-deg injection timing retard.

Locomotive Exhaust Smoke Opacity Tests

The duty-cycle (or notch schedule) used for the smoke tests was not intended to be representative of freight or passenger locomotive service. Its purpose was simply to exercise the locomotive through a series of throttle notch changes to characterize the smoke opacity.

There is no standardized method for rating smoke opacity on locomotive engines. However, several criteria were assigned by SwRI to quantify the locomotive smoke opacity test results from this work. These criteria include:

- *Maximum Opacity*: Figure 11 shows a typical smoke trace recorded for the GE locomotive. The horizontal axis represents the 317-second test duration, and the vertical axis represents the recorded smoke opacity from a low of zero to a maximum of 100-percent opacity. Note the throttle notch events.
- *Peak Width at 1/2 Maximum Opacity:* The duration of the maximum opacity was considered important. It gives an indication of whether the peak opacity occurred only momentarily, or if it was sustained for several seconds and likely unacceptable to public perception.
- *Opacity-Seconds*: In addition to peak opacity, the amount of time the smoke was above some threshold limit was also noted. The threshold of visibility for truck-sized engines is

Table 4 EMD 12-710 G3A engine performance, fuel consumption, and exhaust emissions summary

Notch	Engine Speed (rpm)	BHP^a	Fuel Rate (lb/hr)	BSFC (lb/hp-hr)	HC (g/hr)	CO (g/hr)	NO$_x$ (g/hr)	Part. (g/hr)	SO$_2$^{b} (g/hr)
4° Retarded Timing Test Date = 5-8-92									
8	903	3,190	1,080	0.337	802	2,773	25,234	781	225
7	821	2,520	840	0.333	615	1,199	21,513	538	175
6	726	1,680	572	0.340	442	569	14,583	395	119
5	649	1,380	476	0.345	369	528	11,641	331	99
4	566	1,050	359	0.344	291	279	9,807	263	75
3	491	708	244	0.345	260	201	8,052	208	51
2	339	366	138	0.377	152	224	4,526	78	29
1	339	209	88	0.420	127	172	2,405	45	18
High Idle	339	14	34	NA	131	118	993	40	7
Low Idle	201	10	19	NA	62	59	700	14	4
DB-4^c	566	28	70	NA	239	218	1,292	102	15
Standard Injection Timing Test Date = 5-12-92									
8	903	3,210	1,060	0.331	895	3,663	38,808	670	222
7	821	2,540	833	0.328	557	1869	25,452	440	174
6	726	1,700	572	0.337	384	663	17,390	291	119
5	647	1,390	480	0.345	359	614	14,851	261	100
4	563	1,060	368	0.348	289	277	12,751	190	77
3	489	714	254	0.356	232	192	10,675	135	53
2	337	370	142	0.382	148	208	5,987	54	30
1	337	207	91	0.441	114	153	3,475	30	19
High Idle	339	14	32	NA	93	78	1,147	24	7
Low Idle	201	10	14	NA	35	36	596	8	3
DB-4^c	566	28	79	NA	239	217	2,243	88	17
Standard Timing Repeat Tests Test Date = 5-13-92									
8	903	3,190	1,050	0.329	689	2,556	32,857	664	219
8	903	3,210	1,050	0.327	620	2,697	32,241	620	219
8	903	3,190	1,050	0.329	636	2,698	34,526	632	219
5	649	1,380	474	0.343	310	431	18,067	259	99
5	649	1,390	472	0.339	273	428	17,515	257	98
5	649	1,390	460	0.331	297	430	18,398	273	96
Low Idle	339	10	20	NA	40	47	785	9	4
Low Idle	339	10	20	NA	46	51	716	10	4
Low Idle	339	10	19	NA	44	49	822	9	4

Notes: a–Flywheel BHP provided by EMD and corrected to AAR standard conditions.
b–SO$_2$ computed using diesel fuel sulfur content of 0.023 weight percent.
c–DB-4 represents dynamic brake throttle notch 4 operation.

Table 5 DDC 8V-149 engine performance, fuel consumption, and exhaust emissions summary

Test #	Flywheel BHP^a	Fuel Rate (lb/hr)	BSFC^b (lb/hp-hr)	Alternator Output (kW)	HC (g/hr)	CO (g/hr)	NO$_x$ (g/hr)	Part. (g/hr)	SO$_2$^{c} (g/hr)
1	699	275	0.393	503	315	3,312	7,610	168	57
2	566	226	0.399	407	353	493	7,730	---^{d}	47
3	438	179	0.409	300	305	242	5,800	117	37
4	377	157	0.418	255	275	179	4,690	113	33
5	305	135	0.443	203	255	178	3,800	104	28
6	238	114	0.478	154	258	181	2,930	91	24
7	173	95	0.546	105	248	188	2,170	80	20
8	31	55	1.782	0	274	207	1,000	74	12

Notes: a–Flywheel BHP computed using measured alternator power output, 20 continuous cooling fan horsepower, and alternator efficiencies provided to SwRI by Midwest Power.
b–BSFC based on flywheel horsepower.
c–SO$_2$ computed using diesel fuel sulfur content of 0.023 weight percent.
d–Test # 2, 400-kW particulate data void.

Table 6 GE 7FDL engine performance, fuel consumption, and exhaust emissions summary

Notch	Engine Speed (rpm)	BHP[a]	Fuel Rate[a] (lb/hr)	BSFC[a] (lb/hp-hr)	HC (g/hr)	CO (g/hr)	NO_x (g/hr)	Part. (g/hr)	SO_2[b]
4° Retarded Timing Test Date = 5-18-92									
8-Freight[c]	1,050	3,250	1,119	0.344	1,960	2,170	30,400	514	230
8=7 - HEP[d]	900	2,775	933	0.336	1,140	4,490	29,900	583	194
6 - HEP	900	2,257	769	0.341	1,140	4,420	23,400	---[e]	159
5 - HEP	900	1,773	613	0.346	743	4,340	19,100	513	127
4 - HEP	900	1,021	368	0.360	574	1,440	12,900	375	77
3 - HEP	900	712	267	0.375	427	962	8,380	323	56
2 - HEP	900	431	180	0.418	406	767	5,270	310	36
1 - HEP	900	324	147	0.454	341	762	4,970	344	30
HEP Idle	900	190	82	0.432	543	867	2,440	381	17
Stand-By	720	508	187	0.368	299	638	5,690	297	39
High Idle	450	34	22	NA	148	270	847	56	5
Low Idle	370	22	16	NA	125	235	522	52	4
Standard Injection Timing Test Date = 5-19-92									
8 - Freight[c]	1,050	3,268	1,103	0.338	1,750	2,690	36,700	434	230
8=7 - HEP[d]	900	2,771	929	0.335	1,350	5,690	32,400	487	194
6 - HEP	900	2,254	762	0.338	1,190	5,190	28,300	419	159
5 - HEP	900	1,777	609	0.343	743	4,540	23,200	291	127
4 - HEP	900	1,023	369	0.361	546	1,470	15,200	232	77
3 - HEP	900	713	266	0.373	425	1,060	10,200	220	56
2 - HEP	900	431	174	0.404	398	713	6,520	246	36
1 - HEP	900	322	144	0.447	415	715	5,740	295	30
HEP Idle	900	185	81	0.438	495	903	2,850	413	17
Stand-By	720	512	189	0.369	369	858	7,080	297	39
High Idle	450	34	23	NA	181	223	878	57	5
Low Idle	370	22	17	NA	160	319	517	47	4
Standard Timing Repeat Tests Test Date = 5-20-92									
8 - HEP	900	2,789	934	0.335	1,580	6,740	32,600	592	195
8 - HEP	900	2,764	931	0.337	1,460	6,670	30,700	560	194
8 - HEP	900	2,762	931	0.337	1,480	7,740	31,200	550	194
5 - HEP	900	1,777	609	0.343	732	4,360	21,500	382	127
5 - HEP	900	1,765	610	0.346	753	5,180	22,000	313	127
5 - HEP	900	1,764	611	0.346	738	5,430	21,500	300	128
HEP Idle	900	185	81	0.438	517	958	3,110	353	17
HEP Idle	900	186	82	0.441	514	965	3,070	336	17
HEP Idle	900	185	82	0.443	456	870	2,840	274	17

Notes: a–Corrected BHP and fuel rates supplied to SwRI by GE and is corrected to AAR standard conditions.
b–SO_2 computed using diesel fuel sulfur content of 0.023 weight percent.
c–8-Freight represents throttle Notch 8 in non-HEP operating mode (i.e. 1050 rpm).
d–Notch 8 power equals Notch 7 power in HEP mode.
e–Notch 6-HEP particulate data from 5-18-92.

typically 5-percent opacity. Thirty to forty percent opacity roughly corresponds to a Ringelmann 2 smoke level, which is the limit for stationary sources in California. Ringelmann 1, or roughly 10- to 20-percent opacity, is the limit for stationary sources in the South Coast Air Quality Management District (SCAQMD). Assuming 20-percent opacity as an important threshold criterion, the amount of time combined with the level of smoke opacity above these levels during the smoke tests is an additional criterion for evaluating smoke.

- *Time Over Threshold Level*: Although opacity-seconds gives an indication of the extent of the smoke opacity at or above some threshold level, it is the amount of time exhaust smoke opacity exceeds a given threshold level that was of most concern. The current smoke regulation, as enforced by the SCAQMD, allows a Ringelmann 1 smoke for no more than three cumulative minutes in one hour (i.e., 5 percent of the time). If one assumes that Ringelmann 1 is roughly equal to 20-percent opacity, and the locomotive is operated repeatedly over the operating cycle given in Table 3, then the GE locomotive smoke trace shown in Fig. 11 indicates that the locomotive exceeded the SCAQMD smoke standards approximately 12 percent of the time. Note that this result was extremely duty-cycle sensitive.
- *Cycle Average Opacity*: Average smoke opacity observed over the 317-second smoke test can be used to assess the locomotive exhaust smoke characteristics. The area under the smoke trace was integrated to yield smoke cycle opacity-seconds. This value was divided by the smoke test duration of 317 seconds to yield the cycle average opacity.

Table 7 summarizes the results of locomotive smoke opacity tests based on the SwRI criteria. Peak width was important due to its indication of whether the peak opacity occurred only momentarily, or if it was sustained for several seconds, and therefore less acceptable to the public. In addition to the peak opacity, the amount of time the smoke was above some threshold limit was relevant.

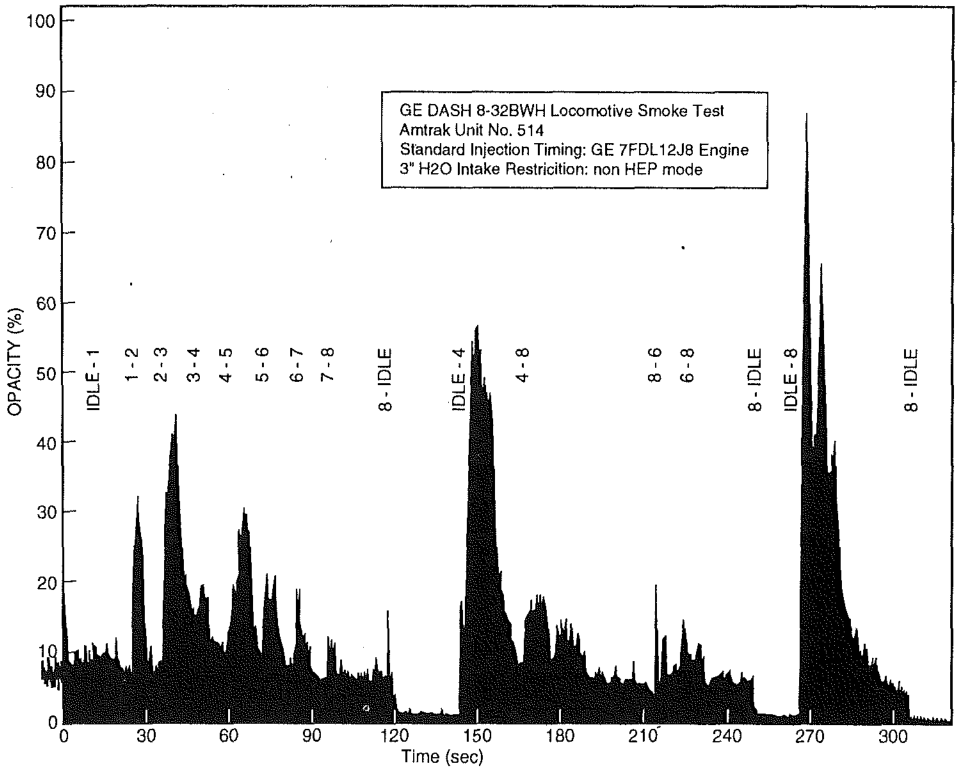

Fig. 11 Typical smoke trace from GE locomotive during smoke test

Table 7 Summary of locomotive smoke opacity tests

Smoke Opacity Criteria for 317-Second SwRI Smoke Test	EMD F59PH		GE DASH8-32BWH[a]	
	Std. Timing	4° Retard	Std. Timing	4° Retard
Peak Opacity, % Opacity	15	20	69	83
Peak Width at 1/2 Peak, seconds	2	20	13	3
Cycle Time 20% Opacity, %	0	0	17	20
Cycle Average Opacity, % Opacity	3.3	5.5	11.8	13.6

Notes: a–GE data recorded during non-HEP operation (i.e., Notch 8=1050 rpm.

Summary—Weighted Composite Results

This paper contains steady-state exhaust emission test results for hydrocarbons (HC), carbon monoxide (CO), oxides of nitrogen (NO_x), and particulate matter (PM) from the two intercity passenger locomotives. Computed sulfur dioxide (SO_2) emissions are also given, and are based on diesel fuel consumption and sulfur content. Table 8 summarizes the composite AAR three-mode duty-cycle weighted emission test results of the prime movers for each locomotive at standard fuel injection timing, and with a 4-deg timing retard.

Note that a comprehensive analysis of fuel economy and exhaust emission characteristics of a specific passenger train would require the data included in this paper, along with specific locomotive duty-cycle and HEP load information.

Table 8 AAR three-mode composite exhaust emissions of the prime movers for each locomotive

AAR 3-Mode Duty-Cycle[a,b] Weighted Emissions (g/hp-hr)	EMD 12-710G3A		GE 7FDL12J8	
	Std. Timing	4° Retard	Std. Timing	4° Retard
Hydrocarbons (HC)	0.3	0.3	0.6	0.6
Carbon Monoxide (CO)	0.9	0.6	1.5	1.4
Oxides of Nitrogen (NO_x)	11.6	8.4	12.0	10.0
Particulate (PM)	0.20	0.25	0.16	0.21
Sulfur Dioxide (SO_2)[c]	0.070[c]	0.072[c]	0.071[c]	0.072[c]
Brake Specific Fuel Consumption Penalty[d]	---	2.4%	---	1.8%

Notes:

a–AAR 3-Mode duty-cycle: Rated power = 25%, 50% power = 25%, Idle = 50%.

b–GE data based on non-HEP mode operation (i.e., Notch 8=1050 rpm).

c–SO2 values computed using 0.023 weight percent Sulfur diesel fuel.

d–corrected to AAR standard conditions (60°F Air, 60°F Fuel, 28.86 in. Hg Barometer, fuel HHV = 19,350 BTU/lb and S.G. = 0.845.

e–EMD standard timing test date = 5/12/92; 4° retarded timing test date = 5/8/92.

f–GE standard timing test date = 5/19/92; 4° retarded timing test date = 5/18/92.

Acknowledgments

This project was funded by the California Department of Transportation. Caltrans technical representatives were Messrs. Steve Longhofer and Steve Fretwell of the Caltrans Division of Rail, and Mr. George Smith of the Caltrans Division of New Technology, Materials, and Research. Key SwRI technical personnel were Messrs. Eddie Grinstead, Research Technologist, and Steve Tenay, Laboratory Assistant in the Department of Emissions Research. In addition to the SwRI project team, many others made significant contributions to the success of the project. Mr. Richard Remillard of Booz • Allen & Hamilton, Inc., performed much of the logistical work in cultivating the project. At the AAR, Messrs. Dave Bowman, Brad Anderson, and Randy Jackson coordinated AAR facilities support. Messrs. Dave Brann, Stan Knight, Brian Lundin, and Ms. Martha Lenz from EMD provided support in the test work on the EMD-built locomotive. Messrs. Ted Stewart, Ron Till, and David Branyon were the GE technical representatives and assisted in testing the GE-built locomotive. Mr. Terry Millar of Midwest Power Detroit-Diesel supported DDC 8V-149 HEP engine testing on the EMD locomotive. Mr. Allen Keller of Amtrak supervised testing of the Amtrak-owned DASH8 locomotive and provided valuable insight into the details of HEP-equipped locomotive operations. GO Transit in Toronto supplied the EMD locomotive for emission testing.

References

1 "Locomotive Exhaust Gaseous and Particulate Emission Test Procedures," draft procedure developed by SwRI for the Association of American Railroads, 1989.

2 Code of Federal Regulations, Title 40, Part 86, Subpart D—Emission Regulations for New Gasoline-Fueled and Diesel Heavy-Duty Engines: Gaseous Exhaust Test Procedure, 1994.

3 ISO/DP 8178-1 RIC Engines—Exhaust Emission Measurement—Part 1: Test Bed Measurement of Gaseous and Particulate Exhaust Emissions From RIC Engines, draft procedure, last updated Jan. 1992.

4 Code of Federal Regulations, Title 40, Part 86, Subpart N-Emission Regulations for New Otto-Cycle and Diesel Heavy-Duty Engines; Gaseous and Particulate Exhaust Test Procedure, July 1, 1991.

5 Fritz, S. G., et al., "Diesel Fuel Specification and Locomotive Improvement Program: Tenth Research Phase Final Report," SwRI Report No. 03-2695, AAR Report No. R-771, Dec. 1989.

6 Fritz, S. G., "Exhaust Emissions From Two Intercity Passenger Locomotives," SwRI Final Report No. 08-4976 for the California Department of Transportation—Division of Rail, Nov. 1992.

Effect of Ring Dynamics and Crevice Flows on Unburned Hydrocarbon Emissions

L. K. Shih

D. N. Assanis

Department of Mechanical and
Industrial Engineering,
University of Illinois,
Urbana-Champaign,
Urbana, IL 61801

A significant source of unburned hydrocarbon emissions from internal combustion engines originates from the flow of unburned fuel/air mixture into and out of crevices in the piston-cylinder-ring assembly. During compression, fuel vapor flows into crevice regions. After top dead center, the trapped fuel vapor that returns into the cylinder escapes complete oxidation and contributes to unburned hydrocarbon emissions. In this work, the crevice flow model developed by Namazian and Heywood is implemented into KIVA-II, a multidimensional, reacting flow code. Two-dimensional, axisymmetric simulations are then performed for a 2.5 liter gasoline engine to investigate the effects of engine speed and selected piston-ring design parameters on crevice flows and on unburned hydrocarbon emissions. Results suggest that engine-out unburned hydrocarbon emissions can be reduced by optimizing the ring end gap area and the piston-cylinder side clearance.

Introduction

An important source of unburned hydrocarbon (HC) emissions from internal combustion engines originates from flows into piston-cylinder-ring crevices. Unburned HC-air mixtures are forced to enter the piston-cylinder-ring crevices during the compression stroke when cylinder pressures exceed crevice-region pressures. Most of the trapped mass in crevice regions eventually returns to the chamber late in the expansion stroke, when conditions prevent complete oxidation of the returned HC vapor and contribute to unburned HC emissions. A portion of the mass trapped in crevices does not return to the chamber, but appears in the crankcase as blowby. Since blowby gas is commonly recirculated into the intake manifold and cylinder, where it can be oxidized in subsequent cycles, blowby does not contribute to unburned HC emissions.

Namazian and Heywood (1982) developed an isothermal compressible flow model to predict flow into and out of the crevice regions between the piston, rings, and cylinder wall. Two types of flow in and out of crevices were identified, a laminar channel flow through the ring side clearance, and a jet flow through the top ring end gap. Their flow model was coupled with a ring motion model so that the amount of unburned HC trapped in the crevices and the amount of charge lost to the crankcase as blowby could be predicted. It was shown that crevice gases constitute a major source of unburned HC emissions, as well as a significant loss in power and efficiency. Although their work predicted flow velocities out of the crevice regions, it could not predict oxidation of the returned unburned HC vapor in the cylinder.

Kuo et al. (1989) modified the crevice-flow model, originally developed by Namazian and Heywood (1982), to run interactively with a hydrodynamic ring-lubrication model (Furuhama, 1959–1961; Dowson et al., 1979; Ruddy et al., 1979; Rohde et al., 1979). Thus, the lubricating oil film thickness on the cylinder liner and the friction force acting on the rings were predicted more realistically. Predictions of blowby differed from measurements by 50 percent, at worst. Measured trends were correctly replicated with variations in both speed and IMEP. Nevertheless, spatial resolution of the in-cylinder HC vapor concentration and gas temperature was still lacking. This resulted in unrealistic modeling of oxidation of the unburned HC mass that returned into the cylinder from the crevices.

Reitz and Kuo (1989) used the KIVA code in conjunction with the Kuo et al. (1989) crevice flow model to predict crevice flow and oxidation of HC vapor returned into the cylinder. Using this code, they studied the effect of intake volumetric efficiency, overall equivalence ratio, spark timing, and engine speed on cylinder pressure and unburned HC in the cylinder. The computed peak cylinder pressure was 6 to 8 percent lower with than without modeling crevice flows. Engine-out unburned HC increased with increasing engine load, decreasing engine speed, decreasing mixture strength, and increasing top-land crevice clearance. However, in their study, other ring design parameters, which could strongly affect ring dynamics, crevice flows, and unburned HC emissions, were not considered.

In this study, an approach similar to that of Reitz and Kuo will be followed to investigate the effects of engine speed, ring end gap area, and piston-cylinder side clearance on crevice flow and unburned HC emissions using KIVA-II, an improved version of the KIVA code. Ring dynamics and crevice flows through ring-side clearances and ring end gaps will be modeled

---

Contributed by the Internal Combustion Engine Division and presented at the 15th Annual Fall Technical Conference of the ASME Internal Combustion Engine Division, Morgantown, West Virginia, September 26–29, 1993. Manuscript received by the Internal Combustion Engine Division January 28, 1994. Associate Technical Editor: W. Cheng.

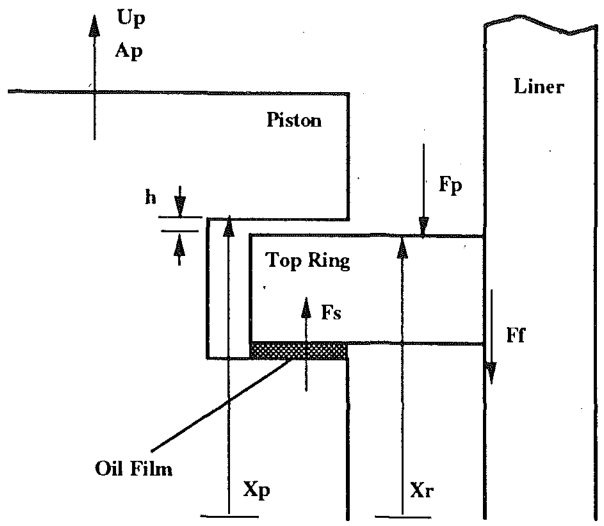

Fig. 1 Conceptual diagram of forces acting on the ring

as proposed by Namazian and Heywood (1982). Crevice flow solutions obtained from the PCRCF code (Piston-Cylinder-Ring Crevice Flow) developed by Namouchi (1989) will be used as boundary conditions in the KIVA-II program. This approach takes advantage of the multidimensional KIVA-II code to predict the distribution of the unburned HC vapor concentration in cylinder, and the localized turbulent flow interactions with the returning crevice backflows; therefore, subsequent oxidation of unburned HC vapor late in the cycle can be accurately predicted as a function of ring design and operating conditions.

Model Description

Crevice flows are modeled by a set of coupled ordinary differential equations, which describes the piston-ring dynamics and the flow motions through the ring-side clearances and through the ring gaps. The solution of these equations is then iterated for several engine cycles in order to ensure convergence of the ring positions at the beginning and at the end of an engine cycle. These flow motion solutions are then used as boundary conditions in the KIVA-II code. A summary of the ring dynamics and crevice flow submodels, and the simulation procedures, follows.

Ring Motion Model. Figure 1 shows the forces that act on each compression ring in the axial direction. Radial forces, ring tilt, and twist inside the groove are ignored. A squeezed oil film prevents the ring from coming in perfect contact with the upper or lower groove surfaces. Thus, the axial ring motion is essentially controlled by the balance of the following three forces: (1) pressure force, (2) frictional force, and (3) resistance of the squeezed oil film. The equation governing the ring dynamics is

$$m_r \frac{d^2x_r}{dt^2} = F_s - F_p - F_f \tag{1}$$

Since $x_r = x_p - h$, Eq. (1) can be rewritten as

$$m_r \frac{d^2h}{dt^2} = F_p + F_f - F_s + m_r A_p \tag{2}$$

where x_r and x_p are the instantaneous displacements of the ring and piston, respectively, measured with respect to an inertial reference frame, h is the instantaneous position of the ring's upper surface with respect to the groove ceiling, m_r is the ring's mass; F_p is the force caused by the pressure difference between the upper and lower surfaces of the ring; F_f is the frictional force between the ring and the cylinder wall; F_s is the oil-resistance force created when the moving ring in the groove squeezes the lubricant in the groove; and A_p is the acceleration of the piston. Note that both kinematic variables and forces are taken as positive in the upward direction. Expressions for the various force terms have been given by Namazian and Heywood (1982), Namouchi (1989), Kuo et al. (1989), and Reitz (1989).

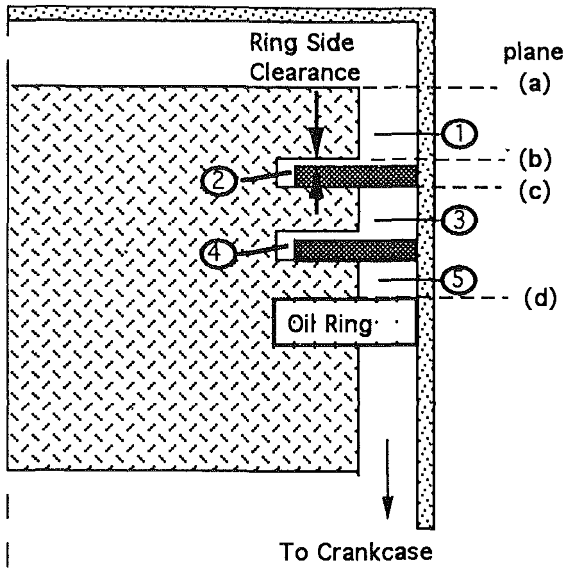

Fig. 2 Conceptual diagram of piston-ring-cylinder assembly, defining crevice regions 1 to 5, and planes *A* to *D*

Crevice Flow Model. Figure 2 shows the assembly of an engine piston, two compression rings, and one oil ring. If the top ring is sitting on the bottom surface of its groove, gas will be transported between Regions 1 and 2 through the top surface of this ring (like a channel flow), while Regions 2 and 3 will only be connected through the ring gap (which allows a jetlike flow). On the contrary, if the top ring is sitting on the upper surface of its groove, then gas transportation between Regions 1 and 2 is conducted through the jetlike flow, while gas transportation between Regions 2 and 3 is conducted through a channel flow. The same principles also apply to Regions 3, 4, and 5 around the second ring. Both the top and second rings can shift to the top or bottom surfaces of their grooves several times in one cycle. During ring transition in a groove, mass is transported between any two neighboring crevice regions through channel flow.

The crevice flow through the ring-side clearance is treated as compressible, laminar, and isothermal (Namazian and Heywood, 1982; Namouchi, 1989) at a temperature that is the average of the piston, cylinder, and ring temperatures. The crevice flow through the ring end gap is treated as orifice jet flow. It is assumed that there is no circumferential flow along the ring-side clearance, the top land crevice region, and the region between the top and second rings. Since the flow passage significantly affects the mass flow rate, it is assumed that there is no leakage between the peripheral face of the ring and the cylinder bore. In other words, there is "perfect sealing" at the ring-cylinder interface. The piston is assumed always centered in the bore so that the crevice clearance is axisymmetric (Amann, 1988). The temperatures of the piston, cylinder, and rings are assumed to be steady throughout the cycle. It is further assumed that there is no deposit formation inside the crevice regions, because deposits reduce the effective crevice volume.

The pressure in the top-land crevice (Region 1) is equal to the pressure in the combustion chamber, while the pressure below the second compression ring (Region 5) is equal to the pressure in the crankcase (Namazian and Heywood, 1982).

Since the size of the crevice region is small, it is assumed that the in and/or out crevice flow will mix with the original charge in the crevice instantaneously so that each crevice region has uniform pressure and chemical composition at each crank angle. However, the pressure and chemical composition in each crevice region varies with crank angle due to the varying pressure and chemical composition in the cylinder.

The following continuity equations are solved for the new pressures in crevice Regions 2, 3, and 4 when mass is transferred into and/or out of these regions (Namazian and Heywood, 1982; Amann, 1988; Kuo et al., 1989):

$$\frac{m_{02}}{p_{02}}\frac{dp_2}{dt}=\dot{m}_{12}-\dot{m}_{23}$$

$$\frac{m_{03}}{p_{03}}\frac{dp_3}{dt}=\dot{m}_{13}+\dot{m}_{23}-\dot{m}_{34}-\dot{m}_{35}$$

$$\frac{m_{04}}{p_{04}}\frac{dp_4}{dt}=\dot{m}_{34}-\dot{m}_{45} \tag{3}$$

where p_i is the pressure in Region i as shown in Fig. 2, p_{0i} is the initial pressure in Region i, m_{0i} is the initial mass stored in Region i under initial pressure, and $\dot{m}_{ij}$ is the mass flow rate from Region i to Region j through either the ring-side clearance or the ring gap.

The mass flow rates across Plates A, B, C, and D, defined in Fig. 2, can be calculated as follows:

$$\dot{m}_a=\frac{m_{01}}{p_{01}}\frac{dp_1}{dt}+\dot{m}_b$$

$$\dot{m}_b=\dot{m}_{13}+\dot{m}_{12}$$

$$\dot{m}_c=\dot{m}_{13}+\dot{m}_{23}$$

$$\dot{m}_d=\dot{m}_{35}+\dot{m}_{45} \tag{4}$$

Simulation Procedure. In order to solve the crevice flow equations, cylinder pressure data are required throughout the cycle. Since KIVA-II can only simulate the closed part of the cycle, measured cylinder pressure data have been provided to the crevice flow program PCRCF (Piston-Cylinder-Ring Crevice Flow) to predict ring dynamics and flows into and out of piston-cylinder-ring crevices (Namouchi, 1989). PCRCF requires estimates of the initial interring pressures and ring positions at the start of the cycle. Equations (1) and (2) are then solved simultaneously using the Runge-Kutta integration method at each crank angle. The piston ring's acceleration/deceleration rate is integrated twice with respect to time to obtain new instantaneous ring positions, and thus flow passages within the ring grooves. With this information, the mass flow rate between two adjacent crevice regions is calculated based on either orifice jet flow or channel flow. Updated mass flow rates are then substituted into Eq. (2) to calculate the updated interring pressures, which are used in subsequent calculations. Upon the completion of an engine cycle simulation, the updated values of interring pressures and ring positions are compared with the original values. This process is iterated until convergence is reached. Converged flow solutions past plane A (see Fig. 2) are then used as boundary conditions in the KIVA-II program.

Results and Discussion

Engine Geometry and Operating Conditions. To illustrate the behavior of the crevice backflow model, a spark-ignition engine was simulated. Specifications of the engine geometry and operating conditions are listed in Tables 1 and 2, respectively. The specifications of the piston-cylinder-ring geometry are summarized in Table 3. Two-dimensional axisymmetric runs were performed in this study for computational expediency. The number of cells in the axial direction of the KIVA-II combustion chamber was set to 22 at the start of the calculation, and was allowed to decrease to a minimum of 5 close to top dead center. The number of cells in the radial direction was set to 16.

Table 1 Gasoline engine specifications

Engine Displacement	2.5	L
Compression Ratio	8.77	
Cylinder Bore	8.75	cm
Stroke	16.40	cm
Connecting Rod Length	15.08	cm
Displaced Volume	624.09	cm^3
Clearance Volume	80.30	cm^3
Piston Bowl Volume	16.88	cm^3
Squish Height	1.035	cm

Table 2 Baseline operating conditions

Engine Speed	2000	rpm
Fuel Type	n-octane	C_8H_{18}
Total Fuel Mass	0.043	g
Ignition Timing	15 deg.	BTDC
Intake Gas Temperature	324	K
Equivalence Ratio	0.989	

Table 3 Piston-cylinder-ring specifications

Ring Groove Height	1.55	mm
Ring Width	3.86	mm
Ring Thickness	1.448	mm
Ring Mass	10.57	g
Ring End Gap Area	0.151	mm^2
Top Land Crevice Height	6.071	mm
Piston-Cylinder Clearance	0.248	mm

Ring Dynamics. The resultant of the pressure and friction forces drives the axial motion of the ring within the groove. In contrast, the squeezed oil film force opposes the action of the axial driving force; it acts as a damping force to prevent perfect contact of the ring with the groove surface. The inertia force, equal to the product of the ring mass times the piston acceleration (see Eq. (2)) also plays an important role in determining the displacement of the ring with respect to the groove ceiling (i.e., in a moving frame of reference). In agreement with previous studies (Namazian and Heywood, 1982; Kuo et al., 1989), the friction force and the squeezed oil force were found to be substantially smaller in magnitude compared to the pressure force and the inertia force. Thus, ring dynamics (which are illustrated in Fig. 3 for the baseline operating conditions) will be explained in terms of the behavior of the inertia and pressure forces throughout the cycle.

Figure 3(*a*) shows the history of the inertia force acting on the top ring. Due to the reciprocating nature of the piston motion, the inertia force switches direction a total of four times during the engine cycle. Early in the intake stroke the piston-ring assembly experiences acceleration. This is followed by deceleration, which reaches its maximum value at approximately 240 CA deg BTDC, and reduces the inertia force. Since the pressure force is very small during intake (see Fig. 3*b*), the inertia force dominates the ring motion during that period. The variation in the inertia force causes the top ring to drop from the groove ceiling to the groove bottom right after the instant of maximum deceleration.

The pressure force, shown in Fig. 3(*b*), is determined by the pressure difference across the ring. During the compression and expansion strokes, the pressure force is much larger than

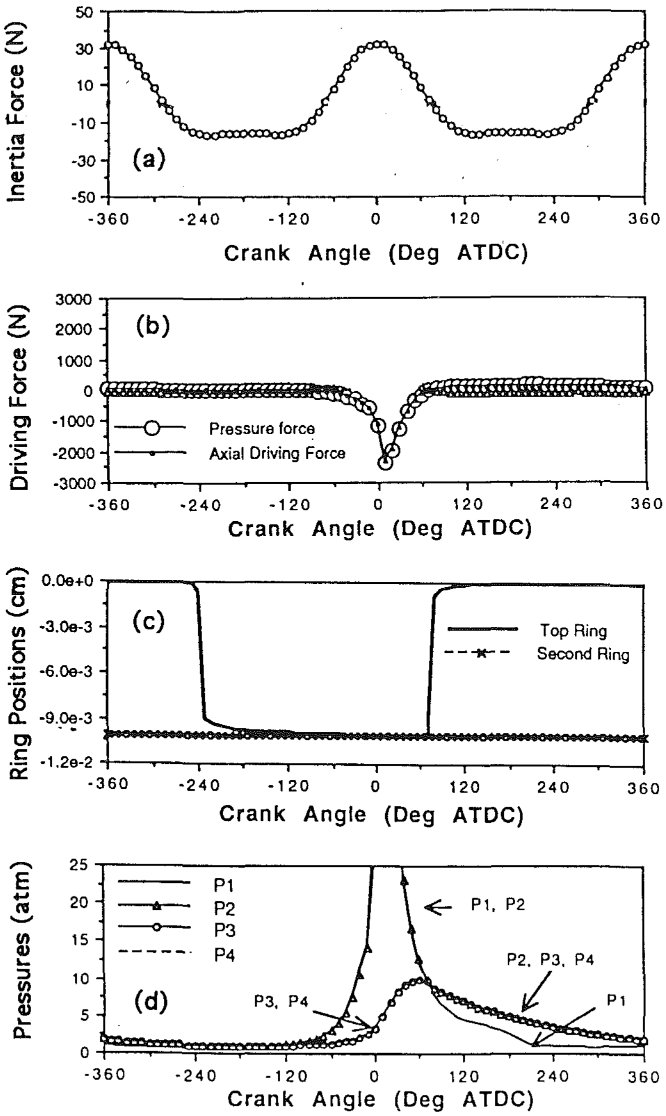

Fig. 3 Ring dynamics at baseline conditions: (*a*) inertia force on top ring, (*b*) pressure and axial driving forces on top ring, (*c*) top and second ring positions, (*d*) measured cylinder pressure P_1 compared with pressure P_2 behind first ring, interring pressure P_3, and pressure P_4 behind second ring

the other forces. After TDC, the pressure force reverses its direction, thus causing the upward ring motion. Therefore, after a certain time delay (the oil in the groove must be squeezed and moved out before the ring can move upward) the ring moves upward again toward the groove ceiling at 70 crank angle deg ATDC during the expansion stroke. Note that, for the assumed geometry and conditions, the second ring sits on the groove bottom throughout the complete engine cycle.

The pressures in the crevice regions are directly affected by the ring positions since the latter control the passages through which cylinder charge can flow. Figure 3(*d*) shows the history of pressures in Regions 1, 2, 3, and 4. During compression and early expansion, the top ring is sitting on the groove bottom. Regions 1 and 2 are then connected through the channel between the groove ceiling and the ring upper surface, and their pressures are the same. However, Regions 1 and 3 are connected through the relatively narrow top ring end gap area; thus, pressure in Region 1 is much higher than pressure in Region 3 during this period (and thus the top ring remains sitting on the bottom of the groove). However, after 70 crank angle deg ATDC, the pressure in Region 1 (equal to cylinder pressure) becomes smaller than the pressure in Region 3 due

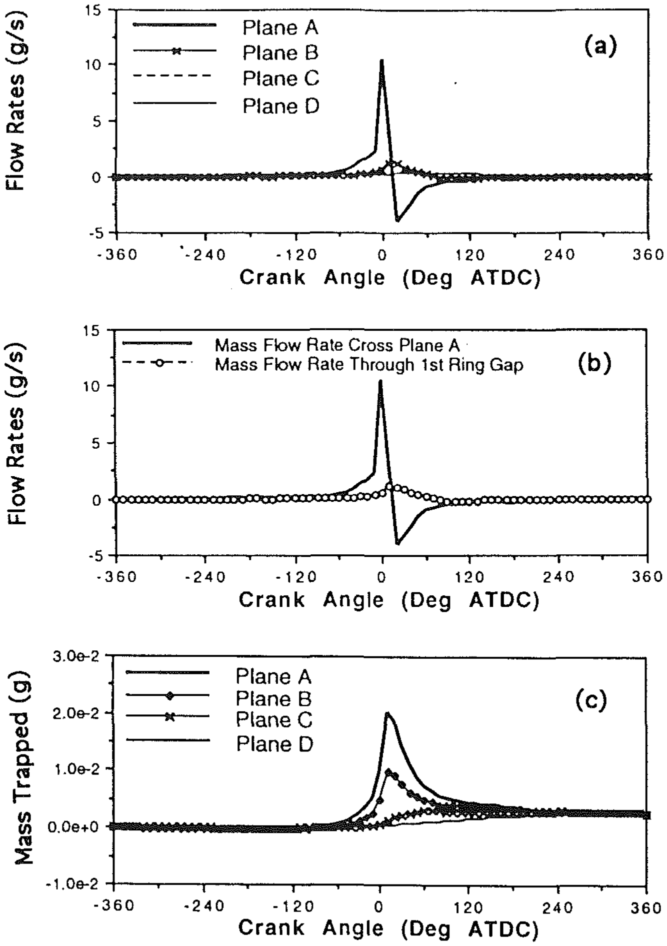

Fig. 4 Crevice flows at baseline conditions: (*a*) mass flow rates through planes *A*, *B*, *C*, *D*, (*b*) mass flow rate through plane *A* versus flow rate through top ring end gap, (*c*) cylinder charge stored below planes *A*, *B*, *C*, and *D*

to expansion. This pressure difference causes the top ring to move toward the groove ceiling as shown in Fig. 3(*c*). After this point, the pressure in Region 3 remains higher than the pressure in Region 1. Since Regions 3 and 1 are connected through the relatively narrow top ring end gap area, a fast pressure release in Region 3 is restricted. When the ring touches the groove ceiling, pressures in Regions 2 and 3 are equalized because they are then connected through the channel between the groove bottom and the ring lower surface.

Crevice Flow Motion. Figure 4(*a*) shows the history of mass flow rates across Planes *A* to *D* as defined in Fig. 2. The peak mass flow rate across Plane *A* occurs at the time when combustion starts, which suggests that the sudden rise of cylinder pressure will result in vigorous gas flow into the crevices. The direction of this crevice flow is reversed at 10 crank angle deg ATDC when this trapped gas starts to be discharged from the crevices into the cylinder.

Figure 4(*b*) compares mass flow rates across Plane *A* and through the top ring end gap under baseline conditions. Only a small portion of the trapped cylinder charge flows through the top ring end gap because of its restricted areas. Most of the cylinder charge trapped in crevices flows through the piston-cylinder side clearance (Region 1 in Fig. 1b). Since Region 1 is freely connected to the main cylinder chamber, the timing when the crevice flow through the piston-cylinder side clearance reverses its direction (from flowing into crevices to flowing out of crevices) is when combustion is completed and cylinder pressure starts to drop due to expansion.

Table 4 Effects of ring design parameters on crevice flows and unburned HC emissions

Engine Speed (rpm)	Ring End Gap Area (mm^2)	Piston-cylinder clearance (mm)	Peak pressure (atm)	Max Trapped Mass (%)	Blowby @ 360 ATC (%)	HC Mass Returned (g)	HC mass @ 180 ATC (g)	Return HC Oxidation (%)
Effect of Engine Speed								
2000	0.151	0.248	54.2	2.93	0.58	0.94e-3	1.56e-4	83
4000	0.151	0.248	58.1	3.23	0.48	1.05e-3	0.85e-4	92
Effect of Ring End Gap Area								
2000	**0.050**	0.248	54.5	2.65	0.24	0.96e-3	1.48e-4	85
2000	**0.453**	0.248	53.9	3.63	1.67	0.90e-3	1.18e-4	87
Effect of Piston-Cylinder Side Clearance								
2000	**0.050**	**0.083**	56.5	0.97	0.25	0.26e-3	0.59e-4	77
2000	**0.453**	**0.743**	47.9	8.75	1.63	2.99e-3	0.30e-4	99

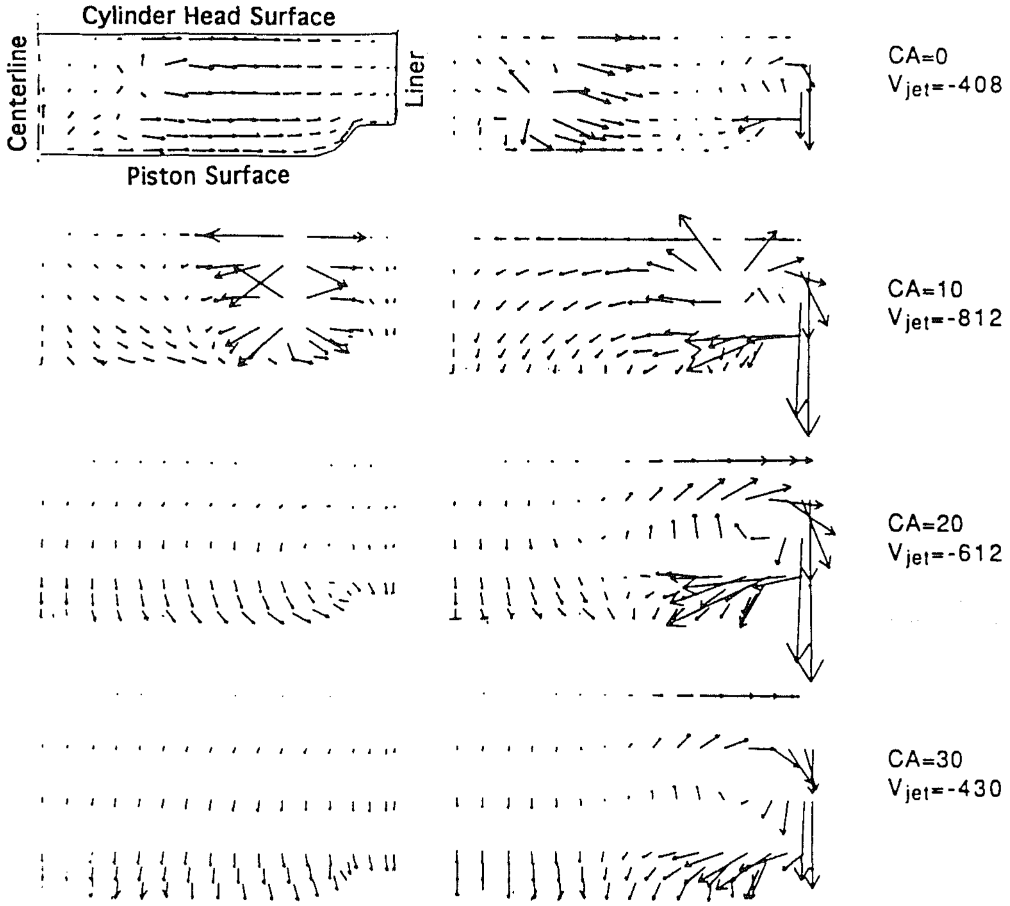

Fig. 5 In-cylinder flow velocity distribution with (right) and without (left) crevice flow model

Figure 4(*c*) shows the history of mass trapped in crevices below Planes *A* to *D*. The maximum fraction of the total cylinder charge trapped in crevices below Plane *A* is about 2.93 percent as shown in Table 4. Only 1.4 percent of the total cylinder charge is trapped below Plane *B*. This is because the top land crevice region has the largest volume among the five crevice regions that can store the trapped mass. Moreover, the top land crevice is the only region freely connected to the main chamber. All other regions are restricted by small passages, so that cylinder charge cannot easily flow into regions below Plane *B*. About 0.58 percent of the cylinder charge is eventually lost to the crankcase as blowby, as shown in Table 4.

Figure 5 compares the in-cylinder flow velocity distribution with and without activating the crevice flow model. The left-hand column shows results from the unmodified KIVA-II code, while the right-hand column shows results from the modified KIVA-II code with the crevice flow model activated. The jet flow into the crevice region is clearly evident. Further, the flow pattern in the right-hand side of Fig. 5 indicates the development of a clockwise vortex in the cylinder due to crevice flow motion. This result is most clearly seen at about 30 crank angle deg ATDC. This clockwise vortex will carry the returned HC vapor from the crevices into the center of cylinder later during the expansion stroke (see Fig. 6).

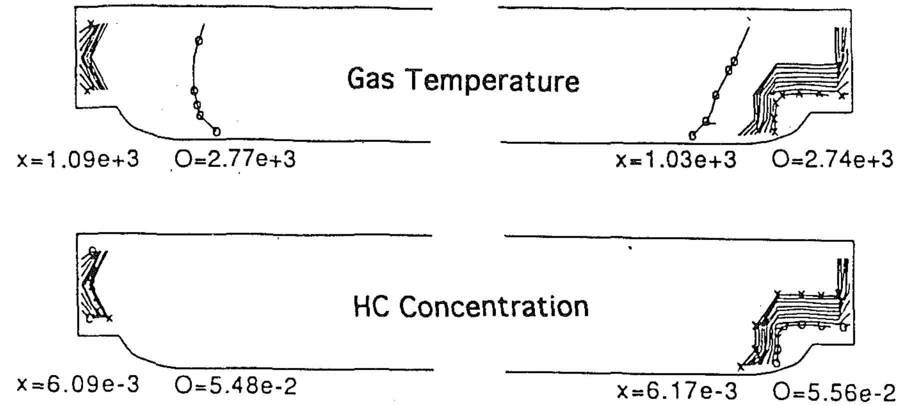

Fig. 6 Gas temperature and HC species distributions late in expansion with (right) and without (left) activating the crevice flow model

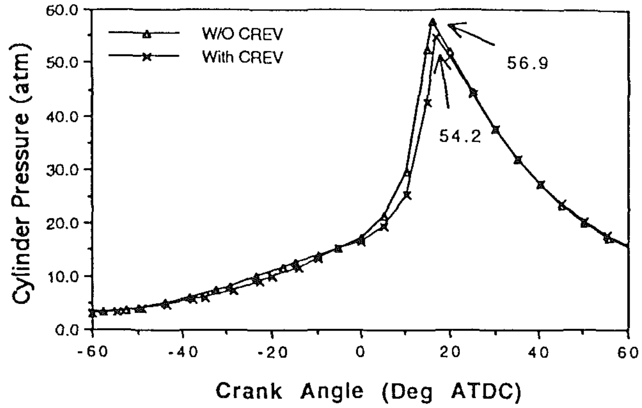

Fig. 7 Comparison of predicted cylinder pressures under baseline conditions, with and without activating the crevice flow model

Reitz and Kuo (1989) found the computed peak cylinder was 6 to 8 percent lower with crevice flow than without. Figure 7 compares the history of the cylinder pressure predicted by the original and the modified KIVA-II code under baseline conditions. When the crevice backflow model is activated, the peak cylinder pressure is reduced from 56.9 atm to 54.2 atm (5 percent reduction). This is because the apparent mass in the cylinder is reduced by approximately 3 percent near TDC, as shown in Table 4, due to the trapped cylinder charge in crevices. Thus, it is essential to include the crevice backflow submodel in KIVA-II for more realistic predictions of trapped cylinder mass and pressure.

Parametric Studies. This section examines the effects of engine speed, ring end gap area, and piston-cylinder side clearance on crevice flow processes and on unburned HC emissions. Results from all parametric studies are summarized in Table 4, and discussed in detail below.

Effect of Engine Speed. For baseline operating conditions, ignition delay and combustion duration are 3.6 and 29.4 crank angle deg, respectively. When the engine speed is increased from 2000 rpm to 4000 rpm, the spark timing is advanced from 15 (baseline) to 19 crank angle deg BTDC in order to achieve the maximum brake torque in each case. Despite the higher turbulence levels associated with higher engine speeds, chemical reaction rates require a finite real time. Thus, ignition delay is increased from 3.6 (baseline) to 4.5 crank angle deg with increasing speed. Further, the completion of combustion is delayed by 5 crank angle deg compared to the baseline case, i.e., the combustion duration is 37.5 crank angle deg at 4000 rpm.

Figures 8(*a*), 8(*b*), and 8(*c*) show the effects of engine speed on the axial driving force acting on the top ring, the history of the top ring position in the groove, and the pressure ($P3$) between the top and second rings. As mentioned earlier, the inertia force moves the top ring from groove ceiling to groove bottom when the piston-cylinder-ring assembly starts to decelerate during the intake stroke. At 4000 rpm, this top ring's downward movement starts earlier (260 CA deg BTDC) than at 2000 rpm (235 CA deg BTDC) due to the higher deceleration rate (higher inertia force). This is shown in Figs. 8(*a*) and 8(*b*).

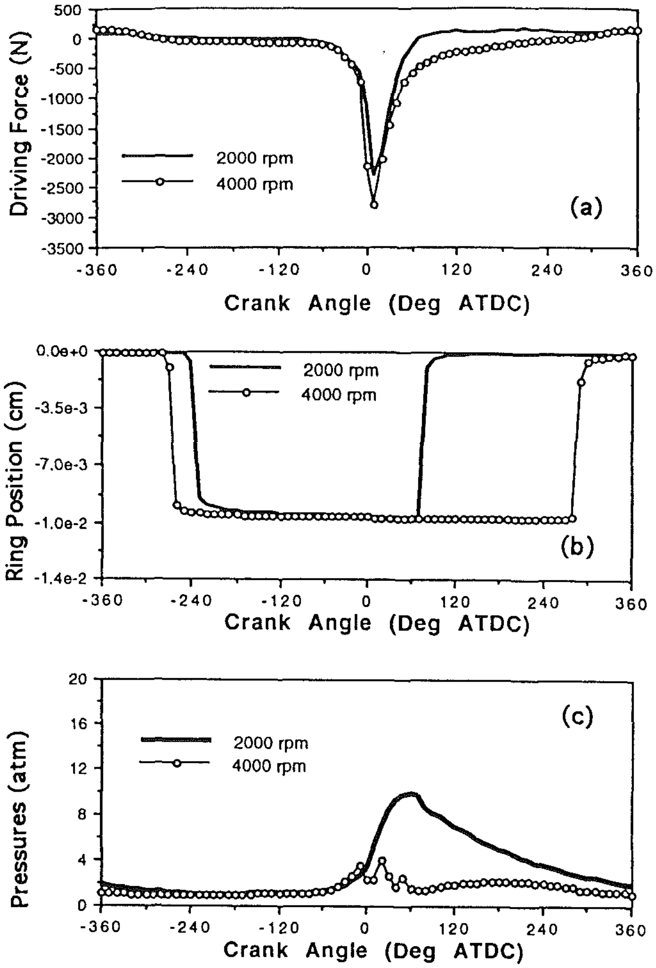

Fig. 8 Effect of engine speed on (*a*) axial driving force acting on top ring, (*b*) top ring's position, (*c*) interring cylinder pressure

In the 2000 rpm case, the top ring moves upward during expansion, when the pressure $P3$ between ring 1 and ring 2 becomes larger than the cylinder pressure. However, when the engine speed is brought up to 4000 rpm, the cylinder charge

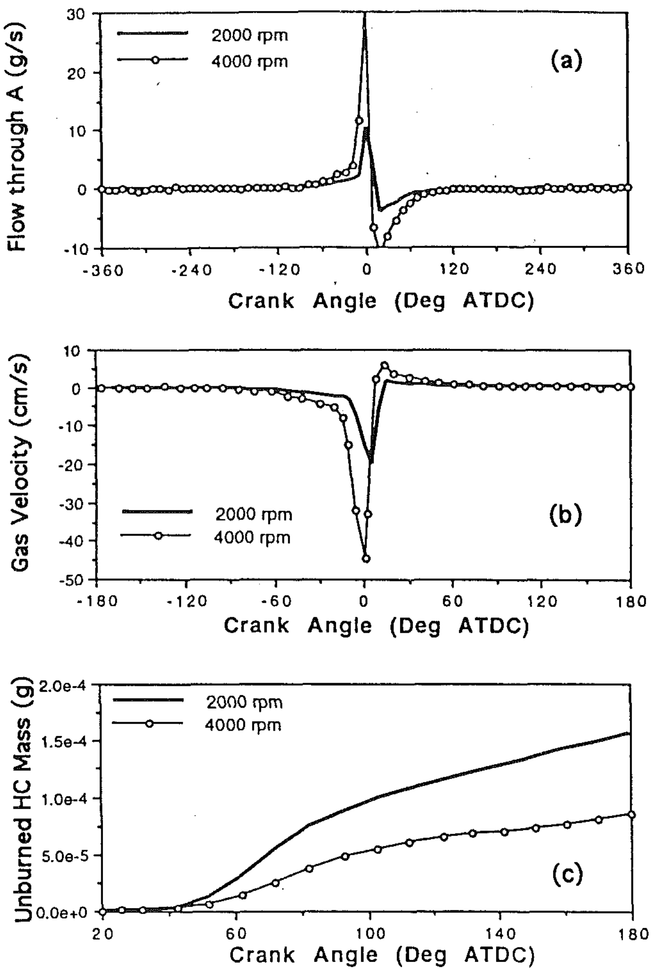

Fig. 9 Effect of engine speed on (*a*) crevice mass flow rates through plane *A*, (*b*) crevice flow velocities, (*c*) unburned HC mass in cylinder

does not have enough time to flow into the crevice region below the top ring; thus, the pressure (*P*3) between ring 1 and ring 2 is decreased as shown in Fig. 8(*c*). At such high engine speeds, the pressure force is no longer dominating the top ring's upward movement during the exhaust stroke. Figure 8(*a*) shows that the axial driving force for the 4000 rpm case is always negative (unlike the baseline case). This indicates that the ring is continuously pressed downward during the entire expansion stroke. Therefore, the top ring's upward movement during the exhaust stroke is again dominated by the inertia force. Figure 8(*b*) shows that, with respect to TDC, the top ring moves downward during intake (−280 deg ATDC) at about the same timing that it moves upward during exhaust (280 deg ATDC).

Figure 9(*a*) and 9(*b*) show the effect of engine speed on the mass flow rate and crevice flow velocity across plane *A*. Clearly, there is a significant increase in mass flow rate and velocity across plane *A*, when the engine speed is increased. Furthermore, the relatively higher pressure difference across the top ring under the higher engine speed allows more cylinder charge to flow into the crevice through the top ring end gap. This higher mass flow rate across plane *A* is, however, compensated by the shorter engine cyclic time under the higher engine speed condition. As a result, the maximum accumulated mass in crevices is only slightly increased in the high speed case. As shown in Table 4, the maximum fraction of the cylinder charge stored in crevices is only slightly increased from 2.93 percent (baseline) to 3.23 percent for the 4000 rpm case.

Figure 9(*c*) shows the effect of engine speed on the cumulative unburned HC mass in the cylinder. With more charge stored in crevices as the engine speed is increased, more HC mass is returned into the cylinder later during the expansion stroke. Nevertheless, since the high engine speed case causes a higher turbulence level inside the cylinder, and a higher crevice backflow momentum, the returning fuel vapor mixes better with oxygen in the cylinder. As a result, the oxidation percentage of the returned HC mass is increased from 83 percent (baseline) to 92 percent for the 4000 rpm case. Thus, at the end of expansion, the unburned HC mass in cylinder is decreased by 45 percent compared with the baseline case. This suggests that increasing engine speed can reduce unburned HC emissions due to crevice backflows.

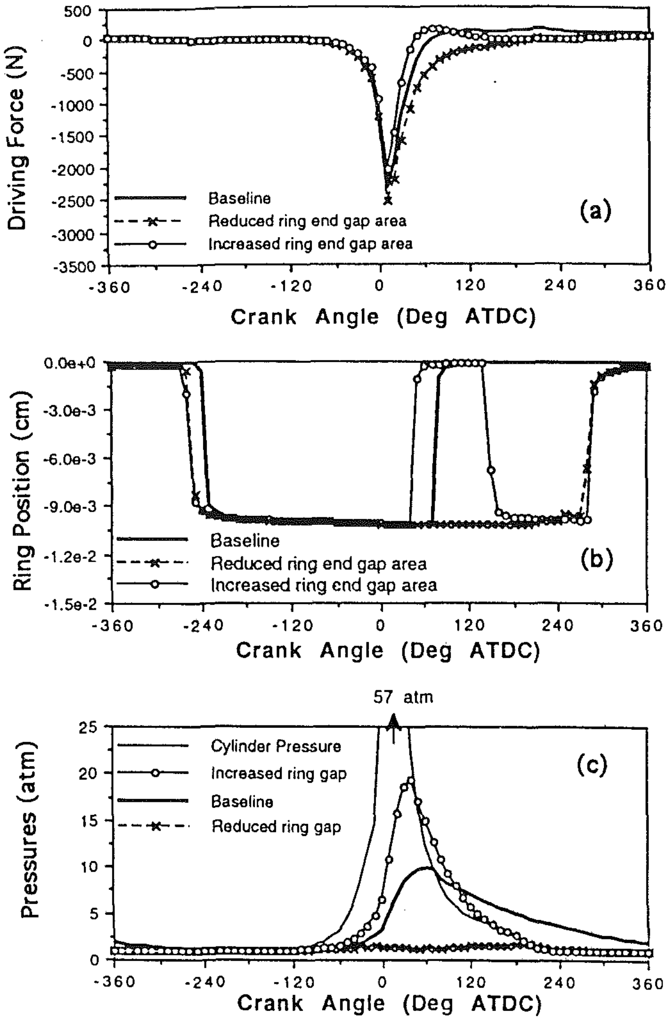

Fig. 10 Effect of ring end gap area on (*a*) axial driving force acting on top ring, (*b*) top ring's position, (*c*) interring cylinder pressure

Table 4 lists the effects of engine speed on the peak cylinder pressure and blowby percentage. The predicted peak cylinder pressure is increased from 54.2 atm to 58.1 atm, when the engine speed is increased from 2000 rpm (baseline) to 4000 rpm. Blowby is not changed significantly between the two cases.

Effect of Ring End Gap Area. Figures 10(*a*), 10(*b*) and 10(*c*) show the effect of ring end gap area on the axial driving force acting on the top ring, the history of the top ring position in the groove, and the pressure between the top and second rings (*P*3). When the ring end gap is reduced by a factor of three, the pressure in Region 3 (*P*3) becomes relatively smaller than the corresponding pressure in the baseline case, as shown in Fig. 10(*c*). This is because the passage (the ring end gap) that allows cylinder charge to flow through is more restricted. The situation is similar to the case of increased engine speed.

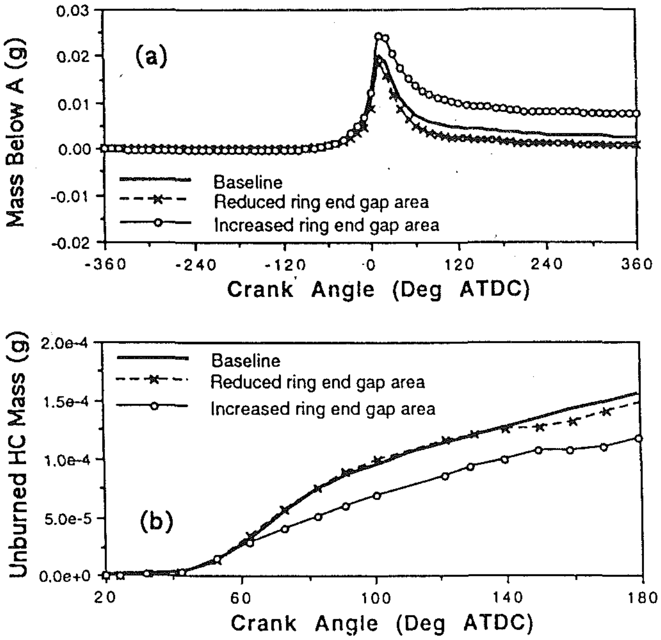

Fig. 11 Effect of ring end gap area on (*a*) mass trapped below plane *A*, and (*b*) unburned HC mass

Under those conditions, the axial driving force is always negative throughout the compression and expansion strokes, thus pressing the ring downward (see Fig. 10*a*). The dominant force that moves the top ring upward late in the exhaust stroke (see Fig. 10*b*) is the inertia force.

In contrast, when the ring end gap area is increased by a factor of three, crevice gas flows more freely through the top ring area, and the pressure in Region 3 (*P*3) is increased, as shown in Fig. 10(*c*). Figures 10(*b*) and 10(*c*) indicate that the top ring moves upward (or downward) during the expansion stroke as soon as pressure *P*3 becomes larger (or smaller) than the cylinder pressure. Figure 10(*a*) also shows that the axial driving force increases to a positive level, and then decreases again to a negative level during the early expansion stroke. This explains why the top ring moves first upward and then downward during expansion. Clearly, the pressure force dominates the top ring movement (upward and downward) during this period. However, the top ring moves upward again later during the exhaust stroke due to the inertia force, as shown in Fig. 10(*b*).

Figure 11(*a*) shows the effect of ring end gap area on the cylinder charge stored below Plane *A*. As summarized in Table 4, the maximum cylinder charge stored in crevices is increased from 2.93 percent (baseline) to 3.63 percent with increased ring end gap area. This is because the larger end gap introduces a flow path more comparable to the ring side clearance. Reducing the ring end gap does not change the amount of trapped mass significantly, since the majority of the cylinder charge flows into crevices through the ring side clearance (see Fig. 4*b*).

Figure 11(*b*) shows the effect of ring end gap area on the history of unburned HC mass in the cylinder. Since the increase in ring end gap area increases blowby (see Table 4), less HC mass is actually returned into the cylinder late in the expansion stroke compared with the baseline case. Also, the increase in ring end gap area allows a higher fraction of the returning cylinder charge to flow through this restriction. Since flow through the ring end gap has a higher velocity than flow through the top land crevice, the momentum of the backflowing crevice gas is increased. As a consequence, the latter penetrates deeper into the cylinder to mix with the unused oxygen. Thus, at the end of expansion the oxidation percentage of the returned HC mass is moderately increased from 83 percent (baseline) to 87 percent, and the unburned HC mass in cylinder is decreased by 24 percent compared with the baseline case. This study indicates that unburned HC mass can be reduced by increasing the ring end gap area, but at the expense of increased blowby (1.67 percent versus 0.58 percent) and reduced peak pressure (53.9 versus 54.2 atm).

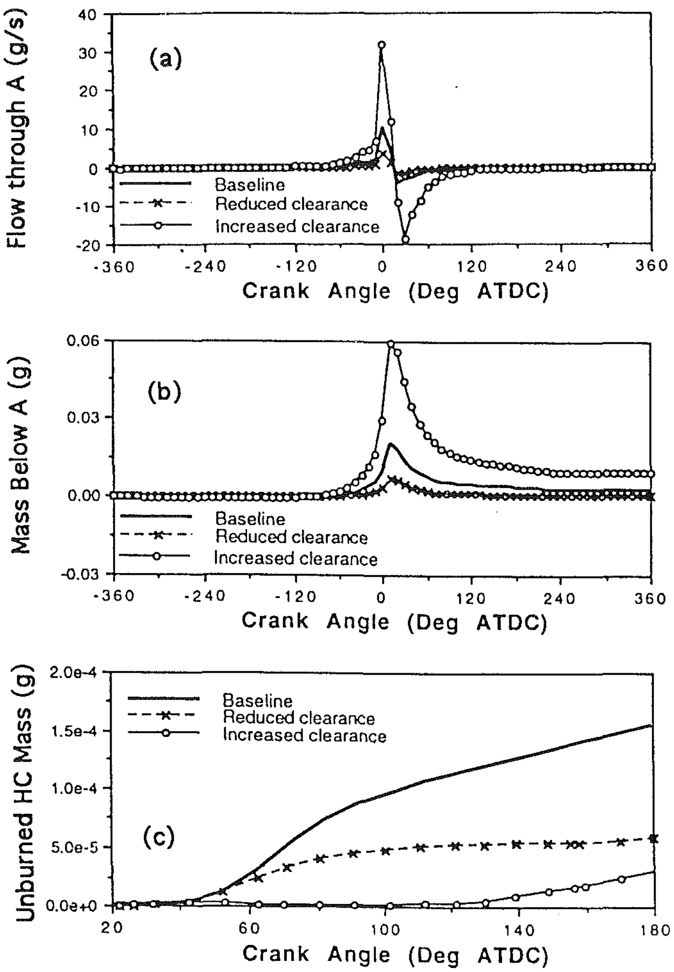

Fig. 12 Effect of piston-to-cylinder side clearance on (*a*) crevice mass flow rates through plane *A*, (*b*) cylinder charge stored below plane *A*, and (*c*) unburned HC mass in cylinder

If the ring end gap area is reduced, even less of the cylinder charge flows through this restriction, and the penetration of the returning HC vapor into the cylinder is practically unchanged. Thus, the unburned HC mass at the end of expansion does not change significantly. For this case, blowby is slightly reduced (0.24 percent versus 0.58 percent) and peak cylinder pressure is slightly increased (54.5 versus 54.2 atm).

Effect of Piston-Cylinder Side Clearance. Reducing (or increasing) the piston-cylinder side clearance proportionately reduces (or increases) both the top land crevice volume and the ring end gap area. Ring dynamics will thus be similar to the previous case, where only ring end gap area was changed. Figures 12(*a*) and 12(*b*) show the effects of changing piston-cylinder side clearance by a factor of three on the mass flow rate across plane *A* and the cylinder charge stored below plane *A*. The maximum cylinder charge stored in crevices is dramatically decreased (from 2.93 to 0.97 percent) or increased (from 2.93 to 8.75 percent), when the piston-cylinder side clearance is reduced or increased by a factor of three. The top land crevice volume accommodates the largest portion of the cylinder charge below Plane *A*. Therefore, the crevice flow rate across plane *A* is significantly changed by changing the piston-cylinder clearance (and thus the top land crevice gap), as shown in Fig. 12(*a*).

Figure 12(*c*) shows the effect of piston-cylinder side clearance on the cumulative unburned HC mass in cylinder. With increased side clearance, and thus increased mass stored in crevices, more unburned HC vapor is returned into the cylinder during the expansion stroke. The higher the fuel vapor concentration in the cylinder, the higher its oxidation rate. Table 4 shows that the oxidation percentage of the returned HC mass is increased from 83 to 99 percent, when the side clearance is increased. Thus, at the end of expansion, the unburned HC mass in cylinder is decreased by 81 percent compared with the baseline case, even though more HC vapor is returned into the cylinder when the side clearance is increased. However, durability of this design would be unsatisfactory in passenger car service (Wentworth, 1971). Furthermore, the increased piston-cylinder clearance would dramatically reduce peak cylinder pressure (from 54.2 to 47.9 atm) and increase blowby (from 0.58 to 1.63 percent).

If the side clearance is reduced, the returned HC mass is also reduced significantly, as shown in Table 4. Despite a reduced oxidation rate (77 percent) of the returned HC mass, at the end of expansion the unburned HC mass is reduced by 62 percent compared with the baseline case. The HC reduction is accompanied by an increase in peak cylinder pressure (from 54.2 to 56.5 atm), and a reduction in blowby (from 0.58 to 0.25 percent).

Conclusions

In this paper, a model for crevice flow processes into and out of piston-cylinder-ring crevices has been implemented in KIVA-II. The model is based on a set of coupled ordinary differential equations that describe the piston-ring dynamics and the flow motions through the ring-side clearances and the ring end gaps. A series of two-dimensional simulations has been performed for a 2.5 L gasoline engine to investigate the effects of speed and selected piston-cylinder-ring design parameters on the crevice flows and their contribution to unburned HC emissions. The major results are the following:

1 The mixture of hydrocarbon and air is forced to enter the piston-cylinder-ring crevices during the compression and early expansion strokes and to return to the cylinder during the later expansion stroke, thus escaping complete oxidation and contributing to unburned HC emissions. The predicted peak cylinder pressure is reduced by approximately 5 percent and the completion of combustion is delayed by approximately 7 crank angle deg if the crevice backflow model is activated in the baseline case. This is because the apparent cylinder mass is reduced by approximately 3 percent near TDC due to the trapped cylinder charge in crevices. About 0.58 percent of the cylinder charge is eventually lost to the crankcase as blowby.

2 As engine speed increases from 2000 rpm to 4000 rpm, the maximum cylinder charge stored in crevices is slightly increased (from 2.93 to 3.23 percent of the total cylinder charge), while the oxidized fraction of the returned HC vapor is increased from 83 (baseline) to 92 percent. Thus, at the end of expansion, the unburned HC mass in cylinder is decreased by 45 percent compared with the baseline amount. This suggests that the contribution of crevice flows on unburned HC emissions is reduced at higher speeds.

3 The maximum cylinder charge stored in crevices is moderately increased if the ring end gap area is increased by three times. However, the fraction of the returned HC vapor that is oxidized in late expansion is also increased from 83 to 87 percent. Moreover, there is less trapped cylinder charge returned to the cylinder due to increase in blowby. Thus, the unburned HC mass in cylinder at the end of expansion is decreased by 24 percent. Conversely, a reduction in ring end gap area seems to have no significant influence on the unburned HC emissions at the end of expansion.

4 The maximum cylinder charge stored in crevices is significantly increased (from 2.93 to 8.75 percent of the total cylinder charge) if the piston-cylinder side clearance is increased three times from its baseline value. Nevertheless, the burned fraction of the returned HC vapor is also increased (from 83 to 99 percent), so that at the end of the expansion stroke the unburned HC mass in cylinder is decreased by 81 percent compared to baseline. However, the increased piston-cylinder clearance would dramatically reduce peak cylinder pressure (from 54.2 to 47.9 atm) and increase blowby (from 0.58 to 1.63 percent). Conversely, significant reductions in trapped crevice gas and, eventually, unburned HC mass can be achieved with a reduction in piston-cylinder side clearance.

Acknowledgments

The contributions of Riadh Namouchi, who developed the ring dynamics and crevice flow code PCRCF, are gratefully acknowledged. This material is based upon work supported by the National Science Foundation under Grant No. CBT-8858310. The National Center for Supercomputing Applications provided computer time on the CRAY Y-MP supercomputer.

References

Allen, D. G., 1975, "Prediction of Piston Ring Cylinder Bore Oil Film Thickness in Two Particular Engines and Correlation With Experimental Evidence," presented at the IMechE Conference on Piston Ring Scuffing, London, United Kingdom.

Amann, C. A., 1988, "Engineering the Spark-Ignition Engine—The Piston-Rings-Cylinder Wall Interface," SAE Paper No. 885056.

Amsden, A. A., O'Rourke, P. J., and Butler, T. D., 1989, "KIVA-II: A Computer Program for Chemically Reactive Flows With Sprays," Los Alamos National Laboratory Report LA-11560-MS.

Dowson, D., Economou, P. N., Ruddy, B.L., Strachan, P. J., and Baker, A. J. S., 1979, "Piston Ring Lubrication—Part II. Theoretical Analysis of a Single Ring and a Complete Ring Pack," *Energy Conservation Through Fluid Film Lubrication Technology: Frontiers in Research and Design*, ASME, New York.

Faro-Barros, A., and Dyson, A., 1960, "Piston Ring Friction—Ring Measurement With Low Viscosity Oils," *Inst. of Petr.*, Vol. 46, No. 433.

Furuhama, S., 1959, 1960, 1961, "A Dynamic Theory of Piston-Ring Lubrication, 1st, 2nd, and 3rd Reports, Calculation, Experiment, and Measurement of Oil Film Thickness," Vols. 2, 3, and 4.

Kuo, T.-W., Sellnau, M. C., Theobald, M. A., and Jones, J. D., 1989, "Calculation of Flow in the Piston-Cylinder-Ring Crevices of a Homogeneous Charge Engine and Comparison With Experiment," SAE Paper No. 890838.

Namazian, M., and Heywood, J. B., 1982, "Flow in the Piston-Cylinder-Ring Crevices of a Spark-Ignition Engine: Effect on Hydrocarbon Emissions, Efficiency and Power," SAE Paper No. 820088.

Namouchi, R., 1989, "Modeling of Piston Ring Dynamics, Crevice Gas Flow, and Hydrodynamic Lubrication in Internal Combustion Engines," M.S. Thesis, University of Illinois.

Reitz, R. D., and Kuo, T. W., 1989, "Modeling of HC Emissions Due to Crevice Flows in Premixed-Charge Engines," SAE Paper No. 892085.

Rohde, S. M., Whitaker, K. W., and McAllister, G. T., 1979, "A Study of the Effects of Piston Ring and Engine Design Variables on Piston Ring Friction," *Energy Conservation Through Fluid Film Lubrication Technology: Frontiers in Research and Design*, ASME, New York.

Ruddy, B. L., Dowson, D., Economou, P. N., and Baker, A. J. S., 1979, "Piston Ring Lubrication—Part III. The Influence of Ring Dynamics and Ring Twist," *Energy Conservation Through Fluid Film Lubrication Technology: Frontiers in Research and Design*, ASME, New York.

Wentworth, J. T., 1971, "The Piston Crevice Volume Effect on Exhaust Hydrocarbon Emission," *Combustion Science and Technology*, Vol. 4, pp. 97-100.

N. S. Mavinahally
University of New Orleans,
New Orleans, LA 70122

D. N. Assanis
University of Illinois, Urbana-Champaign,
Urbana, IL 61801

K. R. Govinda Mallan

K. V. Gopalakrishnan

Indian Institute of Technology,
Madras, India 600-036

Torch Ignition: Ideal for Lean Burn Premixed-Charge Engines

Sluggish flame initiation and propagation, and even potential misfiring, become major problems with lean-fueled, premixed-charge, spark-ignited engines. This work studies torch ignition as a means for improving combustion, fuel economy, and emissions of a retrofitted, large combustion chamber with nonideal spark plug location. A number of alternative configurations, employing different torch chamber designs, spark-plug locations, and materials, were tested under full-load and part-load conditions. Results indicate a considerable extension of the lean operating limit of the engine, especially under part-load conditions. In addition, torch ignition can lead to substantial thermal efficiency gains for either leaner or richer air–fuel ratios than the optimum for the conventional ignition system. On the richer side, in particular, the torch-ignited engine is capable of operating at maximum brake torque spark timings, rather than compromised, knock-limited spark timings used with conventional ignition. This translates into thermal efficiency improvements as high as 8 percent at an air–fuel ratio of 20:1 and full load.

Introduction

Lean burn, premixed charge engines offer the potential for superior fuel economy and greatly reduced NO_x emissions due to reduced gas temperatures (Hansel, 1971). Lean burn could also allow the use of high compression ratios and ensure knock-free operation with fuels of moderate or low octane rating, such as kerosene (Nagesh, 1991). However, the development of satisfactory lean burn engines has been plagued for years with problems associated with sluggish flame initiation and propagation, and even potential misfiring (Quader, 1974, 1976). Such problems directly spring from the over-reliance of the process of combustion on the conventional spark plug. The spark discharge forms a single-point, laminar flame kernel that is subsequently transformed into a turbulent flame front as it propagates through the compressed charge. Instead, multipoint torch ignition has emerged as a promising strategy for improving combustion and emissions of lean burn, premixed-charge engines (Yasuo et al., 1974; Gussak, 1975; Adams, 1978; Katsumi and Yoshiho, 1982; Hano Ryu and Asanuma, 1985; Hano Ryu et al., 1987; Oppenheim et al., 1989; Maxson and Oppenheim, 1991; Hensinger et al., 1992; Oppenheim, 1992).

In a torch ignition system, combustion is initiated in an antechamber from which jet plumes of combustion products issue forth into the main chamber. Each torch acts as a healthy source of ignition to the charge in the main chamber. The multipoint initiation of the combustion process significantly enhances the rate of combustion (Oppenheim, 1992). As a result, it is particularly attractive for igniting highly diluted charge, which cannot be readily ignited by conventional spark-ignition. The diluent should be made out of excess air and products of combustion, whose relatively high temperature and remnant radical activity enhance ignition. The number and location of the ignition sources depends on the configuration of the torch chamber. Four factors controlling torch chamber performance are torch chamber volume, number of torch nozzles, nozzle area, and torch jet direction. The torch chamber volume typically ranges from 2–3 percent (Yasuo et al., 1974; Gussak, 1975) to 8–15 percent (Adams, 1978) of the clearance volume.

This work studies torch ignition as a means for improving combustion, fuel economy, and emissions of a retrofitted, large, lean-burn combustion chamber with nonideal spark plug location. Unlike many of the previously tested torch chambers, the one designed for this work protrudes into the main chamber, thus allowing flexibility in the orientation of the nozzles, and resembles the designs of Kanakaraj (1988), Letsch (1984), and Oppenheim (1992). Oppenheim's design, however, was based on a pulsed jet combustion (PJC) system for the realization of jet plumes. The PJC system used a fuel injector, supplying a rich mixture (fuel–air equivalence ratio on the order of 2) inside a generator plug. In the proposed torch chamber, the fluid trapped in the spark plug chamber is a mixture of lean, unburned fuel–air and residual gas, without requiring the use of a fuel injector.

A number of alternative torch chamber configurations, employing different torch chamber designs, spark-plug locations, and materials, are tested under full-load and part-load conditions. The objective of these tests is to determine whether torch ignition can extend the lean operating limit, as well as the resistance to knock, of an otherwise sluggish burning combustion chamber. For each torch chamber configuration, fuel economy and unburned hydrocarbon emissions are compared against results obtained using conventional ignition. Based on the performance of the optimum torch chamber design, a general assessment of potential gains in fuel economy and emissions over a range of fuel–air ratios and loads is made.

Contributed by the Internal Combustion Engine Division and presented at the Energy-Sources Technology Conference and Exhibition, New Orleans, Louisiana, January 23–27, 1994. Manuscript received by the Internal Combustion Engine Division January 28, 1994. Paper No. 94-ICE-6. Associate Technical Editor: W. Cheng.

Torch Chamber Configuration

The engine used in this work was originally a single-cylinder, compression-ignition, air-cooled Kirloskar TAF1 engine, with a compression ratio of 17.5:1. Basic engine specifications and valve timings are listed in Table 1. The engine was retrofitted to run with premixed, lean gasoline–air mixtures, and spark-ignition. Due to anticipated knock constraints, the clearance volume was considerably increased to reduce the compression ratio to 8:1, thus reducing the squish area from 67.4 to 21.4 percent. Since the spark plug was positioned in the place of the diesel fuel injector, its extreme, noncentral location was not optimized for reducing flame travel distance to the end of the combustion chamber. Even with a clean piston and cylinder head, free of combustion deposits, the engine was unable to develop maximum brake torque without knocking at wide open throttle. It was concluded that sluggish flame propagation speed in an almost quiescent, large chamber allowed enough time for the end gas to preignite, thus causing knock. While the situation could be partially remedied by introducing water cooling in the cylinder head, it was desired to maintain air-cooled engine operation with the unmodified stock cylinder head. Hence, torch ignition was explored as a means of accelerating flame propagation.

Table 1 Engine specifications

Bore	8.75	cm
Stroke	11.0	cm
Connecting rod length	23.2	cm
Displacement	661	cm^3
Valve Timings*:		
Intake valve opens (IVO)	-4.5°	CA
Intake valve closes (IVC)	215°	CA
Exhaust valve opens (EVO)	505°	CA
Exhaust valve closes (EVC)	724.5°	CA

* Referenced after TDC of intake stroke.

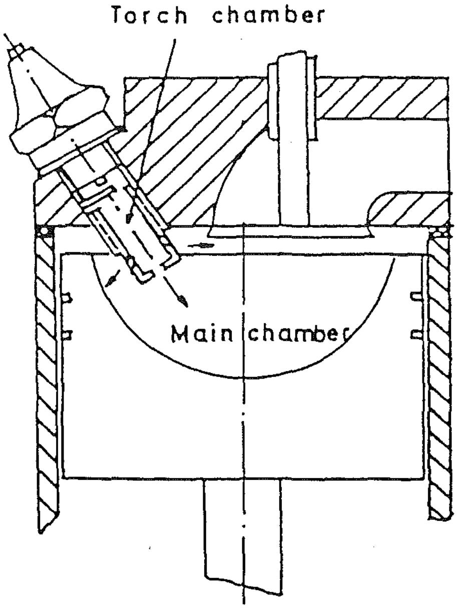

Fig. 1 Schematic of the stock cylinder head with the torch chamber and spark plug

Figure 1 shows a schematic of the stock cylinder head with the torch chamber and spark plug. The antechamber volume, 1.05 percent of the clearance volume of the main chamber at top dead center (TDC), was constrained by the clearance height between the cylinder head and the piston top at TDC, the diameter of the spark plug hole, and the wall thickness of the torch chamber (Nagesh, 1991). The inclination of the torch chamber was fixed at about 60 deg from the cylinder centerline.

As shown in Fig. 2, four alternative configurations of the torch chamber were investigated. In configuration No. 1, Fig. 2(*a*), a single hole that causes the torch to impinge directly on the piston top to produce violent turbulence was tried. In order to have the torch jet spout in multiple directions, particularly toward the larger portion of the main chamber, four holes of 3 mm diameter were drilled around the protruded portion of the torch chamber (configuration No. 2) as shown in Fig. 2(*b*). In torch chamber No. 3, the central hole was enlarged to 9 mm, and in addition to the four holes of 3 mm diameter, eight holes of 2 mm diameter were drilled at two planes as shown in Fig. 2(*c*). Finally, in torch chamber No. 4, Fig. 2(*d*), the center hole was reduced to 2.5 mm at the open end tip of the torch chamber with four holes of 3 mm diameter, three facing the major portion side of the main chamber and one on the opposite side.

A short reach plug was used with torch chamber configurations 1 through 4. The sparking gap was located at the close end of each torch chamber. In addition, in order to assess the effect of sparking gap location on combustion, fuel economy, and emissions, a modified long reach plug was also tried. Figures 3(*a*) and 3(*b*) show the two alternative locations, *A* and *B*, of the sparking gap. In position *B*, the plug gap between the central electrode and the earth electrode (chamber wall in this case) was adjusted to be the same as in position *A*.

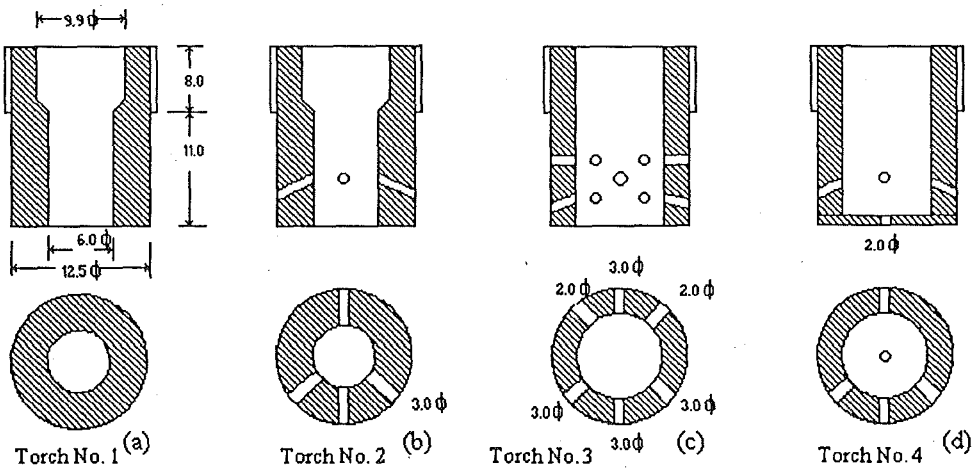

Fig. 2 Alternative torch chamber designs varying number and area of torch nozzles

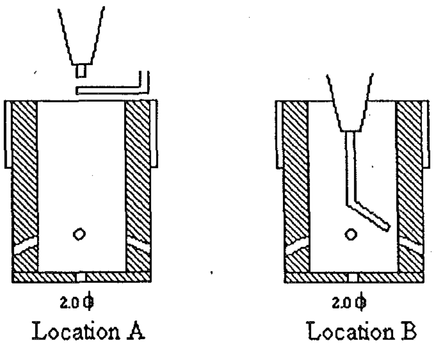

Fig. 3 Alternative locations of spark plug gap within torch chamber

Test Procedure

All dynamometer tests were run on commercial gasoline at a speed of 1500 rpm. For the wide-open throttle tests, the fuel-air ratio was varied between two extremes: leanest possible fuel-air ratio without misfiring, and richest possible ratio on the knock-limited range. For the part-load tests, the fuel-air mixture was adjusted as lean as possible for stable operation at a given throttle opening. At each air-fuel ratio, the spark timing was adjusted for maximum brake torque (MBT) wherever possible. In the knock-limited range, knocking was determined by the audible knocking sound. On the lean side, a steep rise in unburned hydrocarbon emissions (HC) was considered to indicate the lean limit. Tests at different load ranges were carried out with torch chamber 4 and plug gap location *B*, as the combination of these two was found to be the optimum configuration.

Performance and emissions results for all torch chamber configurations were compared with corresponding results for the baseline, retrofitted open chamber. Combustion parameters such as start of combustion, end of combustion, and combustion duration, were determined through analysis of cylinder pressure traces, which were recorded using a digital data acquisition system. HC and CO levels were measured using digital exhaust gas analyzers. Unfortunately, NO_x levels were not measured due to malfunctioning to the NO_x analyzer. Since CO levels were found to be very low (of the order of 0.05 percent by volume), they are not presented here.

Results and Discussion

Effect of Chamber Configuration. Figure 4 compares brake thermal efficiency versus air-fuel ratio for the first three configurations, each with plug gap positioned at *A*. For configuration 1, efficiency was comparable to that of the standard engine for the richer mixtures, while being distinctly lower for the leaner mixtures. Introducing peripheral holes and/or increasing the size of the main orifice improved the lean operating characteristics of the engine compared to chamber No. 1, but not compared to the standard engine. Further, for configurations 2 and 3, knock-limited operation could not be extended below an air-fuel ratio of about 22:1, hence tests were not run on the richer side of the optimum air-fuel ratio. Overall, the first three configuations resulted in degraded engine combustion in comparison with the standard engine. Pressure data from the main chamber and the antechamber (Nagesh, 1991) revealed that a through hole of 6 mm diameter (for chambers No. 1 and No. 2) and 9 mm diameter (for chamber No. 3) was too large to introduce a substantial pressure difference between the two chambers, so as to impart high momentum to the ensuing torch. This was the reason for designing torch 4 with a substantially smaller hole at the open tip of the chamber.

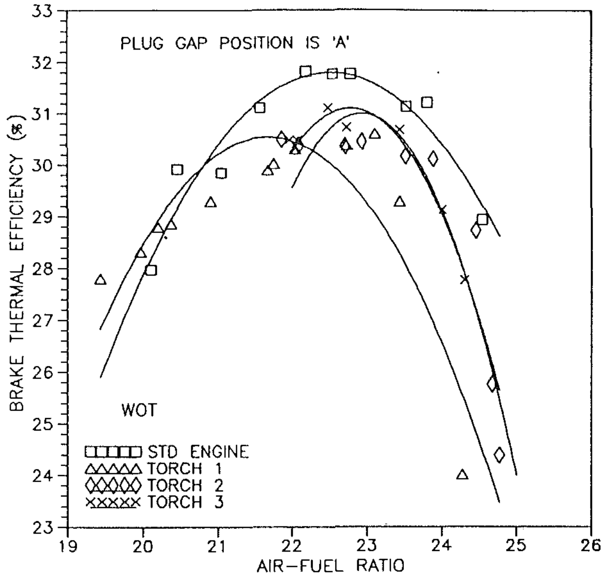

Fig. 4 Brake thermal efficiency versus air-fuel ratio for torch chambers 1, 2, and 3, with spark plug *A*

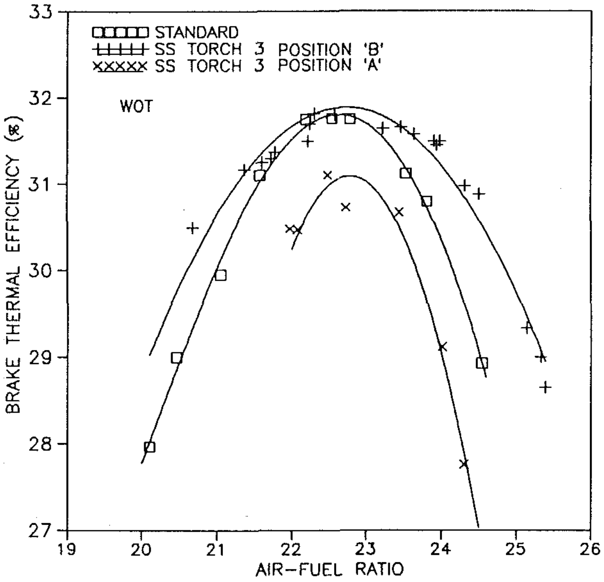

Fig. 5 Effect of sparking gap positioning, within torch chamber 3, on brake thermal efficiency over a range of air-fuel ratios

Figure 5 depicts the effect of sparking gap positioning on thermal efficiency attainable with torch chamber No. 3. With the long reach plug *B* within chamber 3, there is a dramatic improvement in fuel economy compared to positioning the short reach plug *A* on the top of the same chamber. Knock-limited spark timing was extended toward the richer side. Also, the fuel economy on the leaner range was better than the standard engine's. The improvement is attributed to faster and more repeatable flame initiation with the longer reach plug *B*. Ignition delay, defined as the crank angle interval required to burn 10 percent of the fuel-air mixture, is shown to be reduced with sparking gap location *B*, throughout the range of air-fuel ratios (see Fig. 6). On the other hand, poor scavenging and excessive mixture dilution with residual in the vicinity of the spark may be cited as the cause of the longer ignition delay in the case of plug gap position at *A*. As shown in Fig. 7, at any given air-fuel ratio, spark timing is advanced to compensate for the longer ignition delay with spark plug *A* compared with plug *B*. Spark timing also needs to be advanced as mixtures get leaner and less reactive (Fig. 7), thus requiring more time for preflame reactions (Fig. 6).

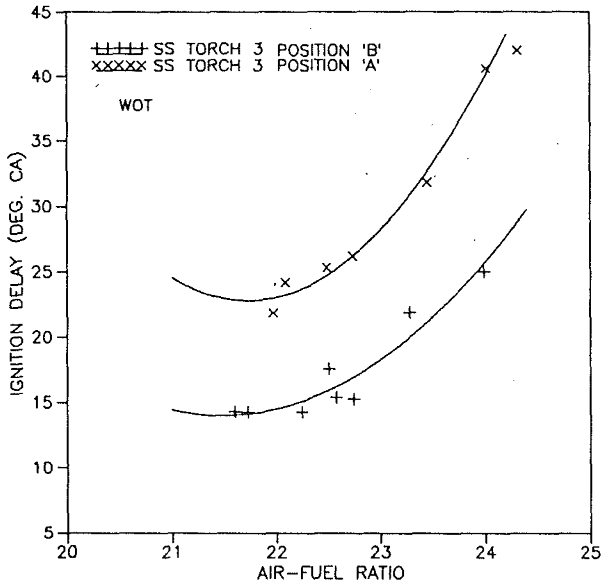

Fig. 6 Effect of sparking gap positioning, within torch chamber 3, on ignition delay over a range of air-fuel ratios

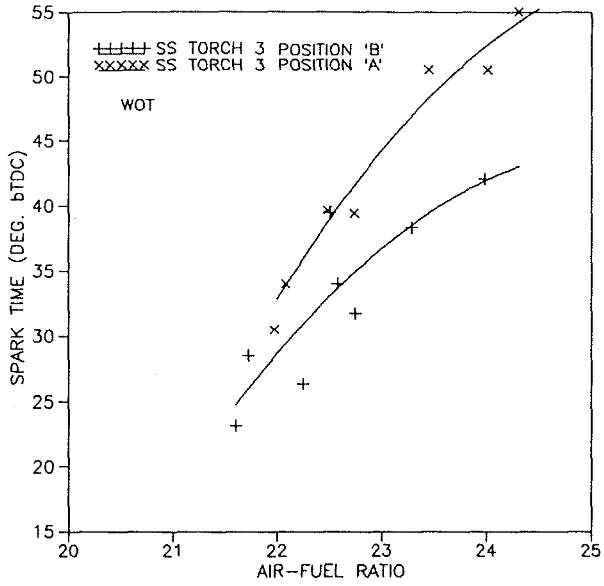

Fig. 7 Effect of sparking gap positioning, within torch chamber 3, on MBT spark timing over a range of air-fuel ratios

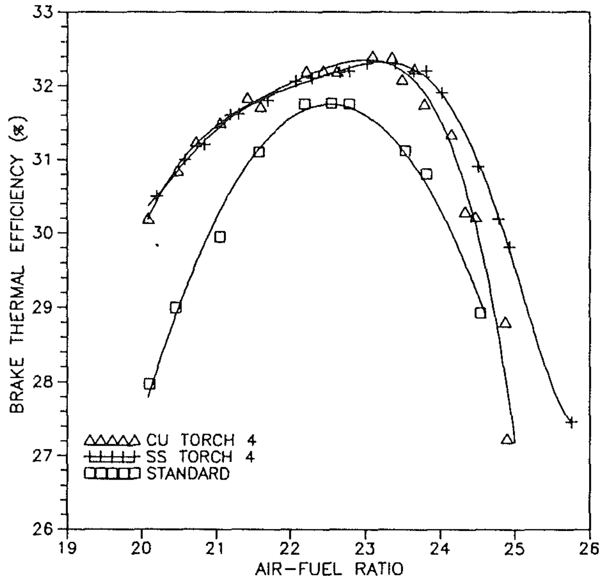

Fig. 8 Effect of conventional versus torch ignition on thermal efficiency over a range of air-fuel ratios. Results shown for both steel and copper versions of torch chamber 4 with long reach spark plug *B*.

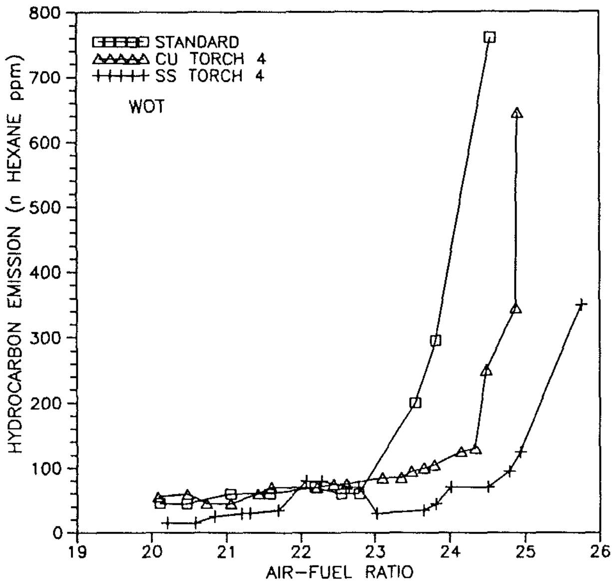

Fig. 9 Effect of conventional versus torch ignition on HC emissions over a range of air-fuel ratios. Results shown for both steel and copper versions of torch chamber 4 with long reach spark plug *B*.

Figure 8 compares the brake thermal efficiency produced by torch chamber No. 4, with the plug gap positioned at *B*, versus the efficiency of the standard engine. In contrast with the first three torch chamber configurations, this modified torch chamber design can improve fuel economy over the standard ignition system. The system exposes the long reach plug to a more reactive mixture than a short reach plug would. In addition, the reduced diameter of the front hole increases pressure drop between the antechamber and the main chamber, thus increasing the momentum of the burning jets ensuing through the peripheral holes. Peak thermal efficiency with optimized torch ignition is 32.5 percent at an air-fuel ratio of 23.2:1, whereas with conventional ignition it is 31.8 percent at 22.5:1. While the peak efficiency improvement is modest (about 2.2 percent), efficiency gains are substantial on either side of the optimum air-fuel ratio for the conventional ignition system. On the leaner side, torch ignition leads to reduced cycle-to-cycle variation in initial flame development. As a result, brake thermal efficiency with torch ignition is about 3.4 percent higher than with conventional ignition at an air-fuel ratio of 23.5:1. On the richer side, the torch ignited engine is capable of operating at true MBT spark timings, rather than compromised, knock-limited spark timings used with conventional ignition. This translates into efficiency improvements around 8 percent at an air-fuel ratio of 20:1.

Figure 9 shows unburned HC emissions from the conventional and torch-ignited engines. The level of HC emissions is generally lower with steel torch chamber ignition, particularly in the lean range. Up to an air-fuel ratio of 22:1, HC emission levels are only somewhat lower (by 20-30 ppm) for the torch-ignited system. However, beyond 23:1, HC levels rise sharply for the conventional ignition system. A steep increase in HC emissions is associated with misfiring cycles, excessive cycle-to-cycle variation, and incomplete combustion, indicating the lean operating limit of the engine. Clearly, using an optimized

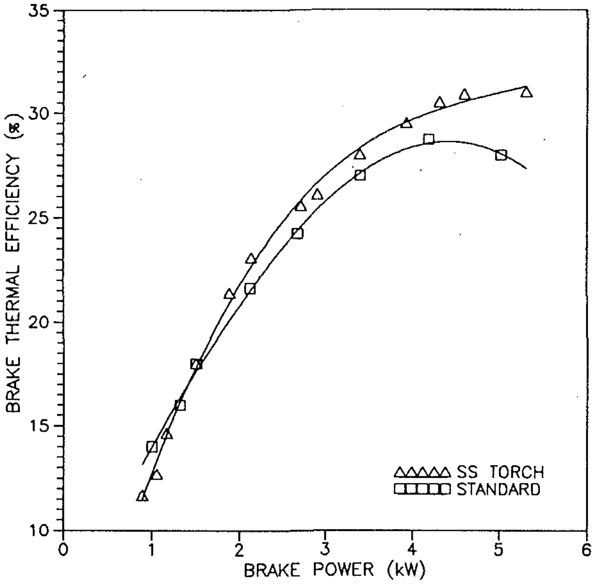

Fig. 10 Comparison of thermal efficiency at different power levels (loads) using conventional and torch ignition

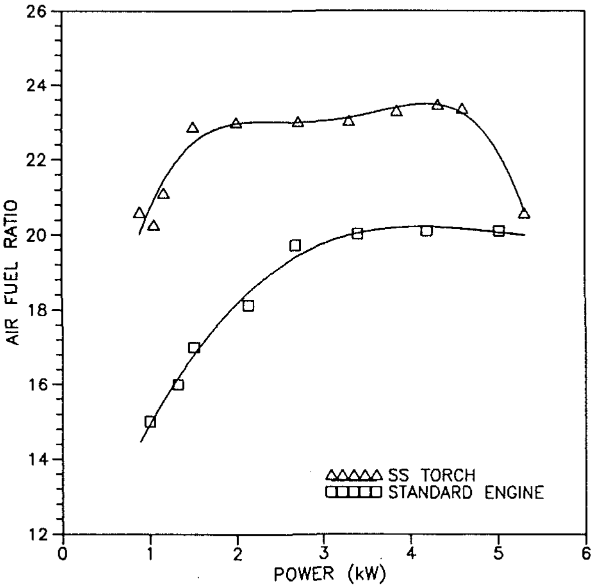

Fig. 11 Maximum air-fuel ratio for stable operation at different power levels (loads) using conventional and torch ignition

torch ignition system can extend the lean operating limit of a premixed-charge S.I. engine considerably, from 23:1 achievable with conventional ignition at full load to 25:1.

Effect of Torch Chamber Material. Earlier work (Dhandapani, 1989) at Indian Institute of Technology, Madras, had shown that copper coating on the piston top can improve the lean operating limit of a S.I. engine. This was attributed to the catalytic effect of copper on combustion of fuel-air mixtures, accelerating heat release rates as evidenced by a steeper cumulative heat release diagram. Based on this finding, an optimally configured torch chamber made of copper was designed and compared with its stainless steel counterpart and the standard chamber, in terms of overall engine thermal efficiency and unburned HC emissions.

Figure 8 shows the effect of torch chamber material on thermal efficiency over a range of air-fuel ratios. Clearly, there is no significant difference between the copper and steel torch chambers in the air-fuel ratio range of 20:1 to 23.5:1. However, using a stainless steel chamber, efficiency drops at a slower rate than with the copper chamber for air-fuel ratios greater than 23.5:1. Also, with the steel chamber, the lean limit is extended further before there is a sharp increase in HC emissions, as shown in Fig. 9. In addition, for almost the same thermal efficiency in the air-fuel range between 22:1 and 20:1, the steel chamber produces lower HC levels by about 20–30 ppm (see Fig. 9). The superior combustion characteristics of the steel chamber are attributed to its approximately ten times lower thermal conductivity, and hence higher wall temperatures, in comparison with the copper chamber. Hotter chamber walls in the vicinity of the sparking gap can reduce cycle-to-cycle variation in igniting leaner mixtures.

Part-Load Performance. Part-load engine tests were carried out for steel torch chamber No. 4 with the spark plug at location *B*. As mentioned above, this configuration was found to be the optimum torch ignition system under wide open throttle conditions. For each test condition, MBT (or knock-limited) spark timing was used, as appropriate. Figure 10 shows the variation of brake thermal efficiency with engine brake power; the latter is directly proportional to load. The torch ignition system performs satisfactorily in the lean range, even at part loads. It is able to run at 20:1 air-fuel ratio at 20 percent of maximum load compared to 15:1 with the conventional ignition system.

Further, fuel economy with torch ignition is better than the standard engine's from about 25 percent of the maximum load to full load (corresponding to an output of 5 kW). As discussed before, the fuel economy improvement at full load is attributed to the fact that the torch-ignited engine can operate knock-free with noncompromised, MBT spark timing; the standard engine uses knock-limited spark timing. As load is reduced, thermal efficiency gains are derived from the ability of the torch-ignited engine to run leaner and with a wider throttle opening for a given load. Figure 11 shows air-fuel ratio plotted against brake power. With torch ignition, the engine runs at a fairly constant air-fuel ratio of about 23:1 throughout the range between 25 to 85 percent of the maximum load. In contrast, for stable operation, fuel-air ratio needs to be enriched progressively with decreasing power output in the standard engine; it ranges from 21:1 at full load to 15:1 at 20 percent of maximum load. Hence, the standard engine relies on throttling more than the torch ignition engine in order to control load, thus suffering higher pumping losses.

Conclusions

A series of torch ignition systems has been developed in an attempt to improve the lean operating limit, as well as the fuel economy, and emissions of a retrofitted, large combustion chamber with nonideal spark plug location. Four designs of a stainless steel torch chamber, each with two alternative spark-plug locations, were tested. For the optimum chamber and plug configuration, a chamber made of copper was also tested. The following conclusions can be drawn from our test results.

- Using an optimized torch ignition system can extend the lean operating limit of a premixed-charge S.I. engine considerably, from 23:1 achievable with conventional ignition at full load to 25:1. Up to an air-fuel ratio of 23:1, HC emission levels are comparable for both types of ignition systems. However, beyond 23:1, HC levels rise sharply for the conventional ignition system due to increased cyclic variation and a larger number of misfiring cycles. The torch ignition system performs satisfactorily in lean range even at part loads. It is able to run at 20:1 air-fuel ratio at 20 percent of maximum load compared to only 15:1 for the conventional ignition system.
- Torch ignition can improve thermal efficiency compared to conventional ignition over a range of air-fuel ratios. Efficiency gains are substantial on either side of the optimum

air-fuel ratio for the conventional ignition system. On the leaner side, torch ignition leads to reduced cycle-to-cycle variation in initial flame development. As a result, brake thermal efficiency with torch ignition is 3.4 percent higher than with conventional ignition at an air-fuel ratio of 23.5:1. On the richer side, the torch-ignited engine is capable of operating at true MBT spark timings, rather than compromised, knock-limited spark timings used with conventional ignition. This translates into efficiency improvements as high as 8 percent at an air-fuel ratio of 20:1.

References

Adams, T. G., 1978, "Theory and Evaluation of Auxiliary Combustion (Torch) Chambers," SAE Paper No. 780631, *SAE Trans.*, Vol. 87, pp. 2328-2339.

Dhandapani, S., 1989, "Experimental and Theoretical Investigation on a Single Cylinder, Four Stroke Lean Burn S. I. Engine," Ph.D Thesis, IIT, Madras.

Gussak, L. A., 1975, "High Chemical Activity of Incomplete Combustion Products and a Method of Prechamber Torch Ignition for Avalanche Activation of Combustion in Internal Combustion Engines," SAE Paper No. 750890, *SAE Trans.*, Vol. 84, pp. 2421-2445.

Hano Ryu, and Asanuma, T., 1985, "Combustion Analysis With Gas Temperature Diagrams Measured in a Prechamber Spark Ignition Engine," *Proceedings of Twentieth Symposium (Int.) on Combustion*, Combustion Institute, Pittsburgh, PA, pp. 195-200.

Hano Ryu, Akihiko, C., and Asanuma, T., 1987, "Effect of Torch Jet Direction on the Combustion and Performance of a Prechamber Spark Ignition Engine," SAE Paper No. 870167, *SAE Trans.*, Vol. 96, pp. 4.201-4.211.

Hansel, J. G., 1971, "Lean Automotive Engine Operation—Hydrocarbon Exhaust Emissions and Combustion Characteristics," SAE Paper No. 710164, *SAE Trans.*, Vol. 80, pp. 708-722.

Hensinger, D. M., Maxson, J. A., Hom, K., and Oppenheim, A. K., 1992, "Jet Plume Injection and Combustion," SAE Paper No. 920414, *SAE Trans.*, Vol. 101:3, pp. 571-580.

Kanakaraj, P., 1988, "A Study of Methods to Enable Lean Mixture Combustion in Two-Stroke S.I. Engines," M. Tech. Thesis, IIT, Madras.

Katsumi, K., and Yoshiyo, H., 1982, "Combustion Process in a Divided Chamber Spark Ignition Engine," *JSME Bulletin*, Vol. 25, pp. 1945-1952.

Letsch, R., 1984, "The Swirl Chamber Spark Plug: A Means of Faster, More Uniform Energy Conversion in the Spark Ignition Engines," SAE Paper No. 840455, *SAE Trans.*, Vol. 93, pp. 3.365-3.377.

Maxson, J. A., and Oppenheim, J. A., 1991, "Pulsed Jet Combustion—Key to a Refinement of the Stratified Charge Concept," *Proceedings of Twenty-Third Symposium (Int.) on Combustion*, The Combustion Institute, Pittsburgh, PA, pp. 1041-1046.

Nagesh, M. S., 1991, "Experimental Investigation on Extended Expansion Concept Applied to a Four Stroke S.I. Engine," Ph.D. Thesis, ITT, Madras.

Oppenheim, A. K., Beltramo, J., Faris, D. W., Maxson, J. A., Hom, K., and Stewart, H. E., 1989, "Combustion by Pulsed Jet Plumes—Key to Controlled Combustion Engines," SAE Paper No. 890153, *SAE Trans.*, Vol. 98:5, pp. 175-182.

Oppenheim, A. K., 1992, "Quo Vadis, Technologia Combustionis," presented at the 2nd International Conference on Fluid Mechanics, and Reliability in Reciprocating Engines, Istituto Motori (Naples), Capri, Sept. 14-19.

Quader, A. A., 1974, "Lean Combustion and the Misfire Limit in Spark Ignition Engines," SAE Paper No. 741055, *SAE Trans.*, Vol. 83, pp. 3274-3296.

Quader, A. A., 1976, "What Limits Lean Operation in Spark Ignition Engines—Flame Initiation or Propagation," SAE Paper No. 760760, *SAE Trans.*, Vol. 85, pp. 2374-2387.

Yasuo, S., Kazuya, K. Saburo, T., and Yasuhiko, N., 1974, "Combustion Characteristics of the Torch Ignited Engine," SAE Paper No. 741167, *SAE Trans.*, Vol. 83, pp. 3504-3512.

Analysis of the Injection Process in Direct Injected Natural Gas Engines: Part I—Study of Unconfined and In-Cylinder Plume Behavior

M. J. Jennings

F. R. Jeske

Computational Fluid Dynamics,
Ricardo North America,
Burr Ridge, IL 60521

A study of natural gas (NG) direct injection (DI) processes has been performed using multidimensional computational fluid dynamics analysis. The purpose was to improve the understanding of mixing in DI NG engines. Calculations of injection into a constant-volume chamber were performed to document unconfined plume behavior. A full three-dimensional calculation of injection into a medium heavy-duty diesel engine cylinder was also performed to study plume behavior in engine geometries. The structure of the NG plume is characterized by a core of unmixed fuel confined to the near-field of the jet. This core contains the bulk of the unmixed fuel and is mixed by the turbulence generated by the jet shear layer. The NG plume development in the engine is dominated by combustion chamber surface interactions. A Coanda effect causes plume attachment to the cylinder head, which has a detrimental impact on mixing. Unconfined plume calculations with different nozzle hole sizes demonstrate that smaller nozzle holes are more effective at mixing the fuel and air.

Introduction

The potential emissions and fuel economy benefits of using natural gas (NG) as an alternative fuel for internal combustion engines has spurred recent development of diesel engine conversions. A central design consideration is choosing an appropriate fuel injection strategy. One of the most promising approaches is direct injection.

Direct injection of NG in diesel engines is becoming more attractive as a means of achieving significant emissions reductions while retaining diesel levels of fuel economy and performance. Direct injected (DI) NG conversions of low and medium-speed diesel engines currently exist, and future possibilities include widespread use of DI NG engines as vehicle powerplants.

The growing popularity of direct injection is due in part to the potential benefits associated with the charge stratification that can occur when the NG is injected very close to the start of combustion. These include the possible reduction of HC emissions due to reduced flame wall quenching, and higher knock tolerance compared to carbureted or throttle body injected NG engines. Further benefits can result depending on the engine application.

Establishing a fundamental understanding of the flow mechanisms that govern the injection process is necessary in order to truly optimize combustion systems (i.e., combustion chamber and injector configurations) for DI NG engines. Also, an understanding of the effect of key design parameters on these mechanisms is needed. A practical and cost effective approach to achieving this understanding is through the use of multidimensional computational fluid dynamic (CFD) analysis in conjunction with an engine test and development program. CFD analysis can provide highly detailed information about the in-cylinder flow field in three dimensions through the engine cycle. This wealth of information can provide fundamental insight to a degree that is not achievable from engine performance measurements. CFD analysis has been successfully applied to the study of other types of NG engines (Jeske et al., 1992; Johns and Jones, 1991), as well as DI diesel engines (McKinley and Primus, 1990).

The present work and the companion paper (Jennings and Jeske, 1994) are concerned with the study of fuel-air mixing during injection, prior to combustion, in DI NG engines using CFD analysis. The focus of the study is on the dynamics of the NG jets within the engine combustion chamber, and the effects of a few key engine design parameters on these dynamics and the resulting fuel-air mixing. The study contributes to the fundamental understanding discussed above, and, in so doing, provides useful guidelines for developing DI NG engine combustion systems.

Contributed by the Internal Combustion Engine Division and presented at the 15th Annual Fall Technical Conference of the ASME Internal Combustion Engine Division, Morgantown, West Virginia, September 26-29, 1993. Manuscript received by the Internal Combustion Engine Division January 28, 1994. Associate Technical Editor: W. Cheng.

Approach

Scope of Analysis. The analysis is based upon a series of CFD calculations of NG injection in engine combustion chambers and constant-volume chambers. Simulations of injection into constant-volume chambers are used to investigate the fundamental behavior of NG jets. A calculation of engine injection, which includes a moving piston, is used to study NG plume behavior in a diesel engine combustion chamber. Additional engine calculations reported by Jennings and Jeske (1994) are used to study the effects of combustion system design.

CFD Methodology. The engine CFD code described by Johns (1984) was used for all the calculations. The code solves the ensemble-averaged Navier–Stokes equations governing turbulent, compressible flow in three dimensions. The solution is based upon the finite volume methodology (Gosman et al., 1969) and the code is suited to treating diesel combustion chamber geometries, including bowl-in-piston designs.

The primary equation set solved consists of continuity, conservation of momentum in three dimensions, conservation of enthalpy, and transport of gas species. The distribution of up to ten different gas species can be tracked as part of the solution. The present analysis considered transport of fuel, oxidant, inerts (which accounts for nitrogen and trace gases present in air), and residuals. The NG fuel was treated as pure methane.

Engine combustion chamber flows are heavily dominated by turbulence, and this is particularly true during injection. Turbulence is modeled using a standard two-equation k–ϵ model (Launder and Spalding, 1972) that has been extended to include effects of compressibility (Reynolds, 1978). Two additional equations are solved as part of the model. These equations account for the transport of turbulence kinetic energy (k) and the transport of the turbulence energy dissipation rate (ϵ).

The k–ϵ model is known to have difficulties representing turbulent transport in complex flows; however, this model has significant practical engineering value and is commonly used for calculations of engine in-cylinder flows (Jennings and Morel, 1988; Gosman, 1985; Johns, 1990). The interpretation of results has to take account of known shortcomings in the model. In spite of these shortcomings, there is still a great deal of useful information that can be extracted from simulations using the model. The present study demonstrates this point.

Engine Geometry. For the purposes of investigating the effects of changes in engine design parameters on the injection process, a baseline engine configuration (geometry and operating conditions) is defined. Subsequent parametric variations considered by Jennings and Jeske (1994) are relative to this geometry.

The baseline engine configuration is patterned after a medium heavy-duty diesel engine typical of engines used for urban bus and Class 4 through 7 truck applications. It is assumed that if DI NG technology proves to be successful, engines that fall into the chosen category will prove to be a mainstream application. A complete summary of the baseline configuration is presented in Table 1 and a schematic of the combustion chamber geometry appears in Fig. 1. The data in Table 1 are categorized in terms of engine geometry, injector geometry, injection data, and performance/operating conditions data.

The configuration is based upon a four-stroke, turbocharged, aftercooled engine featuring a cylinder displacement of 1.64 *l*, a peak 37.3 kW per cylinder, a rated speed of 1800 rpm, and a BMEP of 15 bar. The cylinder dimensions have been deduced from a survey of several diesel engines that fall into the category defined above. The performance parameters (peak power and efficiency) are representative of diesel operation and the operating conditions chosen correspond to full load and rated speed. The equivalence ratio is representative of lean burn operation in DI NG engines.

Table 1 Summary of baseline NG engine configuration

ENGINE GEOMETRY	
Bore	124.5 mm
Stroke	137.2 mm
TDC Clearance Height	4.32 mm
Compression Ratio	16:1
Displaced Volume	1.64 *l*
INJECTOR GEOMETRY	
Number of Holes	8
Nozzle Offset from Head	2.0 mm
Nozzle Offset from Centerline	3.1 mm
Nozzle Angle from Head	15°
Nozzle Diameter	0.413 mm
INJECTION DATA	
Injection Pressure	200 bar
Fuel Temperature	350 K
Injected Fuel Mass	124.4 mg
Injection Duration	40°
Injection Timing	25° BTDC
Injection Profile	Slug
OPERATING CONDITIONS	
Rated Speed	1800 rpm
Equivalence Ratio	0.55
Power/Cylinder	37.3 kW

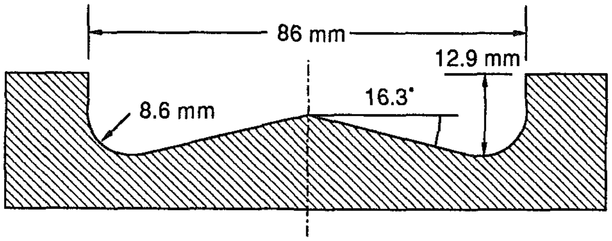

Fig. 1 Schematic of baseline combustion chamber geometry

The injection duration and timing are typical of diesel engine operation. In particular, the injection duration is appropriate for compression ignition. The fuel rate has been deduced from the peak power and thermal efficiency, using the lower heating value of methane.

Nozzle Exit Boundary Conditions. For all calculations discussed, the nozzle exit boundary conditions were assumed to correspond to choked flow conditions. This assumption is justified by the fact that the injection pressure to chamber pressure ratio was well in excess of the critical pressure ratio.

The jet velocity is given by the sonic velocity of NG at the temperature and pressure of the nozzle exit. The ratio of injection pressure to nozzle exit pressure was taken to be equal to the critical pressure ratio. Hence, for all cases, the NG jet is under-expanded. The temperature of the NG in the injector was assumed (see Table 1). The temperature at the nozzle exit was computed by assuming an isentropic expansion of the gas to the critical pressure.

The jet velocity profile at the nozzle exit is assumed to be uniform. The grid resolution across the nozzle was not high enough to capture secondary effects of nonuniform and/or asymmetric jet velocity profiles.

Table 2 Initial conditions for axisymmetric injection

Time	Pressure [bar]	Temperature [K]
BOI	46.0	855
TDC	98.0	970

Quantifying the Fuel Injection Process. The fuel injection process for the different cases was analyzed using a variety of visualization techniques. In addition, a number of measures were devised that could reduce the large amount of three-dimensional flow information to a digestible, quantified form. These measures are referred to throughout the discussion of results and quantify mixing, heat-up, and penetration of the NG during injection. All the measures described below are computed as functions of time from start of injection.

The mixing of NG fuel with air is expressed in terms of the mass of fuel mixed to equivalence ratio (φ) less than 2.0. It is considered that fuel-air mixtures below equivalence ratio 2.0 are combustible, hence the fuel mass mixed to this level represents the fuel mass within the cylinder that is ready to burn. Further, this fuel mass is nondimensionalized by the total instantaneous fuel mass in the cylinder. The resulting quantity gives the fraction of in-cylinder fuel that is mixed well enough to burn. This approach to quantifying the mixing was first suggested by Bracco (1992) and later refined by the present authors.

The NG injected into the combustion chamber is substantially lower in temperature than the surrounding combustion chamber air. Hence, in order for the fuel to become ignitable it must be heated, as well as mixed with the air. For the engine calculations, a measure of fuel heat-up is provided by the mass of fuel above 900 K. This cut-off temperature was chosen because it gave a reasonable compromise between a temperature achievable during the compression stroke for the engine considered and a temperature that was close to the auto-ignition temperature of NG (i.e., around 1000 K (Fraser et al., 1991)).

Axial and radial penetration is quantified by calculating the distance between the injector nozzle exit and the outer edges of the NG plume. The outer boundary of the NG plume is defined by the 0.5 equivalence ratio surface. The maximum radial distance from the nozzle to this surface is used to indicate penetration.

Discussion of Results

Behavior of Unconfined NG Jets. The behavior of the individual NG plumes emanating from a multihole injector, typical of that used in engine applications, was studied by simulating axisymmetric injection into a constant-volume chamber. The purpose of these calculations was to understand the structure of the NG jet and its variation through the injection period. Also, the mixing characteristics of unconfined plumes were documented.

The calculations considered injection into a cylindrical chamber with a diameter of 100 mm and a length of 100 mm. A single-hole injector was mounted in one of the end walls with its nozzle centerline aligned with the cylinder axis. This configuration produces an axisymmetric plume, which penetrates toward the opposite end wall. The injection rate was the same as a single hole of the engine injector.

For all cases discussed, the computational mesh was comprised of 80 cells in the axial directional and 50 cells in the radial direction. Stretching of the grid was applied near the nozzle exit in order to resolve the near field of the jet.

Figure 2 shows the fuel-air mixing of plumes from two different cases over a period of 2.0 ms (which corresponds to approximately 20 crank angle deg at 1800 rpm in the engine). For both cases, the nozzle diameter was the same as the baseline engine nozzle diameter given in Table 1, i.e., 0.413 mm. However, the chamber initial conditions were different. For one case (the solid line of Fig. 2), the initial conditions corresponded to the in-cylinder conditions of the baseline engine at BOI. For the other case (the dashed line of Fig. 2), the initial conditions corresponded to in-cylinder conditions at TDC. Table 2 lists the chamber conditions for each case. The fuel-air mixing displays a nearly exponential character as the mixing increases rapidly over the first 1.0 ms of injection, then slows significantly beyond that time.

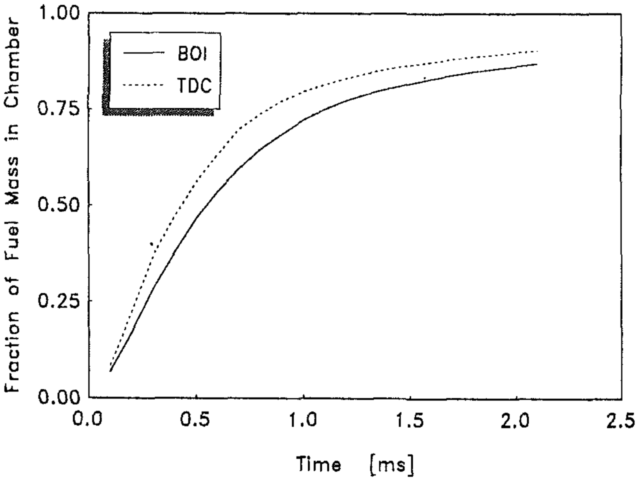

Fig. 2 Fraction of fuel mass in chamber at $\varphi<2.0$ for axisymmetric injection using engine BOI and TDC IC's

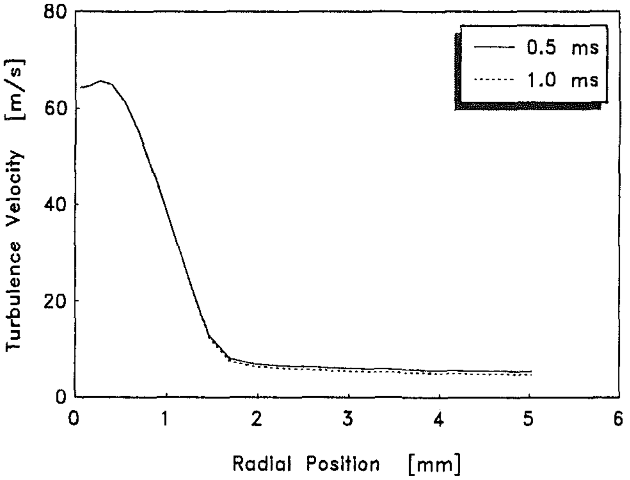

Fig. 3 Radial turbulence velocity ten diameters downstream of the nozzle

From studying the axisymmetric plume behavior, a picture of the structure of the penetrating NG jet emerges. Very early during injection (0.0 to 0.2 ms), high levels of turbulence energy are generated near the nozzle exit by the jet shear layer. After this time, the turbulence energy budget becomes fixed in time and the turbulence field near the nozzle remains frozen. This is demonstrated by Fig. 3, which shows radial turbulence velocity profiles at 0.5 and 1.0 ms ABOI at an axial location of ten diameters downstream of the nozzle. It can be seen that there is no change in the near-field turbulence generated by the jet.

Also, during the initial stages of injection, the fuel-rich core of the NG plume forms. The formation of the core is driven by the initial penetration and diffusion of the completely un-

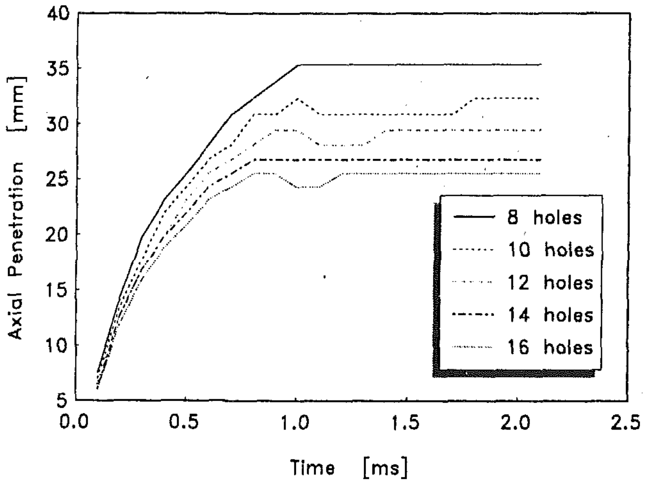

Fig. 4 Axisymmetric NG plume penetration

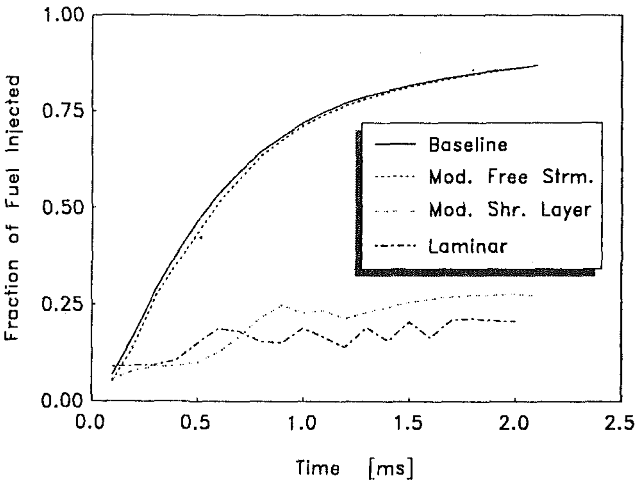

Fig. 5 Fraction of fuel mass injected at $\varphi < 2.0$ for modified turbulence cases

mixed NG fuel emanating from the nozzle exit. The development of the fuel rich core is responsible for the rapid increase in mixing over the first 1.0 ms in Fig. 2.

Later into injection, the fuel-rich core of the plenum reaches a finite size and stops growing; the mixing rate slows considerably. Figure 4 demonstrates the behavior of the plume core with a plot of axial penetration of the 2.0 equivalence ratio contour as a function of time. The 2.0 equivalence ratio contour is taken to indicate the envelope of the plume core. The solid line in Fig. 4 corresponds to the injection case with BOI initial conditions shown in Fig. 2. It can be seen that the core stops penetrating after 1.0 ms of injection. The length of the core is 35 mm, which is only 56 percent of the cylinder radius in the baseline engine. This means that the bulk of the unmixed fuel in the engine will be confined to the central region of the cylinder. By contrast, with diesel injection, the liquid droplets that comprise the bulk of the fuel spray penetrate far into the combustion chamber before evaporating. The fuel vapor to be mixed with air is located in a region of the cylinder that is relatively far from the injector nozzle.

Throughout, injection, the mixing of the fuel-rich plume core is controlled by the turbulence generated in the shear layer. The turbulence produced by the jet is determined by the energy of the jet. Hence the mixing of the jet is highly dependent on its own energy.

The importance of turbulence in the mixing process was demonstrated by performing calculations of axisymmetric injection with artificially imposed modifications to the turbulence field. The modifications included turning the turbulence off (i.e., laminar injection), reducing the initial chamber turbulence level by a factor of five, and artificially suppressing turbulence generation in the jet shear layer. The latter result was obtained by modifying the turbulence model to increase turbulence energy dissipation in the jet. Figure 5 shows the mixing characteristics of these cases compared to the baseline turbulence model. Once again the nozzle hole size was 0.413 mm and the chamber pressure and temperature were set at their BOI values for the engine.

From Fig. 5 it can be seen that, for laminar injection and reduced turbulence generated by the jet, the mixing is drastically reduced The large reduction in chamber turbulence has little impact on mixing. These results demonstrate that the conversion of the jet energy to turbulence energy by shear essentially controls the mixing process.

The mixing is faster for the case using TDC main chamber conditions (Fig. 2) due to the higher density of the main chamber air. The TDC initial conditions case represents the fastest mixing that can be achieved for injection into a chamber with a quiescent mean flow at the given injection rate. This is because the plume has essentially an infinite amount of air available for entrainment and there are no interactions with the combustion chamber surfaces. Further enhancements in mixing beyond that shown in Fig. 2 must come from external flow disturbances or changes in the turbulence producing characteristics of the jet.

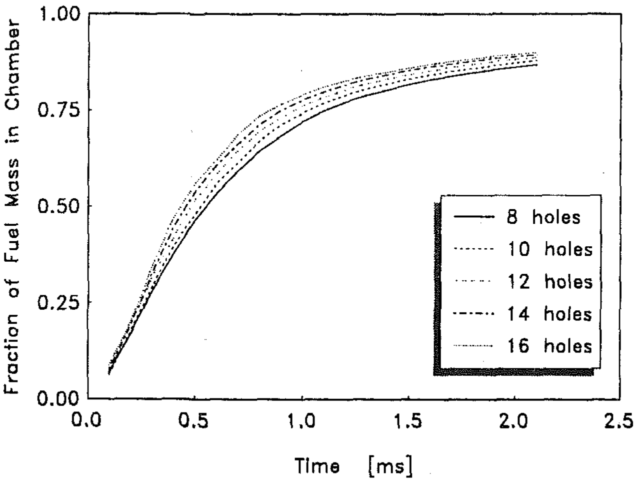

Fig. 6 Fraction of fuel mass in chamber at $\varphi < 2.0$ for all nozzle hole cases

Hole Size Effects on Unconfined Jets. The effect of nozzle hole size on the mixing of unconfined plumes was studied using additional axisymmetric calculations. The insight gained is applied to the investigation of injector design presented by Jennings and Jeske (1994). The hole sizes considered were 0.413, 0.369, 0.317, 0.312, and 0.292 mm, which correspond to injectors with eight, ten, twelve, fourteen, and sixteen holes, respectively, assuming a constant total nozzle area given by the baseline engine injector. Figure 6 shows fuel-air mixing versus time for all of the nozzles.

The comparison of mixing in Fig. 6 is based upon a constant total flow area for the multihole injector. Hence, the injection duration and mass of fuel injected for each nozzle hole size is assumed constant, and the curves represent the most rapid mixing achievable at the given chamber conditions. It can be seen that the smaller holes are most efficient at mixing the fuel. This is because the central fuel rich core of the jet is smaller. The reduction in core size is illustrated by Fig. 4,

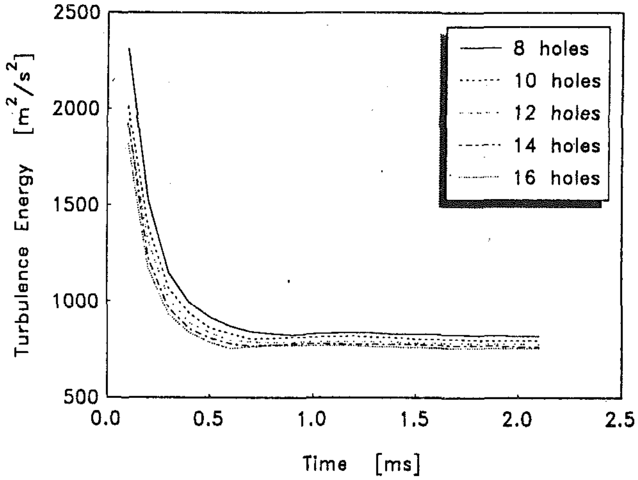

Fig. 7 Axisymmetric injection plume turbulence energy for all nozzle hole cases

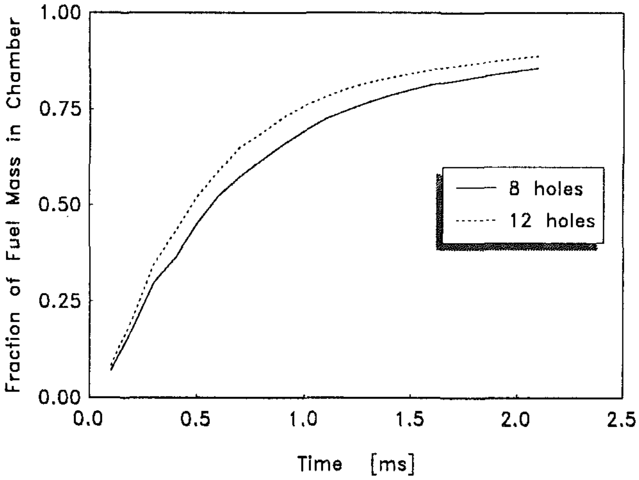

Fig. 8 Fraction of fuel mass in chamber at $\varphi < 2.0$ for in-cylinder, constant-volume chamber eight and twelve-hole nozzle cases

which shows penetration of each plume core defined by the 2.0 equivalence ratio surface.

It can be concluded from Fig. 6 that spreading the injection over a larger number of smaller nozzle holes is more effective at mixing the fuel and air. However, the effects of reduced jet penetration and plume merging are not present in the results of these axisymmetric cases.

One important result of Fig. 6 is that by 2.0 ms, the difference in resultant mixing given by the different nozzle hole sizes is relatively small. The reason can be found from Fig. 7, which shows the average turbulence energy contained within the 2.0 equivalence ratio surface for each nozzle as a function of time. As nozzle size is decreased, the turbulence energy generated by the jet, which controls the mixing, also decreases. This offsets the benefit of reduced plume size.

In the engine, the injector is located at the center of the cylinder and the NG plumes penetrate radially toward the liner. This arrangement is fundamentally different from the axisymmetric configuration discussed so far, in that the amount of air available for mixing increases with radial penetration in the engine. With a larger nozzle hole size, the plumes will penetrate more rapidly to the outer region of the cylinder where the bulk of the air mass resides. A question that arises is whether the improvement in mixing for axisymmetric injection that results from reducing nozzle hole size is negated in the engine by a reduction in radial penetration.

In order to address this issue, three-dimensional calculations of injection into a constant-volume cylindrical chamber were performed with eight and twelve-hole injectors. The injector was positioned on the chamber centerline and the nozzle holes were directed radially outward. The chamber diameter was set equal to the baseline engine cylinder bore (see Table 1) and the chamber height was chosen to be 50 mm, which was large enough to eliminate effects of end wall proximity on plume development. Initial conditions for the chamber were chosen to correspond with combustion chamber BOI conditions for the baseline engine.

The mixing produced by each injector as a function of time is compared in Fig. 8. It can be seen that the mixing for the twelve-hole injector is still better than the eight-hole injector. The difference between the two curves is comparable to that seen in the axisymmetric injection case. This result further establishes the view that a larger number of smaller holes will produce better mixing.

Baseline Engine Injection. A calculation of the baseline engine configuration was performed using the parameters and operating conditions defined above. The initial conditions at BOI were established by performing a CFD calculation of the compression stroke prior to injection. This calculation was begun at IVC (210 deg ATDC). The in-cylinder conditions at IVC were taken to be uniform and were provided by a zero-dimensional thermodynamic calculation of the engine executed using the Ricardo cycle simulation code IRIS. The IRIS code has been used extensively for comprehensive performance and thermal analyses of internal combustion engines (Morel et al., 1988). During injection, cylinder pressure and temperature vary from 45 bar to 100 bar, and 850 K to 1000 K, respectively.

For the baseline engine calculation, advantage was taken of the cyclic symmetry within the cylinder during injection by simulating a 45 deg pie-slice of the cylinder. The slice encompassed a single hole of the injector. The computational grid within the slice consisted of approximately 30,000 cells. The nozzle exit was discretized with a 4×4 matrix of cells. Comparable resolution was used for all of the engine calculations described by Jennings and Jeske (1994).

Plume visualizations for the baseline injection are shown in Figs. 9 and 10 at times of 9 and 17 deg ABOI (344 and 352 deg ATDC). Specifically, the figures show three-dimensional views of the 0.5 equivalence ratio iso-surface. All of the gas contained inside the surface is richer than 0.5 equivalence ratio. Two views are shown in each figure: an oblique view of a 270 deg section of the cylinder looking into the bowl from above; and a cross-sectional view of a 180 deg slice of the cylinder. The oblique view shows six of eight NG plumes.

It can be seen that the penetration of the NG jets is very good. By 17 deg ABOI, the plumes have reached the edge of the piston bowl, and by TDC (not shown here) they are penetrating into the squish region. A significant feature of the injection flow is the deflection of the NG plume towards the cylinder head. This is apparent in all of the plume pictures. In Figs. 9(*a*) and 10(*a*), the openings in the tops of the NG plumes indicate the regions of the plume intersection with the head. In general, this behavior is undesirable since it prevents penetration into the bowl, where a large portion of the air mass resides, and it severely restricts air entrainment from the head side of the plumes, i.e., there is less plume surface area exposed to air.

The mechanism for the jet deflection can be understood by considering the pressure and velocity fields in the vicinity of the nozzle. Figure 11 shows pressure contours and velocity vectors at TDC in an axial-radial plane that cuts through the center of the nozzle. In Fig 11(*a*), two low-pressure areas above and below the jet have formed. These are caused by entrainment of air mass into the jet from the local surrounding volume. Below the jet, air is entrained from the relatively large

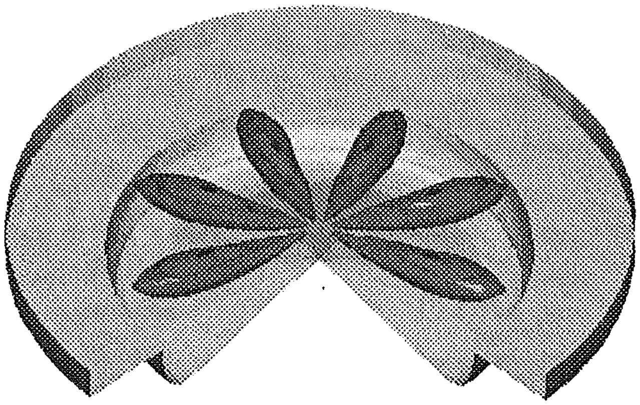

(a) Top view

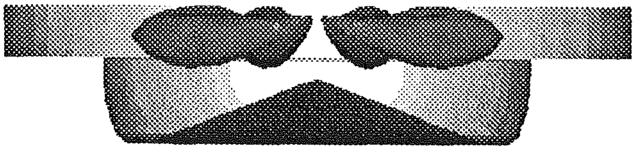

(b) Side view

Fig. 9 Baseline injection plume visualizations at 9 deg ABOI

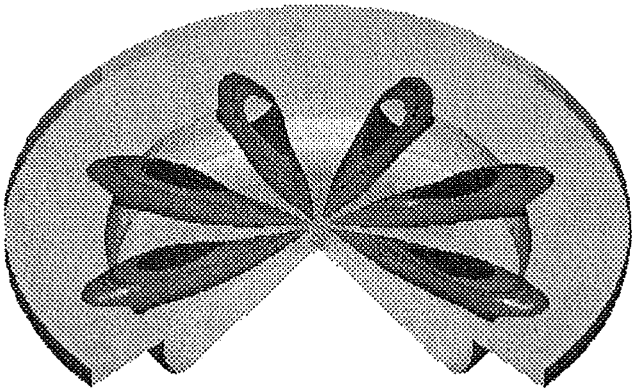

(a) Top view

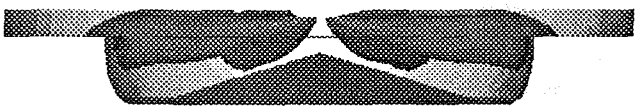

(b) Side view

Fig. 10 Baseline injection plume visualizations at 17 deg ABOI

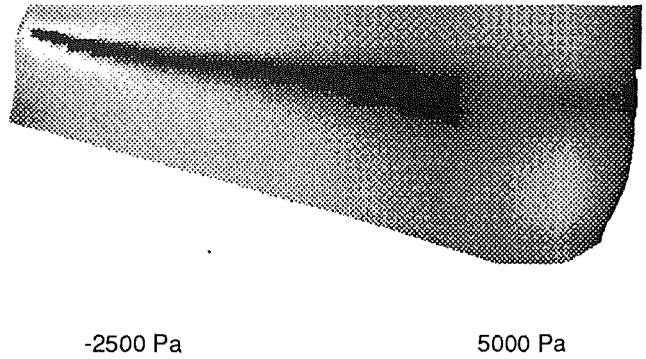

(a) Axial-radial pressure contours

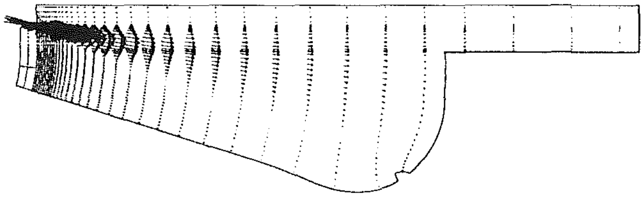

(b) Axial-radial velocity vectors

Fig. 11 Baseline injection at TDC

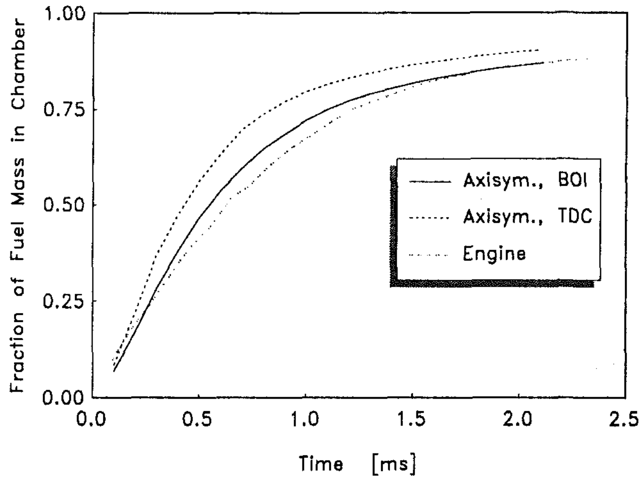

Fig. 12 Fraction of fuel mass in chamber at $\varphi<2.0$ for axisymmetric and baseline injection cases

volume between the piston and injector. Above the jet, air must be entrained from farther downstream of the nozzle due to the limited space between the nozzle and the head. In effect, the entrained mass must be supplied by the region into which the gas jet is penetrating. The flow generated is strong enough to turn the jet toward the head. The flow mechanism driving this phenomenon is known as the Coanda effect. The change in direction of the jet can be readily seen in the velocity vectors of Fig. 11(*b*).

The fuel-air mixing as a function of time for the baseline engine is shown in Fig. 12. Also shown on the figure are the axisymmetric jet mixing curves from Fig. 2. These curves bound the range of best mixing for the given nozzle hole size. It can be seen that improvements can be made to the rate with which mixing occurs in the engine, particularly during the early stages of injection.

The results for injection in the baseline engine configuration have demonstrated the importance of surface interactions on the development of the NG plumes in engine geometries. The sensitivity of the NG jets to surface proximity is not present with diesel injection due to the large difference in density between the fuels. The impact of surface interaction on the NG jet mixing is illustrated by the comparison of Fig. 12. This provides motivation for further investigation of the effect of engine design parameters on the mixing process.

Conclusions

The important conclusions that can be drawn from the analysis are:

1 The structure of the NG plume is characterized by a core of unmixed fuel that is confined to a region near the nozzle exit. The core contains the bulk of the unmixed fuel mass and

the turbulence generated by the jet shear layer controls the mixing of this fuel.

2 For injection in the engine:

- Combustion chamber surface interactions play a key role in the plume penetration and mixing.
- Overall, effects of plume confinement are extremely important. With the injector nozzles close to the head surface, as they are with a diesel injector, jet deflection towards the head can occur due to the Coanda effect; and
- The bulk of the unmixed fuel vapor is confined to the central region of the cylinder, which is fundamentally different from diesel injection.

3 Neglecting plume merging effects, smaller nozzle holes are more effective at mixing the fuel and air because the fuel rich plume core is smaller.

Acknowledgments

This work was supported by GRI funding through contract number 5092-291-2304 and managed by Mr. Allen Wells. The authors gratefully acknowledge the technical assistance of Detroit Diesel Corporation and Catepillar Inc. In particular, the authors would like to thank Drs. Richard Winsor and Albert Lee of Detroit Diesel Corporation and Mr. Bernard Richards, Mr. Martin Willie, Mr. William Hayes, and Dr. John Clarke of Caterpillar Inc. for the useful insights gained from our many discussions.

References

Bracco, F. V., 1992, personal communication via Albert Lee of Detroit Diesel Corporation.

Fraser, R. A., Siebers, D. L., and Edwards, C. F., 1991, "Autoignition of Methane and Natural Gas in a Simulated Diesel Environment," SAE Paper No. 910227.

Gosman, A. D., Pun, W. M., Runchel, A. K., Spälding, D. B., and Wolfshtein, M., 1969, *Heat and Mass Transfer in Recirculating Flows*, Academic Press, New York.

Gosman, A. D., 1985, "Multidimensional Modeling of Cold Flows and Turbulence in Reciprocating Engines," SAE Paper No. 850344.

Jennings, M. J., and Morel, T., 1988, "Observations on the Application of the k-ϵ Model to Internal Combustion Engines Flows," *Combustion Science and Technology*, Vol. 58, pp. 177–193.

Jennings, M. J., and Jeske, F. R., 1994, "Analysis of the Injection Process in Direct Injected Natural Gas Engines: Part II—Effects of Injector and Combustion Chamber Design," ASME JOURNAL OF ENGINEERING FOR GAS TURBINES AND POWER, Vol. 116, this issue, pp. 806–813.

Jeske, F. R., Jennings, M. J., and Welch, A. B., 1992, "Modeling of the Natural Gas Injection Process in a Two Stroke Diesel Engine," SAE Paper No. 920192.

Johns, R. J. R., 1984, "A Unified Method for Calculating Engine Flows," ASME Paper No. 84-DGP-18.

Johns, R. J. R., 1984, "Progress in the Development of a Detailed Model for Diesel Combustion," *Diagnostics and Modeling of Combustion in IC Engines*, COMODIA 90.

Johns, R. J. R., and Jones, P. M., 1990, "Computer Modeling of the Flow in a Lean Burn Natural Gas Engine," Computers in Engine Technology Conference, I. Mech. E., Cambridge University, United Kingdom.

Launder, B. E., and Spalding, D. B., 1972, *Mathematical Models of Turbulence*, Academic Press, New York.

McKinley, T. L., and Primus, R. J., 1990, "Three-Dimensional Calculations of Air Motion, Sprays and Combustion in Quiescent Direct Injection Diesel Engines," presented at the IC Engine Symposium, ASME ETCE Meeting, New Orleans, LA.

Morel, T., Rackmil, C. I., Keriber, R., and Jennings, M. J., 1988, "Model for Heat Transfer and Combustion in Spark Ignited Engines and Its Comparison With Experiments," SAE Paper No. 880198.

Reitz, R. D., and Rutland, C. J., 1991, "3-D Modeling of Diesel Engine Intake Flow, Combustion and Emissions," SAE Paper No. 911789.

Reynolds, W. C., 1978, "Modeling of Fluid Motions in Engines, An Introductory Overview," *Combustion Modeling in Reciprocating Engines*, GMR Laboratories.

Analysis of the Injection Process in Direct Injected Natural Gas Engines: Part II—Effects of Injector and Combustion Chamber Design

M. J. Jennings

F. R. Jeske

Computational Fluid Dynamics,
Ricardo North America,
Burr Ridge, IL 60521

A study of natural gas (NG) direct injection (DI) processes in engines has been performed using multidimensional computational fluid dynamics analysis. The purpose was to investigate the effects of key engine design parameters on the mixing in DI NG engines. Full three-dimensional calculations of injection into a medium heavy-duty diesel engine cylinder were performed. Perturbations on a baseline engine configuration were considered. In spite of single plume axisymmetric injection calculations that show mixing improves as nozzle hole size is reduced: plume merging caused by having too many nozzle holes has a severe negative impact on mixing; and increasing the number of injector holes strengthens plume deflection toward the cylinder head, which also adversely affects mixing. The optimal number of holes for a quiescent engine was found to be that which produces the largest number of separate NG plumes. Increasing the nozzle angle to reduce plume deflection can adversely affect mixing due to reduced jet radial penetration. Increasing the injector tip height is an effective approach to eliminating plume deflection and improving mixing. Extremely high-velocity squish flows, with penetration to the center of the piston bowl, are necessary to have a significant impact on mixing. Possible improvements in mixing can be realized by relieving the center of the piston bowl in typical "Mexican hat" bowl designs. CFD analysis can effectively be used to optimize combustion chamber geometry by fitting the geometry to computed plume shapes.

Introduction

Direct injected (DI) natural gas (NG) engines offer the potential for significant performance and emissions benefits compared to other types of NG engines. These benefits derive primarily from the charge stratification that occurs when the NG is injected very close to the start of combustion. This charge stratification allows for the use of very lean overall equivalence ratios and produces excellent knock tolerance.

The full potential of DI NG engines can only be realized by understanding the flow mechanisms controlling the injection process. The present paper reports on the use of multidimensional computational fluid dynamics (CFD) analysis to achieve that understanding. Previous use of CFD analysis has established the usefulness for improving other types of NG engines (Johns and Jones, 1991; Jeske et al., 1992), and DI diesel engines (McKinley and Primus, 1990). The work presented here is a continuation of the investigation reported by Jennings and Jeske (1994). In that paper, the behavior of NG plumes in nonconfining and engine in-cylinder geometries was studied. Here, an investigation of the effects of key engine design parameters on the injection process is reported.

Approach

CFD calculations of NG injection into a diesel combustion chamber form the basis of the investigation. The effects of perturbations to a baseline engine geometry on the injection process are discussed.

The CFD methodology used is based upon the engine CFD code described by Johns (1984). The code solves the ensemble-averaged Navier–Stokes equations governing turbulent compressible flow in three dimensions. Further details of the code are presented by Jennings and Jeske (1994).

The baseline engine geometry considered was also described by Jennings and Jeske (1994). The engine geometry, injector geometry, injection data, and operating conditions are presented in Table 1. The configuration is based upon a medium heavy-duty four-stroke engine with a displacement of 1.64 *l* per cylinder, and a rated speed and full-load power of 1800

Contributed by the Internal Combustion Engine Division and presented at the 15th Annual Fall Technical Conference of the ASME Internal Combustion Engine Division, Morgantown, West Virginia, September 26–29, 1993. Manuscript received by the Internal Combustion Engine Division January 28, 1994. Associate Technical Editor: W. Cheng.

Table 1 Summary of baseline NG engine configuration

ENGINE GEOMETRY	
Bore	124.5 mm
Stroke	137.2 mm
TDC Clearance Height	4.32 mm
Compression Ratio	16:1
Displaced Volume	1.64 *l*
INJECTOR GEOMETRY	
Number of Holes	8
Nozzle Offset from Head	2.0 mm
Nozzle Offset from Centerline	3.1 mm
Nozzle Angle from Head	15°
Nozzle Diameter	0.413 mm
INJECTION DATA	
Injection Pressure	200 bar
Fuel Temperature	350 K
Injected Fuel Mass	124.4 mg
Injection Duration	40°
Injection Timing	25° BTDC
Injection Profile	Slug
OPERATING CONDITIONS	
Rated Speed	1800 rpm
Equivalence Ratio	0.55
Power/Cylinder	37.3 kW

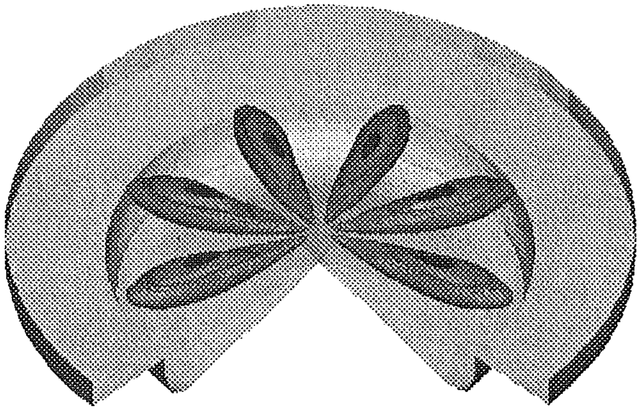
(a) Top View

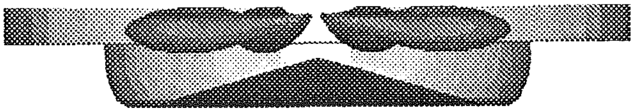
(b) Side View

Fig. 1 Baseline plume visualizations at 10 deg ABOI

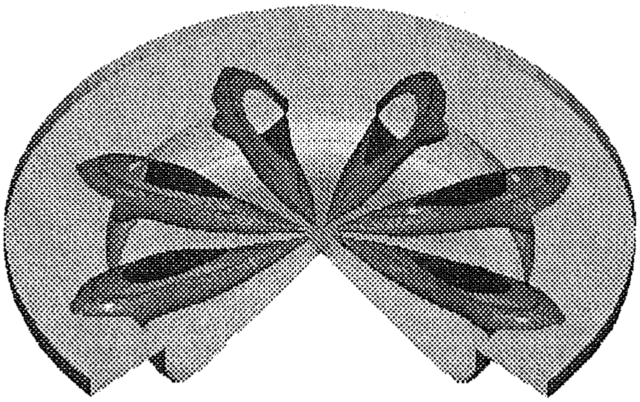
(a) Top View

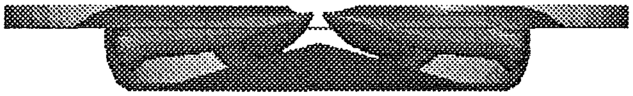
(b) Side View

Fig. 2 Baseline plume visualizations at 20 deg ABOI

rpm and 37.3 kW per cylinder, respectively. All calculations were performed at the rated speed/full load operating point.

The calculated NG plumes are visualized using three-dimensional plots of constant equivalence ratio (φ) surfaces. In addition, the injection process is quantified via measures of fuel-air mixing, fuel heat-up and plume penetration. Fuel-air mixing is expressed in terms of the mass of fuel mixed to equivalence ratio less than 2.0. Fuel heat-up is quantified in terms of the mass of fuel heated above 900 K. Plume penetration is measured in terms of the maximum radial distance from the injector to the outer edges of a selected equivalence ratio iso-surface. Further discussion of the significance of these parameters can be found from Jennings and Jeske (1994).

Discussion of Results

Unconfined Jet Behavior and Baseline Engine Injection. Jennings and Jeske (1994), discussed the structure and mixing of unconfined and in-cylinder NG plumes. The key results from that investigation are:

1 The structure of the NG plume is characterized by a core of unmixed fuel that is confined to a region near the nozzle exit. The core contains the bulk of the unmixed fuel mass, and the turbulence generated by the jet shear layer controls the mixing of this fuel.

2 For engine in-cylinder injection:

- Combustion chamber surface interactions play a key role in the plume penetration and mixing.
- Overall, the effects of plume confinement are extremely important. With the injector nozzles close to the head surface, as they are with a diesel injector, jet deflection toward the head can occur due to the Coanda effect.
- The bulk of the unmixed fuel is confined to the central region of the cylinder.

3 Neglecting plume merging effects, smaller nozzle holes are more effective at mixing because the fuel-rich plume core is smaller.

Figures 1 and 2 show plume visualizations, in terms of the 0.5 equivalence ratio iso-surface, for the baseline engine injection at 10 and 20 deg ABOI (345 and 355 deg ATDC). Plume deflection toward the head surface is readily apparent. Figure 3 shows the fuel-air mixing as a function of time for the baseline engine. Comparison is made to two unconfined plume cases, which represent single nozzle injection along the centerline of a constant volume cylinder. These cases were reported by Jennings and Jeske (1994) and they represent the ideal mixing that can be achieved for injection into a quiescent chamber. The adverse effect of surface interactions on the mixing for the engine case is clearly evident. It can be seen that significant room for improvement in the mixing for the engine injection exists.

Effect of Injector Design. The effect of injector design on

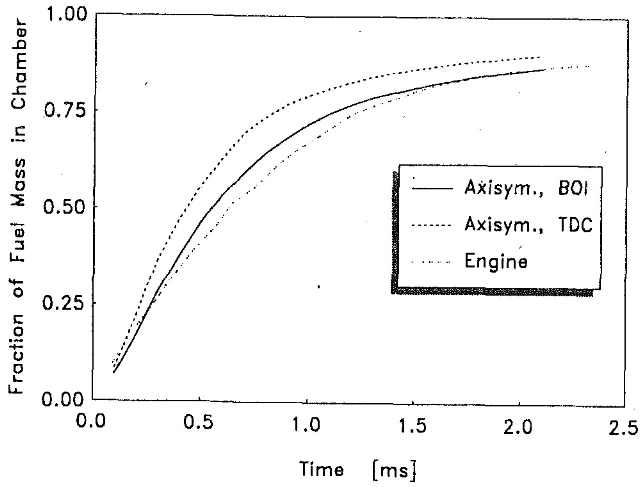

Fig. 3 Fraction of fuel mass in chamber at $\varphi < 2.0$

the fuel injection process was investigated by considering variations in the following key injector parameters:

- Number of nozzle holes/nozzle hole size;
- Nozzle angle; and
- Injector tip height.

Hole Size Effects on Engine Injection. Jennings and Jeske (1994) found that, for unconfined NG plumes, smaller nozzle holes were more efficient for mixing the fuel and air. Full engine calculations were performed using injectors with more holes than the baseline in order to consider directly the effect on the engine injection process. Injectors with twelve and sixteen holes were used. All other configuration and operating parameters were kept at their baseline values.

The plume development of the sixteen-hole injector is depicted in Figs. 4 and 5. These figures show two views each of the NG plumes at 10 deg ABOI (345 deg ATDC), and 20 deg ABOI (355 deg ATDC), respectively. It can be seen that, throughout the injection period, there is substantial plume merging and the plumes remain attached to the cylinder head as a result of the Coanda effect mentioned above. The radial penetration is less than that for the baseline case, due to the smaller hole size.

Comparing Figs. 4 and 5 to the corresponding baseline case results of Figs. 1 and 2 indicates that the deflection of the NG plumes toward the cylinder head is much more severe with the sixteen-hole injector. The more pronounced deflection is caused by the extreme confinement of the plumes in the circumferential direction near the injector. There is less air available from between the plumes for entrainment, therefore entrainment from above and below the plumes becomes stronger. This intensifies the Coanda effect that drives the plume deflection.

The NG plumes produced by the twelve-hole injector display a similar behavior to those of the sixteen-hole injector, with regard to plume attachment to the cylinder head. The plume merging is much less severe than with the sixteen-hole injector.

The fuel mixing characteristics of the three injectors are compared in Fig. 6. The eight and twelve-hole injectors produce much more rapid mixing than the sixteen-hole injector. The twelve-hole injector gives slightly improved mixing over the first 15 deg of injection. Beyond 10 deg BTDC, the mixing for the eight-hole injector exceeds that of the twelve.

The trend with hole size displayed in Fig. 6 is opposite to that given by the axisymmetric injection cases discussed by Jennings and Jeske (1994). The causes of the trend reversal are the increased interaction of the NG plumes with the head surface and the plume merging that occurs when the number

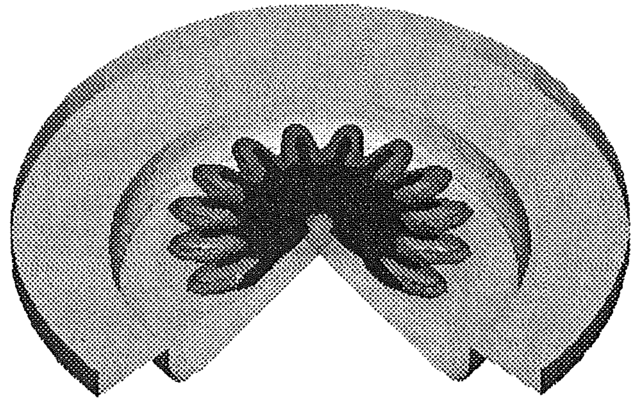

(a) Top View

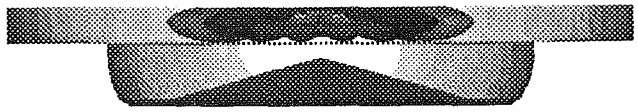

(b) Side View

Fig. 4 Sixteen-hole injector plume visualizations at 10 deg ABOI

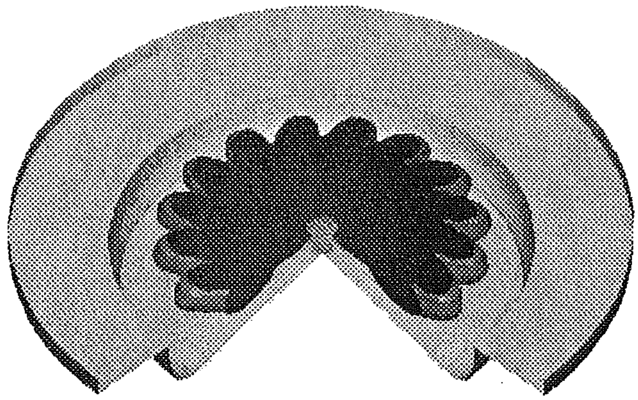

(a) Top View

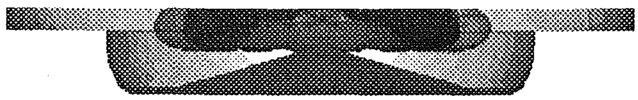

(b) Side View

Fig. 5 Sixteen-nozzle hole injector plume visualizations at 20 deg ABOI

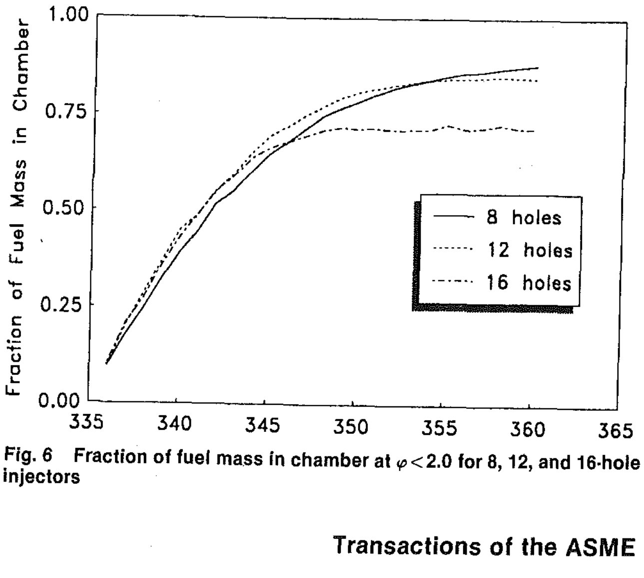

Fig. 6 Fraction of fuel mass in chamber at $\varphi < 2.0$ for 8, 12, and 16-hole injectors

of injector holes is increased. The attachment of the NG plumes to the cylinder head hampers the air entrainment process. In addition, the excessive plume merging, caused by a lack of sufficient air mass between the plumes, significantly degrades the injector performance. These are the primary reasons why the sixteen-hole injector performs much worse than the eight and twelve-hole injectors. The enhancement of the Coanda effect and the plume merging are phenomena that were not present in the constant-volume chamber calculations described above.

The unconfined NG plume behavior suggests that an injector with small holes will produce more rapid mixing. The engine results with different hole sizes indicate that there is a constraint on the maximum number of holes for good mixing in the engine. This constraint is imposed by the merging of plumes. The optimal number of holes is that which produces the largest number of separate plumes.

An alternative view of the effect of the number of holes/hole size is offered by considering the concept of plume surface area. The plume surface area represents the flow area for entrainment of air. The larger the plume surface area, the more air entrainment into the plume, hence the better the mixing. Therefore, the optimal choice for the number of injector holes is that which produces the largest total plume surface area (i.e., counting all of the plumes).

For a given total injector flow area (i.e., counting all of the nozzle holes), a larger number of smaller holes will produce a larger total plume surface area. Plume merging, however, will drastically reduce plume surface area and degrade the mixing. Therefore, by considering plume surface area, the same conclusion is reached, namely that the optimal number of holes is that which produces the largest number of separate plumes. All of these statements regarding plume surface area have been confirmed by computing and comparing plume surface areas for several of the unconfined and engine injection cases.

The CFD results were further used to identify the optimal number of holes for the engine configuration under consideration. This can be accomplished by quantifying the plume circumferential spread angle. The optimal number of holes is then given by the number of spread angles that can be fit circumferentially within the cylinder. The spread angle of the plume from the 0.5 equivalence ratio surface was determined to be approximately 29 deg. The axisymmetric cases indicate that to first order, this angle will not vary significantly with nozzle size. Using a 29 deg spread angle, the optimal number of holes is calculated to be twelve.

The engine injection results discussed above indicate that the performance of the twelve-hole injector is actually worse than the eight-hole injector. This is contrary to the analysis used to deduce that the optimal number of holes is twelve. The reason for the discrepancy is the excessive plume deflection toward the head surface that is produced by the twelve-hole injector. Plume intersection with the head reduces the amount of plume surface area available for entrainment of air. Though not shown here, comparison plots of plume intersection area with the head confirm that the twelve and sixteen-hole injectors produce much larger plume-head intersections than the eight-hole injector. If the jet deflection were eliminated, the twelve hole injector would be expected to produce the most rapid mixing.

Analysis of Jet Deflection. The jet deflection plays a key role in the engine injection process for all the configurations discussed above. An investigation was conducted to identify practical design changes that could be made to eliminate the deflection. The impact on penetration and mixing was assessed.

An important parameter controlling the jet deflection is the proximity of the head surface to the injector nozzles. Reducing the proximity will weaken the Coanda effect, and hence the jet deflection. The injector parameters that directly impact the head surface proximity are the nozzle angle relative to the head and the injector tip height (i.e., the normal distance between the head and the nozzle holes). Increasing either of these parameters will tend to reduce the head proximity.

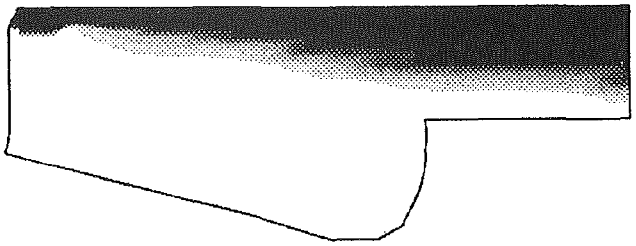

(a) Contours of φ for the 15° injector

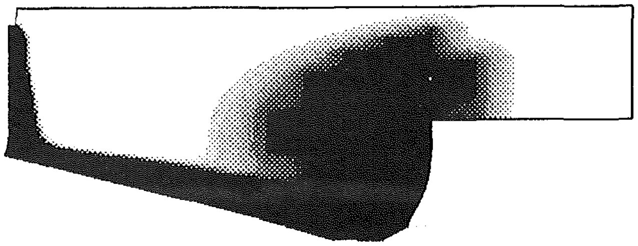

(b) Contours of φ for the 60° injector

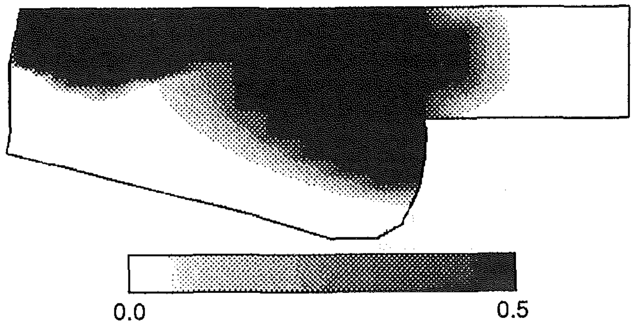

(c) Contours of φ for the 6 mm injector

Fig. 7 Contours of φ at 2.0 ms ABOI for various poppet-valve injectors

A set of simplified constant-volume chamber calculations were performed to study the sensitivity of the jet deflection to nozzle angle and tip height. The chamber was identical in geometry to the engine combustion chamber, with the piston frozen at its BOI position. BOI combustion chamber conditions were used for initial conditions on the injection process.

The injector configuration used featured a poppet valve rather than discrete holes. This produces a single continuous "umbrella" plume that is axisymmetric about the cylinder centerline. The configuration effectively represents an injector with an infinite number of holes. The flow area and injection duration were kept the same as the baseline engine case.

Simulations with the poppet valve injector and constant-volume chamber required significantly less computational effort than full engine calculations. This permitted execution of a comprehensive parametric sweep on nozzle angle and tip height. It is important to note that the structure of the poppet valve plume is different in many respects from that of the plume generated by a discrete hole. In light of this fact, a careful interpretation of the poppet valve results is required. In spite of the differences, useful conclusions can be drawn that are applicable to discrete hole injectors.

With the poppet valve injector, the Coanda effect that causes the jet deflection is maximized, since there is no air entrainment possible in the circumferential direction. In other words the plume confinement in the circumferential direction, which is

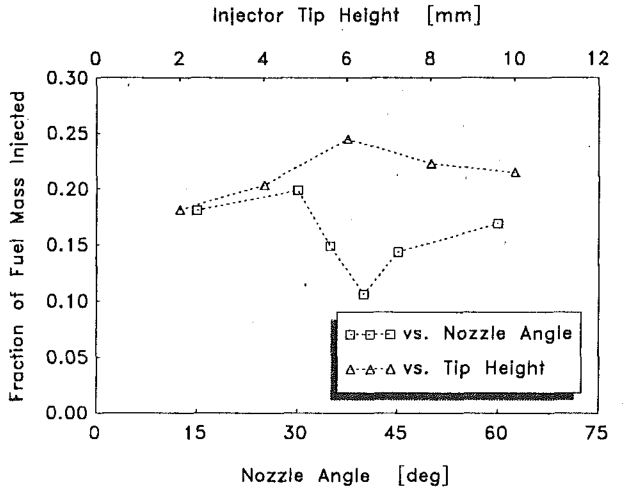

Fig. 8 Fraction of fuel mass in chamber at $\varphi < 2.0$ for various injection angles and tip heights at 2.0 ms ABOI

shown to affect the jet deflection in the cases described above, is the worst case for the poppet valve injector.

Poppet valve injection angles of 15, 30, 35, 40, 45, and 60 deg were considered. The injector tip height was kept at its baseline value of 2.0 mm. Samples of the plumes for the 15 and 60 deg injection angles are shown in Fig. 7. Contours of equivalence ratio 2.0 ms ABOI are displayed within an axial-radial plane. The head surface is at the top of the plane and the centerline is on the left boundary of the plane. The injector is located in the upper left corner of the plane. The solid black color indicates equivalence ratio greater than 0.5.

The plume pictures of Fig. 7 verify that the poppet valve plume is strongly dominated by the Coanda effect. For angles less than 30 deg, the plume attaches to the head surface and penetrates well into the squish zone by 2.0 ms ABOI. For injection angles greater than 40 deg, the plume collapses along the centerline, impinges on the piston bowl, and spreads along the bowl surface. For angles between 30 and 40 deg, the plume remains detached from the head and centerline. However, there is still significant recirculation of NG back to the nozzle exit.

It is worthwhile noting that the plume behavior predicted by the calculations for different injection angles matches well the plume behavior observed in the experimental work of Ouelette and Hill (1992). In this work, visualizations of the plume generated by a poppet valve injector were produced for different injection angles. The measured plume remained attached to the injector mounting surface for injection angles of 30 deg and less. This result establishes some confidence in the accuracy of the numerical predictions.

The mixing performance for each case is illustrated by Fig. 8, which shows fuel mass below equivalence ratio 2.0 at 2.0 ms ABOI as a function of injection angle and tip height. The fuel mass is nondimensionalized by the fuel mass in the chamber at 2.0 ms. It can be seen that the mixing tends to get worse as the injection angle increases. The worst mixing was achieved by the injection angles in the range where the plume remains detached from the head and centerline (i.e., 30 to 40 deg).

The reason for the worsened mixing is that the radial penetration of the NG plume decreases with increasing injection angle. In the engine combustion chamber with injection outward from the centerline, the amount of air available for mixing increases with radial distance. Steepening the injection angle reduces the NG jet radial momentum flux, and hence the radial penetration. The increase in air available for entrainment from above the plume is not enough to offset the effect of the decrease in radial penetration.

The mixing result is relevant to the actual engine, which features discrete NG plumes. Increasing the nozzle angle will create a similar reduction in radial penetration, which could result in poorer mixing. For the engine configuration being considered, the clearance height is large and the plumes generated by the baseline injector penetrate well into the squish region, where there is a large air mass available for mixing. Therefore, it is probable that the reduction in radial penetration caused by steepening the nozzle angle will have a net detrimental effect on the mixing. This is an important consideration for choosing an appropriate nozzle angle for DI NG engines.

The loss in radial penetration and subsequent negative impact on mixing, can be overcome by redesigning the combustion chamber to bring the air closer to the injector. For the engine configuration being investigated, this would mean reducing the squish volume, reducing the bowl diameter, and increasing the bowl depth.

Further calculations were performed with injector tip heights of 2, 4, 6, 8, and 10 mm. The baseline injection angle of 15 deg was used for all cases. Once again, the chamber conditions corresponded to BOI conditions in the engine.

Figure 7(*c*) shows equivalence ratio contours for the 6 mm injector type height. These can be compared with the baseline 2 mm tip height result of Fig. 7(*a*). For tip heights beyond 4 mm, the NG plume detaches from the head and becomes extremely thick. For the 8 and 10 mm tips, the plume is influenced by recirculation in the piston bowl, which tends to reduce radial penetration.

The mixing characteristics of the various tip height injectors are again shown in Fig. 8. Nondimensional fuel mass mixed to equivalence ratios below 2.0 at 2.0 ms ABOI is plotted against injector tip height. The mixing improves significantly with increasing tip height. The best mixing is achieved with a tip height of 6 mm, which would put the injector nozzles in the engine halfway between the piston and head at BOI.

The poppet valve injector simulations have shown that increasing the injector tip height appears to be a more effective approach to eliminating the jet deflection and improving mixing than increasing nozzle angle. This is partly due to the fact that increasing the tip height does not involve reducing the radial momentum flux of the NG plume.

Optimized Injector Calculation. To complete the study of the effect of injector design, an engine calculation was performed using an optimized injector configuration deduced from the analysis described above. The optimized injector featured 12 nozzle holes and a tip height of 6.0 mm. The nozzle angle was left at its baseline value of 15 deg. All other configuration and operating parameters were also kept at their baseline values.

Figures 9 and 10 show plume development for the optimized injector at 10 and 20 deg ABOI, respectively. The plumes are represented by the 0.5 equivalence ratio iso-surface. At 10 deg after injection (Fig. 9), plume development looks good, with no appreciable deflection of the NG jets. The plumes are completely detached from all of the combustion chamber surfaces. Penetration into the bowl is very rapid.

At 20 deg after injection (Fig. 10), the plumes have nearly penetrated to the outer edge of the piston bowl. The plumes are completely contained within the bowl, and intersection with head surface has not occurred. It is evident in Fig. 10(*b*) that the plumes have attached themselves to the bottom of the piston bowl, due to the proximity of this surface to the injector nozzles late in the compression stroke. This will have an adverse affect on mixing.

Figure 11(*a*) shows the mixing performance achieved with the optimized injector compared to the baseline injector with eight holes and a tip height of 2 mm. It can be seen that the optimized injector gives significantly improved mixing over the first 15 deg of injection. Beyond 10 deg BTDC, the mixing rate levels off and becomes slightly worse than the baseline injector by TDC. The plume intersection with the bowl edge

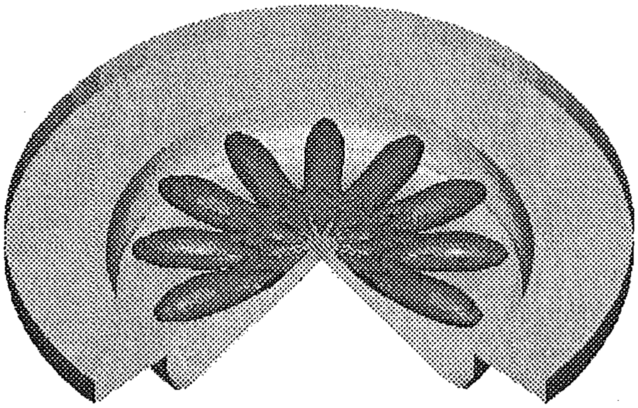

(a) Top View

(b) Side View

Fig. 9 Optimized injector plume visualizations at 10 deg ABOI

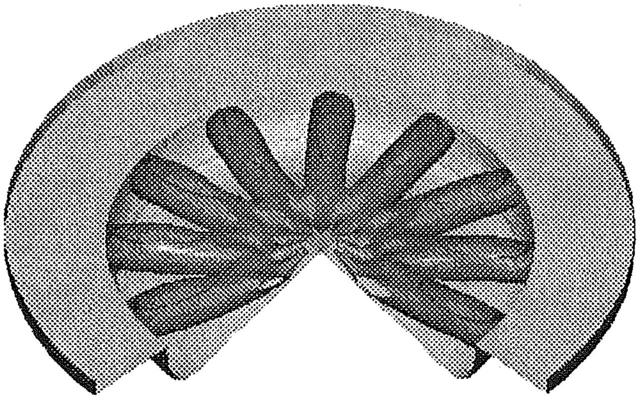

(a) Top View

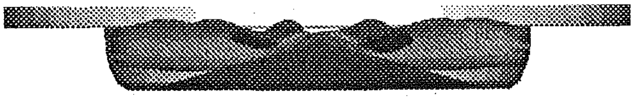

(b) Side View

Fig. 10 Optimized injector plume visualizations at 20 deg ABOI

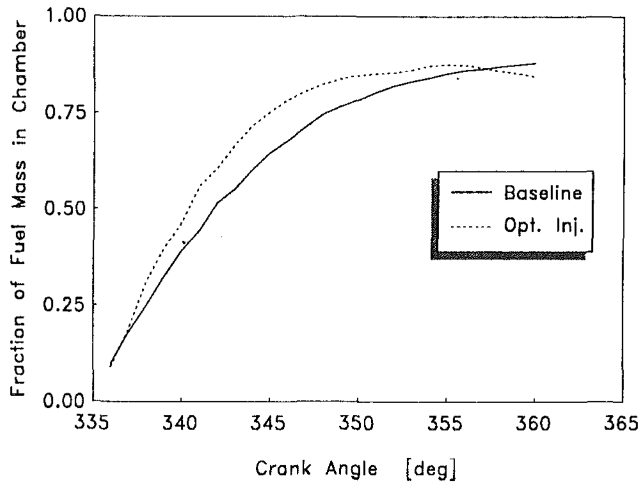

(a) Fraction of fuel mass in chamber at $\varphi<2.0$

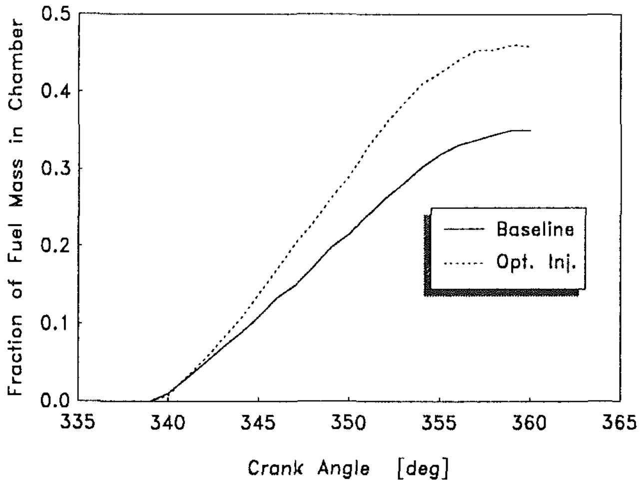

(b) Fraction of fuel mass in chamber at T>900 K

Fig. 11 Mixing characteristics of optimized injector

depicted in Fig. 10(*b*) is responsible for the deterioration in mixing. With the baseline injector, the plumes penetrate into the squish region. The extended tip height of the optimized injector prevents this from happening. Also, late into injection, the optimized injector plumes attach to the bottom of the piston bowl. This will adversely affect the mixing. It is clear that the piston bowl needs to be redesigned to match the penetration characteristics of the optimized injector properly.

The rate at which fuel is heated during injection for the two injectors is shown in Fig. 11(*b*) in terms of the mass of in-cylinder fuel above a temperature of 900 K. It can be seen that the rate of fuel heat-up is markedly improved with the optimized injector. The fraction of fuel above 900 K is much less than that mixed to equivalence ratio less than 2.0, for both cases. Hence, the fuel mass above 900 K is mixed to much lower equivalence ratios than 2.0. The large difference between the curves of Fig. 11(*b*) indicates that significantly more fuel is mixed to low equivalence ratios for the optimized injector case than the baseline case. This results from the extra fuel mixed to equivalence ratio below 2.0 early during injection (see Fig. 11(*a*)) being mixed to even lower equivalence ratios as injection proceeds. The extended mixing raises the temperature of the fuel closer to that of the chamber air.

In general, the optimized injector gives improved performance, in terms of more rapid mixing, for injection into an engine. This supports the conclusions of the prior analysis of the constant volume chamber injection cases.

Effect of Squish Flow and Bowl Design. The effect of squish flow and piston bowl geometry was studied using the results of two additional engine calculations. The first considered injection into a pancake combustion chamber with no piston bowl, and the second considered injection into a combustion chamber featuring reconfigured piston bowl and a reduced TDC clearance height.

The flat piston calculation used the same injector configuration as the baseline engine. The compression ratio was kept at its baseline value of 16:1 by increasing the TDC clearance height to offset the loss of the piston bowl volume. All other parameters were held at their baseline values.

A separate calculation was performed that combined the optimized injector with a reconfigured combustion chamber. The combustion chamber was altered by reducing the TDC clearance height by a factor of 2 (from 4.32 mm to 2.16 mm)

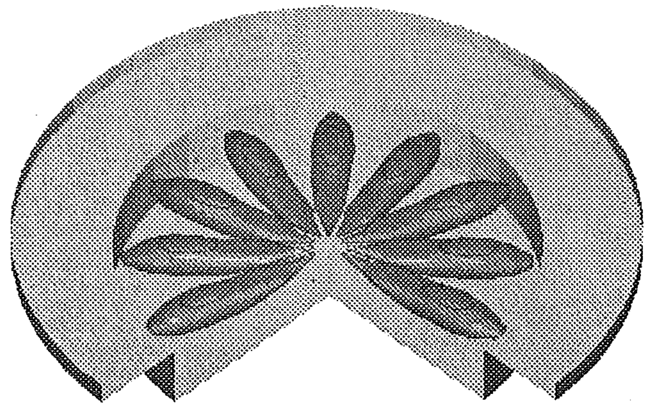

(a) Top View

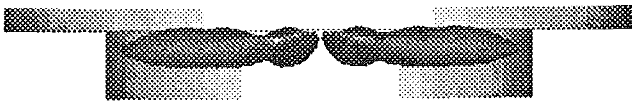

(b) Side View

Fig. 12 Reconfigured combustion chamber plume visualizations at 10 deg ABOI

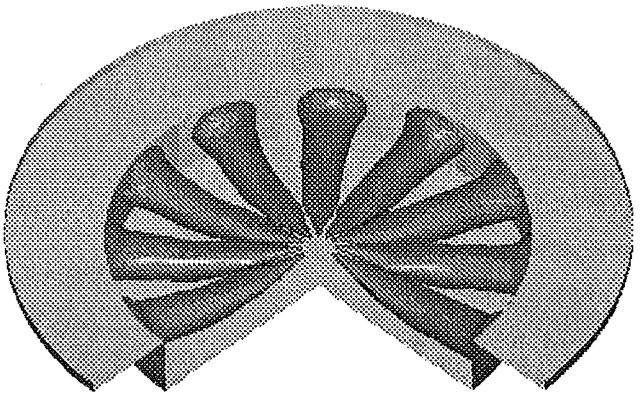

(a) Top View

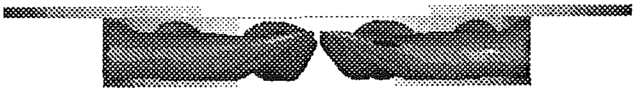

(b) Side View

Fig. 13 Re-configured combustion chamber plume visualizations at 20 deg ABOI

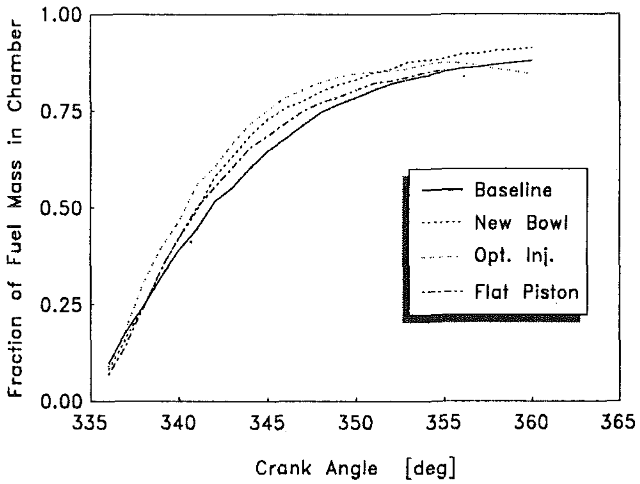

(a) Fraction of fuel mass in chamber at $\varphi<2.0$

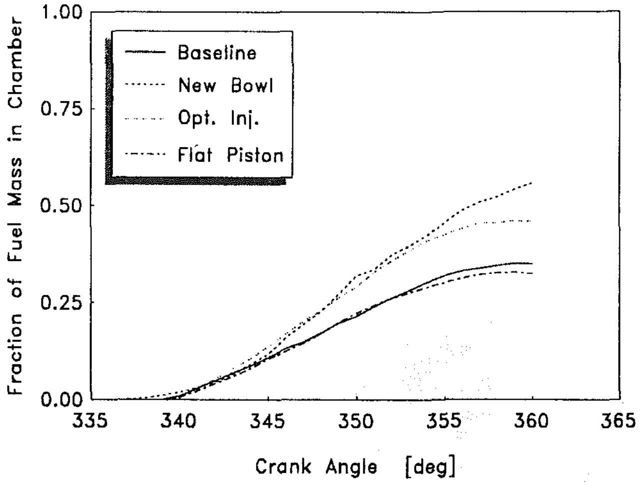

(b) Fraction of fuel mass in chamber at T>900 K

Fig. 14 Mixing characteristics of reconfigured combustion chamber

and by changing the bowl geometry to a square cross section. The bowl diameter was kept the same and the bowl depth was increased to 14.64 mm. The resulting increased bowl volume offset the reduction in squish volume such that the compression ratio remained constant. All other parameters were kept the same as the baseline engine configuration.

For the reconfigured combustion chamber, the TDC clearance height was reduced in order to increase the squish velocity. More than a factor of two increase in peak squish velocity was realized. The center of the piston bowl was relieved in order to provide more air for entrainment into the rich cores of the NG plumes, and to prevent attachment of the NG plumes to the bowl surface during the latter part of the compression stroke.

Figures 12 and 13 show the plume development for the reconfigured combustion chamber at 10 and 20 deg ABOI. The plumes penetrate directly into the bowl volume without interaction with any of the combustion chamber surfaces. In particular, the plumes do not attach to the bottom of the piston bowl, as was the case with the baseline bowl design. By 355 deg the plumes have impacted the bowl edge. This is relatively early in the injection process, indicating that a larger diameter bowl would be appropriate.

Figure 14 shows the fuel-air mixing and fuel heat-up produced by the optimized injector in the new combustion chamber design. Comparison is made to the baseline engine, the optimized injector with the baseline piston bowl, and the flat piston case. It can be seen that the flat piston injection result is nearly identical to the baseline case. There is a slight improvement in fuel-air mixing. The reasons for this are not fully understood. The slight degradation in fuel heat-up with the flat piston case beyond 5 deg BTDC is attributable to heat transfer losses from plume intersection with the piston surface. The similarity in performance to the baseline case indicates that the squish flow generated by the baseline bowl is too weak to influence the mixing. This result is not surprising since the baseline engine squish volume is quite large.

Figure 14 further illustrates that the changes made to the combustion chamber had a beneficial effect beyond 15 deg ABOI. The tapering off of fuel-air mixing present with the baseline bowl is eliminated and there is substantial improvement in the fuel heat-up.

The increased squish velocity produced by the reconfigured combustion chamber shape has little or no effect on the injection process. This conclusion was reached from examination of the velocity field near the bowl edge, when the squish velocity is near its peak. It was found that the squish flow is very weak compared to the jet flow. Considering that the bulk of the unmixed fuel mass is concentrated in the center of the bowl, an extremely high squish velocity would be required in order to have a significant impact on the mixing. Hence, it can be concluded that the improvement in mixing seen in Fig. 14 is due to the elimination of the plume attachment to the center of the bowl late in the injection process.

In general, it is important to remember that, since the bulk of the rich fuel mass is located in the center region of the bowl, substantial improvements in mixing can only be made by forcing air into this region. However, squish velocities generated by conventional bowl designs are too weak to penetrate into the center of the bowl. This suggest that a more radical bowl design, with a large re-entrant lip, may be appropriate. Such a design could induce a squish flow that forces air directly into the fuel rich cores of the NG plumes. CFD analysis is ideal for economically establishing the feasibility of ideas such as these.

The calculation with the reconfigured combustion chamber has demonstrated the usefulness of CFD analysis for optimizing the combustion chamber geometry of DI NG engines. The basis of the approach is to design the chamber to fit the computed plume shapes produced for a given injector. For the engine under consideration, this has meant reducing the squish volume, opening up the center of the bowl, and increasing the bowl diameter. The improvement in mixing that resulted from making the first two of these changes indicates that the approach has potential. Further refinement of the combustion chamber can be achieved via an iterative process, involving a matrix of calculations. For the development of an actual engine, the analysis can be combined with engine testing to arrive at an optimized design in an efficient manner.

Conclusions

A number of important conclusions can be drawn from the analysis as follows:

1 Regarding injector design:
  - Smaller nozzle holes are more effective at mixing the fuel with air;
  - Plume merging caused by having too many holes can reverse this trend;
  - Increasing the number of holes tends to intensify the Coanda effect due to plume confinement in the circumferential direction. This can further negate the benefits of smaller nozzle holes;
  - For a quiescent engine, the optimal number of holes for most rapid mixing will be that which produces the largest number of separate plumes;
  - Increasing nozzle angle to reduce jet deflection can adversely affect mixing due to reduced jet radial penetration; and
  - Increasing tip height appears to be effective for eliminating deflection and improving mixing.

2 Regarding squish flow and bowl design:
  - Extremely high-velocity squish flows, with penetration into the center of the piston bowl, are necessary to have a significant impact on mixing;
  - Possible benefits in mixing can occur by relieving the center of the piston bowl in typical diesel "Mexican hat" bowl designs; and
  - CFD analysis can effectively be used to optimize combustion chamber geometry by fitting the geometry to computed plume shapes.

Acknowledgments

This work was supported by GRI funding through contract number 5092-291-2304 and managed by Mr. Allen Wells. The authors gratefully acknowledge the technical assistance of Detroit Diesel Corporation and Catepillar Inc. In particular, the authors would like to thank Drs. Richard Winsor and Albert Lee of Detroit Diesel Corporation and Mr. Bernard Richards, Mr. Martin Willie, Mr. William Hayes, and Dr. John Clarke of Caterpillar Inc. for the useful insights gained from our many discussions.

References

Jennings, M. J., and Jeske, F. R., 1994, "Analysis of the Injection Process in Direct Injected Natural Gas Engines: Part I—Study of Unconfined and In-Cylinder Plume Behavior," ASME JOURNAL OF ENGINEERING FOR GAS TURBINES AND POWER, Vol. 116, this issue. pp. 799–805.

Jeske, F. R., Jennings, M. J., and Welch, A. B., 1992, "Modeling of a Natural Gas Injection Process in a Two Stroke Diesel Engine," SAE Paper No. 920192.

Johns, R. J. R., 1984, "A Unified Method for Calculating Engine Flows," ASME Paper No. 84-DGP-018.

Johns, R. J. R., and Jones P. M., 1991, "Computer Modeling of the Flow in a Lean Burn Natural Gas Engine," presented at the Computers in Engine Technology Conference, I. Mech. E., Cambridge University, United Kingdom.

McKinley, T. L., and Primus, R. J., 1990, "Three-Dimensional Calculations of Air Motion, Sprays and Combustion in Quiescent Direct Injection Diesel Engines," presented at the IC Engine Symposium, ASME ETCE Meeting, New Orleans, LA.

Ouelette, P., and Hill, P. G., 1992, "Visualization of Natural Gas Injection for a Compression Ignition Engine," SAE Paper No. 921555.

Numerical Analysis Versus Experimental Investigation of a Distributor-Type Diesel Fuel-Injection System

A. E. Catania
Mem. ASME

C. Dongiovanni

A. Mittica

M. Badami

Dipartimento di Energetica,
Politecnico di Torino,
Torino, Italy

F. Lovisolo
Centro Ricerche Fiat,
Orbassano, Italy

A production distributor-type fuel-injection system for diesel engines has been extensively investigated via computer-assisted simulation and experimentation. The investigation was mainly aimed at assessing and validating a sophisticated computational model of the system, developed with specific attention given to the pump and to some important aspects concerning the injection pressure simulation, such as the dynamic effects of the injector needle lift, the flow unsteadiness, and compressibility effects on the nozzle-hole discharge coefficient. The pump delivery assembly was provided with a valve of the reflux type. This presented a flat in the collar, forming a return-flow restriction with the seat, and had no retraction piston. A single-spring injector, with a reduced sac volume, was fitted to the system. The numerical analysis of transient flow phenomena linked to the mechanical unit dynamics, including possible cavitation occurrence in the system, was performed using an implicit finite-difference algorithm, previously set up for in-line injection equipment. Particular care was exercised in modeling the distributor pump so as to match the dynamics of the delivery-valve assembly to the pressure wave propagation in the distributor and its outlets. The so-called minor losses were also taken into account and it was ascertained that sudden expansion and contraction losses were significant for the type of pump examined. The experimental investigation was performed on a test bench at practical pump speeds. Pressures were measured in the pumping chamber, at two different pipe locations, and upstream to the needle seat opening passage. This last measurement was taken in order to evaluate the nozzle-hole flow coefficient with the support of the simulation, using experimental values of the needle lift, injection rate, and injected fuel quantity as known variables. The numerical and experimental results were compared and discussed, showing the validity of the model. The injection pressure time history and the influence of the delivery return-flow restriction on the system performance were numerically examined.

Introduction

Many of the ever-increasing demands placed by emission regulations on diesel engine technology concern the fuel-injection system performance [1-6]. Injection timing, pressure, and fuel delivery time history have all been recognized to play a major role on the engine exhaust and noise emissions [7-11].

The design of new injection systems as well as modifications to existing configurations, in light of specified performance requirements, dictates the need for sophisticated analytical investigation tools. Numerical simulation offers the means to evaluate the effects of geometric and operational parameters on the complex transient flow processes, that determine the performance of the fuel-injection system. The capability to predict local details of flow-property histories is valuable in the system optimization process with respect to fuel consumption and emissions levels, allowing a significant reduction of experimental tests. Such a capability is particularly useful when technical difficulties preclude the direct or precise measurement of quantities that are important to know and control, such as, for example, the injection pressure, i.e., the pressure in the sac volume of the injector nozzle. This pressure has been verified to be an important factor in the engine combustion process because it primarily affects spray penetration and other spray properties [12]. However, the tiny dimension of the inner passage inside the diesel-injector nozzle makes it almost impossible to measure the pressure in the sac chamber correctly, while the experimental evaluation of the injection pressure in reduced-sac or sacless nozzles is virtually impracticable.

This paper reports the results of a theoretical and experimental investigation of a commercial distributor-type fuel-injection system for diesel engines. The main objective of the

---

Contributed by the Internal Combustion Engine Division for publication in the JOURNAL OF ENGINEERING FOR GAS TURBINES AND POWER. Manuscript received by the Internal Combustion Engine Division January 28, 1994. Associate Technical Editor: W. Cheng.

investigation was to assess and validate a computational model of the system, originally developed paying specific attention to the pump and to important factors in the injection pressure simulation, such as the dynamic effects of the injector needle lift and the effects of flow unsteadiness and compressibility of the nozzle-hole discharge coefficient.

A thorough geometric characterization of each system component was carried out and particular care was taken in modeling the distributor pump so as to match the dynamics of the delivery-valve assembly to the pressure wave propagation within the distributor and its outlets. Wave propagation events in the injector drilled passage were also simulated. The model was capable of taking into account the compressibility of the liquid fuel, the wall shear losses, and also the so-called minor losses, with specific reference to sudden expansion and contraction losses, which were shown to be not so "minor" for the type of pump considered. The differential equations of the mechanical unit dynamics and related transient flow phenomena in the pipe, including possible cavitation occurrence, were numerically solved by means of an efficient implicit algorithm, which was previously developed and set up for a more traditional injection equipment with an in-line pump [13, 14].

The experimental investigation was performed at practical engine speeds, ranging from 1000 rpm to 4000 rpm, on a test bench of the type usually used in industry for assessing diesel injection equipment. A high-speed data acquisition unit was used to record pressure histories at different locations in the system, along with the needle lift, the injection rate, and the fuel quantity injected per cycle. Pressures were measured in the pumping chamber, at two pipe locations (one close to the delivery-valve assembly and the other close to the injector) and also inside the injector nozzle at a point ahead of the needle seat opening passage.

This last pressure measurement was also aimed at determining the nonstationary values of the nozzle-hole discharge coefficient, so as to include the dynamic effect of the needle valve and the liquid compressibility effect. Such values were obtained by means of the numerical model, applied to the flow in the injector tip region, using, as input data, the measured needle lift, injection rate, and injected fuel quantity, along with the pressure at the seat opening passage and back pressure downstream to the holes. The correlations obtained for a tip-removed nozzle in [12] were fitted to the discharge coefficient of the needle seat passage.

The results of both theoretical and experimental investigations were compared and discussed; their good agreement substantiated the injection-system mathematical model. Finally, the injection pressure time history and the effects of the delivery return-flow restriction on the system performance were numerically analyzed.

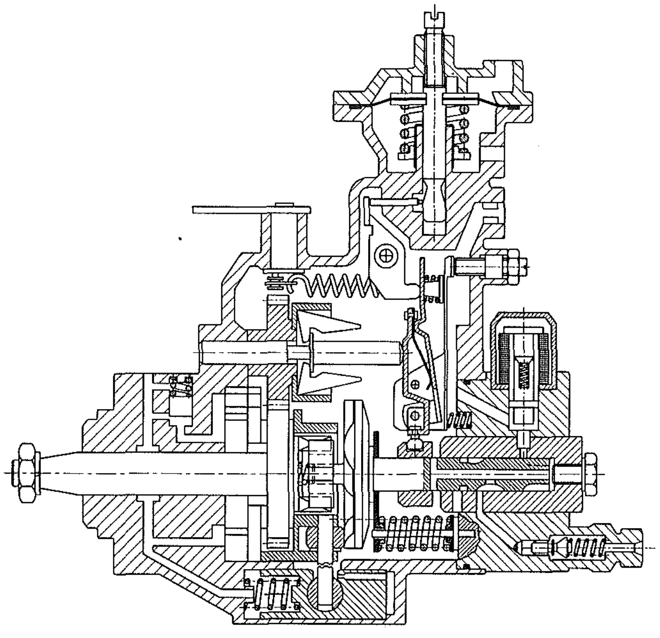

Fig. 1 Bosch distributor-type pump

Fuel-Injection System

The system was made up of one rotative pump of the distributor type, four delivery pipes, and as many nozzle-hole injectors.

The pumping unit, a Bosch distributor pump of the VE type (Fig. 1), was equipped with a mechanical governor, a hydraulic timing device, a vane-type supply pump, and a manifold-pressure compensator. In order to avoid the injector-nozzle reopening, the delivery-valve assembly (Fig. 2) was provided with a valve of the reflux type (Fig. 3). This presented a flat in the collar, forming a return-flow restriction with the seat, without any retraction piston. As will be shown by the numerical analysis of the delivery-valve effects on the pressure distributions in the injection system, the return-flow passage should be properly designed in order to prevent, or at least minimize, possible cavitation occurrence.

For the present investigation, focused on the pump model and a more reliable prediction of the injection pressure, a single-spring injector (Fig. 4) was fitted to the system. The

Nomenclature

A = flow area
a = wave propagation speed; mixture celerity
d = pipe diameter
F = spring force
k = spring rate
l = lift; stroke
m = mass; mobile element
n = pump angular speed
P = plunger
p = pressure; average cross-sectional pressure
Q = flow rate; injection rate
S = surface area perpendicular to the lift axis
t = time
u = average cross-sectional velocity
V = volume
x = axial distance along pipe; lift
α = average cross-sectional void fraction
β = damping
Γ = rate of gas/vapor release per unit volume of fluid
Δt = time increment
Δx = distance increment
θ, ϑ = cam angle
μ = discharge coefficient
ρ = density; mixture density
τ = wall shear stress

Subscripts

0 = reference value
c = pumping chamber
d = delivery valve
e = injection environment
f = fuel injected per cycle
h = injector nozzle holes
i = pump interior
l = liquid phase
M = maximum value
m = mobile element: valve; needle
n = needle
p = plunger
pd = pipe location at the output of the delivery assembly
pi = pipe location at the injector inlet
r = return-flow restriction
s = sac chamber
sp = needle seat passage
v = gaseous/vaporous phase

injector nozzle (Fig. 5) was of the orifice type and presented a reduced sac volume.

Computational Model

Literature Review. Numerical models of fuel-injection systems have long been developed and applied to both conventional pump-line-nozzle equipment, usually of the in-line type, and to unit injectors [13-23]. However, distributor-type diesel injection systems have generally not been given due attention, despite their application to light-duty engines and the continuous evolution they are undergoing, as shown by the fact that the production of an electronically governed diesel distributor pump is planned for the near future [24]. Hence there is a lack of accurate simulation algorithms for production equipment with a rotative pump of the distributor type [20]. Furthermore, in orifice-type fuel-injector nozzles, the predicted sac-chamber or injection pressure, as well as other flow properties relevant to the system performance, are sensibly dependent on the expression used for the nozzle-hole discharge coefficient [12, 13, 19]. Ordinary geometric or semi-empirical correlations of this coefficient to the needle lift, based on measurements taken in steady-flow test rigs, were applied [13, 19, 25, 26], unless simply constant values were employed. Only recently have correlations between hole discharge coefficient and needle lift been determined for a single orifice injector nozzle with a sac chamber, taking the needle lift dynamic effects, as well as the flow unsteadiness and compressibility effects, into account [12]. Direct measurements of injection pressure have also been carried out, in order to evaluate the fuel flow coefficient, but using enlarged model nozzles, which were similar to the real ones in the configuration, except for the sac volume [27]. Therefore, a major effort is required to achieve more reliable discharge coefficients, especially in reduced sac or sacless injector nozzles.

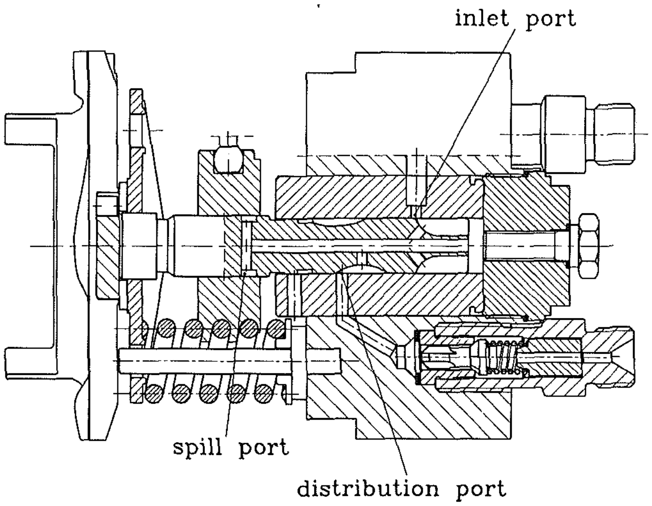

Fig. 2 Distributor and delivery valve assembly

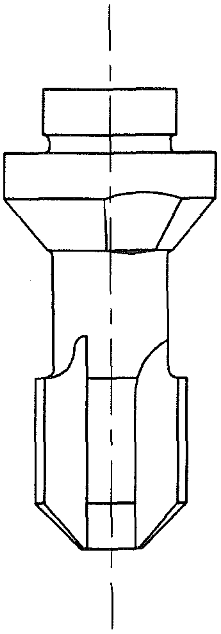

Fig. 3 Valve of the reflux type

In most of the injection-system models, the ordinary differential equations simulating the pump and injector dynamics were solved separately, with numerical techniques different from those used to solve the one-dimensional partial differential equations governing the pipe flow. This is mainly explained by the fact that the solution of the mechanical unit equations gives rise to a stiff problem, owing to the extremely rapid response time of these components, usually treated as boundary conditions for the pressure pipe. Consequently, one must be careful to assure a consistent and real solution of the complete differential equation set describing the whole system. Details on the numerical algorithms commonly used for injection equipment simulation are reported in [13], together with comments on their limits and approximations. An implicit multistep scheme, suitable for stiff problems, was chosen in [13] for the finite-difference approximation of the pump and injector equations. In conformity with this, a one-step implicit upwind scheme was proposed to obtain the difference analogue of the pipe flow equations. The set of nonlinear algebraic equations resulting from both discretization procedures was solved using the Newton-Raphson method and a very fast advanced-direct method was employed to solve the linearized equations. In fact, these could be easily reduced to an *n*-diagonal system of algebraic equations, so as to require no pivoting for accuracy or stability reasons, and an extension of the Thomas solver was applied to them. The method developed in this way was shown to be much faster than the one using the subroutine provided in [28] to solve a block tridiagonal system, to which the set of linear equations could also be reduced [14]. Furthermore, a cycle-by-cycle computational analysis was performed in [14], starting from different initial conditions, e.g., the pipe residual pressure, and neglecting any

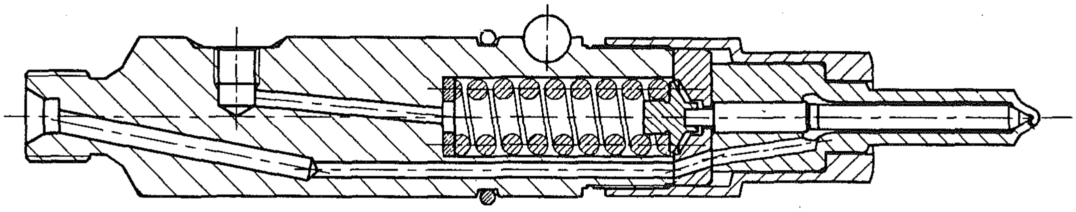

Fig. 4 Injector

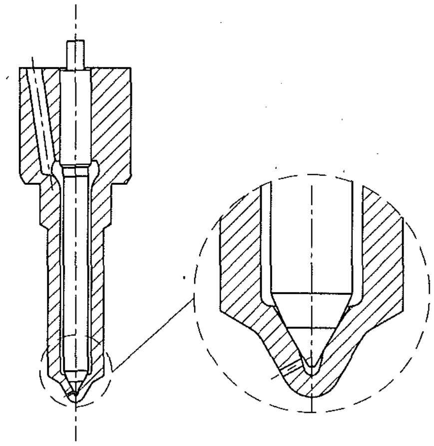

Fig. 5 Injector nozzle

cause of cyclic fluctuations, in order to assess the diffusivity and stability of the model in its convergence to the same asymptotic behavior of the system. Therefore, a compact, efficient, stable, and sufficiently accurate numerical algorithm was attained in [13], capable of essentially matching the transient pipe flow to the dynamics of the mechanical elements at its boundary, and overcoming some difficulties ordinarily ascribed to implicit methods, such as those connected to the computational time.

As far as the simulation of cavitation phenomena in transient pipe flows is concerned, one can refer to [13] for references. It is worth recalling that, unless disregarded [15, 22], cavitation propagation is not generally simulated in fuel-injection systems, but rather its effects are taken into account by rough simplifications, which neglect the mutual influence of the cavitating region on the surrounding liquid properties and so lead to inconsistent solutions in the vicinity of that region, with effects that amplify in subsequent time instants [16-21]. Most cavitation studies in steady and unsteady pipe-flow conditions were carried out for gaseous cavitation occurrence [29-32]. Transient gas-liquid two-phase flows in pipelines have long been simulated using different numerical schemes and mixture models [33-36]. However, in general, either drastic simplifications are accepted in the bubble-dynamics model, or semi-empirical expressions are used for the wave propagation speed of the mixture, yielding satisfactorily results in the respective field of application. A consistent wave speed of the mixture is obtained in [31], though the contribution of the gas component is neglected in the momentum balance. The cavitation simulation in [13, 14] is based on a simple mixture model of transient two-phase flow in pipes and can incorporate the effects of gaseous cavitation occurrence. Comments on the wave propagation speed of a vapor-liquid mixture are reported in [14].

Multidimensional modeling has recently been applied to the simulation of flow field details in specific regions of a fuel injector, such as the nozzle tip, for their optimization [37-39]. However, at present it is impractical and may be unnecessary for the whole system numerical analysis.

Pipe-Flow Equations. The fuel flowing in the pressure pipe is normally in the liquid state. However, it is not at all exceptional that cavitation phenomena develop in more or less wide regions of the pipe, or, in general, of the whole system, depending on the design and operational factors. This may occur specifically as a result of depression wave enhancement or protraction in the pipe, due to the delivery valve configuration, subsequent to the spill port opening. In such a case the fluid becomes a mixture of liquid and vapor, including the presence of free gas. Therefore, the transient pipe-flow conservation equations are written, in general, for a homogeneous, bubbly, two-phase fluid, so that the pure-liquid flow equations can be directly derived as a particular case. Vapor cavitation is described by a dependent variable termed void fraction and defined as the volume of the gaseous component per unit volume of the mixture. A virtually isothermal flow is assumed, requiring only mass and momentum conservation equations for its simulation. This assumption is consistent with negligible thermal effects related to fluid change of phase, and is generally acceptable owing to the very small amount of liquid involved. Furthermore, the momentum interchange between the vapor and liquid components is ignored so that the vapor bubbles and liquid possess the same velocity. An average cross-sectional representation of void fraction, mixture velocity, and component densities is employed. Therefore, following a control volume approach, with reference to a pipe element made of elastic material, the conservation of mass for the vapor and liquid phases and the mixture momentum balance, under negligible body forces, can be written in the following matrix form [13]:

$$\frac{\partial \mathbf{w}}{\partial t} + [A]\frac{\partial \mathbf{w}}{\partial x} = \mathbf{H} \tag{1}$$

where

$$\mathbf{w} = \begin{bmatrix} u \\ p \\ \alpha \end{bmatrix} \quad [A] = \begin{bmatrix} u & \frac{1}{\rho} & 0 \\ \rho a^2 & u & 0 \\ \alpha\left(1 - \frac{\rho a^2}{\rho_v a_v^2}\right) & 0 & u \end{bmatrix}$$

$$\mathbf{H} = \begin{bmatrix} -\frac{4\tau}{\rho d} \\ \frac{\Gamma}{\rho_v}\left(1 - \frac{\rho_v}{\rho_l}\right)\rho a^2 \\ \frac{\Gamma}{\rho_v}\left[1 - \alpha\left(1 - \frac{\rho_v}{\rho_l}\right)\frac{\rho a^2}{\rho_v a_v^2}\right] \end{bmatrix}$$

The mixture density ρ is defined as

$$\rho = \alpha\rho_v + (1 - \alpha)\rho_l \tag{2}$$

α being the void fraction.

a_v and a_l designate the isothermal wave propagation speed of the gas/vapor and liquid, respectively, as specified in [13].

The variable a is given by

$$\frac{1}{\rho a^2} = \frac{\alpha}{\rho_v a_v^2} + \frac{1 - \alpha}{\rho_l a_l^2} \tag{3}$$

and expresses the celerity or wave propagation speed of the mixture, as can be easily verified by determining the eigenvalues, λ, of the matrix $[A]$:

$$\lambda_{1,2} = u \pm a, \quad \lambda_3 = u$$

The single-phase, liquid or gas/vapor, flow equations are directly derived from Eq. (1) by making the void fraction α equal to zero or one, respectively, and the source term Γ (defined in the Nomenclature, as are the other terms) equal to zero. In these limit cases Eq. (3) gives $a = a_l$ and $a = a_v$, in agreement with the eigenvalues of the matrix $[A]$, which reduce to $\lambda_{1,2} = u \pm a_l$ and $\lambda_{1,2} = u \pm a_v$, respectively.

Another interesting limit case included in Eq. (1) is that of vapor cavitation development at constant pressure $p = p_v$, by considering the pure vapor-liquid mixture to be in thermal equilibrium. In this case, taking $Dp/Dt = 0$, with $\partial p/\partial t = 0$ and $\partial p/\partial x = 0$ within a region of persistent cavitation, one obtains $\Gamma = [\rho_l\rho_v/(\rho_l - \rho_v)](\partial u/\partial x)$ and $a = 0$, according to the eigenvalues of $[A]$, which become $\lambda_{1,2} = u$. Particular care is required for the boundary conditions of the cavitating region.

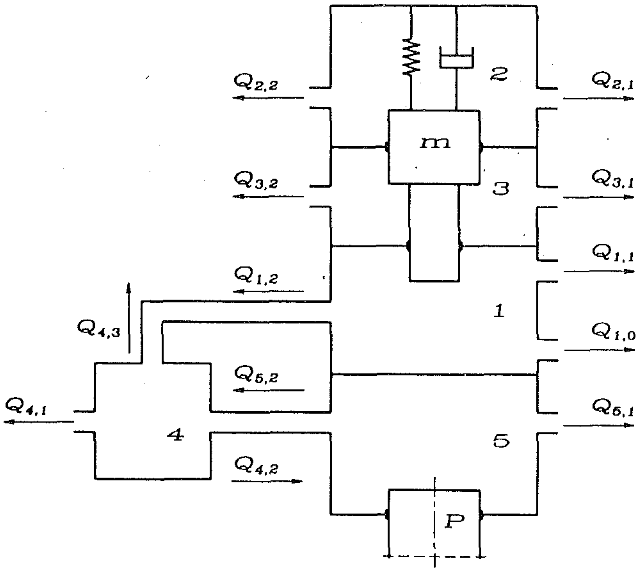

Fig. 6 Mathematical model of pump and injector

Pump and Injector Mathematical Model. Pressure wave propagation phenomena were simulated in the pump distributor, its outlets, and in the injector drilled passage, by means of Eq. (1). A conventional lumped mass model was used to write the continuity and compressibility equations that allow for flow rates through the concentrated and isobaric volumes of the pump and injector, as follows (Fig. 6):

$$\sum_{k=1-\delta_{j1}}^{2+\delta_{j4}} Q_{j,k}+V_{0_j}\zeta_j=\delta_{j5}S_p\left(x_p\zeta_j+\frac{dx_p}{dt}\right)$$
$$+(-1+\delta_{j4}+\delta_{j5})^j S_{m_j}\left(x_m\zeta_j+\frac{dx_m}{dt}\right)$$
$$j\neq j_0,\quad j=1,\,2,\,3,\,4,\,5 \qquad (4)$$

where

$$Q_{j,n}=\frac{p_j-p_{j,n}}{|p_j-p_{j,n}|}\,\mu_{j,n}A_{j,n}\sqrt{\frac{2}{\rho}\,|p_j-p_{j,n}|}$$
$$j=1,\,2,\,3,\,4,\,5 \quad n=0,\,1$$

$Q_{j,k}$, with $k=2$, 3, expresses the volumetric flow rates from the chambers to the internal connecting lines and pipe;

$$\delta_{lm}=\begin{cases}1 & l=m\\ 0 & l\neq m\end{cases} \quad \zeta_j=\begin{cases}\dfrac{1}{E}\dfrac{dp_j}{dt} & p_j>p_v\\[2ex] \left(\dfrac{\rho_l}{\rho_v-\rho_l}+\alpha_j\right)^{-1}\dfrac{d\alpha_j}{dt} & p_j=p_v\end{cases}$$

$$\text{pump:}\quad j_0=3 \quad \begin{aligned}&Q_{1,0}=0\\ &Q_{1,1}=-Q_{2,1}\\ &p_{1,1}=p_2\\ &p_{2,1}=p_1\\ &p_{4,1}=p_i\\ &p_{5,1}=p_i\end{aligned}$$

$$\text{injector:}\quad j_0=2,\,4,\,5 \quad \begin{aligned}&Q_{1,2}=0\\ &Q_{3,1}=-Q_{1,1}\\ &p_{1,0}=p_e\\ &p_{1,1}=p_3\\ &p_{3,1}=p_1\end{aligned}$$

The dynamics of valves (the injector needle is also referred to as the nozzle valve) are simulated by ordinary differential equations, according to the second-order linear system model of Fig. 7, as follows:

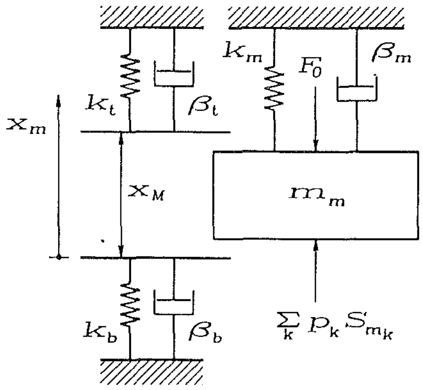

Fig. 7 Second-order dynamics model for valves

$$m_m\frac{d^2x_m}{dt^2}+\bar{\beta}_m\frac{dx_m}{dt}+\bar{k}_m x_m+\bar{F}_0+\sum_{\substack{k=1\\k\neq j_0}}^{3}(-1)^k p_k S_{m_k}=0 \qquad (5)$$

in which the terms $\bar{k}_m$, $\bar{\beta}_m$, and $\bar{F}_0$ are expressed by

$$\begin{array}{llll} x_m<0 & \bar{k}_m=k_m+k_b & \bar{F}_0=F_0 & \bar{\beta}_m=\beta_m+\beta_b\\ 0\leq x_m\leq x_M & \bar{k}_m=k_m & \bar{F}_0=F_0 & \bar{\beta}_m=\beta_m\\ x_M<x_m & \bar{k}_m=k_m+k_t & \bar{F}_0=F_0-k_t x_M & \bar{\beta}_m=\beta_m+\beta_t \end{array}$$

Geometric Characterization. The pump performance is conditioned by the geometric configuration and opening state of the inlet port, distribution port, and spill port, that are indicated in the distributor and delivery-valve assembly drawn in Fig. 2. The opening degree of these ports is a function of the plunger stroke and control collar location. As can be inferred from Figs. 1 and 2, the cam plate (left side in Fig. 2), which bears on the cam roller rings (Fig. 1), imparts a rotation stroke motion to the distributor-pump plunger. The rotating motion causes the opening and closing of the inlet and distribution ports. Fuel distribution and delivery to the individual outlet take place through a distribution groove in the plunger. Pressure is produced by the stroking motion of the plunger after the inlet port has been closed. The high pressure lifts the delivery valve off its seat and the fuel is forced through the pressure pipe to the injection nozzle. When the spill port of the distributor-pump plunger reaches the edge of the control collar, the fuel delivery is terminated. From this instant on, the high-pressure chamber is connected to the pump interior by the port internal to the plunger. During the remaining stroke of the plunger the excess fuel is forced back into the pump interior.

The analytical equations for the opened section of ports are reported in the appendix with reference to the plunger null-stroke position and the rotational angle corresponding to the start of the distribution-port opening. In the present case of null plunger prestroke ($f=0$ in Eq. (1A) of the appendix), Fig. 8 plots the pattern of each port opening, along with the plunger stroke, as a function of the cam angle, for a given position of the control collar edge.

The flow area of the delivery-valve and the needle-valve seat opening passages are also geometrically described in the appendix. Their distributions are plotted versus the respective valve lift in Figs. 9 and 10. The minimum flow areas of needle seat passage and nozzle openings are shown in Fig. 10 by a thick line.

Geometric and mechanical quantities relevant to the model, such as lengths, volumes, masses, spring rates, and others, were thoroughly measured.

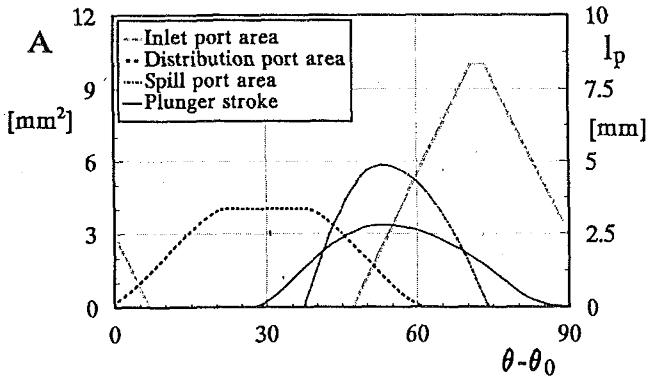

Fig. 8 Distribution of port opening and plunger stroke as a function of cam angle

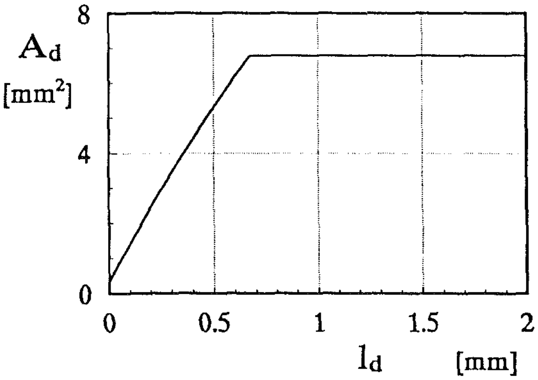

Fig. 9 Delivery valve flow area

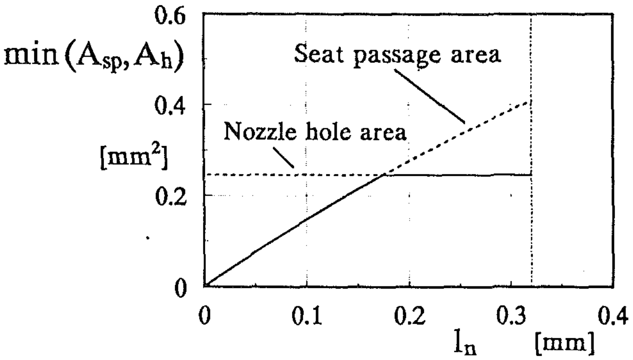

Fig. 10 Minimum flow areas of needle seat passage and nozzle holes as a function of the needle lift

Numerical Algorithm. The choice of an implicit numerical algorithm to solve the complete set of differential equations describing the whole injection equipment was mainly conditioned by the fact that BDF (backward differentiation formula) implicit multistep schemes of second- or higher-order accuracy, suitable for stiff problems, were selected for the discretization of the ordinary differential equations modeling the pump and injector dynamics. This choice was also supported by the fact that implicit numerical methods meet stability conditions that are generally far less restrictive than those of the explicit techniques. A BDF approximation of p-order accuracy ($p \leq 6$) to the first-order time derivative of any time-function variable y, at the instant $n+1$, is given by

$$\left(\frac{dy}{dt}\right)^{n+1} = \frac{1}{\Delta t}\sum_{j=0}^{p} \kappa_j y^{n+1-j} + O(\Delta t^p) \qquad (6)$$

in which κ_j are suitable numerical constants.

The one-step BSBT (backward space, backward time) finite-difference scheme of first-order accuracy, proposed in [13], was used to discretize the partial differential Eq. (1) of the pressure pipe-flow, as follows:

$$\left([I] + \frac{\Delta t}{\Delta x}[A]^{n+1}\right)\mathbf{w}_i^{n+1} - \frac{\Delta t}{\Delta x}[A]^{n+1}\mathbf{w}_{i-1}^{n+1} - \Delta t\mathbf{H}^{n+1} = \mathbf{w}_i^n \qquad (7)$$

where the time-marching coordinate in the computational grid is indicated by the superscript and the spatial coordinate by the subscript, Δt and Δx being the time and space interval, respectively, of the grid.

Following a conventional procedure in computational fluid-dynamics [28], the *consistency*, as well as the order of the *truncation error*, and the *stability* of this difference representation were assessed through the application of the BSBT scheme to the equation system (1) locally linearized by holding $[A]$ constant. As can be easily verified, this was equivalent to carrying out such evaluations on the one-dimensional linear wave equation, or simply the wave equation, which is derived from Eq. (1) by replacing $\mathbf{w}$ with u, $[A]$ with the constant wave speed a, and $\mathbf{H}$ with zero.

The *modified equation* representing the BSBT finite-difference approximation to the wave equation results to be

$$\frac{\partial u}{\partial t} + a\frac{\partial u}{\partial x} = \frac{a}{2}(1+\nu)\Delta x\frac{\partial^2 u}{\partial x^2} - \frac{a}{6}(1+3\nu+2\nu^2)(\Delta x)^2\frac{\partial^3 u}{\partial x^3}$$
$$+ O[(\Delta x)^3, (\Delta x)^2\Delta t, \Delta x(\Delta t)^2, (\Delta t)^3] \qquad (8)$$

where $\nu = a\Delta t/\Delta x$ is the *Courant number*. In other words, Eq. (8) is the partial differential equation, which is actually solved when the BSBT scheme is applied to the wave equation. The right-hand side of Eq. (8), that is the truncation error, vanishes under grid refinement, showing the *consistency* of the discretization procedure. The lowest-order term in the truncation error, giving the accuracy order of the method, is of $O[\Delta t, \Delta x]$, that is of the first order. Because of the even partial derivative, this term is similar to the viscous term in one-dimensional fluid flow equations; it gives rise to an implicit artificial viscosity tending to reduce all gradients in the solution when $\nu \neq -1$. For this reason the numerical scheme is said to be predominantly dissipative and does not provide very good resolution in the vicinity of discontinuities, such as those induced by cavitation phenomena in the flow properties. Nevertheless, it was preferred to any of the most popular second-order implicit numerical schemes, since these give rise to unacceptable oscillations at discontinuities, and so require an explicit artificial viscosity to be purposely introduced into the solution. On the other hand, since the duration of the injection is very short, the dissipative error produced by the BSBT scheme was generally assessed to be very small through both test cases [13] and cycle-by-cycle injection simulation [14]. The high-order accurate nonoscillatory schemes developed in [40] are too cumbersome to apply to injection systems. At present, a novel implicit numerical scheme of second-order accuracy, providing very good resolution at discontinuities with minor oscillation problems, is being implemented and setup.

From the von Neumann *stability* analysis of the BSBT difference approximation to the wave equation, it follows that, for each frequency present in the solution for the error ϵ (written as a Fourier series), the amplification factor, representing the growth of a general error component ϵ_j from one time step to the next, is given as

$$G = \frac{\epsilon_j^{n+1}}{\epsilon_j^n} = [1 + \nu(1 - e^{-i\beta})]^{-1} \qquad (9)$$

where

$$\beta = k_m\Delta x, \quad k_m = \frac{m\pi}{L}, \quad m = 0, 1, 2, \ldots, M,$$

M being the number of intervals Δx units long contained in length L.

The resulting stability condition $|G| \leq 1$ becomes $\nu(1+\nu) \geq 0$, which implies $\nu \geq 0$ or $\nu \leq -1$. Therefore, the present differentiation scheme can, in practice, be considered to be unconditionally stable, as stated in [13], since it is stable for all values of ν, except those in the narrow interval $0 > \nu > -1$, and it is possible to select the mesh size Δt or Δx so as to meet these stability conditions.

The difference analogs to the partial differential equations of the pipe flow and to the ordinary differential equations of the pump and injector led to a system of nonlinear algebraic equations, which can be written, in vector notations, as

$$\mathbf{F}(\mathbf{x}) = 0 \tag{10}$$

where $\mathbf{x}$ is the vector of the unknown variables.

This system of nonlinear equations was solved using the Newton-Raphson iterative method, which transforms it into the following linear form:

$$[J^{(i)}]\Delta\mathbf{x}^{(i)} = -\mathbf{F}(\mathbf{x}^{(i)}) \tag{11}$$

where $\mathbf{x}^{(i)}$ is an iterative approximation of the exact solution, $[J^{(i)}]$ is the Jacobian matrix of the system, evaluated for the vector $\mathbf{x}^{(i)}$, and $\Delta\mathbf{x}^{(i)}$ the iterative correction

$$\mathbf{x}^{(i+1)} = \mathbf{x}^{(i)} + \Delta\mathbf{x}^{(i)} \tag{12}$$

The solution of the linear equation system (11) is obtained using a very fast direct method, detailed and tested in [14], which can be summarized as follows. First, system (11) was cast into a multidiagonal form

$$[B]\mathbf{z} = \mathbf{c} \tag{13}$$

with the $n \times n$ matrix of coefficients given by

$$[B] = \begin{bmatrix} b_{1,1} & b_{1,2} & \cdot & \cdot & b_{1,n_b} & & & & \\ b_{2,1} & \cdot & \cdot & \cdot & \cdot & \cdot & & 0 & \\ \cdot & \cdot & \cdot & \cdot & \cdot & \cdot & (n_b) & & \\ \cdot & \cdot & \cdot & \cdot & (m_b-1) & \cdot & \cdot & \cdot & \\ b_{n_b,1} & \cdot & \cdot & (n_b-1) & (m_b) & \cdot & \cdot & \cdot & b_{n-n_b+1,n} \\ & \cdot & \cdot & \cdot & \cdot & \cdot & \cdot & \cdot & \cdot \\ & & (1) & \cdot & \cdot & \cdot & \cdot & \cdot & \cdot \\ & 0 & & \cdot & \cdot & \cdot & \cdot & \cdot & b_{n-1,n} \\ & & & & b_{n,n-n_b+1} & \cdot & \cdot & b_{n,n-1} & b_{n,n} \end{bmatrix} \tag{14}$$

and structured so that no pivoting was necessary to improve accuracy or remove any instability problems. The numeration of the $m_b = 2n_b - 1$ diagonals of $[B]$ is designated by round brackets in Eq. (14) and n_b is the number of diagonals in the upper and lower triangular part of the matrix, respectively, including the main diagonal. In Eq. (13) $\mathbf{z}$ is the column vector of the unknowns $\Delta\mathbf{x}^{(i)}$ and $\mathbf{c}$ is the column vector of the known quantities $-\mathbf{F}(\mathbf{x}^{(i)})$. On the analogy of the LU "factorization" procedure, the matrix $[B]$ was then reduced to the product of two triangular matrices, a lower $[L]$ and an upper one $[U]$, both having n_b diagonals of nonzero elements, the main diagonal of $[L]$ being the unit diagonal. In this way, system (13) was decomposed into a lower triangular form

$$[L]\mathbf{q} = \mathbf{c} \tag{15}$$

and an upper one

$$[U]\mathbf{z} = \mathbf{q} \tag{16}$$

Analytical details about an efficient evaluation of the coefficient matrices $[L]$ and $[U]$ and the subsequent resolution of the systems (15) and (16) are given in [14].

In order to save computer memory, only the m_b diagonals of the coefficient matrix $[B]$ were stored by giving it the storage structure of the following $n \times m_b$ matrix $[\overline{B}]$, which is also suitable from a mnemonic point of view

$$[\overline{B}] = \begin{bmatrix} & & & b_{1,n_b} & \cdots & b_{1,2} & b_{1,1} \\ & 0 & b_{2,1} & \cdot & & \cdot & \cdot \\ & \cdot & \cdot & (n_b) & & (m_b-1) & (m_b) \\ & \cdot & \cdot & \cdot & & \cdot & \cdot \\ & \cdot & \cdot & b_{n-n_b+1,n} & & \cdot & \cdot \\ b_{n_b,1} & & \cdot & & \cdot & \cdot & \cdot \\ \cdot & & \cdot & & \cdot & \cdot & \cdot \\ (1) & & (n_b-1) & & \cdot & \cdot & \cdot \\ \cdot & & \cdot & & 0 & b_{n-1,n} & \cdot \\ b_{n,n-n_b+1} \cdots & & b_{n,n-1} & & & & b_{n,n} \end{bmatrix} \tag{17}$$

The element $\overline{b}_{i,k}$ of $[\overline{B}]$ is equal to the coefficient located at the crossing of row i and diagonal k in $[B]$, with $k = 1, \ldots, m_b$, as shown by the bracketed numbers in Eqs. (14) and (17). $[L]$ and $[U]$ were also given the storage structure of $n \times n_b$ matrices, $[\overline{L}]$ and $[\overline{U}]$, respectively, through the following conversion formulas:

$$i = 1,2,..,n \begin{cases} \bar{l}_{i,j} = \dfrac{\overline{b}_{i,j} - \displaystyle\sum_{k=\max(1,n_b-i+1)}^{j-1} \bar{l}_{i,k}\overline{u}_{k+i-n_b,k-j+m_b}}{\overline{u}_{i+j-n_b,m_b}} \\ \qquad j = \max(1, n_b - i + 1),..,n_b - 1 \\ \overline{u}_{i,j} = \overline{b}_{i,j} - \displaystyle\sum_{k=\max(n_b-i+1,m_b-j+1)}^{n_b-1} \bar{l}_{i,k}\overline{u}_{k+i-n_b,k+j-n_b} \\ \qquad j = m_b, m_b - 1,..,\max(n_b, i + m_b - n) \end{cases} \tag{18}$$

linking the element $\overline{b}_{i,j}$ of $[\overline{B}]$ to the elements $\bar{l}_{i,j}$ of $[\overline{L}]$ and $\overline{u}_{i,j}$ of $[\overline{U}]$. Therefore, the solution of system (13) reduced to

$$\begin{aligned} q_i &= c_i - \sum_{k=1}^{\min(n_b-1,i-1)} \bar{l}_{i,n_b-k} q_{i-k} \qquad i = 1, 2, \ldots, n \\ z_i &= \frac{q_i - \displaystyle\sum_{k=\max(i+m_b-n,n_b)}^{m_b-1} \overline{u}_{i,k} z_{i+m_b-k}}{\overline{u}_{i,m_b}} \qquad i = n, n-1, \ldots, 1 \end{aligned} \tag{19}$$

Equations (18) and (19) can be considered as an extension of the Thomas algorithm to the multidiagonal system of algebraic equations (13). At a computational level it is not necessary explicitly to make up the matrices $[\overline{L}]$ and $[\overline{U}]$ because their elements can be stored in place of the corresponding elements of $[\overline{B}]$. Furthermore, the heavy calculation of maximum and minimum functions in Eqs. (18) and (19) can be eluded by skillful programming.

Experimental System and Procedure

The experimental investigation of a commercial fuel-injection system, equipped with a Bosch VER 286/1 distributor-type pump (Fig. 1), was performed on a test bench that was specifically instrumented at the Fiat Research Center in order to examine the changes caused by different delivery valves and injectors in the system performance. A delivery valve of the reflux type (Fig. 3) and a single-stage injector with a reduced-sac nozzle (Figs. 4 and 5) were considered for the present study. The pump shaft was driven by an electric motor at an angular speed kept equal to half the engine speed and constant, within less than ±0.5 percent, through a selection and control unit. The injection system was operated with a special test oil, meeting ISO specifications. The fluid was supplied by a hydraulic circuit at a pressure of 0.135 MPa and a temperature of 46°C, held constant with an accuracy better than ±2.5 percent during the tests.

The experiment was carried out at four pump speeds, 500, 1000, 1500, and 2000 rpm, keeping the control-lever of the pump governor in its full-load position and the manifold-pressure compensator (ordinarily used for pressure-charged engines) at a constant charge-air pressure of 0.2 MPa. In each measurement set, taken at a given pump speed, the following average quantities were determined: the pressure in the pump interior, the injected fuel quantity per cycle, and the residual pressure in the pipe. A high-frequency data acquisition system was used to record the pressure time histories in the pump high-pressure changer (p_c), in the pipe at the output of the delivery valve assembly (p_{pd}) as well as at the injector inlet (p_{pi}), and also in the injector nozzle at the needle seat opening passage (p_{sp}); the needle lift and the injected flow rate were also recorded. Pressures were measured with piezoresistive transducers, carefully mounted at the walls; the needle lift data were acquired by means of an inductive transducer and the injection rate was determined using a Bosch indicator, equipped with strain gages and their related measuring chains. A scheme of the system layout with measurement parameters and locations is shown in Fig. 11.

A good repeatability was observed cycle-by-cycle for all the measured quantities in each test and an overall uncertainty of less than ±10 percent was prudentially ascribed to the experimental results.

Results

Discharge Coefficient of the Nozzle Holes. The discharge coefficient μ_h of the injector-nozzle holes is conventionally defined as the ratio between the actual flow rate discharged and the ideal one evaluated through the pressure difference across the holes, according to Bernoulli's equation

$$\mu_h = Q\left(\frac{p_s-p_e}{|p_s-p_e|}A_h\sqrt{\frac{2|p_s-p_e|}{\rho_l}}\right)^{-1} \qquad (20)$$

where: Q is the injected volumetric flow rate, A_h the geometric cross-sectional area of the nozzle holes, p_s the injection pres-

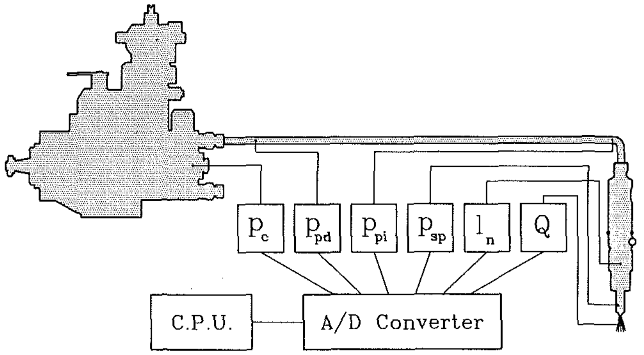

Fig. 11 Measurement system layout

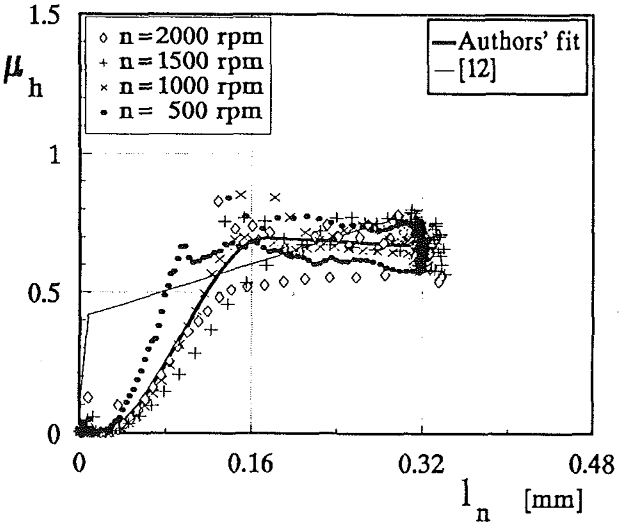

Fig. 12 Nozzle hole flow coefficient

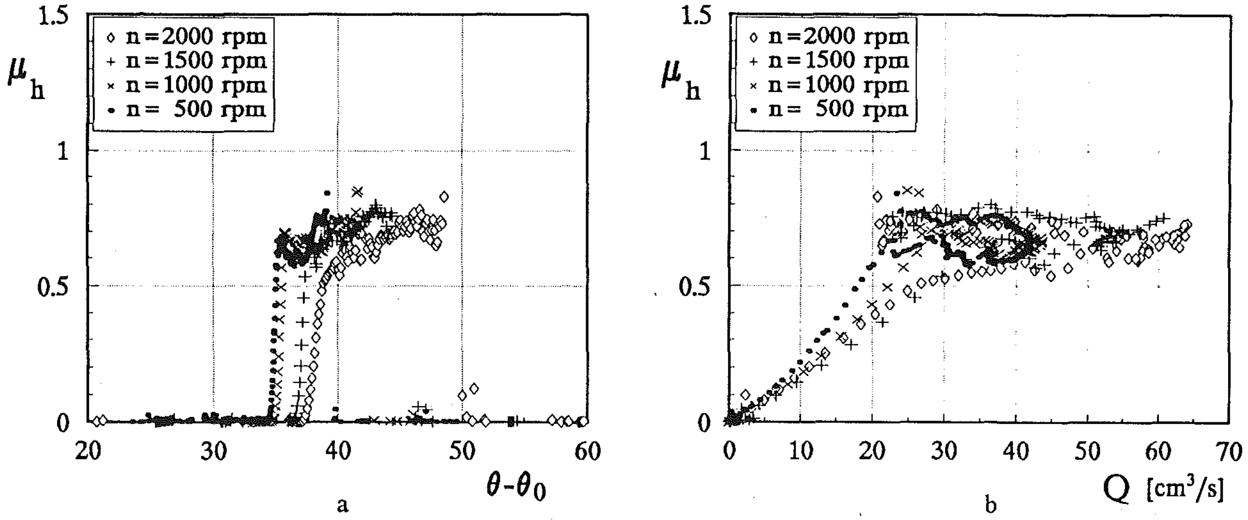

a

b

Fig. 13 Nozzle hole flow coefficient

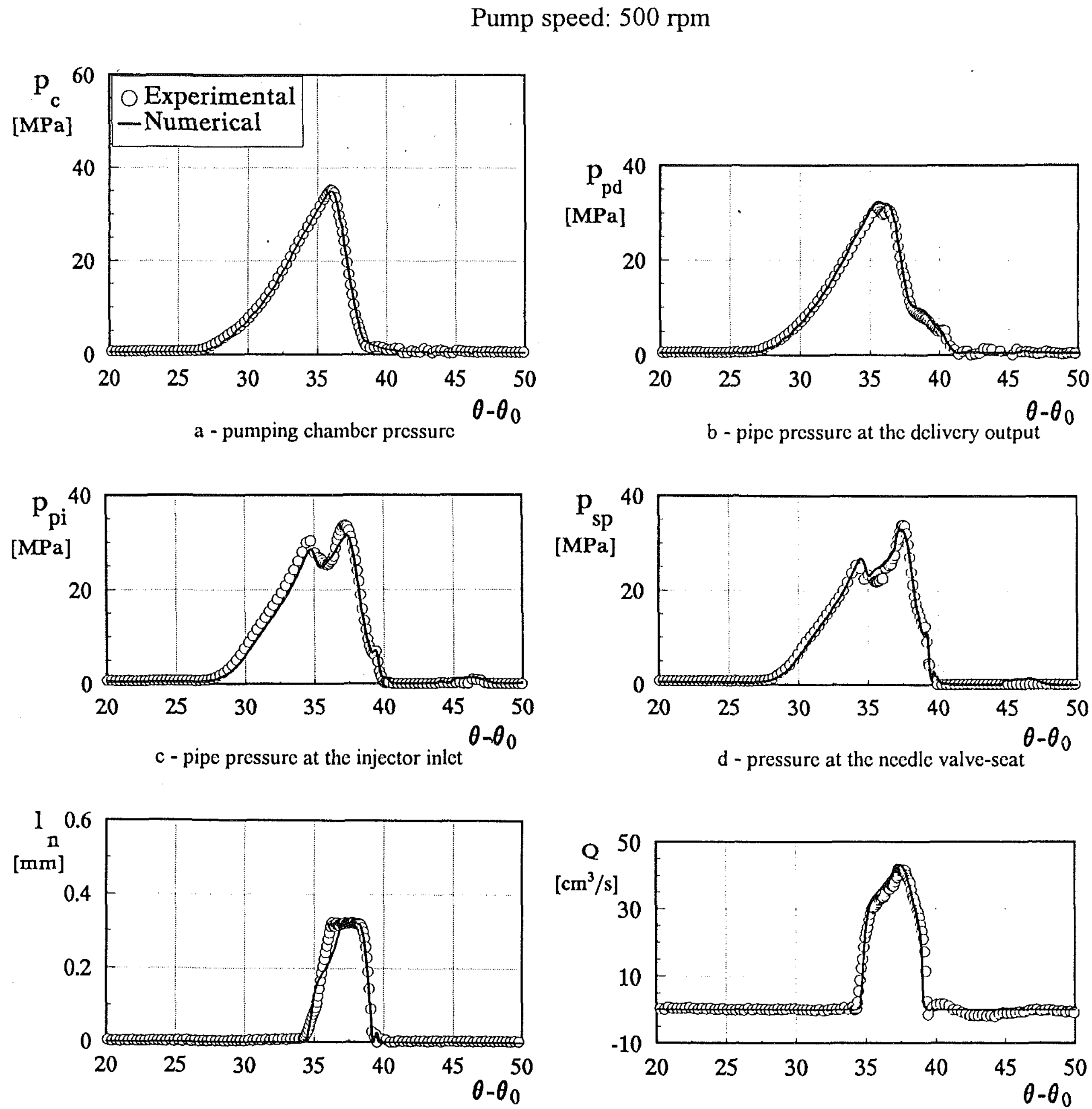

a - pumping chamber pressure

b - pipe pressure at the delivery output

c - pipe pressure at the injector inlet

d - pressure at the needle valve-seat

e - needle lift

f - injection rate

Fig. 14 Comparison between numerical and experimental results

sure, and p_e the nozzle back-pressure. Therefore, for a given liquid, if the injection rate, the cross-sectional area of the holes, and the pressures on both sides of the holes are known, the discharge coefficient can be obtained from Eq. (20). In order to take the unsteadiness and compressibility flow effects as well as the dynamic effects of the needle lift and the influence of the needle seat passage area into account, the flow parameters in Eq. (20) and the needle lift were determined, as functions of time, under real test conditions. Due to the practical impossibility of measuring the injection pressure, that is the pressure in the reduced sac, the pressure time history was recorded upstream to the needle seat opening passage. For this purpose a hole was made by electro-erosion in the nozzle wall and a collar with a piezoresistive transducer was fitted to it. The injection pressure was then determined as the solution of the continuity equation for the sac chamber, which is designated by number 1 in Fig. 6. The experimental pressure values at the seat passage, along with the measured injection rate and needle lift, were introduced as known variables in this equation; the correlations obtained in [12] for a tip-removed nozzle (with a needle tip similar to the present one) were fitted to the flow coefficient of the needle seat opening passage in the equation term expressing the flow rate through the passage. The nozzle-hole discharge coefficient was then obtained from Eq. (20) for a back pressure equal to the ambient pressure. It has to be specified that, even though the injection rate was measured using a Bosch indicator and consequently with an average back pressure higher than the ambient pressure, it was virtually independent of the back pressure [41–43], as the pressure at the injector inlet and at the seat opening passage, as well as the needle lift, were verified to be.

Figures 12 and 13 show the distributions of the actual un-

Pump speed: 1000 rpm

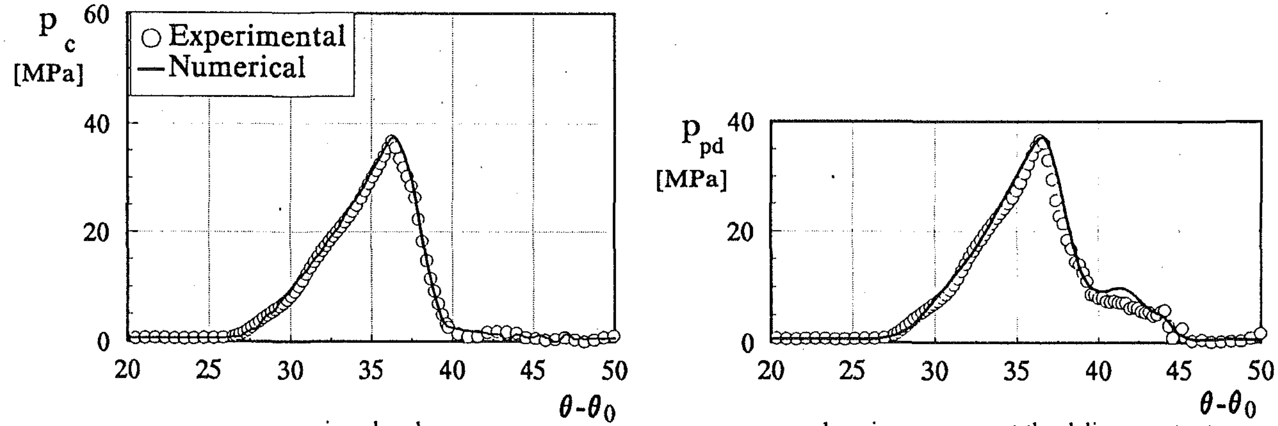

a - pumping chamber pressure

b - pipe pressure at the delivery output

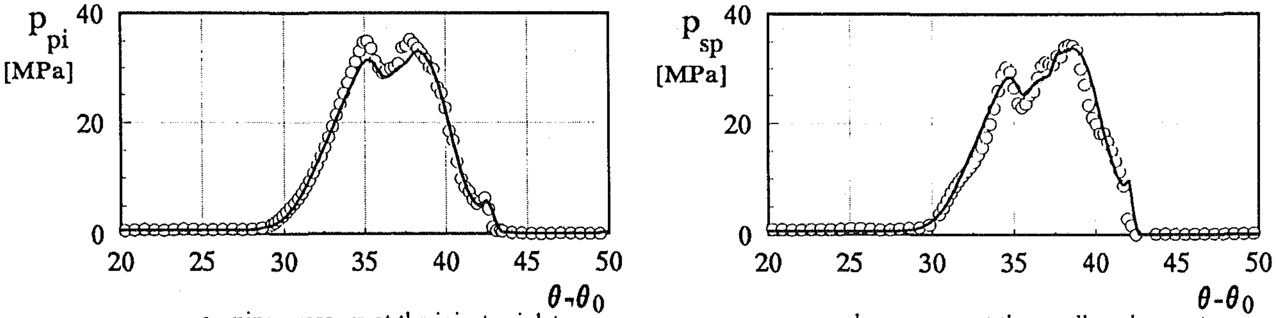

c - pipe pressure at the injector inlet

d - pressure at the needle valve-seat

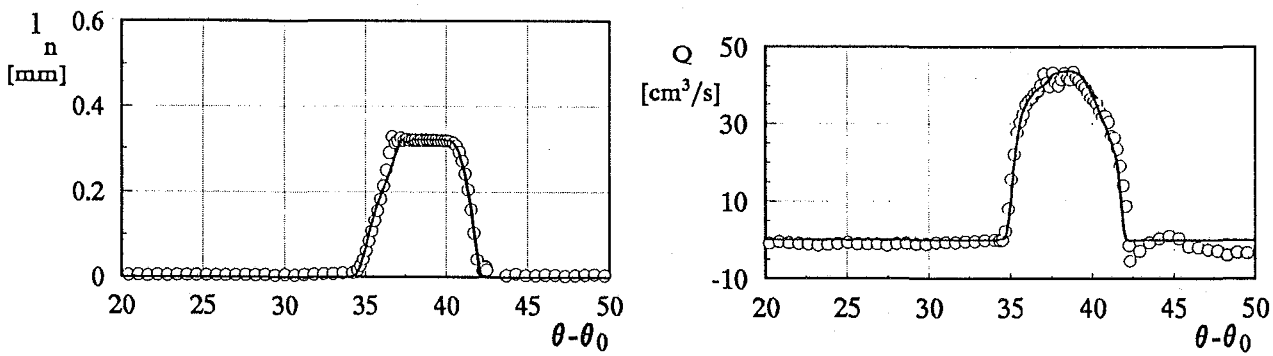

e - needle lift

f - injection rate

Fig. 15 Comparison between numerical and experimental results

steady flow coefficient of the nozzle holes determined at different pump speeds as a function of the needle lift (Fig. 12), of the cam angle (Fig. 13*a*) and also of the injection rate, that is equivalent to the Reynolds number (Fig. 13*b*). The increasing trend of the flow coefficient versus cam angle is due to the unsteadiness of the flow during the opening of the needle valve and to the dynamic effects of the valve during its closure. This causes a hysteresis-like phenomenon, as suggested by the patterns in Fig. 12. The decrease of the discharge coefficient at the end of the needle-valve closure is so fast as to imply a poor experimental resolution.

The thick continuous line in Fig. 12 represents the analytical fit of the indirectly measured data used by the authors for computation; though a dependence of the flow coefficient on pump speed may be suggested by this figure, the same fit for all the data sets was preferred and, in addition, with the same pattern during the opening and closing of the needle valve. At present, experiments are in progress to find correlations of more general application to reduced-sac or sacless multihole injectors. For comparison purposes, the thin broken line reported in Fig. 12 shows the fit obtained in [12] for a different geometry of injector nozzle with a single co-axial hole and a relatively large sac chamber.

Injection-System Analysis. Figures 14–17 compare the numerical and experimental results in terms of pumping chamber pressure (p_c), pipe pressure at the output of the delivery-valve assembly (p_{pd}), pipe pressure at the injector inlet (p_{pi}), pressure at the needle seat opening passage (p_{sp}), needle lift (l_n), and injection rate (Q), as functions of the cam angle ($\theta - \theta_0$), obtained for the pump-shaft angular speeds reported at the top of the figures. The injection rate was normalized through

Pump speed: 1500 rpm

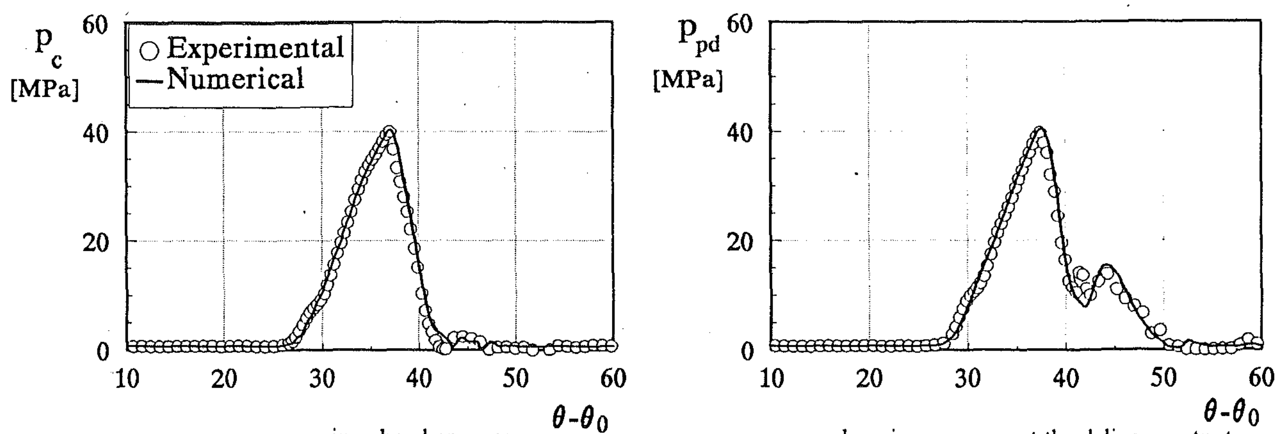

a - pumping chamber pressure

b - pipe pressure at the delivery output

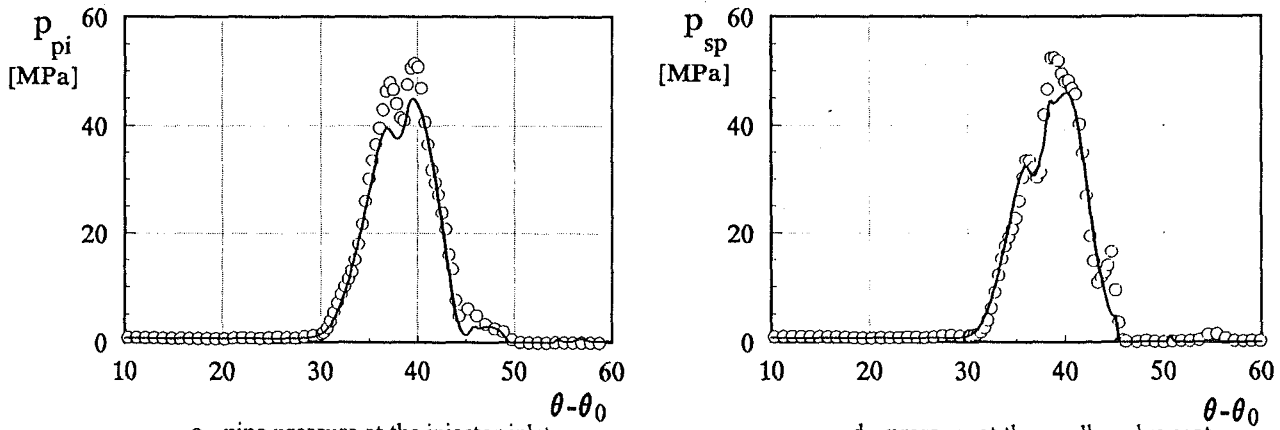

c - pipe pressure at the injector inlet

d - pressure at the needle-valve seat

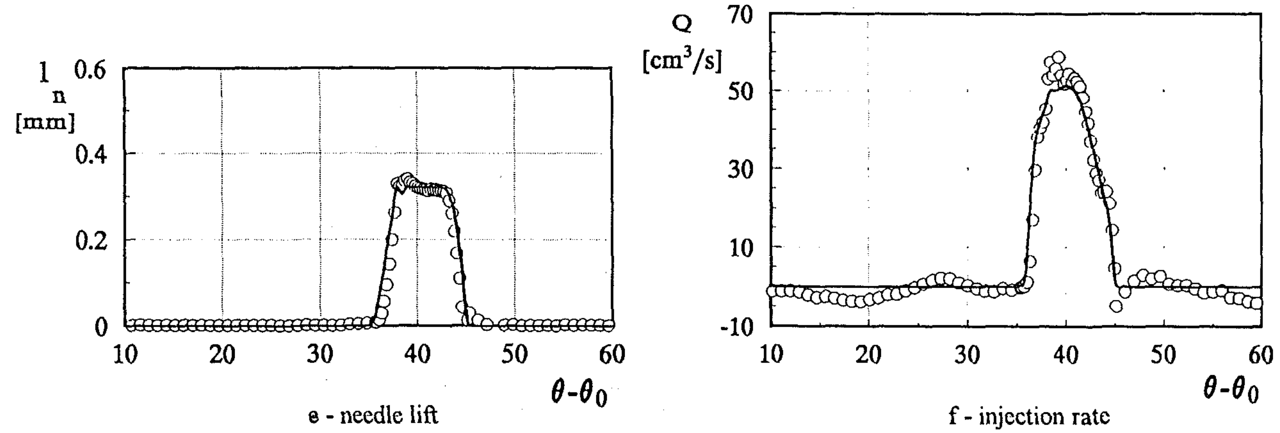

e - needle lift

f - injection rate

Fig. 16 Comparison between numerical and experimental results

the injected fuel quantity per cycle (V_f), measured by means of a graduate. Figure 18 shows the numerical and experimental values of V_f at different pump speeds.

The good agreement evident from these figures substantiates the validity of the injection-system mathematical model and, in particular, of the pump. A significant contribution to the accuracy of the numerical analysis was found to be given by the simulation of the wave propagation phenomena in the distributor drilled passages and its outlets, as well as by the modeling of the minor losses, with particular reference to the sudden expansion and contraction losses. These losses were evaluated on the basis of global mass and momentum conservation with the assumption of local quasi-steady conditions. Furthermore, an important role in the numerical results was played by the nozzle-hole discharge coefficient and it can be easily inferred from the experimental distributions of μ_h in Fig. 12 and their fit used in the model, that a further, but not substantial, improvement of the agreement between theoretical and experimental results could be obtained by a more refined evaluation of this coefficient. At the present stage, the accuracy

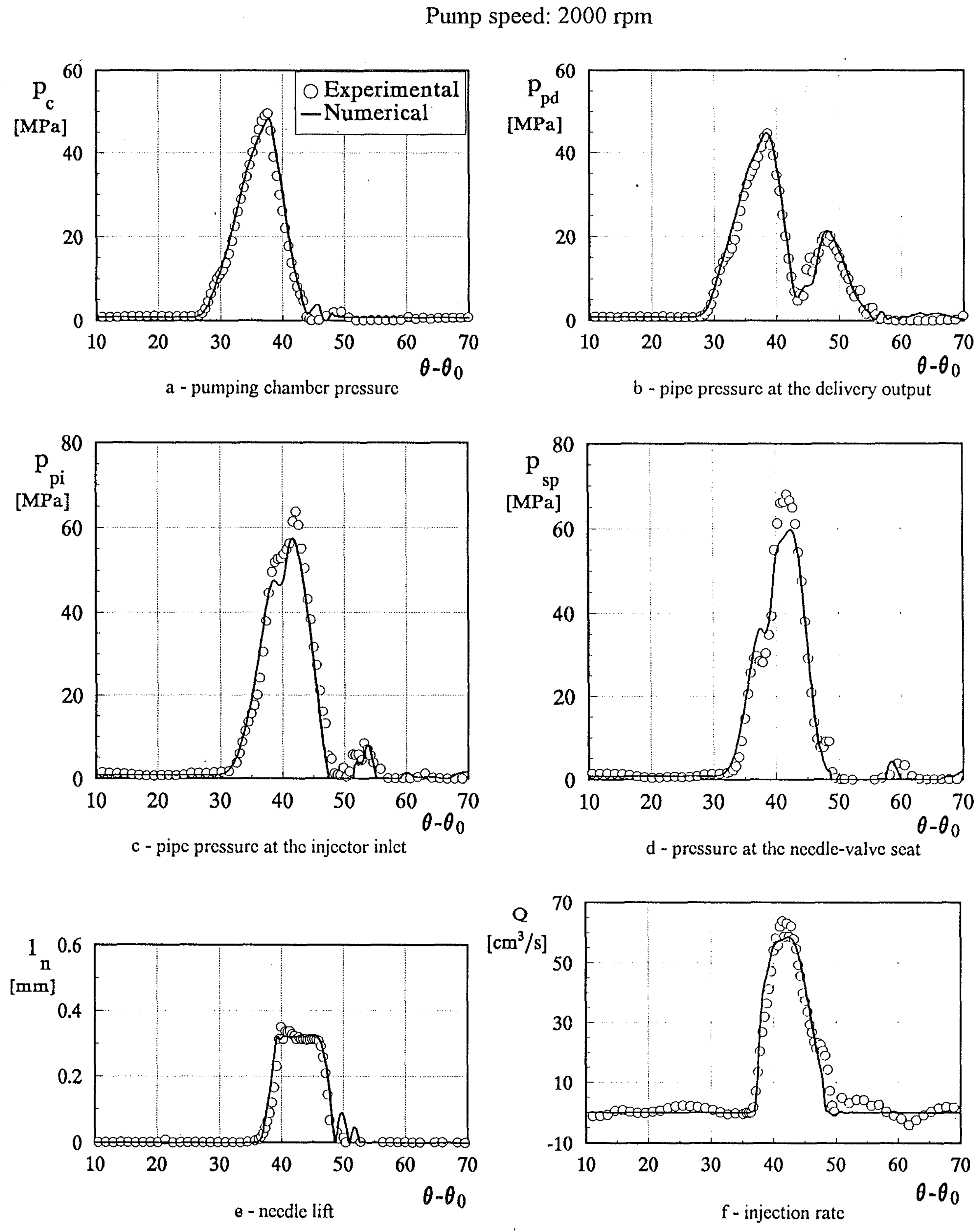

a - pumping chamber pressure

b - pipe pressure at the delivery output

c - pipe pressure at the injector inlet

d - pressure at the needle-valve seat

e - needle lift

f - injection rate

Fig. 17 Comparison between numerical and experimental results

degree of the injection-system numerical model is quite satisfactory. The discrepancy still existing between numerical and experimental results in the peaks of pressures p_{pi} and p_{sp} as well as of the injection rate at high pump speed (Figs. 16 and 17) may also be ascribed to the accuracy order of the BSBT scheme, due to their high frequency content. A better agreement between numerical and experimental results in this case can be expected using a second-order accurate numerical scheme.

In order to give application examples of the injection-system numerical model as a powerful investigation tool complementary to experimentation, the injection pressure (that is, the pressure in the sac chamber) was numerically evaluated for the conditions in Figs. 14–17, and the system performance was examined for the two cases in which the area of the delivery return-flow restriction (A_r) is made equal to zero or twice as high as the actual value (A_{r_0}).

Figure 19 shows the computed distributions of injection pressure versus cam angle, at the four pump speeds considered. For comparison, the so-called test-derived distributions of p_s are also reported in the figure. These were obtained from the measured needle lift, injection rate, and pressure at the needle seat passage, as specified in the previous section, and are plotted only in the cam-angle interval where the injection rate was significant. Their uncertainty could be estimated as being very close to the experimental one, because a second-order accurate BDF numerical scheme was used to solve the sac continuity equation and the uncertainty due to the seat-passage flow coefficient was assessed to exert a negligible influence, owing to its relatively high values in the region where it was important. Therefore, considering that the nozzle-hole flow coefficient was obtained from test-derived p_s, the results of Fig. 19 give an indication of the numerical-model accuracy, including the deviation of the fit, used for μ_h in computation, from the indirectly measured values of this coefficient (Fig. 12). The first peak in the distribution of p_s, at the start of the needle-valve opening (related to the very small values of μ_h), is mainly a consequence of the flow unsteadiness and gives rise to a perturbation propagating upstream to the sac chamber, while the second and principal peak, at the full opening of the needle valve, originates from the distributor pump. Therefore, it can be inferred from Figs. 12 and 19 that the attenuation of this peak in the numerical results at high pump speed (Figs. 19*c* and 19*d*) is in part due to the dissipative character of the BSBT scheme.

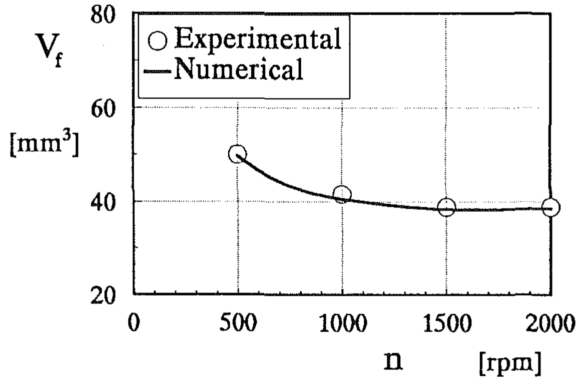

Fig. 18 Volume of fuel injected per cycle

Figure 20 reports the computed distributions of p_c, p_{pd}, p_{pi}, p_{sp}, l_n, and Q, as functions of the cam angle, at the pump speed $n = 1500$ rpm, for the three values of the delivery-return-flow restriction area $A_r = 0$, $A_r = A_{r_0}$, and $A_r = 2A_{r_0}$, A_{r_0} being the actual value referred to in Fig. 16. It is interesting to observe that the results for $A_r = 0$ not only show a reopening of the needle (Fig. 20*e*), with a consequent fuel reinjection (Fig. 20*f*), but also exhibit higher pressure distributions everywhere in the system (pumping chamber included (Fig. 20*a*)) before and during the regular injection phase. As can be deduced from

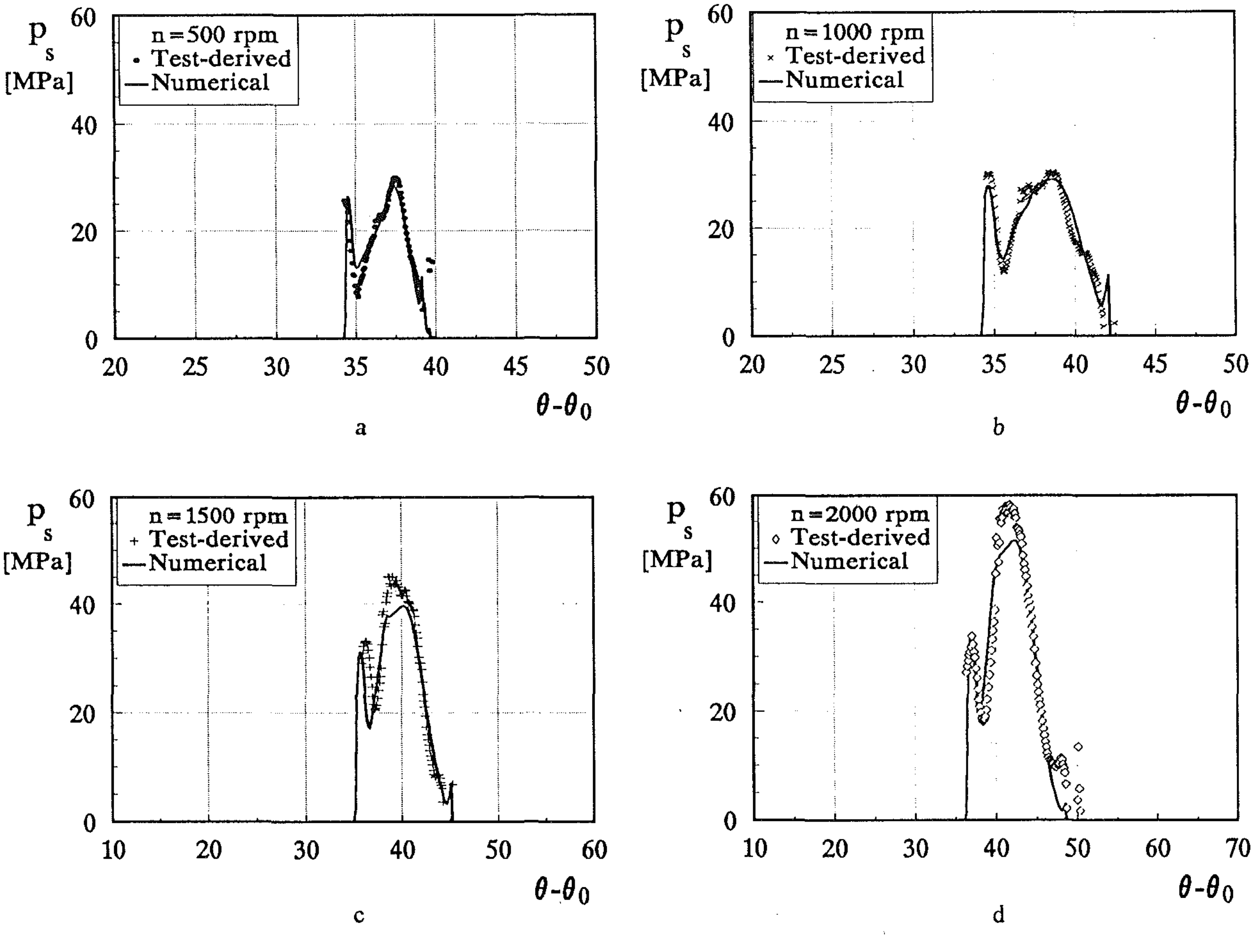

Fig. 19 Injection pressure

Pump speed: 1500 rpm

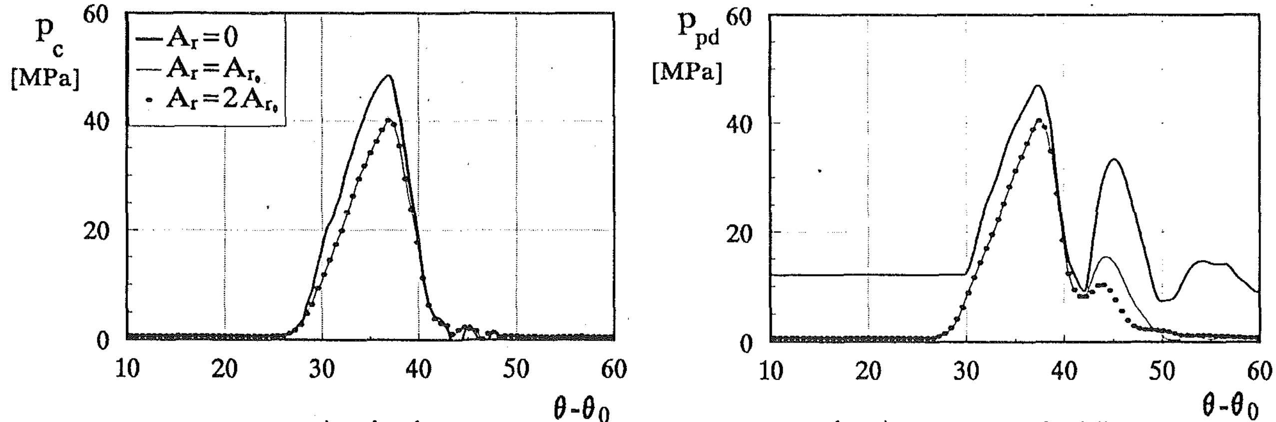

a - pumping chamber pressure

b - pipe pressure at the delivery output

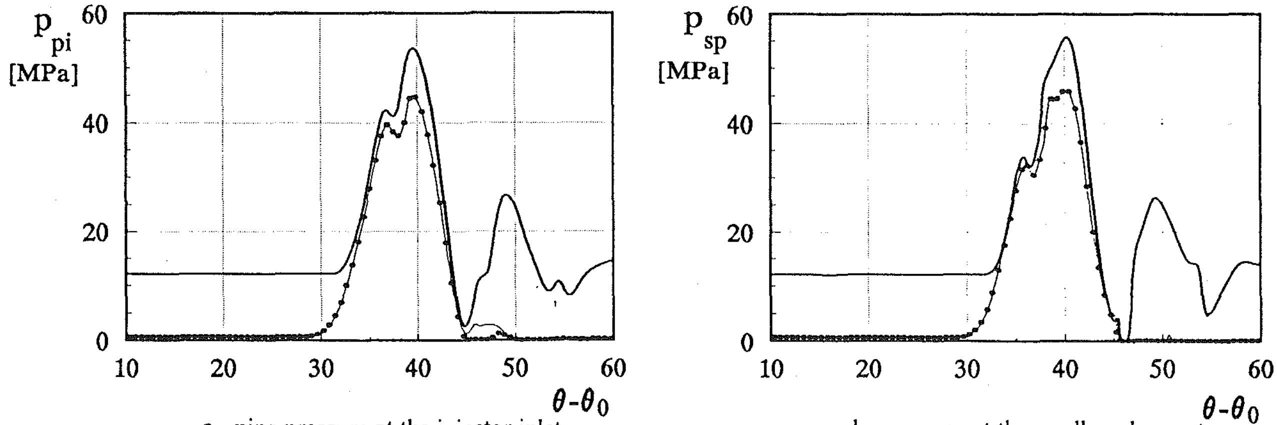

c - pipe pressure at the injector inlet

d - pressure at the needle-valve seat

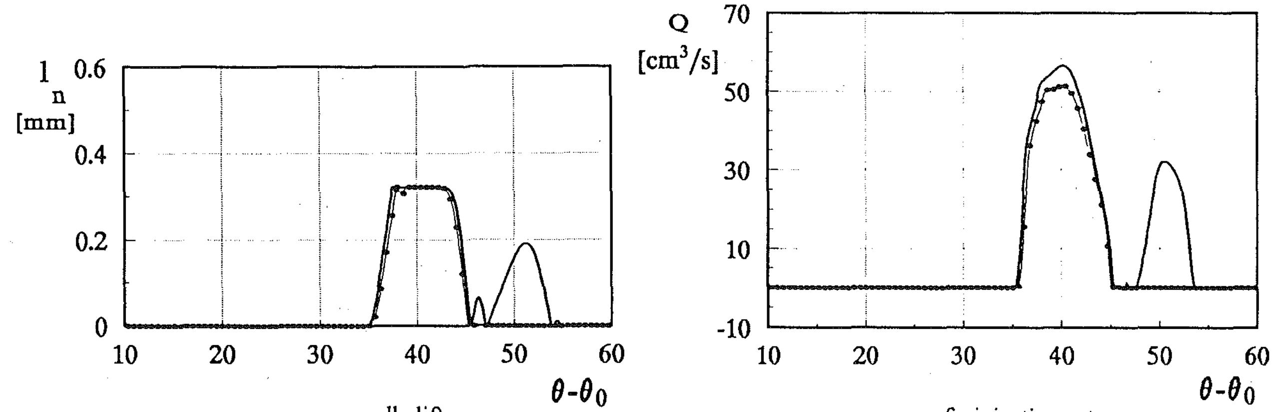

e - needle lift

f - injection rate

Fig. 20 Influence of the return-flow restriction on the system performance

Figs. 20(b-e), this latter phenomenon is due to the higher residual pressure in the pipe, consequent to the fact that the more intense pressure-wave reflected at the delivery valve plate, which causes the needle reopening, is not damped by the return-flow restriction. The residual pressure in Fig. 20 was therefore the result of a cycle-by-cycle computation. For $A_r = 2A_{r0}$ virtually the same pressure distributions were obtained as for $A_r = A_{r0}$, with the exception of a lower pressure wave reflection, at the delivery valve plate, and a more intense pipe cavitation in the former case (Fig. 20c).

Conclusion

A new mathematical model of distributor-type fuel-injection systems for diesel engines was developed, validated, and applied to the analysis of the injection pressure in a production system, equipped with a Bosch VE distributor pump. The efficient and fast implicit numerical algorithm used was shown essentially to match the transient pipe flow, including possible cavitation, to the dynamics of the mechanical units at its boundary.

A significant contribution to the accuracy of the pump model was given by the simulation of wave propagation phenomena in the distributor and its outlets as well as by the estimation of the minor losses, with particular reference to the sudden expansion and contraction losses.

An important role in the injector modeling was found to be played by the nozzle-hole discharge coefficient; however, there is a lack of expressions for this parameter taking the unsteadiness and compressibility flow effects into account, along with the dynamic effects of the needle lift and the influence of the needle seat passage. For the first time in the case of a reduced-sac multihole nozzle this coefficient was experimentally derived by the authors under real test conditions, showing an increasing trend during the injection phase due to unsteadiness effects. The persisting high values of the nozzle flow coefficient during most of the needle closure lift could be mainly ascribed to the dynamic effects of the needle valve. Nevertheless, the fit used for all the data sets at different pump speeds in the model, with the same distribution versus the needle lift during the opening and closing of the needle valve, led to satisfactory results. At present, experiments are in progress to find correlations of more general application to reduced-sac or sacless multihole single-stage injectors.

The comparison between numerical and experimental results showed the validity of the injection-system model. In particular, the good agreement obtained between the computed and the test-derived injection pressure (that is, the pressure in the sac chamber) gave an indication of the numerical-model accuracy, including the deviation of the fit used for the nozzle flow-coefficient from the indirectly measured values of this parameter. Definitely, a finite-difference scheme with an accuracy order higher than that of the BSBT method can improve the agreement in the main peaks of the injection rate and of the pipe pressures far from the delivery valve at the highest pump speeds.

The influence of the delivery-valve return-flow restriction on the system performance was also numerically investigated and it was found that for a restriction area equal to zero there was not only a reopening of the nozzle, with a second injection stage, but also a sensible increase of the pressure distributions everywhere in the system, including the pump chamber. On the other hand, for a restriction area twice as large as the actual value, a more intense pipe cavitation appeared.

Acknowledgments

This work was financially supported by C.N.R.-P.F.T. 2 (Consiglio Nazionale delle Ricerche–Progetto Finalizzato Trasporti 2) under Contract No. 91.02480.PF74.

References

1 Parker, R. F., "Future Fuel Injection System Requirements of Diesel Engines for Mobile Power," SAE Paper No. 760125, 1976.

2 Beck, N. J., Uyehara, O. A., and Johnson, W. P., "The Effect of Fuel Injection on Diesel Combustion," SAE Paper No. 880299, 1988.

3 Stumpp, G., Polach, W., Muller, N., and Warga, J., "Fuel Injection Equipment for Heavy Duty Diesel Engines for U.S. 1991/1994 Emission Limits," SAE Paper No. 890851, 1989.

4 Schulte, H., Duernholz, M., and Wuebbeke, K., "The Contribution of the Fuel Injection System to Meeting Future Demands on Truck Diesel Engines," SAE Paper No. 900822, 1990.

5 Itoh, S., Sasaki, S., and Arai, K., "Advanced In-Line Pump for Medium-Duty Diesel Engines to Meet Future Emission Regulations," SAE Paper No. 910182, 1991.

6 Schweimer, G. W., and Bader, T., "Hydraulic Unit Injector for Passenger Car DI-Diesel Engines," SAE Paper No. 920628, 1992.

7 Oblaender, K., Kollmann, K., Kraemer, M., and Kutschera, I., "The Influene of High Pressure Fuel Injection on Performance and Exhaust Emissions of a High Speed Direct Injection Diesel Engine," SAE Paper No. 890438, 1989.

8 Aoyama, T., Mizuta, J., and Oshima, Y., "NO_x Reduction by Injection Control," SAE Paper No. 900637, 1990.

9 Beck, N. J., and Chen, S. K., "Injection Rate Shaping and High Speed Combustion Analysis—New Tools for Diesel Engine Combustion Development," SAE Paper No. 900639, 1990.

10 Greeves, G., and Wang, C. H. T., "Two-Stage Lift Injection and HSDI Combustion," SAE Paper No. 905025, 1990.

11 Yokota, H., Kamimoto, T., Kosaka, H., and Tsujimura, K., "Fast Burning and Reduced Soot Formation via Ultra-High Pressure Diesel Fuel Injection," SAE Paper No. 910225, 1991.

12 Xu, M., Nishida, K., and Hiroyasu, H., "A Practical Calculation Method for Injection Pressure and Spray Penetration in Diesel Engines," SAE Paper No. 920624, 1992.

13 Catania, A. E., Dongiovanni, C., and Mittica, A., "Implicit Numerical Model of a High-Pressure Injection System," ASME JOURNAL OF ENGINEERING FOR GAS TURBINES AND POWER, Vol. 114, 1992, pp. 534–543.

14 Catania, A. E., Dongiovanni, C., and Mittica, A., "On the Numerical Simulation of High-Pressure Injection Systems" [in Italian], *ATA Automotive Engineering*, Vol. 46, 1993, pp. 338–354.

15 Huber, E. W., and Schaffits, W., "Experimental and Theoretical Research for the Simulation of Diesel Injection Systems" [in German], *MTZ*, Vol. 27, 1966, pp. 35–42.

16 Brown, G. W., and McCallion, H., "Simulation of an Injection System With Delivery Pipe Cavitation Using a Digital Computer," *IMechE*, Vol. 182, 1968, pp. 215–225.

17 Becchi, G. A., "Analytical Simulation of Fuel Injection in Diesel Engines," SAE Paper No. 710568, 1971.

18 Wylie, E. B., Bolt, J. A., and El-Erian, M. F., "Diesel Fuel Injection System Simulation and Experimental Correlation," SAE Paper No. 710569, 1971.

19 Matsuoka, S., Yokota, K., Kamimoto, T., and Igoshi, M., "A Study of Fuel Injection Systems in Diesel Engines," SAE Paper No. 760551, 1976.

20 Goyal, M., "Modular Approach to Fuel Injection System Simulation," SAE Paper No. 780162, 1978.

21 Kumar, K., Gajendra Babu, M. K., Gaur, R. R., and Garg, R. D., "A Finite Difference Scheme for the Simulation of a Fuel Injection System," SAE Paper No. 831337, 1983.

22 Gibson, D. H., "A Flexible Fuel Injection Simulation," SAE Paper No. 861567, 1986.

23 Krepec, T., To, C. H., and Lisio, C., "Investigation on Dynamic Response of a Closed Fuel Injector in a Diesel Engine at Low Speed," SAE Paper No. 880297, 1988.

24 Fischer, W., Fuchs, W., Laufer, H., and Reuter, U., "Solenoid-Valve Controlled Diesel Distributor Injection Pump," SAE Paper No. 930327, 1993.

25 Hardenberg, H., "The Needle Lift Dependency of Flow Coefficients of Hole Nozzles for Direct Injection Diesel Engines" [in German], *MTZ*, Vol. 46, 1985, pp. 143–146.

26 Ziejewski, M., and Goettler, H. J., "Discharge Coefficients for Multihole Fuel Injection Nozzle for Alternate Fuels," SAE Paper No. 890448, 1989.

27 Date, K., Nobechi, H., Kano, H., Kato, M., and Oya, T., "Experimental Analysis on Fuel Flow Characteristics in the Nozzle for Direct Injection Engines," SAE Paper No. 931002, 1993.

28 Anderson, D. A., Tannehill, J. C., and Pletcher, R. H., *Computational Fluid Mechanics and Heat Transfer*, McGraw-Hill, New York, 1984.

29 Weyler, M. E., Streeter, V. L., and Larsen, P. S., "An Investigation of the Effect of Cavitation Bubbles on the Momentum Loss in Transient Pipe Flow," ASME *Journal of Basic Engineering*, Vol. 93, 1971, pp. 1–10.

30 Kranenburg, C., "Gas Release During Transient Cavitation in Pipes," ASCE *Journal of the Hydraulics Division*, Vol. 100, 1974, pp. 1383–1398.

31 Wiggert, D. C., and Sundquist, M. J., "The Effect of Gaseous Cavitation on Fluid Transients," ASME *Journal of Fluids Engineering*, Vol. 101, 1979, pp. 79–86.

32 Kamiyama, S., and Yamasaki, T., "Critical Condition on Cavitation Occurrence in Various Liquids," ASME *Journal of Fluids Engineering*, Vol. 108, 1986, pp. 428–432.

33 Driels, M. R., "An Investigation of Pressure Transients in a System Containing a Liquid Capable of Air Absorption," ASME *Journal of Fluids Engineering*, Vol. 95, 1973, pp. 408–414.

34 Chaudhry, M. H., and Hussaini, M. Y., "Second-Order Accurate Explicit Finite-Difference Schemes for Waterhammer Analysis," ASME *Journal of Fluids Engineering*, Vol. 107, 1985, pp. 523–529.

35 Kohda, K., Suzukawa, Y., and Furukawa, H., "Analysis of Transient Gas-Liquid Two-Phase Flow in Pipelines," ASME *Journal of Energy Resources Technology*, Vol. 110, 1988, pp. 93–101.

36 Chaudhry, M. H., Bhallamudi, S. M., Martin, C. S., and Naghash, M., "Analysis of Transient Pressures in Bubbly, Homogeneous, Gas-Liquid Mixtures," ASME *Journal of Fluids Engineering*, Vol. 112, 1990, pp. 225–231.

37 Kano, H., Kato, M., Kojima, T., and Katagiri, M., "Contribution of Optimum Design for Nozzle Configuration to Spray Formation," SAE Paper No. 900824, 1990.

38 Okajima, M., Kato, M., Kano, H., Tojo, S., and Katagiri, M., "Contribution of Optimum Nozzle Design to Injection Rate Control," SAE Paper No. 910185, 1991.

39 Date, K., Manabe, M., Kano, H., Kato, M., and Oya, T., "Contribution of Fuel Flow Improvement in Nozzle to Spray Formation," SAE Paper No. 920622, 1992.

40 Harten, A., Engquist, B., Osher, S., and Chakravarthy, S. R., "Uniformly High Order Accurate Essentially Non-oscillatory Schemes, III," *Journal of Computational Physics*, Vol. 71, 1987, pp. 231–303.

41 Bosch, W., "The Fuel Rate Indicator: A New Measuring Instrument for Display of the Characteristics of Individual Injection," SAE Paper No. 660749, 1966.

42 Bower, G. R., and Foster, D. E., "A Comparison of the Bosch and Zeuch Rate of Injection Meters," SAE Paper No. 910724, 1991.
43 Takamura, A., Ohta, T., Fukushima, S., and Kamimoto, T., "A Study on Precise Measurement of Diesel Fuel Injection Rate," SAE Paper No. 920630, 1992.

APPENDIX

Figures A1 and A2 show a longitudinal section of the distributor-pump plunger and its external surface drawn as a plane, respectively.

The analytical equations for the opened section of ports are written with reference to the null stroke position $s_{p_0}=0$, to the rotation angle of the plunger $\vartheta_0=0$, and to the nomenclature given in Fig. A2. The right side of this figure represents an enlargement of the external surface of the distributor-pump plunger. The plunger stroke s_p and the curvilinear abscissa $r\vartheta$ (r being the plunger radius and ϑ its rotation angle) are reported in the reference frame shown at the top left of the enlargement in Fig. A2.

From the intersection between the rectangular areas at the top of Fig. A2 in their relative motion one obtains the equation set (1A) giving the relations for the inlet port area A_{in} (A_{in_M} indicates the maximum value of this area in the barrel).

$$A_{in}=\xi(f-s_p)g+\delta_1[e-\xi(f-s_p)]\left[\left(\delta_1-\frac{|\delta_2|}{2}\right)g+\left(1-\delta_1+\frac{|\delta_2|}{2}\right)d+\delta_2\left(h-r\vartheta+\frac{d}{2}\right)+\delta_3\frac{\pi}{4}r\right]$$

$$i\frac{\pi}{2}r\le r\vartheta<h+d+\frac{g}{2}+\frac{\pi}{2}(i-1/2)r \quad \delta_1=1 \quad \delta_2=1 \quad \delta_3=-1$$

$$h+d+\frac{g}{2}+\frac{\pi}{2}(i-1/2)r\le r\vartheta<h-\frac{g}{2}+\frac{\pi}{2}(i-1/2)r \quad \delta_1=0$$

$$h-\frac{g}{2}+\frac{\pi}{2}(i+1/2)r\le r\vartheta<h+\frac{g}{2}+\frac{\pi}{2}(i+1/2)r$$
$$\delta_1=1 \quad \delta_2=-1 \quad \delta_3=-1$$

$$h+\frac{g}{2}+\frac{\pi}{2}(i+1/2)r\le r\vartheta<h+d-\frac{g}{2}+\frac{\pi}{2}(i+1/2)r$$
$$\delta_1=1 \quad \delta_2=0 \quad \delta_3=0$$

$$h+d-\frac{g}{2}+\frac{\pi}{2}(i+1/2)r\le r\vartheta<\frac{\pi}{2}(i+1)r$$
$$\delta_1=1 \quad \delta_2=1 \quad \delta_3=1$$

with

$$\xi=\begin{cases}1 & 0\le s_p<f\\ 0 & f\le s_p\end{cases} \quad \text{and} \quad i=0,\ 1,\ 2,\ 3 \qquad (1A)$$

The distribution port A_{out}, in the middle of Fig. A2, is expressed as the intersection between rectangular and circular areas by the equation set (2A) (A_{out_M} indicates the maximum value of the distribution port area):

$$A_{\text{out}}=\frac{\pi}{2}r_d^2+\delta[(\xi-1)\sqrt{\xi(2-\xi)}-\arcsin(1-\xi)]r_d^2$$

$$i\pi r\le r\vartheta<2r_d+i\pi r \qquad \delta=1 \qquad \xi=\frac{r(\vartheta-i\pi)}{r_d}$$

$$2r_d+i\pi r\le r\vartheta<a+i\pi r \qquad \delta=1 \qquad \xi=2$$

$$a+i\pi r\le r\vartheta<a+i\pi r+2r_d \qquad \delta=-1 \qquad \xi=\frac{r(\vartheta-i\pi)-a}{r_d}$$

$$a+i\pi r+2r_d\le r\vartheta<(i+1)\pi r \qquad \delta=-1 \qquad \xi=2$$
$$\text{with } i=0,\ 1 \qquad (2A)$$

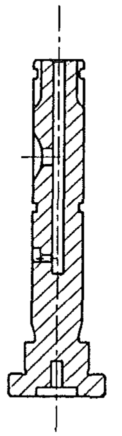

Fig. A1 Longitudinal section of the distributor-pump plunger

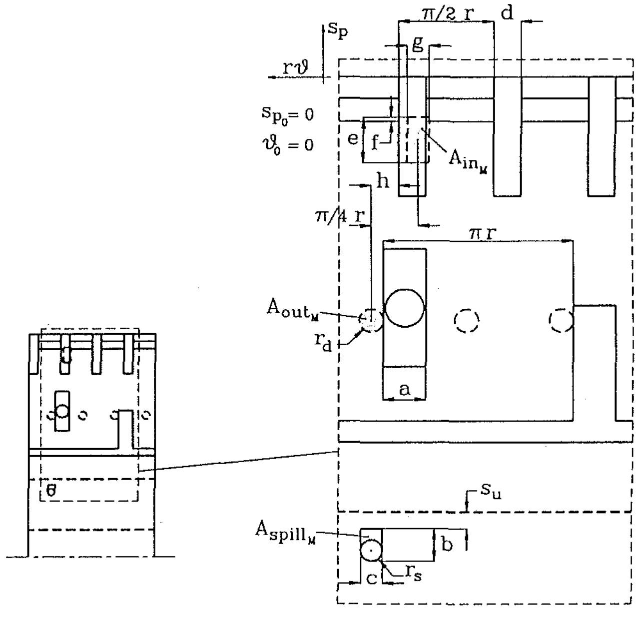

Fig. A2 External surface of plunger drawn as a plane

The spill port A_{spill}, whose maximum value is indicated at the bottom of Fig. A2, causes the end of injection. The amplitude of this port opening is determined by the position of the edge of the control collar with respect to the plunger; this position is indicated as s_u in Fig. A2, where the control edge is indicated by the thick dashed line. A_{spill} is expressed by the equation set (3A):

$$A_{\text{spill}}=\delta c(b-r_s)+r_s^2[\xi\sqrt{1-\xi^2}+\arcsin(\xi)]$$

$$0\le s_p<s_u \qquad \delta=0 \qquad \xi=0$$

$$s_u\le s_p<s_u+b-r_s \qquad \delta=\frac{s_p-s_u}{b-r_s} \qquad \xi=0$$

$$s_u+b-r_s\le s_p<s_u+b \qquad \delta=1 \qquad \xi=\frac{s_p-(s_u+b-r_s)}{r_s}$$

$$s_u+b\le s_p \qquad \delta=1 \qquad \xi=1 \qquad (3A)$$

The area A_d of the delivery valve seat passage (Fig. A3) is expressed by the equation set (4A):

$$A_d=A_r=r^2\arcsin\left(\frac{g}{2r}\right)-\frac{g}{4}\sqrt{4r^2-g^2} \qquad l_d\le 0$$

$$A_d=\pi l_d(2r-l_d\sin\alpha\cos\alpha)\sin\alpha \qquad 0<l_d\le l_d^*$$

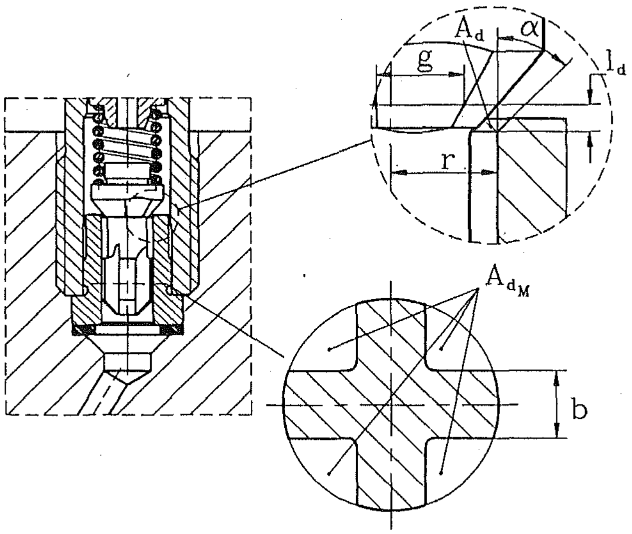

Fig. A3 Delivery valve geometry

$$A_d = A_{d_M} = r^2\left[\pi - 4\arcsin\left(\frac{b}{2r}\right)\right] + b\left(b - \sqrt{4r^2 - b^2}\right) \qquad l_d^* < l_d \tag{4A}$$

where l_d^* is the value corresponding to the $A_d(l_d^*) = A_{d_M}$ condition.

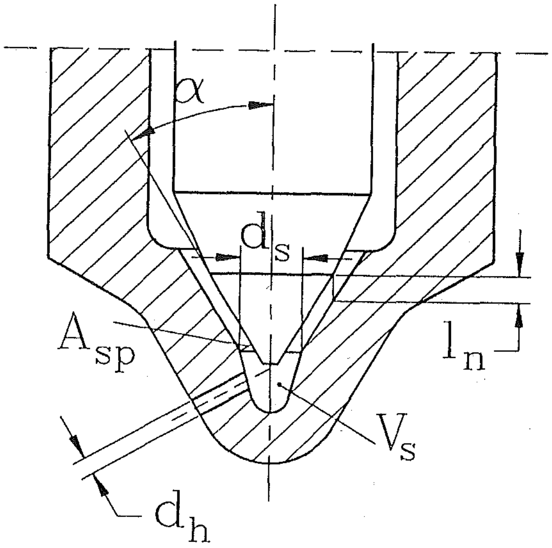

Fig. A4 Geometry of injector nozzle tip

The area A_{sp} of the needle seat opening passage is given by

$$A_{sp} = \pi l_n(d_s - l_n \sin\alpha \cos\alpha)\sin\alpha \tag{5A}$$

The cross-sectional area A_h of the four nozzle holes is:

$$A_h = 4\left(\pi\frac{d_h^2}{4}\right) \tag{6A}$$

d_h being the diameter of each hole.

A Rayleigh-Type Inclusion of Shaft Inertia in Torsional Vibration Analysis

S. Doughty
Doughty and Company,
Registered Professional Engineers,
939 High Hill Creek Road,
La Grange, TX 78945-4407

This paper considers the problem of properly accounting for the shafting inertia in torsional vibration analysis. It begins with a brief review of the two well-established methods: (1) arbitrarily lumping the shaft inertia with that of the disks, and (2) the continuum model, which considers both the flexibility and the inertia as distributed properties. Comments regarding the advantages and disadvantages of each are offered as motivation for the new method to be presented here. The new approach is then developed, using a Rayleigh-type approximation for the displacement between stations, with the full theory underlying it. The results of all three methods are then compared by application to several test cases.

Introduction

The method of analysis of torsional vibrations most often used today was presented by H. Holzer (1921). Holzer's method is usually presented as a means for determining natural frequencies and mode shapes for close-coupled systems. While this is true, the method is applicable also to the forced response of both undampled and damped systems. Originally, Holzer's calculation was presented in a form for tabular computation; today the same steps are easily implemented in a digital computer program.

Holzer's analysis is based entirely on a discrete model, which is to say that the stiffness, inertia, and damping of the system are each associated with a particular (discrete) part of the system. Thus, the compliance is associated with the shafting, which is considered to be massless (in the first approximation), while the inertia is attributed to discrete, rigid disks. The damping is assumed to be either (1) station-to-ground viscous coupling between a station and ground, or (2) station-to-station viscous coupling between two adjacent stations. Both types of damping are readily accommodated within a system model. The prolonged wide acceptance of this method suggests that this type of model must be not too far from the truth.

A more elegant model, reflecting much more closely the reality of distributed inertia and compliance, has been given by a number of authors, including Timoshenko (1928, pp. 216–219), Tuplin (1934, pp. 271–274), and Eshelman (1974). This model leads to a partial differential equation, the wave equation, for the motion of the shaft. Discrete, rigid disks may also be included within this model.

For a single degree of freedom, spring-mass oscillator, there is a widely known, approximate method to account for the effect of the mass of the spring when one end is stationary. The motion is assumed to be linearly distributed between the fixed and moving ends, and on this basis, the kinetic energy of the spring is calculated. The result is that the (approximate) effective mass of the spring is 1/3 of the actual mass of the spring, considered to be concentrated at the moving end of the spring. This approximation has been presented by many authors, including most recently Thomson (1993, pp. 24–25), and Dimarogonas and Haddad (1992, pp. 464–465). An application of this idea to torsional vibration is given by Timoshenko (1928, p. 219) and again by Tuplin (1934, pp. 44–45). In each of the latter two cases, the authors discuss a torsional system consisting of a single shaft connecting two disks. For such a system, there must be a nodal point between the two disks, and neither disk would vibrate differently if the shaft were clamped at the node. Once the shaft is considered clamped at the node, either end of the system may be considered as a single inertia connected to the nodal support through that part of the shafting adjacent to the disk.The application of the approximation then is clear: 1/3 of the shaft inertia, *for that part of the shaft between the disk and the node*, is to be added to the inertia of the disk. This raises the question, "How can this idea be applied to a many-station model representing an actual machine train?"

Established Methods

The two established method have been introduced above. These are (1) the completely discrete model, with some fraction of the inertia of the shafting arbitrarily lumped at the stations, and (2) the continuum model. The first of these will be called the "Holzer" model. The second will be referred to as the "Eshleman" model, in recognition that, while Eshleman did not originate this model, his work contributed very significantly to its application in torsional vibration analysis. Looking ahead to the new method, it will be termed the "Rayleigh"

Contributed by the Internal Combustion Engine Division and presented at the Energy-Sources Technology Conference and Exhibition, New Orleans, Louisiana, January 23–27, 1994. Manuscript received by the Internal Combustion Engine Division January 28, 1994. Paper No. 94-ICE-2. Associate Technical Editor: W. Cheng.

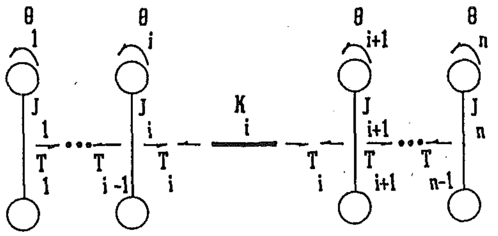

Fig. 1 Partial Holzer model

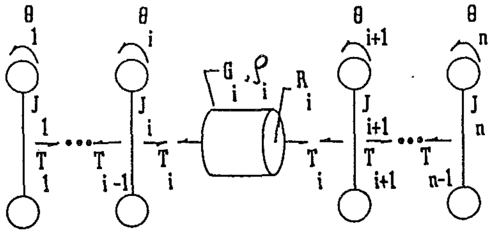

Fig. 2 Partial Eshleman model

model, in view of the use of Rayleigh's principle in its development.

Holzer Model. A partial Holzer model is shown in Fig. 1. As mentioned above, as a first approximation, the inertia of the shaft can be simply neglected; in this case, the only inertias in the model are those of the disks. The method of analysis for natural frequencies is one of testing an assumed value to see if the boundary conditions are satisfied. The process begins at one end, and the motion associated with the assumed frequency value is sequentially determined by stepping from station to station. At the left end of the shaft, the applicable boundary condition is no torque from the left, where there is no connection to the shaft. This boundary condition is explicitly taken into the calculations. Omitting damping for this discussion, the equations used to step from the ith station to the $i+1$th station are:

$$T_{i+1}=\left(1-\omega^2\frac{J_{i+1}}{K_i}\right)T_i-\omega^2 J_{i+1}\theta_i \tag{1}$$

and

$$\theta_{i+1}=\frac{T_i}{K_i}+\theta_i \tag{2}$$

where ω is the assumed frequency value. To begin the process, the equations describing the motion of the first station, and explicitly reflecting the absence of torque before the first station, are:

$$T_i=-\omega^2 J_i\theta_i=-\omega^2 J_i \tag{3}$$

$$\theta_1=1 \tag{4}$$

If the torque after the last station, known as the *residual torque*, is zero, then both boundary conditions are satisfied, and the assumed value is in fact a natural frequency. If the boundary conditions are not satisfied, then another trial value is assumed and the process repeated.

It is not difficult to see that the analyst is free to adjust the disk inertias by including some fraction of the shaft inertia with each disk inertia. The question is, "How much of the shaft inertia should go to each disk?" There is no obvious answer if the situation is more complex than the two-disk model described earlier. Tuplin (1934, pp. 44–45) gives a set of four rules, including the 1/3 rule described previously, to be followed in different situations. All of these rules depend on a knowledge of the location of the nearest node. Conceivably this could be satisfactory for an analysis of free vibrations, but in the case of forced vibrations, the concept of a node, as a system property, is not meaningful. Even if applied iteratively, a different allocation of the shaft inertia is required for each excitation frequency, which is not very convenient.

Eshleman Model. The continuum model, here termed the Eshleman model, is as shown in Fig. 2. As formulated by Eshleman (1974, p. 442), the model is restricted to a uniform cylindrical segment, possibly having a concentric hollow bore. This model leads to the wave equation, for which the solution is well known. The eventual result is the following pair of equations for stepping from the ith station to the $(i+1)$th station:

$$T_{i+1}=\left[\frac{K_i-\omega^2 J_i}{p_i G_{i+1}J_{i+1}}\sin(p_iL_i)+\frac{G_iJ_i}{G_{i+1}J_{i+1}}\cos(p_iL_i)\right]T_i+\left[\frac{K_i-\omega^2 J_i}{G_{i+1}J_{i+1}}\cos(p_iL_i)-\frac{p_iG_iJ_i}{G_{i+1}J_{i+1}}\sin(p_iL_i)\right]\theta_i \tag{5}$$

and

$$\theta_{i+1}=\frac{1}{p_i}\sin(p_iL_i)T_i+\cos(p_iL_i)\theta_i \tag{6}$$

where

G_i = shear modulus for section i,
L_i = length of section i,
ρ_i = mass density for section i,
and
$p_i=\omega\sqrt{(\rho_i/G_i)}$

As given above, this formulation applies only to cylindrical cross sections. While that is quite common, it is by no means the only cross section encountered. In particular, stepped shafts are very common, and tapered shafts occur as well. In principle, this model can be applied to the stepped shaft, simply considering each step as a separate cylindrical segment. There are two problems with this, one theoretical and one practical. Inherent in the model is the idea that the shear stress varies linearly with the radius over the entire cross section. At each step, there is an exposed transverse face on which there is no stress; this contradicts the assumption that shear stress is proportional to the radius. As a practical matter, applying the Eshleman model to each step of a shaft with many steps can quickly lead to a very large model. The writer has seen models of several hundred stations that resulted from this approach. This wastes resources, does not accommodate station-to-station damping, does not lend itself to compensating for additional flexibility at the steps, and requires working with a larger, more cumbersome model.

It should be mentioned that Holzer (1921, pp. 79–91) also addressed the problem of including the mass of the shaft by a continuum model, including tapering cross sections. After formulating the problem, the term associated with the taper was dropped, so that Holzer's result is simply that obtained from solving the wave equation.

New Method

The purpose here is to develop an approximate means for including, in a torsional vibration model, the inertia of the shaft, in a many-station model, particularly applicable to a stepped shaft without increasing the size of the model. This effort will draw upon the ideas behind the well-known approximation for the effect of the mass of a massive spring in a spring-mass oscillator.

Rayleigh Model. Consider first the uniform shaft segment shown in Fig. 3, which may include a hollow concentric bore (not shown). Let θ_1 and θ_2 denote the rotations of the left and right ends as measured from a fixed reference. The length of

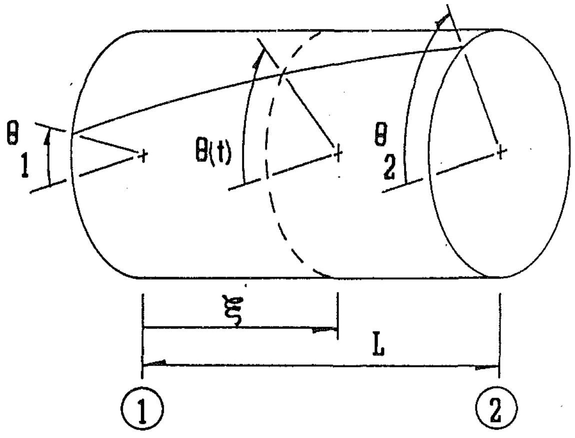

Fig. 3 Rayleigh shaft segment

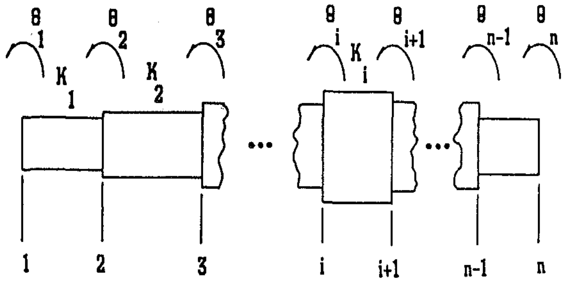

Fig. 4 Rayleigh shaft section

the segment is L, so that at any position ξ, the static rotation of that section is $\phi(\xi)$,

$$\phi(\xi)=\theta_1+\xi\,\frac{(\theta_2-\theta_1)}{L} \tag{7}$$

If this linear relation is assumed to describe the dynamic displacement as well, the angular velocity at this location is

$$\frac{d\phi}{dt}=\frac{d\theta_1}{dt}\left(1-\frac{\xi}{L}\right)+\frac{\xi}{L}\frac{d\theta_2}{dt} \tag{8}$$

The mass moment of inertia for a differential slice at this location is

$$dJ=\int_A \rho r^2 dA\ d\xi=\rho J_{\mathrm{AREA}}d\xi \tag{9}$$

where

ρ = mass density of the shaft material, and
J_{AREA} = area moment of inertia of the segment.

The kinetic energy of the complete shaft segment can then be written as

$$T=\frac{1}{2}\int_J\left(\frac{d\phi}{dt}\right)^2 dJ$$

$$=\frac{1}{2}\int_0^L \rho J_{\mathrm{AREA}}\left[\frac{d\theta_1}{dt}\left(1-\frac{\xi}{L}\right)+\frac{\xi}{L}\frac{d\theta_2}{dt}\right]^2 d\xi$$

$$=\frac{\rho J_{\mathrm{AREA}}L}{2}\left[\frac{1}{3}\left(\frac{d\theta_1}{dt}\right)^2+\frac{1}{3}\frac{d\theta_1}{dt}\frac{d\theta_2}{dt}+\frac{1}{3}\left(\frac{d\theta_2}{dt}\right)^2\right]$$

$$=\frac{\rho J_{\mathrm{AREA}}L}{2}\left(\frac{d\theta_1}{dt},\frac{d\theta_2}{dt}\right)\begin{bmatrix}\frac{1}{3} & \frac{1}{6}\\ \frac{1}{6} & \frac{1}{3}\end{bmatrix}\begin{Bmatrix}\frac{d\theta_1}{dt}\\ \frac{d\theta_2}{dt}\end{Bmatrix} \tag{10}$$

This completes the development for a single, cylindrical segment. This result was given by Tuplin (1934, p. 44).

Consider next the shaft section shown in Fig. 4, consisting of several cylindrical segments. For the ith segment, the stiffness is

$$K_i=\frac{J_{\mathrm{AREA}-i}G_i}{L_i} \tag{11}$$

based on the properties of the segment and using a static, strength-of-materials approach. The stiffness of the entire segment shown is

$$K_E=\left(\frac{1}{K_1}+\frac{1}{K_2}+\ldots\right)^{-1} \tag{12}$$

Now consider the matter of determining the rotation at each step in the section. For a section of n segments, $n-1$ independent equilibrium equations of the form

$$\begin{aligned}\mathrm{Torque}&=K_1(\theta_2-\theta_L)=K_E(\theta_R-\theta_L)\\ \mathrm{Torque}&=K_2(\theta_3-\theta_2)=K_E(\theta_R-\theta_L)\end{aligned} \tag{13}$$

can be written. The rotations of all locations, including both ends and the interior steps, can then be expressed in terms of the rotations at the ends of the section as

$$\{\theta_i\}=\begin{bmatrix}1 & 0 & 0 & 0 & \ldots & 0\\ 0 & K_1 & 0 & 0 & \ldots & 0\\ 0 & -K_2 & K_2 & 0 & \ldots & 0\\ 0 & 0 & \ddots & \ddots & \ldots & 0\\ 0 & 0 & 0 & -K_{n-1} & K_{n-1} & 0\\ 0 & 0 & 0 & 0 & 0 & -1\end{bmatrix}^{-1}$$

$$\times\left(\begin{Bmatrix}1\\ K_1-K_E\\ -K_E\\ \vdots\\ -K_E\\ 0\end{Bmatrix}\theta_L+\begin{Bmatrix}0\\ K_E\\ K_E\\ \vdots\\ K_E\\ 1\end{Bmatrix}\theta_R\right)=\{P_L\}\theta_L+\{P_R\}\theta_R \tag{14}$$

where the column matrices $\{P_L\}$ and $\{P_R\}$ are defined by the indicated matrix products. This result means that the rotation at each step can be expressed as a linear combination of the rotations at the two ends of the section. Again assuming that the static form describes the dynamic displacement as well, a similar relation applies to the angular velocities at each step expressed in terms of the angular velocities of the two ends,

$$\left\{\frac{d\theta_i}{dt}\right\}=\{P_L\}\frac{d\theta_L}{dt}+\{P_R\}\frac{d\theta_R}{dtd} \tag{15}$$

The kinetic energy of the whole section is considered next. If T_i is the kinetic energy of the ith segment, and drawing on Eq.(15) for the components of $\{P_L\}$ and $\{P_R\}$, then the total kinetic energy is

$$T=\sum_{i=1}^{n}T_i$$

$$=\sum_{i=1}^{n}\frac{\rho_i J_{\mathrm{AREA}-i}L_i}{2}\left(\frac{d\theta_i}{dt},\frac{d\theta_{i+1}}{dt}\right)\begin{bmatrix}\frac{1}{3} & \frac{1}{6}\\ \frac{1}{6} & \frac{1}{3}\end{bmatrix}\begin{Bmatrix}\frac{d\theta_i}{dt}\\ \frac{d\theta_{i+1}}{dt}\end{Bmatrix}$$

$$T=\sum_{i=1}^{n}\frac{\rho_i J_{\text{AREA-}i}L_i}{2}\left(\frac{d\theta_L}{dt},\frac{d\theta_R}{dt}\right)\begin{bmatrix}P_{L_i} & P_{L_{i+1}}\\ P_{R_i} & P_{R_{i+1}}\end{bmatrix}$$

$$\times\begin{bmatrix}\frac{1}{3} & \frac{1}{6}\\ \frac{1}{6} & \frac{1}{3}\end{bmatrix}\begin{bmatrix}P_{L_i} & P_{R_i}\\ P_{L_{i+1}} & P_{R_{i+1}}\end{bmatrix}\begin{Bmatrix}\frac{d\theta_L}{dt}\\ \frac{d\theta_R}{dt}\end{Bmatrix}$$

$$=\frac{1}{2}\left(\frac{d\theta_L}{dt},\frac{d\theta_R}{dt}\right)\sum_{i=1}^{n}\rho_i J_{\text{AREA-i}}L_i\begin{bmatrix}F_{11_i} & F_{12_i}\\ F_{21_i} & F_{22_i}\end{bmatrix}\begin{Bmatrix}\frac{d\theta_L}{dt}\\ \frac{d\theta_R}{dt}\end{Bmatrix} \tag{16}$$

where the elements of $[F]$ are

$$F_{11_i}=\frac{1}{3}\ (P_{L_i}^2+P_{L_i}P_{L_{i+1}}+P_{1_{i+1}}^2)$$

$$F_{12_i}=\frac{1}{6}\ (2P_{L_i}P_{R_i}+P_{L_i}P_{R_{i+1}}+P_{L_{i+1}}P_{R_i}+2P_{L_{i+1}}P_{R_{i+1}})$$

$$F_{21_i}=F_{12_i}$$

$$F_{22_i}=\frac{1}{3}\ (P_{R_i}^2+P_{R_i}P_{R_{i+1}}+P_{R_{i+1}}^2) \tag{17}$$

The sums of the 2 × 2 matrices in the center of the product given above is the shaft inertia matrix for the Rayleigh model:

$$[J_S]=\begin{bmatrix}\Sigma\rho_i J_{\text{AREA-i}}L_iF_{11_i} & \Sigma\rho_i J_{\text{AREA-i}}L_iF_{12_i}\\ \Sigma\rho_i J_{\text{AREA-i}}L_iF_{21_i} & \Sigma\rho_i J_{\text{AREA-i}}L_iF_{22_i}\end{bmatrix} \tag{18}$$

The quantity J_{S11} is the portion of the shaft inertia that is to be added to the station at the left end of the section, and similarly, J_{S22} is to be added to the station at the right end. The off-diagonal terms, J_{S12} and J_{S21}, describe a dynamic coupling situation. Thus the quantity $J_{S12}\ d^2\theta_R/d^2t$ must be included in the equation of motion for the disk at the left end of the section. In the same fashion, the term $J_{S21}\ d^2\theta_L/d^2t$ is required in the equation of motion for the station at the right end of the section.

At an interior station there will be contributions to the equation of motion from stations both to the left and to the right. At the ends, the contribution is from one side only. The inertia matrix for the complete shaft has the triple band diagonal form

$$[J_{SS}]=\begin{bmatrix}J_{S_{11}} & J_{S_{12}} & 0 & 0 & 0 & 0\cdots & 0\\ J_{S1_{21}} & J_{S1_{22}}+J_{S2_{11}} & J_{S2_{12}} & 0 & 0 & 0\cdots & 0\\ 0 & J_{S2_{21}} & J_{S2_{22}}+J_{S3_{31}} & J_{S3_{12}} & 0 & 0\cdots & 0\\ 0 & 0 & \ddots & \ddots & \ddots & 0\cdots & 0\\ \vdots & & & & & & 0\\ \vdots & & & & & & \ddots\\ 0 & 0 & 0 & \cdots\cdots & & 0\ \ddots & \ddots\end{bmatrix} \tag{19}$$

It is necessary at this point to consider how this shaft inertia matrix can be used, still keeping with the station-to-station sequential calculation associated with the Holzer approach. To that end, the equations of motion for the system are first written in matrix form for a model consisting of N_{STA} stations:

$$([J_{\text{STA}}]+[J_{SS}])\begin{Bmatrix}\frac{d^2\theta_i}{d^2t}\end{Bmatrix}+[K]\{\theta_i\}=\{T_i^E\} \tag{20}$$

where

$\{\theta_i\}$ = column vector of angular displacements (N_{STA} × 1),

$[J_{\text{STA}}]$ = diagonal matrix of station (disk) inertias (N_{STA} × N_{STA}),

$[J_{SS}]$ = triple band diagonal matrix of shaft inertia contributions (N_{STA} × N_{STA}),

$[K]$ = triple band diagonal stiffness matrix (N_{STA} × N_{STA}),

$\{T_i^B\}$ = column vector of external torques (N_{STA} × 1).

If all displacements are assumed to be harmonic at frequency ω, the displacement vector can be written as

$$\{\theta_i\}=\{A_i\}\ \sin\omega t \tag{21}$$

This form is differentiated, substituted into Eq. (20), and the equations written for all stations. If the equations are written out, they will appear as

$$K_{11}-\omega^2(J_1+J_{SS_{11}})]A_1+(K_{12}-\omega^2J_{SS_{12}})A_2=T_1^E$$

$$(K_{21}-\omega^2J_{SS_{21}})A_1+[K_{22}-\omega^2(J_2+J_{SS_{22}})]A_2$$

$$+(K_{23}-\omega^2J_{SS_{23}})A_3=T_2^E$$

$$\vdots$$

$$(K_{\text{NSTA-1 NSTA-2}}-\omega^2J_{SS_{\text{NSTA-1 NSTA-2}}})A_{\text{NSTA-2}}$$

$$+(K_{\text{NSTA-1 NSTA-1}}-\omega^2(J_{\text{NSTA}}+J_{SS_{\text{NSTA-1 NSTA-1}}})A_{\text{NSTA-1}}$$

$$+(K_{\text{NSTA-1 NSTA}}-\omega^2J_{SS_{\text{NSTA-1 NSTA}}})A_{\text{NSTA}}=T_{\text{NSTA-1}}^E$$

$$(K_{\text{NSTA NSTA-1}}-\omega^2J_{SS_{\text{NSTA NSTA-1}}})A_{\text{NSTA-1}}$$

$$+[K_{\text{NSTA NSTA}}-\omega^2(J_{\text{NSTA}}+J_{SS_{\text{NSTA NSTA}}})]A_{\text{NSTA}}=T_{\text{NSTA}}^E \tag{22}$$

If A_1 is assigned any convenient value, say A_1 = 1.0, then the first of these equations can be solved for A_2. With both A_1 and A_2 known, the value for A_3 can be determined from the second equation. Evidently, the first N_{STA}-1 equations are sufficient to determine all of the displacements. The final equation can be reformulated to include a term representing the (nonexistent) torque to the right of the last station. It was omitted when the equations were written earlier, but it can be easily introduced at this point.

For a natural frequency determination, all of the T_i^E are set to zero, a value is assumed for ω, and the calculations made to evaluate the torque to the right of the last station. When this torque has been reduced to zero by proper choice for ω, that value of ω is a natural frequency.

For a harmonic forced response calculation at a frequency Ω, the process is more lengthy. For the first step, all of the T_i^E are set to zero, A_1 is set to 1.0, and the calculations carried out at frequency Ω to evaluate the residual torque to the right of the last station, R_1. Secondly, all of the T_i^E are set to their actual values, A_1 is set to 0.0, and the calculations are made again at frequency Ω to determine the residual torque value, R_2. The correct initial amplitude, satisfying the boundary conditions at both ends, is then determined from

$$A_1=-\frac{R_2}{R_1} \tag{23}$$

If the calculations are made again at frequency Ω with the T_i^E set to their actual values and using the value of A_1 determined from Eq. (22), the residual will be zero.

The development given above was done without damping, and damping is clearly important in many cases of interest. The modified development to include viscous damping from station-to-station and from station-to-ground follows the general outline of the development above. This completes the development of the Rayleigh shaft model.

Table 1 Torsional natural frequencies for a uniform rod; all frequencies are in rad/s

	Exact	Holzer-A[1]	Holzer-B[2]
Mode 1	20 032	24 434 (+22)	19 950 (-.4)
Mode 2	40 065	48 266 (+20)	39 409 (-2)
Mode 3	60 097	70 909 (+18)	57 897 (-4)
Mode 4	80 129	91 807 (+15)	74 960 (-6)
Mode 5	100 162	110 444 (+10)	90 177 (-10)
Mode 6	120 194	126 362 (+ 5)	103 174 (-14)
Mode 7	140 226	139 168 (- .8)	1136 30 (-19)

Notes:

[1] Holzer-A uses 1/3 of the mass of each section lumped to each end.

[2] Holzer-B uses 1/2 of the mass of each section lumped to each end.

- The quantity in parentheses is the percent error, in each case compared to the exact value.

Comparisons

In order to evaluate the utility of the Rayleigh model for shaft inertia, three test cases are considered below. For most purposes, it appears reasonable to consider the Eshleman model to be the most nearly correct for cases where the necessary assumptions are met; it is the closest approximation to reality of the three models considered.

Case 1: Torsional Natural Frequency of a Uniform Circular Rod. For this comparison, the torsional natural frequency of a uniform circular rod, 20 mm in diameter and 500 mm in length, is evaluated using each of the three models. Since there are no added disks, this is a problem that is particularly sensitive to the inertia of the shaft. For this, and for the later cases as well, the specific weight of the material is 76,500 N/m^3, the shear modulus for the materials is 7.93×10^{10} Pa, and the acceleration of gravity is taken as 9.806 m/s^2.

This is a problem for which there is an exact solution available for comparison, based on the wave equation model (Dimarogonas and Haddad, 1992, p. 422).

$$\omega_n = \frac{n\pi}{L}\sqrt{\frac{Gg}{\gamma}} \tag{24}$$

where n = mode number,

ω_n = natural frequency for nth mode,

G = shear modulus for material,

L = length of section,

γ = specific weight of material,

g = acceleration of gravity.

The results are presented in Tables 1 and 2.

The results shown in Table 1 indicate the variability associated with the arbitrary lumping procedure applied to the Holzer calculation. Depending on the amount of the shaft inertia lumped to each end of a section, there is an approximate difference of 19–22 percent, as the fraction is varied between 1/3 to 1/2. Essentially, any desired result, over a wide range, can be obtained simply by the choice of the fraction to be lumped to each end. It is interesting to note that the percent error decreases (algebraically, as a signed value) with increasing mode number.

Table 2 shows the results from the Eshleman and Rayleigh models compared to the exact solution. It is not surprising that the Eshleman model predicts exactly the correct values (to the accuracy of the numerical calculation); it is a form of the same model used for the exact solution.

Table 2 Torsional natural frequencies for a uniform bar; all frequencies are in rad/s

	Exact	Eshleman	Rayleigh
Mode 1	20 032	20 032 (0)	20 115 (+ .4)
Mode 2	40 065	40 065 (0)	40 727 (+1.7)
Mode 3	60 097	60 097 (0)	62 338 (+3.7)
Mode 4	.80 129	80 129 (0)	85 443 (+6.6)
Mode 5	100 162	100 162 (0)	110 444 (10.3)
Mode 6	120 194	120 194 (0)	137 423 (14.3)
Mode 7	140 226	140 226 (0)	165 616 (18.1)

The quantity in parentheses is the percent error, in each case compared to the exact value.

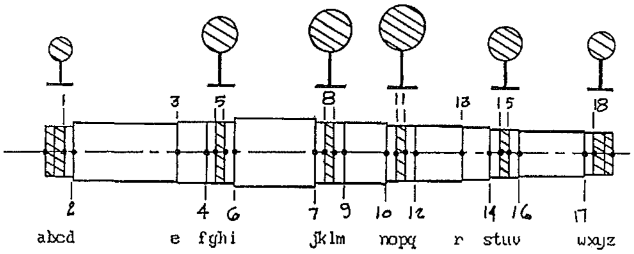

Fig. 5 Stepped shaft

The results obtained from the Rayleigh model show the percent error increasing with increasing mode number, exactly opposite to the results obtained from the Holzer model. Since this is a Rayleigh model, the calculated natural frequencies are known to err consistently on the high side (Thomson, p. 271).

Case 2: Torsional Natural Frequencies of a Stepped Shaft With Added Disks. This case is based on the stepped shaft and six disks shown in Fig. 5. The dimensional data for the shaft are given in Table 3, along with identification of the shaft model nodes corresponding to the disk locations and the effective stiffness calculated for each shaft section. The inertia data for the disks are given in Table 4.

At the location of each disk, the motion from either side is assumed to penetrate 1/3 of the hub length. The center 1/3 of the shaft inside the hub is assumed to rotate with the disk, so the inertia of that part is added directly to the inertia of the disk. In order to focus attention on the differences in the inertia modeling, there has been no attempt to incorporate the additional flexibility associated with each step; this could not be done in the Eshleman model as pointed out above

For the Holzer model used here and in the following case, only that part of the shaft assumed not to twist is included in the model; the twisting portion of the shaft is assumed to be massless.

The Eshleman model used for this and the following case consists of 18 stations. This gives a model for which the uniform shaft assumption of the Eshleman model is satisfied.

For the Rayleigh model used here and in the following case, the terms on the diagonal in the $[J_{SS}]$ matrix range from 4.1×10^{-4} to 8.0×10^{-3} kg-m^2. The off-diagonal terms range from 28.1×10^{-5} to 2.6×10^{-4} kg-m^2. Because these values are in the range three to five orders of magnitude less than the disk inertias, it is to be expected that they will have only a small effect on the results.

The results are tabulated in Table 5. It is not surprising that the Holzer model predicts the highest natural frequencies; the twisting shaft segments have been assumed to be completely

Table 3 Shaft dimensional data; all dimensions are in millimeters

Node	Axial Pos	Diam to Right	Section Stiffness N-m/rad.
a	0	80	
b	20	80	
c	40	80	
d	60	95	$Sta.1$
e	280	98	
f	340	100	$K_1 = 1.9371 \cdot 10^6$
g	360	100	
h	380	100	$Sta.2$
i	400	115	
j	570	100	$K_2 = 5.6745 \cdot 10^6$
k	590	100	
l	610	100	$Sta.3$
m	630	98	
n	720	92	$K_3 = 5.3510 \cdot 10^6$
o	740	92	
p	760	92	$Sta.4$
q	780	90	
r	880	85	$K_4 = 2.1717 \cdot 10^6$
s	940	75	
t	960	75	
u	980	75	
v	1000	72	$Sta.5$
w	1140	68	
x	1160	68	$K_5 = 1.1488 \cdot 10^6$
y	1180	68	
z	1200	68	$Sta.6$

Table 4 Mass moments of inertia for added rigid disks

Station	Mass MOI kg-m^2
1	1.00
2	2.50
3	3.00
4	3.30
5	2.00
6	1.50

Table 5 Comparison of computed natural frequencies; all frequencies are in rad/s

	Holzer	Eshleman	Rayleigh
Mode 1	671.3406	670.3001	670.3028
Mode 2	1146.3786	1144.1104	1144.1168
Mode 3	1477.5882	1475.7432	1475.7453
Mode 4	1822.2415	1819.6658	1819.6649
Mode 5	2464.2012	2461.4079	2461.4170

Table 6 Comparison of harmonic forced response; all rotations in milliradians

	Holzer	Eshleman	Rayleigh
$\Omega = 650$ rad/s			
Sta. 1	3.3818	3.5244	3.5241
Sta. 2	2.1205	2.2262	2.2259
Sta. 3	1.2972	1.3666	1.3664
Sta. 4	1.1673	1.2901	1.2896
Sta. 5	−2.8670	−3.0028	−3.0025
Sta. 6	−6.3980	−6.7088	−6.7080
$\Omega = 1300$ rad/s			
Sta. 1	−0.4351	−0.3144	−0.3145
Sta. 2	−0.5598	−0.5541	−0.5542
Sta. 3	−0.2190	−0.2194	−0.2194
Sta. 4	0.3499	0.3450	0.3450
Sta. 5	0.8529	0.8470	0.8470
Sta. 6	−0.7063	−0.7010	−0.7011
$\Omega = 1950$ rad/s			
Sta. 1	−0.7652	−0.7514	−0.7514
Sta. 2	0.2276	0.2204	0.2204
Sta. 3	0.1832	0.1797	0.1797
Sta. 4	−0.2547	−0.2487	−0.2487
Sta. 5	0.1384	0.1351	0.1351
Sta. 6	−0.3488	−0.3409	−0.3409

massless. If a fraction of the shafting inertia is included, the calculated natural frequencies move down accordingly.

The results of the Eshleman model should again be considered as the basis for comparison. The assumption of uniform circular shaft segments has been met, so this model closely approximates the physical system. Its greatest drawback is its relatively large size.

The Rayleigh model in remarkably close agreement with the Eshleman model, even though only six stations were used. As expected for a Rayleigh model, the natural frequencies are (very) slightly above the true values.

Case 3: Harmonic Forced Response for a Stepped Shaft With Added Disks. The system considered here is again the stepped shaft with six disks shown in Fig. 5, with all dimensions and material properties unchanged. The shaft is excited with a sinusoidal torque of amplitude 1000 N-m with three excitation frequencies considered: 650 rad/s, 1300 rad/s, and 1950 rad/s.

The result of all three models at the three excitation frequencies is given in Table 6. The location of these excitation frequencies with respect to the natural frequencies determined in Case 2 (Table 5) should be noted. The most notable aspect of these results is again the very close agreement of the six-station Rayleigh model with the 18-station Eshleman model. The Holzer model is not in nearly such close agreement.

Conclusion

The Rayleigh model offers an attractive alternative to the Eshleman model. This is significant because of the ability to handle stepped shafts, the ability to include all types of discrete damping, and the lesser number of stations required for comparable results. It seems clear that this alternative will degrade progressively as the frequencies involved go higher. The limitation is ultimately a question of how well a sequence of straight lines can approximate the sinusoid that describes the true displacement.

While it may appear that the calculations required to implement the Rayleigh model are involved, the whole process is readily automated within a computer program. This makes the additional modeling effort invisible to the user.

References

Dimarogonas, A. D., and Haddad, S., 1992, *Vibration for Engineers*, Prentice-Hall, Englewood Cliffs, NJ.

Eshleman, R. L., 1974, "Torsional Response of Internal Combustion Engines," ASME *Journal of Engineering for Industry*, Vol. 96, pp. 441-449.

Holzer, H., 1921, *Die Berechnung der Drehschwingungen*, Springer-Verlag, Berlin.

Porter, F. P., 1943, "Harmonic Coefficients of Engine Torque Curves," ASME *Journal of Engineering for Industry*, Vol. 65, pp. A-33-A-48.

Thomson, W. T., 1993, *Theory of Vibration With Applications*, 4th ed., Prentice-Hall, Englewood Cliffs, NJ.

Timoshenko, S., 1928, *Vibration Problems in Engineering*, Von Nostrand, New York.

Tuplin, W. A., 1934, *Torsional Vibration*, Wiley, New York.